A Control Volume Unstructured Grid Approach to the Solution of the Elastic Stress - Strain Equations

YVONNE DELIA FRYER

A thesis submitted in partial fulfilment of the
requirements of the University of Greenwich
for the Degree of Doctor of Philosophy

December 1993

Centre for Numerical Modelling and Process Analysis
School of Mathematics Statistics and Computing
University of Greenwich
London, UK.

DEDICATION

For my father,
JOHN DENNIS FRYER
(11/10/21 - 8/7/93)

ACKNOWLEDGEMENTS

There are two groups of people who are to be thanked for their help over the duration of this research.

The first group are those people with some connection with the project who have provided help as well as encouragement. The first of this group is my first supervisor Professor Mark Cross, who has been a great source of advice and guidance for me at all stages of the work. Other researchers at the University that have contributed to the project over the years, and are to be thanked for answering my questions, are Chris Bailey, Peter Chow, Andy Chan, Choi-Hong Lai and Koulis Pericleous. Finally thanks go to Keith Preddy for the entertaining metallurgy lectures and the provision of experimental data, and Professor John Campbell for information on porosity formation.

The second group of people are those who are unconnected with the project, but have given me the support and encouragement to finish it. These include fellow researchers at the University, especially Miltiadis Petridis for his patience, understanding and diversion tactics and Surita Nadarajan and Cos Ierotheou for the more entertaining times. Lastly in this group are all my family and friends who have been very patient and understanding, particularly my parents who have always encouraged me whilst at the University of Greenwich.

Finally, the financial support provided by the S.E.R.C. is gratefully acknowledged.

ABSTRACT

The aim of the research is to develop and apply algorithms for the solution of elastic stress-strain equations based upon a control volume approach on unstructured meshes. The purpose is to integrate the solution of solid mechanics with that of fluid flow and heat transfer within the context of solidification problems in the casting of metals.

The conventional way of solving stress-strain problems is to use a finite element approach which yields a set of linear equations relating loads to displacements. This approach works very well and can also deal well with temperature loading, but becomes problematic when flow and change of phase are included in a transient context. A major set of projects are under way to develop an integrated suite of algorithms to model the flow-cooling-solidification-residual stress development process. This project concerns the component associated with the development of stress-strain distributions under temperature and other loads.

A control volume formulation solution procedure for the elastic stress-strain equations in two-dimensions has been developed that solves directly for displacements. The formulation works for mixtures of quadrilateral and triangular elements in an unstructured mesh. The control volume finite element code has been tested on a range of problems, such as a cantilever loaded at one end, a beam with a thermal gradient applied and a multi-material mixed element non-regular shape with a load applied. The results for these test cases have been compared to those obtained by standard finite element codes and analytical solutions where available. Besides the plane stress and plane strain options, the model has been extended to include axisymmetric problems. Two examples are used to test the validity of the algorithm for axisymmetric problems. The results compare very well against other numerical results and analytic solutions for the three special two-dimensional cases.

Another problem considered at an interface is that of friction between two solids. This non-linear boundary condition has been included in the model. An example of this is Silica in a mould being pressed, results for the stress-strain code are compared to previous results.

The control volume stress-strain code has been integrated with the solidification heat transfer code. Problems of simple castings have been considered. When a liquid solidifies it may deform away from the mould, so possible air gap formation at the mould/metal interface has been included in the model. Prediction of hole formation in solidification, in the form of volumetric shrinkage and porosity, has been included into the coupled heat transfer stress code via a simple model. Examples show encouraging results when compared to experimental porosity results.

CONTENTS

LIST OF ILLUSTRATIONS

Figure **Page**

Figure Page

Figure **Page**

Figure **Page**

LIST OF TABLES

Table **Page**

Table **Page**

Chapter 1
Introduction

This chapter details the reasons for performing the research described in this thesis. The aim of the research is to produce a deformation algorithm that couples easily with a computational fluid dynamics procedure using a generically similar solution technique that can be applied to the casting process. Existing methods of solving the elastic stress-strain equations are discussed including brief details concerning solution of the computational fluid dynamics equations by the same methods. The new technique combining the control volume method and unstructured meshes for solving the elasticity equations is presented along with details of its use in heat transfer and solidification codes. A brief outline of the following chapters is then presented.

1.1 Existing Numerical Solution of the Elasticity Equations

The historical background of the three main discretisation techniques, finite difference or finite volume, finite element and boundary element methods, with respect to solid mechanics are briefly detailed. Where appropriate the influence of a particular method in the computational fluid dynamics area is also mentioned.

1.1.1 Finite Difference Method

Timoshenko and Goodier (1970) attribute the first application of finite difference equations in elasticity to Runge when solving torsional problems around 1908, where the problems were reduced to a linear system of equations. A couple of years later Richardson solved such algebraic equations with an iterative process resulting in approximate values of the stresses produced in dams by gravity forces and water pressure. More publications resulted on the finite difference method by Southwell in 1946.

A variety of attempts have been made over the years to solve the elastic stress-strain equations using finite difference based approaches. One of the earliest approaches for two-dimensional problems derived an equation with the Airy stress function, Ψ, as the one variable [Griffin and Varga (1963)]. Although a finite difference discretisation of this fourth-order equation in Ψ can be solved relatively straightforwardly, it was not amenable to complex geometries for all the usual reasons and so has effectively been abandoned.

Some attempts to solve the coupled displacement equations iteratively were reported in the 1960s and subsequently, but only for rather restricted forms of boundary conditions [Konovalov (1964), Samarskii (1964), Havner and Stanton (1967), Johnson (1970)].

With the advent of computers, it became possible to provide numerical solutions to several thousand linear equations. Griffin and Kellogg (1967) used a finite difference method for the solution of axially symmetric and plane elasticity problems making use of the then high speed digital computers available. Winslow (1966) used a triangular mesh and Concus (1967) a rectangular mesh to demonstrate the applicability of the finite difference method to two-dimensional magnetostatic problems.

In the past 20 years there has been a focus upon finite difference or, in its cell integrated form, control volume otherwise called finite volume, approaches to the solution of problems involving fluid flow such as in the area of computational fluid dynamics. Computational fluid dynamics deals with the solution of discretised forms of the partial differential equations representing transport of mass, momentum and energy. The reason for the success is that in primitive variable form, the solution of the velocity components and pressure requires a strongly coupled solution procedure that is best effected at a nodal level [Patankar (1980)]. Hence the solution of computational fluid dynamics problems in a control volume context involves iteration to solve for all variables at a node and then over the whole set of nodes, repeatedly until convergence is obtained.

In the last few years interest in control volume formulations has been revived in an attempt to produce an integrated analysis framework, and so further work has been published by a number of workers [Ng and Benchariff (1989), Dow, Jones and Harwood (1990), Hattel and Hansen (1990)].

Hattel and Hansen (1991) use a finite difference method technique to solve the three-dimensional elasticity equations using a staggered mesh. Solidification results and temperature values are obtained from the Magmasoft code when solving the deformation and stress prediction of a casting problem.

The algorithms described in the above papers definitely work on the problems shown where appropriate but are either rather complex, using large discretisation molecules, and so unsuitable for unstructured meshes or restrictive in their potential capability.

With regard to the representation of the physical complexity of flow processes, control volume-based computational fluid dynamics codes have certainly represented the state of the art in most cases [PHOENICS, FLUENT, FLOW3D]. However, until recently, they have been behind the finite element community in two respects, firstly using a structured mesh has restricted codes in their representation of complex geometries and secondly no practical algorithms existed in a control volume framework for modelling deformation processes.

1.1.2 Finite Element Method

The finite element method is a numerical procedure for solving the differential equations of physics and engineering, prominent names include Argyris, Clough and Zienkiewicz. More detailed historical accounts of finite element development can be found in Segerlind (1976), Zienkiewicz (1970),(1983) and Zienkiewicz and Taylor (1989). It is generally agreed that the finite element method developed in the 1950's is a useful tool in the aerospace industry for providing solutions to stress analysis problems, where the great rewards for slight improvements in weight made it profitable to pioneer the development and application of the new technique. There was early work in the 1940's by people such as Hrenikoff, presenting a useful but limited method solving plane stress problems by replacing plate elements with bars thus reducing a plate problem to one in structural analysis [Bowes and Russell (1975)]. The credit of approximating directly to a continuum region by an element with multiple connecting points must go to Turner, Clough, Martin and Topp (1956) when the first complete presentation of the method was made. The publication stimulated other researchers and resulted in several technical articles that discussed the application of the method to structural and solid mechanics plus the name finite element method was adopted. The derivation of the basic properties was achieved by physical arguments relating stress or displacement distribution within the subregion [Zienkiewicz (1970)].

The main catalysts behind the rapid development of the finite element method were the evolution of computers at the same time as the practical demands of the engineers which lead to the solution of real complex elastic problems. The finite element method is not very practical without the aid of computers with large amounts of storage space required, and so development of the method and machines has progressed at much the same pace [Bowes and Russell (1975)].

Only in the late 1960's did mathematicians take a widespread interest in the method and subsequently contributed significantly to the theoretical understanding and refinement of the method [Owen and Hinton (1980)]. Melosh (1963) showed that the finite element method was really a variation of the well known Raleigh-Ritz procedure. The connecting of the finite element method with a minimisation procedure quickly led to its use in other engineering areas. The method can be applied to problems governed by the Laplace or Poisson equations because the equations are closely related to the minimisation of a functional [Segerlind (1976)]. With the irregular elements there followed rapid extension of finite element method into nonstructural fields such as Zienkiewicz and Cheung (1965) who demonstrate the applicability to fluid mechanics and heat conduction. The application to fluid flow mechanics followed immediately [Zienkiewicz (1970)].

It soon became evident that all the features of the finite difference method and indeed of other numerical procedures were particular examples of the generalised trial function, finite element method. Thus Zienkiewicz (1977) concluded that it must contain all the merits of the other techniques plus additional advantages. The method is now firmly established as a powerful and versatile solution technique for a large range of advanced engineering problems. The advancement from a numerical procedure for solving structural problems to a general numerical procedure for solving differential equations or a system of differential equations has been accomplished in 15 years aided by the advancement of computers [Segerlind (1976)].

Cook, Malkus and Plesha reported on the recent research activity concerning the finite element method [Ottosen and Petersson (1992)], that only 10 papers were published in 1961 on the finite element method increasing to a cumulative total of over 20,000 by 1986. There are many books on the finite element method such as Zienkiewicz (1977), Zienkiewicz and Taylor (1989) and Ottosen and Petersson (1992).

The advantages of the finite element method are; the material of individual elements can vary, irregular domains are no longer a problem, the size of the element can be varied and boundary conditions such as discontinuous surface loadings present no problem. The disadvantages include the unstructured mesh that results in very large system matrices. When it comes to topological considerations the finite element method has the edge while for highly nonlinear flows involving turbulence and/or combustion control volume methods are preferable.

Exact stress analysis by the theory of elasticity can be done in very few bodies of simple geometry and those only when the loads are of particular form. Finite difference approximations have extended the categories of problems that can be solved enabling the problems to be converted from those expressed in partial differential equations to simultaneous linear equations that can be solved to give approximate solutions. Although this extends the realm of tractable problems, setting up each new problem is a formidable programming task. The energy approach to the finite element method does not deal with partial differential equations of equilibrium or compatibility. The elastic stress-strain equations over a finite element mesh can be transformed into a linear system of equations relating force and displacement at a point, which can be solved by various elimination techniques. Solving problems by the finite element method therefore requires a working knowledge of matrix methods. Using finite elements the types of problems that can be solved are almost limitless, as a result of this all the significant software products that address the problems of solid deformation under load are finite element based such as ANSYS, ABAQUS and NASTRAN. Finite element based procedures have been used successfully over the past 30 years for the solution of a whole range of very complex deformation problems, dominating the solution of deformation processes [Zienkiewicz (1977)].

[Zienkiewicz and Oñate (1990), Oñate, Cervera and Zienkiewicz (1992)] compared a finite volume method using triangular elments to the finite element method when applied to structural mechanics problems. They found the finite element method to be more accurate.

1.1.3 Boundary Element Method

There has been comparatively recent interest in the boundary element method, also known as the boundary integral equation method, for solving engineering problems [Fenner (1986)], with a small number of books available on subject such as Jaswon and Symm (1977), Brebbia (1978), Chen and Zhou (1992). The boundary element method has developed in the shadow of the finite difference and finite element methods [Crouch and Starfield (1983)].

The term boundary elements is used to indicate the method whereby the external surface of a domain is divided into a series of elements over which the functions under consideration can vary in different ways, in much the same manner as finite elements [Brebbia (1978)]. This capacity is very important as, previously integral equation type formulations were generally restricted to constant sources assumed to be concentrated at a series of points on the external surface of the body. Crouch and Starfield (1983) claim that the boundary element methods are inherently very simple to use and flexible for many kinds of problems, yet they have not received the attention they deserve, particularly in the various fields of engineering practice dominated by finite elements and finite difference methods.

The boundary element technique claims several important advantages over 'domain' type solutions such as finite elements and finite differences [Brebbia (1978)]. It requires a much smaller system of equations than the previous methods mentioned which results in a reduction in data needed to run a problem. In addition the numerical accuracy of boundary elements is generally greater than that of finite elements. The advantages are more noticeable in two-dimensional and three-dimensional problems. The method is also suited to problem solving with infinite domains such as those frequently occurring in soil mechanics and hydraulics for which the classic domain methods are unsuitable.

Several reasons are given for the lack of use of the method [Crouch and Starfield (1983)]. Firstly, there are a number of general finite difference and finite element packages that exist, but the boundary element programs that exist have generally been written to solve specific problems for certain groups of users. Secondly, practical papers on boundary element methods describe the subject in the context of a particular problem, so that it is not always evident that method applied to one type of problem applies to another. Thirdly, Crouch and Starfield (1983) consider, the theoretical papers on boundary element methods to be viewed by many scientists and engineers as somewhat incomprehensible.

Computers have increased the general awareness and understanding of the method with accurate numerical results to many continuum mechanics problems being produced. Boundary element methods *do provide fast and efficient techniques for obtaining* boundary displacement and stress results, but are not to be used here because of the need for an algorithm that is compatible with computational fluid dynamics.

1.2 Control Volume-Unstructured Mesh Method

There are an increasing range of problems that require the solution of both flow and deformation simultaneously. Two such problem areas include fluid-solid interaction and the casting of metals components, which involves a transformation from liquid to solid as the key feature of its processing.

The eventual casting code should handle all the major components of the casting process: the mould filling, heat transfer, solidification, residual stress development and deformation of cast. All these components have previously been solved independently and by a variety of methods. It is hoped the control volume-unstructured mesh method can deal with all the processes mentioned simultaneously and with the same qualities that have been shown by the individual methods.

Recently there has been clear evidence that both methods, finite elements and finite volume, are moving toward a common ground. Algorithms and techniques developed solely for use by one method are now being adapted and employed in a similar procedure by the other. Therefore in future will be difficult to distinguish between the two techniques resulting in hybrid methods.

Finite element formulations to solve the navier-Stokes equations have been developed that tend to involve a cross between the control volume-computational fluid dynamics approach with the solver route followed in conventional finite element analysis [Minkowycz, Sparrow, Schneider and Pletcher (1988)]. Such codes, for example FIDAP, can be accurate but are generally relatively more expensive in computer time, since convergence is a good deal more difficult to achieve than with full control volume formulations. Recently, finite element algorithms for free surface flows based upon the ideas of the VOF-control volume fraternity have begun to emerge [Gao, Dhatt, Belanger and Ben Cheikh (1989), Lewis, Usamani and Huang (1991)]. Hence at this stage for Casting simulation it appears that the finite element approach has the potential to address all the key physical components of the technology, albeit rather more slowly than its control volume counterpart.

In the past year or two a significant effort has been made to develop conventional control volume-computational fluid dynamics algorithms in the context of unstructured meshes. Three commercial computational fluid dynamics-codes based upon control volume-unstructured mesh formulations have recently appeared in the marketplace; RAMPANT, ASTEC and STAR-CD represent some products of this effort. Other work has demonstrated the efficacy of control volume-unstructured mesh algorithms in the solution of solidification problems [Chow and Cross (1992)]. Hence the one remaining research issue with regard to assembling a comprehensive analyses capability within a control volume-unstructured mesh framework is the development of practical algorithms for the solution of, initially, elastic deformation processes. The purpose of this thesis is to describe just such an approach in the context of an unstructured mesh [Fryer, Bailey, Cross and Lai (1991)]: an algorithm for the solution of elastic-stress strain equations in two dimensions, subject to both temperature and other body force loading, is described. The algorithm is readily extendable to three-dimensional domains, and the resulting code can be modularised so that it easily bolts onto any existing control volume-computational fluid dynamics code.

For the solution of the elasticity equations the vertex centred approach of the control volume-unstructured mesh method is used here so that it can be fully coupled with the fluid flow, heat transfer and solidification code of Chow (1993). The fully integrated code is then applied to the casting processes, in an effort to avoid the problems of previous casting codes with respect to a lack of integration between the solidification code and the stress code.

The control volume-unstructured mesh (CV-UM) methods can in general be categorised into two types, a vertex-centred or cell-centred approach. The classification of the approach is based on the relationship between the control volume and the finite element style unstructured mesh. The vertex-centred approach of the control volume-unstructured mesh technique, also known as the control volume based-finite element method, was originally presented in the late seventies and early eighties by Baliga and Patankar

(1980). The basic idea behind the method is to discretise the calculation domain into elements, just like in finite element calculation, a control volume is then formulated around the vertices of the element and the conservation principles applied to it. Baliga and Patankar (1980) described a general method for convection-diffusion problems in two-dimensions that used three node triangle elements to form polygonal control volumes as used by Winslow (1966). The method was soon extended to fluid flow and heat transfer [Baliga and Patankar (1983), Baliga, Pham and Patankar (1983)]. Like many finite element procedures the method was an unequal order type, where the pressure was computed at much fewer grid points than the velocity due to the use of macro and micro sub elements. Prakash and Patankar (1985) then proposed an equal-order velocity interpolation. Schneider and Raw (1986) using shape functions described a quadrilateral element control volume-based finite-element algorithm for convection diffusion problems. Many more enhancements of the control volume finite element methods followed with respect to fluid flow and heat transfer [Prakash (1986), (1987), Schneider and Raw (1987a), (1987b), Prakash and Patankar (1987a), (1987b), Hookey, Baliga and Prakash (1988), Hookey and Baliga (1988), Kettleborough, Hussain and Prakash (1989)]. Good descriptions of the method are given by Baliga and Patankar (1988), Schneider (1988). The method of Prakash (1987) has been applied by Letniowski and Forsyth (1991) in three-dimensions to groundwater contamination problems. The second approach described as cell-centred, or named irregular control volume method [Chow (1993)], is viewed as an extension of the control volume method [Patankar (1980)], since when a structured rectangular mesh is used it is a direct analogue of the standard control volume method.

1.3 Outline of Thesis

Chapter 2 contains details about how the elastic stress-strains equations were discretised for the special cases of plane stress and plane strain in cartesian coordinates and axisymmetry in cylindrical polar coordinates, using the control volume unstructured mesh approach. The resulting algorithm was developed as a FORTRAN program that has options of plane stress, plane strain or axisymmetry for possible thermally and mechanically loaded objects.

To test the validity of the algorithm and program developed in Chapter 2 various test cases for the plane stress and plane strain options, some with known analytical displacement or stress results, were examined in Chapter 3. Fryer, Bailey, Cross and Lai (1991) describe the algorithm development used in Chapter 2 and give brief examples demonstrating the soundness of the program, comparing the displacements obtained against analytical results and a standard finite element code results. The time taken for the program to reach a converged solution was noted and compared to the finite element program timing. Chapter 3 details the displacements and stresses obtained using a standard finite element code, IFECS, and compares these results and the time taken using the different techniques. The problems considered include a cantilever with a point loading, a thermally loaded beam and a multi-material cusp type problem. For each test case various mesh types such as quadrilateral elements, triangular elements and a mixed mesh containing both types of elements were used. The meshes were also refined to see the effect on the solutions with respect to how close they reached the analytical displacements. The effect of tolerance and relaxation parameter used were also studied. An example of a plate with a hole in the centre with forces applied at two edges was used to test the accuracy of the stress results obtained from the displacement results. Two test cases for the axisymmetric option of the program are used to test the validity of the algorithm and program comparing the results obtained to standard finite element results (MicroFIELD) and analytical results where appropriate. The axisymmetry results are shown in Chapter 3 where, as with the cartesian cases, the mesh size and type are altered to study the effect on the solution and the time taken to reach a converged solution. The examples studied include a hollow sphere with a linear temperature gradient through it in the radial direction and a thermally and mechanically loaded hollow sphere.

Friction at the surfaces of the object when it is in contact with a neighbouring object has been included into the program as a possible effect. Chapter 4 describes the development of the friction algorithm and the inclusion of it into the deformation code. Results were collected for a simple test block shape that 'slid' across another object. The displacements along the contact edge were noted and compared for results obtained when the block and neighbouring object were rotated to evaluate the generality of the friction algorithm in producing consistent relative displacement results. A silica brick with test case results was used as a test to check the friction consistency of displacement results.

In Chapter 6 the elastic stress-strain procedure is coupled with an existing heat transfer solidification procedure in the department that uses a similar control volume-unstructured mesh discretisation technique. The resulting code is fully coupled and integrated. The code is applied to castings where a molten material solidifies and deforms in a mould. Typically at the mould/metal interface the prediction of an air gap is included [Bailey, Fryer, Cross and Chow (1993)]. An example comparison of inclusion and exclusion of the deformation prediction, and hence the air gap formation, enable the visible effect on the temperature of the casting to be seen.

A porosity prediction model is included in the fully coupled heat transfer, solidification, deformation code in Chapter 6. The porosity model used is unlike others in the literature which are entirely empirical because it takes into account the deformation of the casting as it solidifies. The results produced for various test cases look encouraging when compared with experimental results where available [Fryer, Bailey, Cross and Chow (1993)].

Finally, conclusions and suggestions for future work are proposed in Chapter 7, with references and other auxiliary material completing the thesis.

Chapter 2

Control Volume - Unstructured Mesh Solution of the Stress-Strain Equations

This chapter explains the development of a control volume unstructured mesh code that solves the two-dimensional elastic stress-strain equations. The algorithm is developed for the two-dimensional options of plane stress, plane strain and axisymmetry. Discretisation of the algorithm using an unstructured mesh is detailed and attention to the solution procedure is also included. A computer program was written in FORTRAN 77 that can obtain the displacement of an object suitably approximated to either a plane stress, plane strain or axisymmetric condition. From the deformation of the object the stresses acting on the object can then be obtained.

2.1 Elasticity Equations

The three-dimensional stress equilibrium equations can be reduced to two-dimensional equations for special circumstances. The two-dimensional stress equilibrium equations for the plane stress, plane strain and axisymmetric instances are manipulated using integration techniques to obtain equations for the resulting deformation of an object when temperature effects and mechanical loading are applied to the object. The plane stress and plane strain options use the cartesian axis directions x and y result in the deformation u and v respectively. The axisymmetric alternative uses the cylindrical polar axis directions r and z to obtain the displacement of an object in terms of u and w respectively. More details concerning the derivation of the stress equilibrium equations and other stress-strain relationships used further in the derivation of the deformation algorithms can be found in numerous elasticity books such as Fenner (1986), Timoshenko and Goodier (1970) and Boley and Weiner (1967). The two-dimensional stress equilibrium equations are integrated over an unstructured control volume defined as Figure 2.1.

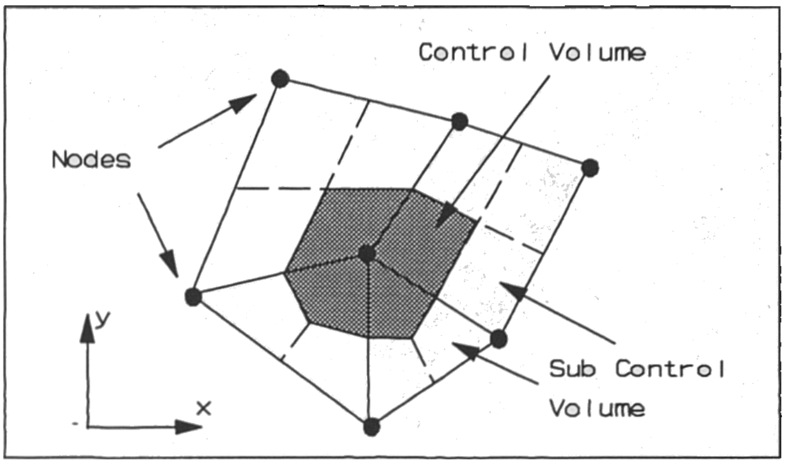

Figure 2.1: Control Volume for Unstructured Meshes

2.1.1 Plane Stress/Plane Strain Approximations

The three-dimensional elasticity stress equilibrium equations are shown in Appendix A.2 as documented in the elasticity books mentioned previously. Reducing the equations to axes directions x and y produces the two-dimensional stress equations for equilibrium shown below:

$$
\begin{aligned}
\frac{\partial \sigma_{xx}}{\partial x} + \frac{\partial \sigma_{xy}}{\partial y} + F_x &= 0 \\
\frac{\partial \sigma_{xy}}{\partial x} + \frac{\partial \sigma_{yy}}{\partial y} + F_y &= 0
\end{aligned}
\tag{2.1}
$$

The equations apply at each point within the solid where F_x and F_y are internal body forces. The equilibrium equations are integrated over any closed surface or control volume as seen in Figure 2.1 where the volume has unit thickness in the z-axis direction,

$$
\begin{aligned}
\iint\left(\frac{\partial\sigma_{xx}}{\partial x} + \frac{\partial\sigma_{xy}}{\partial y}\right)dx\,dy &= \iint -F_x\,dx\,dy \\
\iint\left(\frac{\partial\sigma_{xy}}{\partial x} + \frac{\partial\sigma_{yy}}{\partial y}\right)dx\,dy &= \iint -F_y\,dx\,dy
\end{aligned}
\qquad (2.2)
$$

Stokes's theorem [Bourne and Kendall (1992)] as in Appendix A.1, for two-dimensional cartesian coordinates applied to the cartesian equilibrium equations produces

$$
\begin{aligned}
\oint_c(\sigma_{xx}dy - \sigma_{xy}dx) &= \iint -F_x\,dx\,dy \\
\oint_c(\sigma_{xy}dy - \sigma_{yy}dx) &= \iint -F_y\,dx\,dy
\end{aligned}
\qquad (2.3)
$$

There are well known relationships between stress and displacement [Fenner (1986), Timoshenko and Goodier (1970)], the three-dimensional relationships are shown in Appendix A.2 for the stress-strain equations and the strain-displacement equations, where E represents Young's modulus, ν represents Poisson's ratio and α the coefficient of thermal expansion.

2.1.1.1 Plane Stress

One approximation to two dimensions can be made when the thickness of an object in the z-axis direction is small compared to its other dimensions as shown in Figure 2.2.

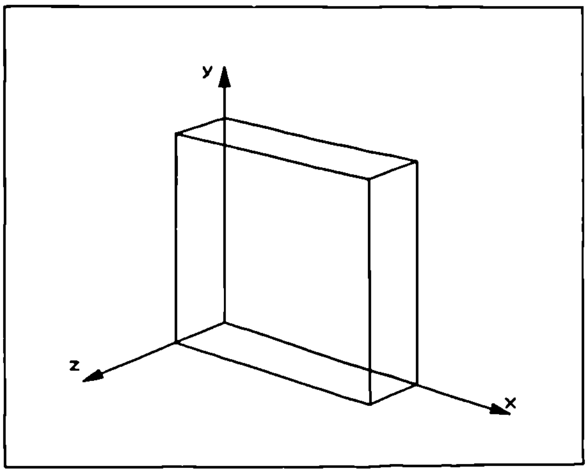

Figure 2.2: Plane Stress

If forces are applied at the boundary parallel to the plate and distributed uniformly over the thickness, then the stresses in the z-axis direction are assumed to be extremely small and approximated to zero such that:

$$\sigma_{zz} = \sigma_{xz} = \sigma_{yz} = 0 \tag{2.4}$$

which results in the following stress-displacement equations including possible temperature loading for the plane stress approximation:-

$$\begin{aligned}
\sigma_{xx} &= \frac{E}{(1-\nu^2)}\left\{\frac{\partial u}{\partial x} + \nu\frac{\partial v}{\partial y} - (1+\nu)\alpha T\right\} \\
\sigma_{yy} &= \frac{E}{(1-\nu^2)}\left\{\frac{\partial v}{\partial y} + \nu\frac{\partial u}{\partial x} - (1+\nu)\alpha T\right\} \\
\sigma_{xy} &= \frac{E}{2(1+\nu)}\left\{\frac{\partial u}{\partial y} + \frac{\partial v}{\partial x}\right\}
\end{aligned} \tag{2.5}$$

Substituting the stress-displacement equations (2.5) into the integrated equilibrium equations (2.3) yields

$$\begin{aligned}
&\oint_c \left(\frac{E}{(1-\nu^2)}\frac{\partial u}{\partial x}.dy - \frac{E}{2(1+\nu)}\frac{\partial u}{\partial y}.dx\right) = S_u \\
&\oint_c \left(\frac{E}{2(1+\nu)}\frac{\partial v}{\partial x}.dy - \frac{E}{(1-\nu^2)}\frac{\partial v}{\partial y}.dx\right) = S_v
\end{aligned} \tag{2.6}$$

where the sources, S_u and S_v, of the above equations are given by

$$\begin{aligned}
S_u &= \oint_c \left(\frac{E}{2(1+\nu)}\frac{\partial v}{\partial x}.dx - \frac{E}{(1-\nu^2)}\left[\nu\frac{\partial v}{\partial y} - (1+\nu)\alpha T\right]dy\right) \\
&\qquad - \iint F_x dxdy \\
S_v &= \oint_c \left(\frac{E}{(1-\nu^2)}\left[\nu\frac{\partial u}{\partial x} - (1+\nu)\alpha T\right]dx - \frac{E}{2(1+\nu)}\frac{\partial u}{\partial y}.dy\right) \\
&\qquad - \iint F_y dxdy
\end{aligned} \tag{2.7}$$

Note that the first equation of (2.6) is a control volume formulation for the *u*-displacement with a source term that involves only the *v*-displacement and temperature. Similarly, the second equation of (2.6) is a control volume formulation for the *v*-displacement with a source term involving only the *u*-displacement and temperature.

2.1.1.2 Plane Strain

If an object is very large in the z-axis direction compared to the other dimensions and an x-y plane section is considered at the centre of the object as seen in Figure 2.3, the resulting state of strain in such a section is two-dimensional and independent of z with no displacement in the z-axis direction.

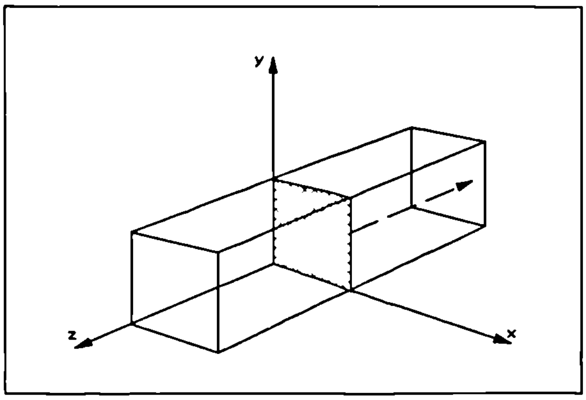

Figure 2.3: Plane Strain

It is assumed that external forces are applied parallel to the x-y plane and are independent of the position along the object, then for a section through the centre of the object, the following will apply in the instance of plane strain

$$e_{zz} = e_{xz} = e_{yz} = 0 \tag{2.8}$$

From the three-dimensional stress-strain and strain displacement cartesian relationships as listed in Appendix A.2 using the strain approximations as in equation (2.8) results in the following plane strain stress-displacement equations

$$\begin{aligned}
\sigma_{xx} &= \frac{E}{(1+\nu)(1-2\nu)}\left\{(1-\nu)\frac{\partial u}{\partial x} + \nu\frac{\partial v}{\partial y} - (1+\nu)\alpha T\right\} \\
\sigma_{yy} &= \frac{E}{(1+\nu)(1-2\nu)}\left\{(1-\nu)\frac{\partial v}{\partial y} + \nu\frac{\partial u}{\partial x} - (1+\nu)\alpha T\right\} \qquad (2.9) \\
\sigma_{xy} &= \frac{E}{2(1+\nu)}\left\{\frac{\partial u}{\partial y} + \frac{\partial v}{\partial x}\right\}
\end{aligned}$$

Substituting the stress-displacement equations (2.9) into the integrated equilibrium equations (2.3) yields

$$\begin{aligned}
&\oint_c\left(\frac{E(1-\nu)}{(1+\nu)(1-2\nu)}\frac{\partial u}{\partial x}.dy - \frac{E}{2(1+\nu)}\frac{\partial u}{\partial y}.dx\right) = S_u \\
&\qquad\qquad\qquad\qquad\qquad\qquad\qquad\qquad (2.10) \\
&\oint_c\left(\frac{E}{2(1+\nu)}\frac{\partial v}{\partial x}.dy - \frac{E(1-\nu)}{(1+\nu)(1-2\nu)}\frac{\partial v}{\partial y}.dx\right) = S_v
\end{aligned}$$

where the sources, S_u and S_v, of the above equations are given by

$$\begin{aligned}
S_u &= \oint_c\left(\frac{E}{2(1+\nu)}\frac{\partial v}{\partial x}.dx - \frac{E}{(1+\nu)(1-2\nu)}\left[\nu\frac{\partial v}{\partial y} - (1+\nu)\alpha T\right]dy\right) \\
&\quad - \iint F_x dxdy \\
&\qquad\qquad\qquad\qquad\qquad\qquad\qquad\qquad (2.11) \\
S_v &= \oint_c\left(\frac{E}{(1+\nu)(1-2\nu)}\left[\nu\frac{\partial u}{\partial x} - (1+\nu)\alpha T\right]dx - \frac{E}{2(1+\nu)}\frac{\partial u}{\partial y}.dy\right) \\
&\quad - \iint F_y dxdy
\end{aligned}$$

Note that, as with the plane stress approximation, the first equation of (2.10) is a control volume formulation for the u-displacement with a source term that involves only the v-displacement and temperature. Similarly, the second equation of (2.10) is a control volume formulation for the v-displacement with a source term involving only the u-displacement and temperature.

The plane stress and plane strain approximations both produce equations for the displacements *u* and *v* of the form:

$$\oint_c \left(k_1 \frac{\partial u}{\partial x}.dy - k_2 \frac{\partial u}{\partial y}.dx \right) = \oint_c \left(k_2 \frac{\partial v}{\partial x}.dx \ - \ k_1 \left[\nu^* \frac{\partial v}{\partial y} - (1+\nu^*)\alpha^* T \right] dy \right)$$
$$- \iint F_x dxdy \tag{2.12}$$

$$\oint_c \left(k_2 \frac{\partial v}{\partial x}.dy - k_1 \frac{\partial v}{\partial y}.dx \right) = \oint_c \left(k_1 \left[\nu^* \frac{\partial u}{\partial x} - (1+\nu^*)\alpha^* T \right] dx \ - \ k_2 \frac{\partial u}{\partial y}.dy \right)$$
$$- \iint F_y dxdy$$

where

$$k_1 = \frac{E^*}{(1-\nu^{*2})} \qquad k_2 = \frac{E^*}{2(1+\nu^*)} \tag{2.13}$$

with

$$E^* = E \qquad \nu^* = \nu \qquad \alpha^* = \alpha \tag{2.14}$$

for plane stress, and

$$E^* = \frac{E}{(1-\nu^2)} \qquad \nu^* = \frac{\nu}{(1-\nu)} \qquad \alpha^* = (1+\nu)\alpha \tag{2.15}$$

for plane strain.

2.1.2 Axisymmetric Approximation

Often cylindrical polar coordinates are convenient for use with solid geometries where coordinates *r*, θ, and *z* are measured in the radial direction relative to the axis, the angular direction about the axis and the axial direction, respectively. Figure 2.4 shows a cylinder defined in the *r*, θ and *z* axis directions. The corresponding displacements for the cylindrical polar coordinate system *r*, θ and *z*, are *u*, *v* and *w* respectively. When the effects of temperature and mechanical loading do not vary in the angular direction, θ, a section through the object in the r-z plane can be used as a two-dimensional cylindrical polar coordinate approximation to the original three-dimensional problem.

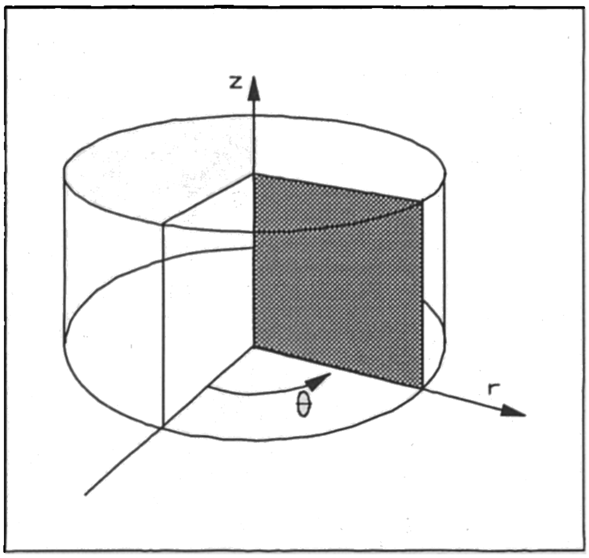

Figure 2.4: Cylinder Defined in Cylindrical Polar Coordinates

The three-dimensional stress equations of equilibrium in cylindrical polar coordinates are shown in Appendix A.3. When a problem is symmetrical with respect to the axial direction and independent of the angle θ with the displacement v zero, such as a cylinder under internal pressure, an axisymmetric approximation can be used. The stress equilibrium equations reduce to:

$$\begin{aligned} &\frac{\partial \sigma_{rr}}{\partial r} + \frac{\partial \sigma_{rz}}{\partial z} + \frac{\sigma_{rr} - \sigma_{\theta\theta}}{r} + F_r = 0 \\ &\frac{\partial \sigma_{zr}}{\partial r} + \frac{\partial \sigma_{zz}}{\partial z} + \frac{\sigma_{zr}}{r} + F_z = 0 \end{aligned} \tag{2.16}$$

Using the expressions below

$$\begin{aligned} &\frac{1}{r}\frac{\partial (r\sigma_{rr})}{\partial r} = \frac{1}{r}\frac{r\partial \sigma_{rr}}{\partial r} + \frac{\sigma_{rr}}{r} \\ &\frac{1}{r}\frac{\partial (r\sigma_{rz})}{\partial r} = \frac{1}{r}\frac{r\partial \sigma_{rz}}{\partial r} + \frac{\sigma_{rz}}{r} \end{aligned} \tag{2.17}$$

the equilibrium equations for the axisymmetric condition simplify to:

$$\frac{1}{r}\frac{\partial(r\sigma_{rr})}{\partial r} + \frac{\partial\sigma_{rz}}{\partial z} - \frac{\sigma_{\theta\theta}}{r} + F_r = 0$$
$$\frac{1}{r}\frac{\partial(r\sigma_{zr})}{\partial r} + \frac{\partial\sigma_{zz}}{\partial z} + F_z = 0 \tag{2.18}$$

Integrating the simplified equilibrium equations with respect to the control volume as in Figure 2.1 produces:

$$\iint\left(\frac{1}{r}\frac{\partial(r\sigma_{rr})}{\partial r} + \frac{\partial\sigma_{rz}}{\partial z} - \frac{\sigma_{\theta\theta}}{r} + F_r\right)rdrdz = 0$$
$$\iint\left(\frac{1}{r}\frac{\partial(r\sigma_{zr})}{\partial r} + \frac{\partial\sigma_{zz}}{\partial z} + F_z\right)rdrdz = 0 \tag{2.19}$$

where the thickness.of the control volume in the axial direction varies with the radius r. Using Stoke's theorem for two-dimensional cylindrical polar coordinates as defined in Appendix A.1 in terms of *r* and *z* the integrated equations become:

$$\oint_c (r\sigma_{rr}dz - r\sigma_{rz}dr) = \iint(F_r r - \sigma_{\theta\theta})drdz$$
$$\oint_c (r\sigma_{zr}dz - r\sigma_{zz}dr) = \iint F_z rdrdz \tag{2.20}$$

where the left hand side of the equations are now surface integrals to be evaluated at the surface of the control volume.

The three-dimensional stress-strain and strain-displacement relationships for cylindrical polar coordinates are seen in Appendix A.3. For the axisymmetric case when the displacement $v = 0$, the stress-displacement equations reduce to:

$$\begin{aligned}
\sigma_{rr} &= \frac{E}{(1+\nu)(1-2\nu)}\left\{(1-\nu)\frac{\partial u}{\partial r}+\nu\left(\frac{u}{r}+\frac{\partial w}{\partial z}\right)-(1+\nu)\alpha T\right\}\\
\sigma_{\theta\theta} &= \frac{E}{(1+\nu)(1-2\nu)}\left\{(1-\nu)\frac{u}{r}+\nu\left(\frac{\partial u}{\partial r}+\frac{\partial w}{\partial z}\right)-(1+\nu)\alpha T\right\}\\
\sigma_{zz} &= \frac{E}{(1+\nu)(1-2\nu)}\left\{(1-\nu)\frac{\partial w}{\partial z}+\nu\left(\frac{\partial u}{\partial r}+\frac{u}{r}\right)-(1+\nu)\alpha T\right\}\\
\sigma_{rz} &= \frac{E}{2(1+\nu)}\left\{\frac{\partial u}{\partial z}+\frac{\partial w}{\partial r}\right\}
\end{aligned} \tag{2.21}$$

Substituting the stress-displacement equations (2.21) into the simplified integrated equilibrium equations (2.18) yields

$$\begin{aligned}
&\oint_c\left(\frac{E(1-\nu)}{(1+\nu)(1-2\nu)}\frac{\partial u}{\partial r}r.dz - \frac{E}{2(1+\nu)}\frac{\partial u}{\partial z}r.dr\right)\\
&+\oint_c\frac{E\nu}{(1+\nu)(1-2\nu)}udz + \iint\frac{E}{(1+\nu)(1-2\nu)}\left((1-\nu)\frac{u}{r}+\nu\frac{\partial u}{\partial r}\right)drdz = S_u\\
&\oint_c\left(\frac{E}{2(1+\nu)}\frac{\partial w}{\partial r}r.dz - \frac{E(1-\nu)}{(1+\nu)(1-2\nu)}\frac{\partial w}{\partial z}r.dr\right) = S_w
\end{aligned} \tag{2.22}$$

where the sources, S_u and S_w, of the above equations are given by

$$\begin{aligned}
S_u = {}&\oint_c\left(\frac{E}{2(1+\nu)}\frac{\partial w}{\partial r}r.dr - \frac{E}{(1+\nu)(1-2\nu)}\left[\nu\frac{\partial w}{\partial z}-(1+\nu)\alpha T\right]r.dz\right)\\
&-\iint\frac{E\nu}{(1+\nu)(1-2\nu)}\frac{\partial w}{\partial z}drdz + \iint\frac{E}{(1-2\nu)}\alpha Tdrdz + \iint F_r rdrdz
\end{aligned} \tag{2.23}$$

$$\begin{aligned}
S_w = {}&\oint_c\left(\frac{E}{(1+\nu)(1-2\nu)}\left[\nu\frac{\partial u}{\partial r}-(1+\nu)\alpha T\right]r.dr - \frac{E}{2(1+\nu)}\frac{\partial u}{\partial z}r.dz\right)\\
&+\oint_c\frac{E\nu}{(1+\nu)(1-2\nu)}udr + \iint F_z rdrdz
\end{aligned}$$

Note that, as with the cartesian two-dimensional approximations, the first equation of (2.22) is a control volume formulation for the *u*-displacement with a source term that involves only the *w*-displacement and temperature. Similarly, the second equation of (2.22) is a control volume formulation for the *w*-displacement with a source term involving only the *u*-displacement and temperature.

The deformation equations (2.22) and (2.23), for the displacements *u* and *w* of the axisymmetric case of cylindrical polar coordinates, are of a similar format to the deformation equations (2.12) for the displacements *u* and *v* in cartesian coordinates where the coefficients, k_1 and k_2, are defined as in the plane strain case equations 2.13, 2.15:

$$k_1 = \frac{E}{(1+\nu)(1-2\nu)} \qquad k_2 = \frac{E}{2(1+\nu)} \tag{2.24}$$

and *x*, *y*, *u* and *v* are replaced by *r*, *z*, *u* and *w* respectively. The original surface integrals present in the cartesian equations are calculated in the axisymmetric case with the radius *r* taken into account. A few extra terms are also used in the axisymmetric approximation that are not present in the cartesian approximations.

2.1.3 Boundary Conditions

The axis directions x and y used in this section are general axis directions representing either the x and y axes of the cartesian coordinate system or the r and z axes of the cylindrical polar coordinate system. A boundary point can be described as fixed in either or both the x and y axis directions so that the associated displacement in the x and y axes directions is prescribed as zero. Otherwise at a boundary the equilibrium equations have the following form:

$$\begin{aligned} \sigma_{xx} n_x + \sigma_{xy} n_y &= D_x \\ \sigma_{xy} n_x + \sigma_{yy} n_y &= D_y \end{aligned} \tag{2.25}$$

Where D_x and D_y are the components of a stress applied on the boundary as shown in Figure 2.5.

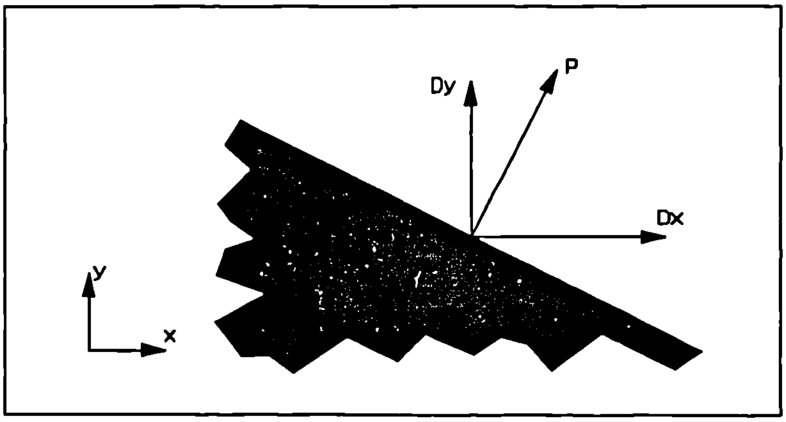

Figure 2.5: Stress Applied to Boundary

Nodes lying on the boundary may have external point loads acting on them. For loads concentrated at these nodes their effect is incorporated into the deformation models via

$$\begin{aligned} S_u &= S_u + D_x \\ S_v &= S_v + D_y \end{aligned} \tag{2.26}$$

2.2 Vertex Centred Discretisation

This section describes a vertex centred approach used with a control volume unstructured mesh formulation to obtain a discretised solution to the deformation equations derived in section 2.1. The domain, over which the deformation equations are to be applied, is discretised into elements. Shape functions are used to transform the global element geometry to the local domain geometry. The control volumes are defined as the area surrounding the element vertices or nodes over which the conservation principle is to be applied. The displacement variables u and v along with the temperature, T, are stored at the nodes, whereas the material properties are stored within a cell or element. It is then straightforward to ensure that internal boundaries are coincident with cell vertices. This section describes the control volume based-finite element mesh method [Baliga and Patankar (1988), Schneider (1988)] used here for the two-dimensional elasticity deformation equations.

2.2.1 Domain Discretisation

The solution domain is subdivided into smaller regions and nodes are distributed throughout the domain forming a mesh of elements. A typical finite element mesh, as seen in Figure 2.6, consists of sub-regions referred to as elements, a mixed mesh with both triangular and quadrilateral elements is shown. The vertices of the elements are called nodal locations, a triangular element has three and a quadrilateral element four.

The control volume unstructured mesh formulation uses the same finite element mesh, consisting typically of triangular and quadrilateral elements, so ensuring the full geometric flexibility associated with the finite element method is preserved.

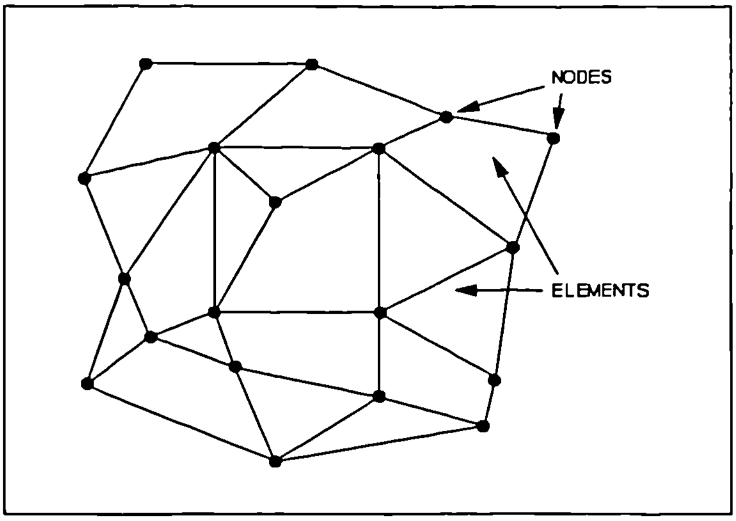

Figure 2.6: Unstructured Mesh

A typical unstructured mesh consists of nodes at the corners of the irregular elements. Variables such as the displacements, u and v, and temperature, T, are stored at the node with the material properties, such as Young's modulus, E, and Poisson's ratio, ν, stored at the element centre as a representative value of the whole element. For this reason it is easy to safeguard that internal boundaries are coincident with vertices and no element will contain more than one material.

2.2.2 Local-Global Coordinate Transformation

In the finite element context it is convenient to work in local coordinates so that each element may be treated identically, for each individual class of elements, irrespective of how distorted any element may actually be in terms of global coordinates. The local coordinate system used is shown in Figure 2.7 for triangular and quadrilateral elements.

It is necessary to relate the global and local coordinates since the conservation law is applied in terms of global coordinates. This is done using standard shape functions as shown in Appendix A.4. The coordinate variation within an element is expressed in terms of the local coordinate system (s, t), so that if for example s is changed whilst t is kept constant, then in general, both x and y will change with a linear dependence on s for the case of the bilinear element considered here.

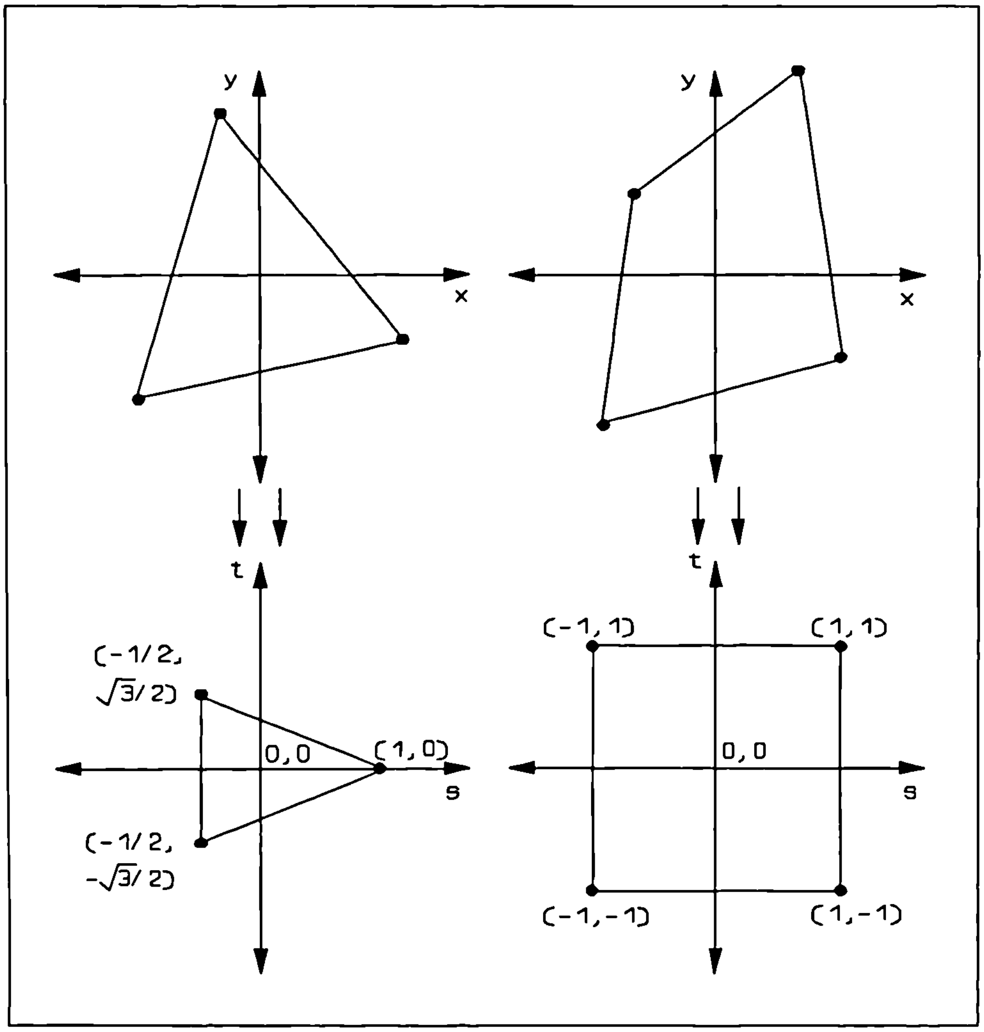

Figure 2.7: Local-Global Coordinate System

Given that x_i and y_i are the global coordinates at local node i, the coordinate variation is conveniently described by

$$\begin{aligned} x(s,t) &= \sum_{i=1}^{N_{PT}} N_i(s,t)x_i \\ y(s,t) &= \sum_{i=1}^{N_{PT}} N_i(s,t)y_i \end{aligned} \tag{2.27}$$

where N_{PT} denotes the number of nodes for the element under consideration, N_{PT} for a triangular element will be three and for a quadrilateral element will be four. Similarly with any variable ϕ defined at the nodes, its variation within the element can be described by the same shape functions employed for the geometric description

$$\phi(s,t) = \sum_{i=1}^{N_{PT}} N_i \phi_i \tag{2.28}$$

Since the shape functions are continuous, the x and y derivatives of the variable ϕ can be differentiated to yield

$$\begin{aligned} \left.\frac{\partial \phi}{\partial x}\right|_{s,t} &= \sum_{i=1}^{N_{PT}} \left.\frac{\partial N_i}{\partial x}\right|_{s,t} \phi_i \\ \left.\frac{\partial \phi}{\partial y}\right|_{s,t} &= \sum_{i=1}^{N_{PT}} \left.\frac{\partial N_i}{\partial y}\right|_{s,t} \phi_i \end{aligned} \tag{2.29}$$

Using the chain rule for partial derivatives, the x and y derivatives of the shape functions can be determined. In matrix form

$$\begin{bmatrix} \dfrac{\partial N_i}{\partial s} \\ \dfrac{\partial N_i}{\partial t} \end{bmatrix} = \begin{bmatrix} \dfrac{\partial x}{\partial s} & \dfrac{\partial y}{\partial s} \\ \dfrac{\partial x}{\partial t} & \dfrac{\partial y}{\partial t} \end{bmatrix} \begin{bmatrix} \dfrac{\partial N_i}{\partial x} \\ \dfrac{\partial N_i}{\partial y} \end{bmatrix} \tag{2.30}$$

where

$$\begin{aligned} \frac{\partial x}{\partial s} &= \sum_{i=1}^{N_{PT}} \frac{\partial N_i}{\partial s} x_i & \frac{\partial x}{\partial t} &= \sum_{i=1}^{N_{PT}} \frac{\partial N_i}{\partial t} x_i \\ \frac{\partial y}{\partial s} &= \sum_{i=1}^{N_{PT}} \frac{\partial N_i}{\partial s} y_i & \frac{\partial y}{\partial t} &= \sum_{i=1}^{N_{PT}} \frac{\partial N_i}{\partial t} y_i \end{aligned} \tag{2.31}$$

The local derivatives of the shape functions are determined by differentiating the equations as shown in Appendix A.4 for quadrilateral and triangular elements. Rearranging equation 2.30 the x and y derivatives of N_i can be determined

$$\begin{bmatrix} \dfrac{\partial N_i}{\partial x} \\ \dfrac{\partial N_i}{\partial y} \end{bmatrix} = \frac{1}{J} \begin{bmatrix} \dfrac{\partial y}{\partial t} & -\dfrac{\partial y}{\partial s} \\ -\dfrac{\partial x}{\partial t} & \dfrac{\partial x}{\partial s} \end{bmatrix} \begin{bmatrix} \dfrac{\partial N_i}{\partial s} \\ \dfrac{\partial N_i}{\partial t} \end{bmatrix} \tag{2.32}$$

where

$$J = \frac{\partial x}{\partial s}\frac{\partial y}{\partial t} - \frac{\partial y}{\partial s}\frac{\partial x}{\partial t} \tag{2.33}$$

Equations (2.29) to (2.33) contain all the necessary steps to calculate global x and y derivatives of ϕ in terms of local s and t coordinates and the nodal values.

Figure 2.8 shows a typical surface in the x-y plane.

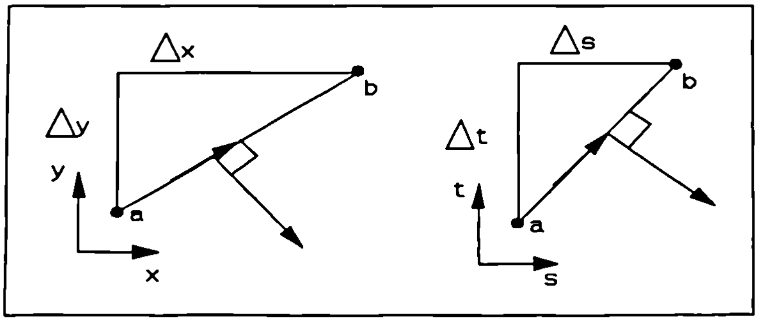

Figure 2.8: Line Segment of Control Volume

where the distances Δx and Δy are defined by

$$\Delta x = x_b - x_a \qquad \Delta y = y_b - y_a \tag{2.34}$$

By using the chain rule we have:

$$\begin{aligned} dx &= \frac{\partial x}{\partial s}ds + \frac{\partial x}{\partial t}dt \\ dy &= \frac{\partial y}{\partial s}ds + \frac{\partial y}{\partial t}dt \end{aligned} \tag{2.35}$$

therefore Δx and Δy become

$$\Delta x = \int_a^b \frac{\partial x}{\partial s} ds + \int_a^b \frac{\partial x}{\partial t} dt$$
$$\Delta y = \int_a^b \frac{\partial y}{\partial s} ds + \int_a^b \frac{\partial y}{\partial t} dt \tag{2.36}$$

If the variation of x and y is linear with respect to s and t then

$$\Delta x = \left.\frac{\partial x}{\partial s}\right|_m \Delta s + \left.\frac{\partial x}{\partial t}\right|_m \Delta t$$
$$\Delta y = \left.\frac{\partial y}{\partial s}\right|_m \Delta s + \left.\frac{\partial y}{\partial t}\right|_m \Delta t \tag{2.37}$$

where the partial differentials with respect to s and t are evaluated at the midpoint m of the line segment and

$$\Delta s = s_b - s_a \qquad \Delta t = t_b - t_a \tag{2.38}$$

The transformation information described above has been motivated by the requirements to determine derivatives and integrals as they apply to a control volume.

2.2.3 Control Volume Definition

In the solution domain each node is associated with one control volume. Each surface of the control volume is defined from the centroid of the element to the midpoint of one of its sides as shown in Figure 2.1. Each of the elements is divided into several quadrants, three for a triangle and four for a quadrilateral, by these control surfaces. The quadrants are known as sub-control volumes (SCV) and are illustrated in Figure 2.1. A control volume is therefore made up of the sub-control volumes and is polygonal in shape, which can be assembled at the element level. As neighbouring elements may consist of different materials, a control volume may be made up of different material sub-control volumes. The surface integrals developed previously in section 2.1 can be approximated by values at the midpoint of the control volume sub surfaces. Such points are called integration points for internal surfaces and boundary integration points for the surfaces of sub-control volumes that lie on the solid surface, as shown in Figure 2.9.

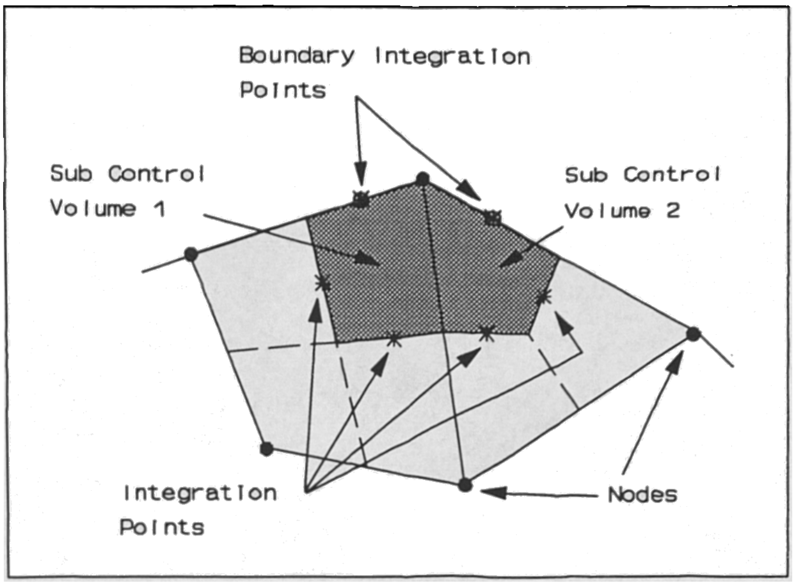

Figure 2.9: Integration Points

2.2.4 Discretisation of Deformation Equations

The deformation equations developed in section 2.1 in the integration format are discretised as suitable over the control volume domain. Figure 2.10 shows a general node P surrounded by a number of elements. The local geometry defined for each element surrounding P identifies the control volume edges by the lines $s = 0$ and $t = 0$.

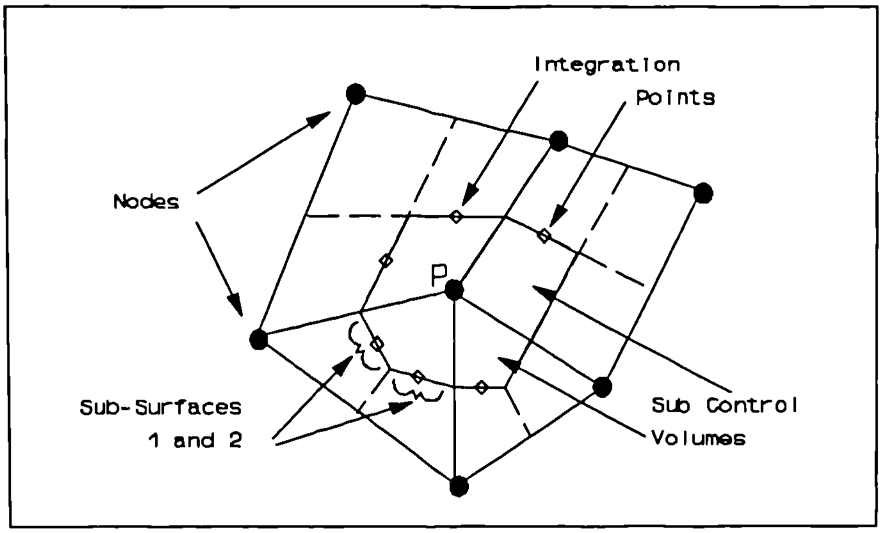

Figure 2.10: Sub-Control Volumes

For each element a sub-control volume is produced so that the discretisation is the sum of the contributions from the N_{SCV} surrounding sub-control volumes. Where a line integral is required, a particular sub-control volume will result in two surfaces where the midpoint of each results in an approximation of the line integral over the surface using shape functions and the nodes at the vertices of the element concerned.

2.2.4.1 Plane Stress/Plane Strain

From equation (2.12) the general form of the plane stress and plane strain deformation equations for the displacements u and v are:

$$\oint_c M\frac{\partial u}{\partial x}.dy - \oint_c L\frac{\partial u}{\partial y}.dx = \oint_c L\frac{\partial v}{\partial x}.dx - \oint_c R\frac{\partial v}{\partial y}.dy + \oint_c QT.dy$$

$$\oint_c L\frac{\partial v}{\partial x}.dy - \oint_c M\frac{\partial v}{\partial y}.dx = \oint_c R\frac{\partial u}{\partial x}.dx - \oint_c QT.dx - \oint_c L\frac{\partial u}{\partial y}.dy \tag{2.39}$$

where

$$M = k_1 \qquad L = k_2 \qquad R = k_1\nu^* \qquad Q = k_1(1+\nu^*)\alpha^* \tag{2.40}$$

are the material dependent coefficients and the internal body forces are neglected.

Considering a typical displacement term from equation (2.39) such as

$$\oint_c M\frac{\partial u}{\partial x}.dy \tag{2.41}$$

this can be discretised over the control volume surrounding the node P, such that

$$\oint_c M\frac{\partial u}{\partial x}.dy = \sum_{k=1}^{N_{scv}} M^k \left[\sum_{j=1}^{2} \left[\sum_{i=1}^{N_{PT}^k} \frac{\partial N_{ij}^k}{\partial x} u_{ij}^k\right] \Delta y_j^k\right] \tag{2.42}$$

and for a typical temperature term discretisation

$$\oint_c QT.dy = \sum_{k=1}^{N_{scv}} Q^k \left[\sum_{j=1}^{2} \left[\sum_{i=1}^{N_{PT}^k} N_{ij}^k T_{ij}^k\right] \Delta y_j^k\right] \tag{2.43}$$

where the surface integrals are approximated over the N_{SCV} sub-control volumes and the coefficients M^k and Q^k consist of the element dependent material properties. Each element resulting in a sub-control volume surrounding the node P, consists of N_{PT}^k nodes typically three for triangular elements or four for quadrilaterals. Each sub-control volume contributes two surfaces where the length, Δy_j^k, is dependent on the surface and the sub-control volume.

Collecting the contributions from all the sub-control volumes surrounding a node produces equations of the familiar form

$$a_P^u u_P = \sum_{i=1}^{N_{nb}} a_i^u u_i + b_P^u$$
$$a_P^v v_P = \sum_{i=1}^{N_{nb}} a_i^v v_i + b_P^v \tag{2.44}$$

where the displacement u and v at the node P is dependent on the displacement of the N_{nb} neighbouring nodes and the source term including the temperature effects.

2.2.4.2 Axisymmetric

From equations (2.22) and (2.23) the general form of the axisymmetric deformation equations for the displacements u and w are:

$$\oint_c M\frac{\partial u}{\partial r}.rdz - \oint_c L\frac{\partial u}{\partial z}.rdr + \oint_c Ru.dz + \iint M\frac{u}{r}drdz + \iint R\frac{\partial u}{\partial r}drdz =$$
$$\oint_c L\frac{\partial w}{\partial r}.rdr - \oint_c R\frac{\partial w}{\partial z}.rdz + \oint_c QT.rdz - \iint R\frac{\partial w}{\partial z}drdz + \iint QTdrdz$$

$$\tag{2.45}$$

$$\oint_c L\frac{\partial w}{\partial r}.rdz - \oint_c M\frac{\partial w}{\partial z}.rdx =$$
$$\oint_c R\frac{\partial u}{\partial r}.rdr - \oint_c QT.rdr - \oint_c L\frac{\partial u}{\partial z}.rdz + \oint_c Ru.dr$$

where

$$L = \frac{E}{2(1+\nu)} \qquad Q = \frac{E}{(1-2\nu)}$$
$$M = \frac{E(1-\nu)}{(1+\nu)(1-2\nu)} \qquad R = \frac{E\nu}{(1+\nu)(1-2\nu)} \tag{2.46}$$

are the material dependent coefficients and the internal body forces are neglected.

Considering a typical surface integral displacement term from equation (2.45) such that

$$\oint_c M\frac{\partial u}{\partial r}.rdz \tag{2.47}$$

this can be discretised over the control volume surrounding the node P, such that

$$\oint_c M\frac{\partial u}{\partial r}.rdz = \sum_{k=1}^{N_{scv}} M^k \left[\sum_{j=1}^{2}\left[\sum_{i=1}^{N_{PT}^k}\frac{\partial N_{ij}^k}{\partial r}u_{ij}^k\right]\left[\sum_{i=1}^{N_{PT}^k} N_{ij}^k r_{ij}^k\right]\Delta z_j^k\right] \tag{2.48}$$

and for a typical temperature line integral discretisation

$$\oint_c QT.rdz = \sum_{k=1}^{N_{scv}} Q^k \left[\sum_{j=1}^{2}\left[\sum_{i=1}^{N_{PT}^k} N_{ij}^k T_{ij}^k\right]\left[\sum_{j=1}^{N_{PT}^k} N_{ij}^k r_{ij}^k\right]\Delta z_j^k\right] \tag{2.49}$$

The extra terms not included in the plane stress/plane strain approximations are discretised as follows

$$\iint R\frac{\partial u}{\partial r}drdz = \sum_{k=1}^{N_{scv}} R^k\left[\sum_{i=1}^{N_{PT}^k}\frac{\partial N_i^k}{\partial r}u_i^k\right]\Delta V^k$$
$$\iint R\frac{\partial w}{\partial z}drdz = \sum_{k=1}^{N_{scv}} R^k\left[\sum_{i=1}^{N_{PT}^k}\frac{\partial N_i^k}{\partial z}w_i^k\right]\Delta V^k \tag{2.50}$$
$$\iint QTdrdz = \sum_{k=1}^{N_{scv}} Q^k\left[\sum_{i=1}^{N_{PT}^k} N_i^k T_i^k\right]\Delta V^k$$

$$\oint_c Ru.dz = \sum_{k=1}^{N_{SCV}} R^k \left[\sum_{j=1}^{2} \left[\sum_{i=1}^{N_{PT}^k} N_{ij}^k u_{ij}^k \right] \Delta z_j^k \right]$$

$$\oint_c Ru.dr = \sum_{k=1}^{N_{SCV}} R^k \left[\sum_{j=1}^{2} \left[\sum_{i=1}^{N_{PT}^k} N_{ij}^k u_{ij}^k \right] \Delta r_j^k \right]$$

and the final term

$$\iint M \frac{u}{r} dr dz = \sum_{k=1}^{N_{SCV}} M^k \left[\sum_{i=1}^{N_{PT}^k} N_i^k \frac{u_i^k}{r_i^k} \right] \Delta V^k$$

When the radius r_i is zero the displacement u_i is also zero the u_i/r_i term is taken to be zero using L'Hospital's rule, but contributions are still obtained from other nodes in the particular sub-control volume

The surface integrals and volume integrals are approximated over N_{SCV} sub-control volumes that surround the node P. For the surface integrals evaluation takes place at the midpoints of the two surfaces for each sub-control volume, but the volume integrals are approximated at the centre of the sub-control volume. The coefficients M^k, L^k, Q^k and R^k are the element dependent material properties. ΔV^k represents the volume of a particular sub-control volume surrounding the node P.

Collecting the contributions from all the sub-control volumes surrounding a node produces equations of the familiar form

$$\begin{aligned} a_P^u u_P &= \sum_{i=1}^{N_{nb}} a_i^u u_i + b_P^u \\ a_P^w w_P &= \sum_{i=1}^{N_{nb}} a_i^w w_i + b_P^w \end{aligned} \tag{2.51}$$

where the displacement u and w at the node P is dependent on the displacement of the N_{nb} neighbouring nodes and the source term including the temperature effects.

2.3 Solution Procedure/2D Code - CV-UM

Equation (2.44) consists of a set of equations that define the displacement components *u* and *v* in a coupled form for the cartesian two-dimensional circumstance and equation (2.51) consists of a set of equations that define the displacement *u* and *w* in a coupled form for the two-dimensional axisymmetric instance. It is then possible to develop a straightforward iterative algorithm for solving these displacement equations of the general form

$$a_P \phi_P = \sum_{i=1}^{N_{nb}} a_i \phi_i + b_P \qquad (2.52)$$

where the node P is surrounded by N_{nb} neighbouring nodes and ϕ represents the displacements *u* or *v* for the cartesian case and *u* or *w* for the cylindrical polar case.

The coupled equations may now be solved by using the iterative procedure as displayed in Figure 2.11, translated to a FORTRAN code that for simplicity is referred to in later chapters as 'CV-UM' (Control Volume-Unstructured Mesh). Note that *Y* represents either *Y* or *Z*, *v* represents either *v* or *w* depending on whether the plane stress, plane strain or axisymmetric option is chosen. At the start of the procedure the initial data is read in from files, which includes the information on coordinate points, element topology, the temperature distribution *T(x,y)*, material properties and boundary conditions D_x and D_y as appropriate.

An initial guess for the *v* displacement of the problem is made typically zero at each nodal point in the domain. The discretised *u*-displacement equation is then solved obtaining the *u* displacements using *T(x,y)* and the latest available approximate solution for *v*. The latest available approximate solution for *u* is then used with *T(x,y)* to solve for *v* using the discretised *v*-displacement equation. After the new *v* displacements have been obtained a check for convergence of *u* and *v* is made, if the solutions have not converged and the number of global iterations is less than the maximum number allowed a new iteration proceeds with the *u*-displacement equations being solved with the latest

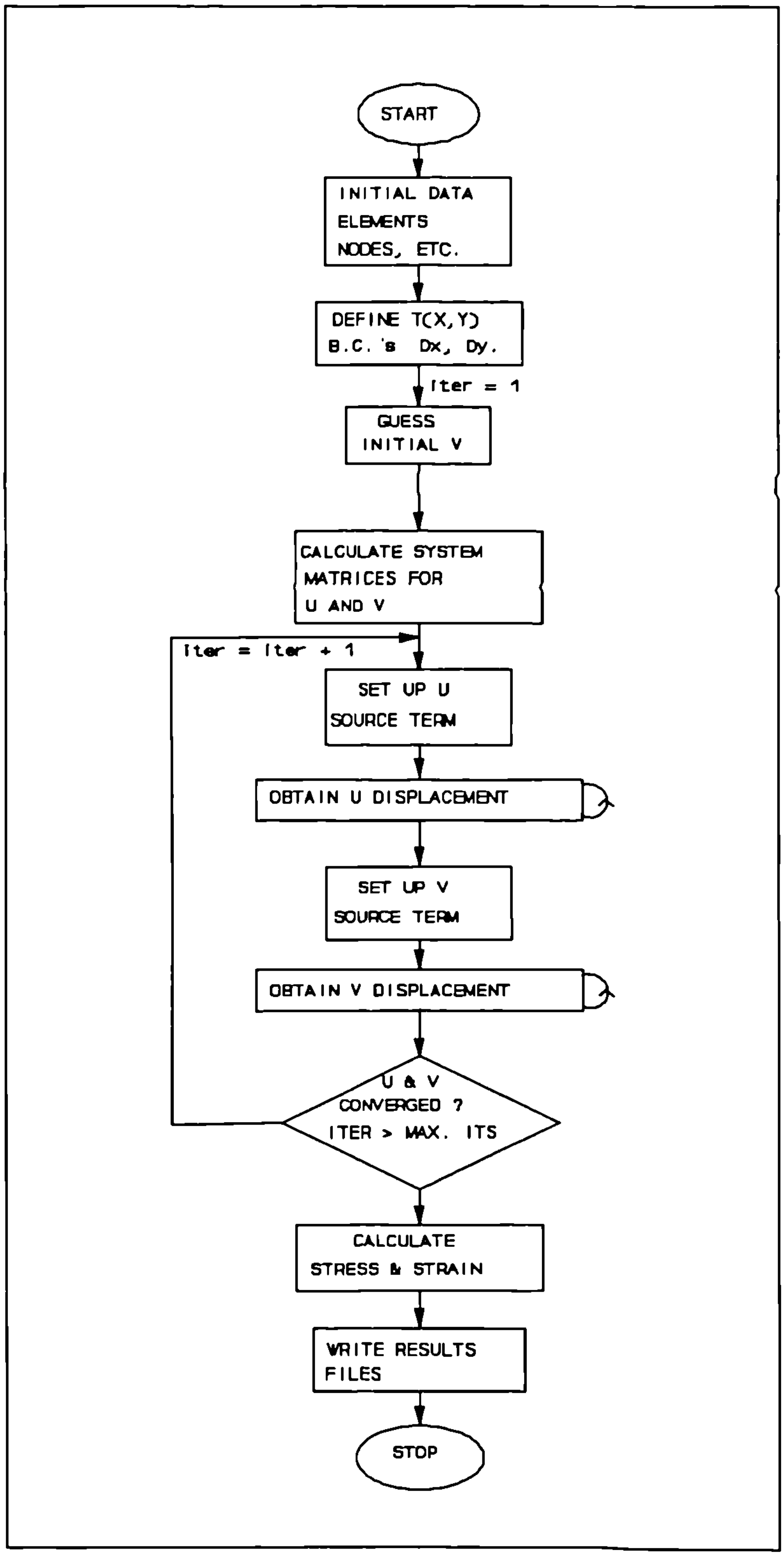

Figure 2.11: Solution Procedure - CV-UM

v displacements until either convergence is reached or the maximum number of iterations is exceeded. For a converged solution the displacements are written to a file for use with post-processing facilities to observe the deformed mesh.

The general discretised equations in the form of equation (2.52) are actually solved using the correction format, that is,

$$a_P \phi_P^c = \sum_{i=1}^{N_{nb}} a_i (\phi_i^{old} + \phi_i^c) + b_P - a_P \phi_P^{old} \tag{2.53}$$

where

$$\phi_P^{new} = \phi_P^{old} + \phi_P^c \tag{2.54}$$

For the inner loops of the iterative procedure when the solution of either displacement, u or v, is obtained, the tolerance is set to 0.1 because there is no need to achieve strict convergence as this is guaranteed by overall convergence, ie,

$$\frac{|\boldsymbol{R}^k\|}{|\boldsymbol{R}^o\|} \leq 0.1 \tag{2.55}$$

where $\boldsymbol{R}^k$ is the residual vector whose elements are $\{\phi_P^c\}^k$ in the kth iteration of the linear solver.

The linear equations (2.53) in corrected form can be arranged in typical matrix form

$$A \phi^c = \boldsymbol{b}^c \tag{2.56}$$

where A is the matrix of coefficients, ϕ^c the vector of displacement corrections and $\boldsymbol{b}^c$ the vector in corrected format containing source terms and old displacement values. This is solved by a conventional conjugate gradient technique with simple Jacobi preconditioning [Lai and Liddell (1987), Bercovier and Rosenthal (1986)], such that

$$\hat{A} \hat{\phi}^c = \hat{\boldsymbol{b}}^c \tag{2.57}$$

where the transformed values are

$$\hat{a}_{ij} = \frac{a_{ij}}{\sqrt{a_{ii}a_{jj}}} \qquad \hat{\phi}_i^c = \phi_i^c\sqrt{a_{ii}} \qquad \hat{b}_i^c = \frac{b_i^c}{\sqrt{a_{ii}}} \tag{2.58}$$

The classic conjugate gradient algorithm is then used to obtain the transformed values, which can then be recovered using

$$\phi_i^c = \frac{\hat{\phi}_i^c}{\sqrt{a_{ii}}} \tag{2.59}$$

to obtain the displacement corrections. This solution technique yields much quicker convergence than other procedures such as Jacobi and Gauss-Seidel iteration methods.

To ensure rapid convergence of the solution, the displacement term ϕ_p, in each instance of equation (2.53) is over-relaxed so that

$$\phi_P^{new} = \phi_P^{old} + \omega(\phi_P^{new} - \phi_P^{old}) \tag{2.60}$$

where the relaxation factor ω lies between 1 and 2.

The criterion for stopping the overall solution procedure is that when the overall convergence is checked in the iterative solution procedure the equations below are computed

$$\begin{aligned} CNORM &= \frac{\|D^j - D^{j-1}\|}{\|D^j\|} \\ RNORM &= \frac{\|L^j - L^{j-1}\|}{\|L^j\|} \end{aligned} \tag{2.61}$$

where D^j is the dependent variable vector and L^j is the source vector, at each outer iteration j, for each of u and v. The solution is then terminated when

$$Max(CNORM, RNORM) \leq TOL \tag{2.62}$$

is true for both the u and v equations. A converged displacement solution has been obtained so the object deformation and corresponding stresses are output and the algorithm finishes.

2.4 Conclusion

The stress conservation equations for three two-dimensional cases, plane stress, plane strain and axisymmetric, have been integrated over an unstructured control volume. The resulting equations produced containing surface and volume integrals in terms of displacement have been discretised and approximated at points either on the control volume surface or the sub-control volume centre. The general equations produced can be solved using a preconditioned conjugate gradient solver. An algorithm developed to obtain the displacement results for various thermally and mechanically loaded solid objects has been written into a FORTRAN code. Using the algorithm the deformation of solid objects can be obtained after the domain has been subdivided into a mesh of elements. Effects to be considered include nodal temperature loading throughout the domain and application of forces at the surface of the domain. The algorithm and computer code have to be tested and compared to problems with standard analytical solutions to determine the validity of the method, as discussed in chapter 3.

Chapter 3

Application to Solid Mechanics

The stress-strain control volume unstructured mesh code, 'CV-UM', developed in Chapter 2 is applied and tested in this chapter. Various examples, some with known analytical solutions, are applied to the two-dimensional stress-strain code so that the algorithm can be validated. The collected results are tabulated and compared to results produced by a standard finite element program for the same problem. The relaxation parameter and displacement residual tolerance used are altered to observe the effect on the accuracy of the results and the time taken to obtain the results. Comparisons are made between differing meshes for the two-dimensional code such as quadrilaterals, triangles and mixed meshes containing both triangles and quadrilaterals. The algorithm's capacity for handling more complex geometries and unstructured meshes is also investigated.

3.1 Example 1: Loaded Cantilever

The first example used to test the accuracy of the two-dimensional code is that of a cantilever with a point load at the free end. This shows the capabilities of the algorithm to function with fixed displacements and forces applied to boundaries. The cantilever beam is long in the x-axis direction compared to the other directions so the assumption of plane stress is suitable for this problem. The analytical solution to the problem is known and used for comparison to the two-dimensional displacement results of the control volume unstructured mesh code. Three styles of mesh were used:- the first all quadrilaterals; the second all triangles and the third a mixed mesh containing both triangles and quadrilaterals. For each case a coarse mesh of 33 nodes was used, then a finer mesh with 105 nodes and the third mesh containing 369 nodes. Results were collected for various displacement residual tolerances and relaxation parameter values. A standard finite element code was used to solve the problem and the results compared to the unstructured mesh code.

3.1.1 Problem Specification

The beam has a length of 1,000mm, a height of 200mm and a width of 40mm. The point load at the end of the cantilever is 35,000N spread over the width of the 40mm. To model a two-dimensional slice through the cantilever a unit width of one implies the force applied at the corner node is 875N. A section through the cantilever can be seen in Figure 3.1.

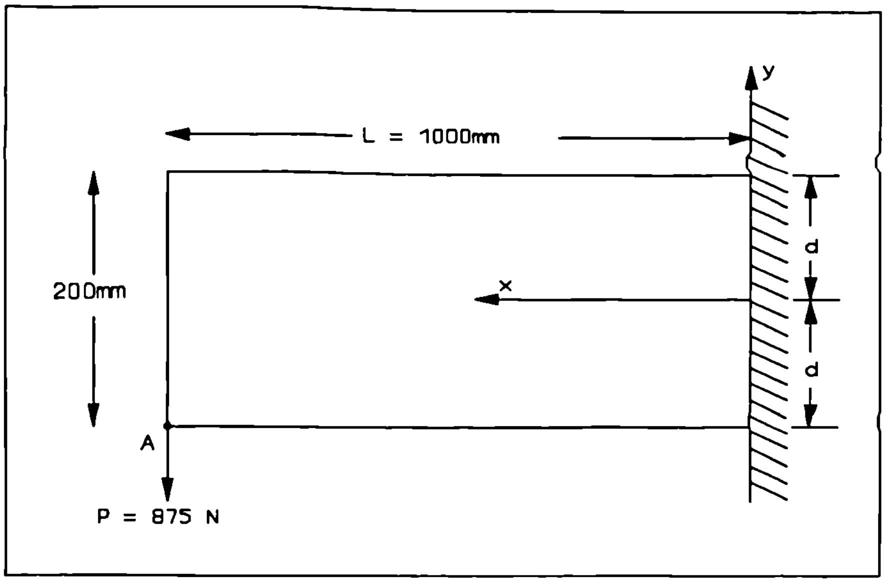

Figure 3.1: Cantilever Description

For the material properties of the cantilever a Poisson's ratio of 0.25 was used with Young's Modulus, E of 210,000N/mm^2. For use with the analytical solution the second moment of area for the unit thick section through the cantilever, I is 2/3*10^{5}mm^4.

3.1.2 Analytical Results

Analytical results for the displacement of the cantilever are available from standard solid mechanics and elasticity books [Timoshenko and Goodier (1970), Fenner (1986), Moscardini (1985)]. Fenner (1986) gives the *u* and *v* displacement equations for the cantilever as:-

$$\begin{aligned} u &= \frac{P}{EI}(Lx-\frac{x^2}{2})y - \frac{P(2+\nu)}{6EI}\left(\frac{d}{2}\right)^2 y + \frac{P(2+\nu)}{6EI}y^3 \\ v &- - \frac{\nu P}{2EI}(L-x)y^2 - \frac{P(4+5\nu)}{6EI}\left(\frac{d}{2}\right)^2 x + \frac{P}{EI}\left(\frac{x^3}{6}-\frac{Lx^2}{2}\right) \end{aligned} \tag{3.1}$$

For this particular cantilever the equations reduce to:-

$$\begin{aligned} u &= \frac{y}{160{,}000{,}000}\left(1{,}000x-\frac{x^2}{2} + \frac{3}{8}(y^2-100^2)\right) \\ v &- \frac{1}{160{,}000{,}000}\left(\frac{(x-1000)}{8}y^2 - \frac{7}{8}100^2x + \frac{x^2}{2}(\frac{x}{3}-1000)\right) \end{aligned} \tag{3.2}$$

At the point A (1000,-100) in Figure 3.1 the *u* and *v* displacements are then -0.3125mm and -2.13802mm to five decimal places respectively.

Moscardini (1985) using the cantilever approximations by Timoshenko and Goodier (1970) obtains a value for the *v* displacement at the point A of -2.16mm, where the fixed end of the cantilever is allowed to distort slightly. The control volume unstructured mesh code does not produce distortions at the fixed end so the Fenner (1986) solution is used for comparison. Figure 3.2 shows the cantilever with the displacements resulting from the applied load.

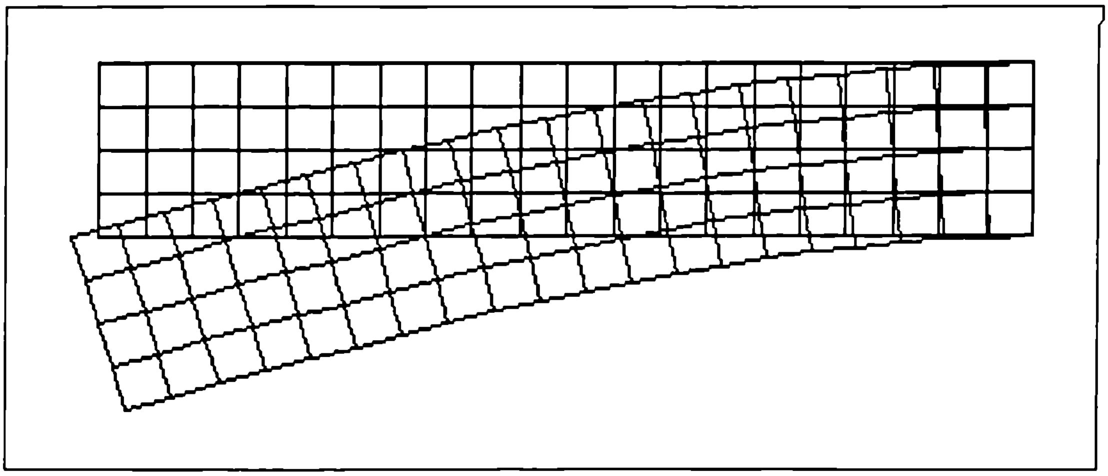

Figure 3.2: Displaced Cantilever (x 100)

3.1.3 Finite Element Results

The finite element package IFECS, Interactive Finite Element Computing System [Lewis and Cross (1978)], was used for the same problem and the results for the displacement of the cantilever at the point A in Figure 3.1 were collected. Figure 3.3 shows the standard triangular mesh generated by IFECS and used for the 33 node example. Appendix B, Figures B.4-B.6, show the node and element structure for the three different sized triangular meshes used, 33 nodes, 105 nodes and 369 nodes respectively.

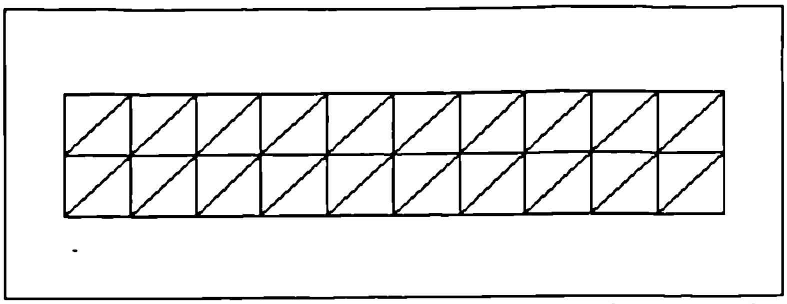

Figure 3.3: Triangular Mesh - 33 Nodes

The IFECS two-dimensional code was used on a 386 machine to obtain the displacement results though the finite element code is essentially a 286 based code. The times for the finite element code to reach a final solution are displayed in Table 3.1 along with the *u* and *v* displacements at the point A. The displacements are seen to increase in accuracy as the mesh is refined.

Number of Nodes	displacement at A		Time for solution (s)
	u (mm)	v (mm)	
33	-0.172	-1.17	11
105	-0.263	-1.76	68
369	-0.305	-2.04	366

Table 3.1: Finite Element Results - Cantilever

3.1.4 CV-UM results

The control volume-unstructured mesh algorithm was used to obtain a solution to the problem for meshes of varying types and sizes. The relaxation parameter, ω, was varied to see what effect it had on the convergence rate. The times for the solution to converge were also noted for given tolerances and tabulated along with the displacement and the number of global iterations needed for required convergence.

3.1.4.1 Quadrilaterals

A regular quadrilateral mesh was used for the cantilever problem as shown in Figure 3.4, which displays the 33 node quadrilateral mesh. The control volume unstructured mesh code does not use the structured characteristics of the quadrilateral mesh. The displacement results for this mesh are shown in Table 3.2 for the various tolerances and relaxation parameters used. The results for the quadrilateral mesh with 105 nodes are displayed in Table 3.3 and the results for the cantilever with 369 nodes and quadrilateral elements are shown in Table 3.4. The node and element structure for the three different sized quadrilateral meshes used can be seen in Appendix B, Figures B.1-B.3. Appendix B, Figures B.10-B.13, illustrate the variation in the number of global iterations needed before the required tolerance is reached for a particular relaxation parameter and quadrilateral mesh.

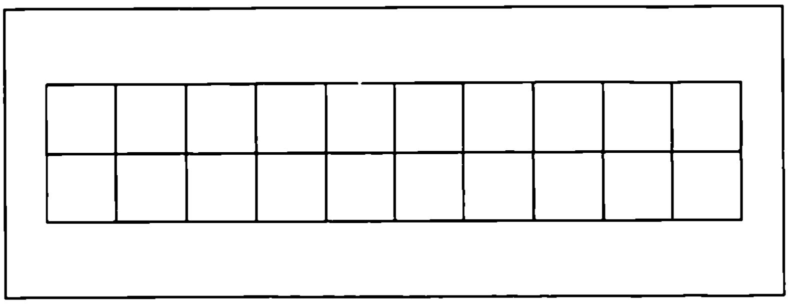

Figure 3.4: Quadrilateral Mesh - 33 Nodes

From Table 3.4 the 369 node quadrilateral mesh, the *u* displacement obtained at the point A by the unstructured code is -0.314mm and the *v* displacement -2.115mm. The results are reasonably close to the analytical solution.

3.1.4.2 Triangles

The triangular mesh used to solve the cantilever with the unstructured code was the same as for the finite element code, Figure 3.3, and can be seen for the three different sized meshes in Appendix B, Figures B.4-B.6. The displacement results and the solution timings for the triangular mesh with 33 nodes are shown in the Table 3.5; the triangular mesh with 105 nodes in Table 3.6 and the 369 node triangular mesh results in Table 3.7. From Table 3.7, the mesh with 369 nodes produces *u* and *v* displacements at point A of -0.304mm and -2.043mm. The results, though not as good as the quadrilateral displacement results, are very close to the values produced by the finite element code IFECS. Figures B.14-B.17 in Appendix B illustrate the variation for convergence of the various relaxation parameters used for the different triangular meshes.

3.1.4.3 Mixed Mesh

An arbitrary mesh with mixed triangles and quadrilaterals was designed to test the algorithm's capability for solving mixed mesh problems. An example of the mesh used for the beam with 33 nodes is shown in Figure 3.5.

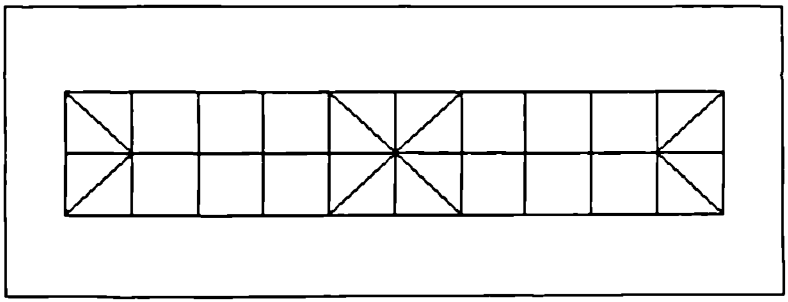

Figure 3.5: Mixed Mesh - 33 Nodes

Appendix B, Figures B.7-B.9, show in more detail the node and element arrangement for the different sized mixed meshes. Results for the mixed mesh solution of the cantilever problem were collected and tabulated. Table 3.8 shows the 33 node mixed mesh displacements for the various tolerances and relaxation parameters used. Tables 3.9 and 3.10 display the results for the 105 node mesh and the 369 node mesh respectively. From Table 3.10 the *u* and *v* displacement results produced for point A are -0.31mm and -2.095mm, values between the results produced by the triangular and quadrilateral meshes. The number of global iterations required to reach a particular tolerance are compared for the three mixed meshes in Figures B.18-B.21 in Appendix B.

3.1.5 Comparison of Results

Comparing the time for the finite element code and the control volume unstructured mesh code on the same 386 personal computer, from the timings displayed in Tables 3.1-3.10, it is seen that the finite element results may be quicker but the accuracy is not as good. For much larger meshes, with many more nodes, it is expected that the control volume unstructured mesh code will improve in time taken to reach solution compared to the finite element solution for the same problem. From the results due to varying the relaxation parameter ω, it is seen that choosing an appropriate value for ω can greatly influence the time taken and the number of global iterations taken until convergence to the required tolerance is reached.

Studying the displacement results for the quadrilateral meshes and the triangular meshes, the cantilever beam is seen to be more suitable for solution using the quadrilateral elements as the geometry of the beam itself implies. The quadrilateral element mesh results are closest to the analytical solution followed by the mixed element mesh and then the triangular element mesh.

Using the cantilever results for a mesh with 369 nodes and quadrilateral elements, Figure 3.6 demonstrates how the time taken varies with the relaxation parameter used. Graphs B.10-B.12 in Appendix B show how the number of iterations varies depending on the relaxation parameter chosen. Figure B.13-B.21, Appendix B, illustrate for the triangular and mixed meshes how the number of global iterations necessary for a required tolerance to be reached varies with the relaxation parameter used. The optimum relaxation parameter can be calculated before the displacement results are obtained using a formula containing the spectral radius of the neighbouring node coefficient matrix [Smith (1975)]. For simplicity, a rough mesh can be used to solve the problem with varying relaxation parameters, so that an approximate optimum value is obtained. The graphs in Appendix B show this approximate relaxation value can then be used with a much finer mesh to obtain more accurate displacement results.

Tolerance = 0.01, u & v displacements measured at Point A				
Relaxation(ω)	Time (s)	Iterations	u disp. (mm)	v disp (mm)
1.0	32.0313	51	-0.175806	-1.23303
1.2	26.4844	42	-0.193642	-1.34827
1.5	15.5703	29	-0.217330	-1.50081
1.7	12.5273	19	-0.232897	-1.60081
1.9	20.0000	31	-0.249818	-1.71016

Tolerance = 0.001, u & v displacements measured at Point A				
Relaxation(ω)	Time (s)	Iterations	u disp. (mm)	v disp (mm)
1.0	78.6797	127	-0.232716	-1.59403
1.2	59.0078	95	-0.235755	-1.61353
1.5	34.6133	55	-0.238755	-1.63283
1.7	19.3945	30	-0.240640	-1.64475
1.9	33.0195	52	-0.241479	-1.65234

Tolerance = 0.0001, u & v displacements measured at Point A				
Relaxation(ω)	Time (s)	Iterations	u disp. (mm)	v disp (mm)
1.0	131.430	213	-0.240553	-1.64373
1.2	94.0117	152	-0.240868	-1.64576
1.5	51.9258	83	-0.241192	-1.64782
1.7	26.2656	41	-0.241370	-1.64897
1.9	46.6133	79	-0.241431	-1.64943

Table 3.2: Cantilever Results - 33 Nodes and Quadrilateral Elements

<table>
<tr><th colspan="5">Tolerance = 0.01, u & v displacements measured at Point A</th></tr>
<tr><th>Relaxation(ω)</th><th>Time (s)</th><th>Iterations</th><th>u disp. (mm)</th><th>v disp (mm)</th></tr>
<tr><td>1.0</td><td>120.824</td><td>56</td><td>-0.204505</td><td>-1.42438</td></tr>
<tr><td>1.2</td><td>101.758</td><td>47</td><td>-0.228898</td><td>-1.58166</td></tr>
<tr><td>1.5</td><td>72.2539</td><td>33</td><td>-0.260429</td><td>-1.78480</td></tr>
<tr><td>1.7</td><td>49.0664</td><td>22</td><td>-0.280182</td><td>-1.91146</td></tr>
<tr><td>1.9</td><td>71.3203</td><td>33</td><td>-0.293071</td><td>-1.99317</td></tr>
</table>

<table>
<tr><th colspan="5">Tolerance = 0.001, u & v displacements measured at Point A</th></tr>
<tr><th>Relaxation(ω)</th><th>Time (s)</th><th>Iterations</th><th>u disp. (mm)</th><th>v disp (mm)</th></tr>
<tr><td>1.0</td><td>311.813</td><td>146</td><td>-0.282151</td><td>-1.91762</td></tr>
<tr><td>1.2</td><td>233.406</td><td>109</td><td>-0.286264</td><td>-1.94405</td></tr>
<tr><td>1.5</td><td>138.461</td><td>64</td><td>-0.290686</td><td>-1.97242</td></tr>
<tr><td>1.7</td><td>79.1758</td><td>36</td><td>-0.293114</td><td>-1.98791</td></tr>
<tr><td>1.9</td><td>112.090</td><td>56</td><td>-0.295004</td><td>-2.00033</td></tr>
</table>

<table>
<tr><th colspan="5">Tolerance = 0.0001, u & v displacements measured at Point A</th></tr>
<tr><th>Relaxation(ω)</th><th>Time (s)</th><th>Iterations</th><th>u disp. (mm)</th><th>v disp (mm)</th></tr>
<tr><td>1.0</td><td>534.781</td><td>251</td><td>-0.293491</td><td>-1.98966</td></tr>
<tr><td>1.2</td><td>384.398</td><td>180</td><td>-0.293956</td><td>-1.99260</td></tr>
<tr><td>1.5</td><td>208.957</td><td>97</td><td>-0.294340</td><td>-1.99508</td></tr>
<tr><td>1.7</td><td>113.625</td><td>52</td><td>-0.294636</td><td>-1.99701</td></tr>
<tr><td>1.9</td><td>148.023</td><td>80</td><td>-0.295101</td><td>-2.00024</td></tr>
</table>

Table 3.3: Cantilever Results - 105 Nodes and Quadrilateral Elements

Tolerance = 0.01, u & v displacements measured at Point A				
Relaxation(ω)	Time (s)	Iterations	u disp. (mm)	v disp (mm)
1.0	570.824	57	-0.214801	-1.48149
1.2	482.914	48	-0.241279	-1.65217
1.5	349.340	34	-0.275531	-1.87241
1.7	241.484	23	-0.297193	-2.01211
1.9	384.012	45	-0.322732	-2.19350

Tolerance = 0.001, u & v displacements measured at Point A				
Relaxation(ω)	Time (s)	Iterations	u disp. (mm)	v disp (mm)
1.0	1502.25	152	-0.300703	-2.02712
1.2	1132.04	114	-0.305355	-2.05697
1.5	688.297	68	-0.310293	-2.08858
1.7	401.648	39	-0.312787	-2.10474
1.9	709.668	88	-0.316891	-2.13105

Tolerance = 0.0001, u & v displacements measured at Point A				
Relaxation(ω)	Time (s)	Iterations	u disp. (mm)	v disp (mm)
1.0	2594.34	263	-0.313308	-2.10718
1.2	1872.36	189	-0.313810	-2.11038
1.5	1034.39	103	-0.314250	-2.11318
1.7	578.406	57	-0.314566	-2.11518
1.9	1016.16	131	-0.314743	-2.11608

Table 3.4: Cantilever Results - 369 Nodes and Quadrilateral Elements

Tolerance = 0.01, u & v displacements measured at Point A

Relaxation(ω)	Time (s)	Iterations	u disp. (mm)	v disp (mm)
1.0	25.3320	44	-0.136678	-0.976973
1.2	20.9883	36	-0.148104	-1.05134
1.5	14.6172	24	-0.161707	-1.13988
1.7	9.61717	15	-0.171898	-1.20453
1.9	19.8359	34	-0.169609	-1.19909

Tolerance = 0.001, u & v displacements measured at Point A

Relaxation(ω)	Time (s)	Iterations	u disp. (mm)	v disp (mm)
1.0	56.4297	101	-0.169182	-1.18494
1.2	42.0898	75	-0.170854	-1.19580
1.5	24.8320	43	-0.172565	-1.20684
1.7	12.3047	20	-0.173860	-1.21452
1.9	31.1061	55	-0.173541	-1.21278

Tolerance = 0.0001, u & v displacements measured at Point A

Relaxation(ω)	Time (s)	Iterations	u disp. (mm)	v disp (mm)
1.0	90.3828	164	-0.173325	-1.21164
1.2	64.5078	116	-0.173485	-1.21268
1.5	35.1094	62	-0.173665	-1.21381
1.7	15.6055	26	-0.173841	-1.21490
1.9	45.5469	82	-0.173800	-1.21473

Table 3.5: Cantilever Results - 33 Nodes and Triangular Elements

Tolerance = 0.01, u & v displacements measured at Point A				
Relaxation(ω)	Time (s)	Iterations	u disp. (mm)	v disp (mm)
1.0	128.461	53	-0.186615	-1.31116
1.2	107.145	44	-0.206949	-1.44266
1.5	76.5391	31	-0.234330	-1.61920
1.7	50.6602	20	-0.249957	-1.72015
1.9	96.1523	41	-0.260350	-1.78333

Tolerance = 0.001, *u & v displacements measured at Point A*				
Relaxation(ω)	Time (s)	Iterations	u disp. (mm)	v disp (mm)
1.0	325.109	135	-0.251464	-1.72353
1.2	243.959	101	-0.254900	-1.74564
1.5	144.395	59	-0.258361	-1.76790
1.7	82.4688	33	-0.260378	-1.78093
1.9	151.867	67	-0.261908	-1.79193

Tolerance = 0.0001, u & v displacements measured at Point A				
Relaxation(ω)	Time (s)	Iterations	u disp. (mm)	v disp (mm)
1.0	544.838	227	-0.260435	-1.78058
1.2	389.891	162	-0.260795	-1.78289
1.5	216.648	89	-0.261162	-1.78525
1.7	114.121	48	-0.261361	-1.78654
1.9	217.805	98	-0.261549	-1.78772

Table 3.6: Cantilever Results - 105 Nodes and Triangular Elements

Tolerance = 0.01, u & v displacements measured at Point A				
Relaxation(ω)	Time (s)	Iterations	u disp. (mm)	v disp (mm)
1.0	621.484	56	-0.209555	-1.44288
1.2	523.953	47	-0.234646	-1.60463
1.5	375.879	33	-0.266870	-1.81247
1.7	256.703	22	-0.287491	-1.94470
1.9	469.672	49	-0.313132	-2.11522

Tolerance = 0.001, u & v displacements measured at Point A				
Relaxation(ω)	Time (s)	Iterations	u disp. (mm)	v disp (mm)
1.0	1617.86	148	-0.291130	-1.96059
1.2	1194.43	111	-0.295519	-1.98881
1.5	756.758	66	-0.300194	-2.01884
1.7	412.286	38	-0.302740	-2.03503
1.9	944.696	96	-0.304766	-2.04643

Tolerance = 0.0001, u & v displacements measured at Point A				
Relaxation(ω)	Time (s)	Iterations	u disp. (mm)	v disp (mm)
1.0	2621.24	253	-0.302936	-2.03553
1.2	1864.91	180	-0.303368	-2.03831
1.5	1146.64	100	-0.303883	-2.04155
1.7	581.869	55	-0.304204	-2.04367
1.9	1229.72	137	-0.304331	-2.04427

Table 3.7: Cantilever Results - 369 Nodes and Triangular Elements

Tolerance = 0.01, u & v displacements measured at Point A				
Relaxation(ω)	Time (s)	Iterations	u disp. (mm)	v disp (mm)
1.0	25.4375	49	-0.163166	-1.14690
1.2	21.9219	41	-0.180227	-1.25647
1.5	15.1133	28	-0.20018	-1.38439
1.7	10.2188	18	-0.213332	-1.46800
1.9	16.0977	30	-0.227796	-1.56370

Tolerance = 0.001, u & v displacements measured at Point A				
Relaxation(ω)	Time (s)	Iterations	u disp. (mm)	v disp (mm)
1.0	101.977	120	-0.212191	-1.45633
1.2	45.000	89	-0.214606	-1.47180
1.5	26.9258	52	-0.217298	-1.48897
1.7	14.7266	27	-0.218742	-1.49811
1.9	27.9866	54	-0.219835	-1.50218

Tolerance = 0.0001, u & v displacements measured at Point A				
Relaxation(ω)	Time (s)	Iterations	u disp. (mm)	v disp (mm)
1.0	104.945	198	-0.218618	-1.49689
1.2	70.4414	141	-0.218880	-1.49856
1.5	38.7930	76	-0.219144	-1.50025
1.7	19.0117	36	-0.219303	-1.50126
1.9	37.9141	75	-0.219339	-1.50129

Table 3.8: Cantilever Results - 33 Nodes and Mixed Elements

Tolerance = 0.01, u & v displacements measured at Point A				
Relaxation(ω)	Time (s)	Iterations	u disp. (mm)	v disp (mm)
1.0	112.031	55	-0.197964	-1.38780
1.2	93.9570	46	-0.221141	-1.53727
1.5	66.4805	32	-0.250957	-1.72941
1.7	47.1445	22	-0.271865	-1.86256
1.9	73.2422	37	-0.274670	-1.87342

Tolerance = 0.001, u & v displacements measured at Point A				
Relaxation(ω)	Time (s)	Iterations	u disp. (mm)	v disp (mm)
1.0	284.832	143	-0.272275	-1.85970
1.2	214.941	107	-0.276230	-1.88508
1.5	128.625	63	-0.280431	-1.91201
1.7	77.5869	35	-0.286360	-1.92613
1.9	123.953	65	-0.284034	-1.93286

Tolerance = 0.0001, u & v displacements measured at Point A				
Relaxation(ω)	Time (s)	Iterations	u disp. (mm)	v disp (mm)
1.0	483.352	244	-0.282890	-1.92709
1.2	346.648	174	-0.283299	-1.92972
1.5	190.988	95	-0.283722	-1.93243
1.7	108.570	49	-0.283951	-1.93391
1.9	182.691	98	-0.284100	-1.93471

Table 3.9: Cantilever Results - 105 Nodes and Mixed Elements

Tolerance = 0.01, u & v displacements measured at Point A				
Relaxation(ω)	Time (s)	Iterations	u disp. (mm)	v disp (mm)
1.0	537.252	57	-0.212152	-1.47315
1.2	453.406	48	-0.238312	-1.64172
1.5	330.824	34	-0.272305	-1.86025
1.7	229.508	23	-0.293159	-1.99487
1.9	421.594	51	-0.306392	-2.04918

Tolerance = 0.001, u & v displacements measured at Point A				
Relaxation(ω)	Time (s)	Iterations	u disp. (mm)	v disp (mm)
1.0	1404.78	151	-0.296381	-2.00818
1.2	1057.64	113	-0.300888	-2.03714
1.5	651.98	67	-0.305647	-2.06770
1.7	377.910	39	-0.308412	-2.08519
1.9	782.637	100	-0.308643	-2.08336

Tolerance = 0.0001, u & v displacements measured at Point A				
Relaxation(ω)	Time (s)	Iterations	u disp. (mm)	v disp (mm)
1.0	2726.76	259	-0.308720	-2.08656
1.2	1753.57	189	-0.309321	-2.09043
1.5	969.398	103	-0.309747	-2.09312
1.7	534.016	56	-0.309990	-2.09460
1.9	1269.56	162	-0.310238	-2.09598

Table 3.10: Cantilever Results - 369 Nodes and Mixed Elements

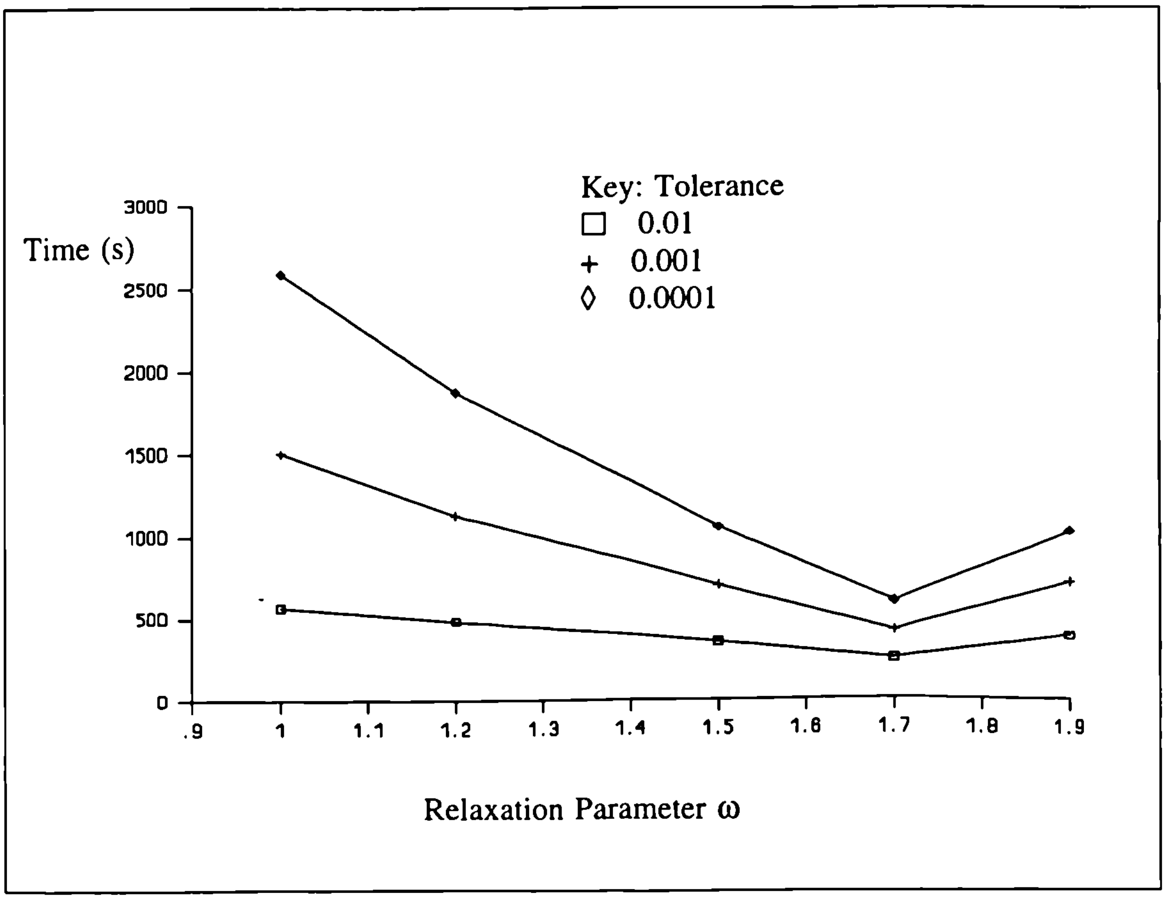

Figure 3.6: The Graph of Time against Relaxation Parameter
369 Node Cantilever - Quadrilateral Elements

Although the time taken varies depending on the relaxation parameter used, as long as the mesh is fine enough and a suitably small tolerance is used, the solution will approximate to the same value, though it may take 4 to 5 times as long to reach a converged solution as seen in Appendix B Figure B.13. Figure 3.6 indicates that if a stricter tolerance than 0.0001 is necessary to obtain a more accurate solution, the quickest solution time will be achieved with a relaxation parameter of approximately 1.7 when the number of global iterations is a minimum.

3.2 Example 2: Thermal Beam

The thermal beam example tests the algorithms ability to obtain accurate results for thermal problems. The beam is free to move everywhere except the very centre which is fixed in the x and y axis directions. The top edge of the beam is heated and the bottom edge cooled. The assumption of plane stress is again applicable as the length of the beam is much greater than the other dimensions. The same meshes that were used for the cantilever problem are used here along with the various relaxation parameter values and tolerances.

3.2.1 Problem Specification

The beam has a length of 1,000mm and a height of 200mm. The temperature increase along the top edge of the beam is 25 degrees centigrade and there is a decrease in temperature of 25 degrees centigrade along the bottom edge. There is a linear thermal gradient through the beam acting in the y-axis direction so that along the centreline of the beam the temperature is 0°C. The only point fixed is the node at the very centre of the beam. Figure 3.7 shows the initial beam and conditions applied.

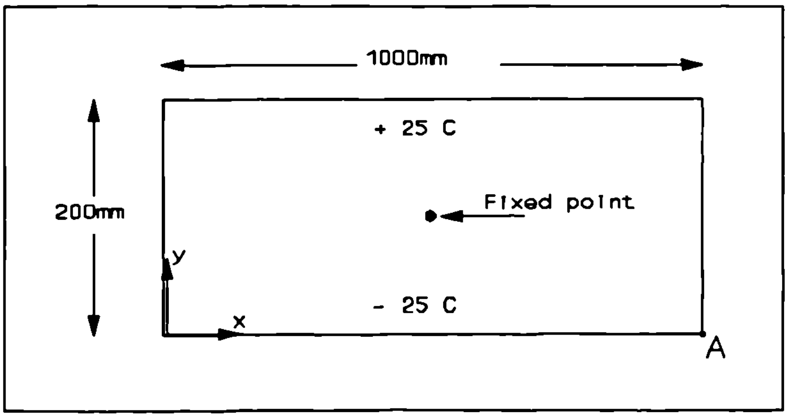

Figure 3.7: Thermal Beam Description

For the material properties of the beam a Poisson's ratio of 0.25 was used with a Young's Modulus of 210,000N/mm^2. The coefficient of thermal expansion, α, was set at 0.01°C^{-1}, so that the displacements of the beam were clearly visible.

As with the cantilever beam, three styles of mesh were used:- the first all quadrilaterals; the second all triangles and the third a mixture containing both triangles and quadrilaterals. Meshes with 33 nodes, 105 nodes and 369 nodes were used to collect results for the thermal beam.

3.2.2 Analytical Results

Figure 3.8 shows a general beam which has a temperature gradient in the y-axis direction only so the temperature function, *T*, throughout the beam is dependent only on the y-axis values.

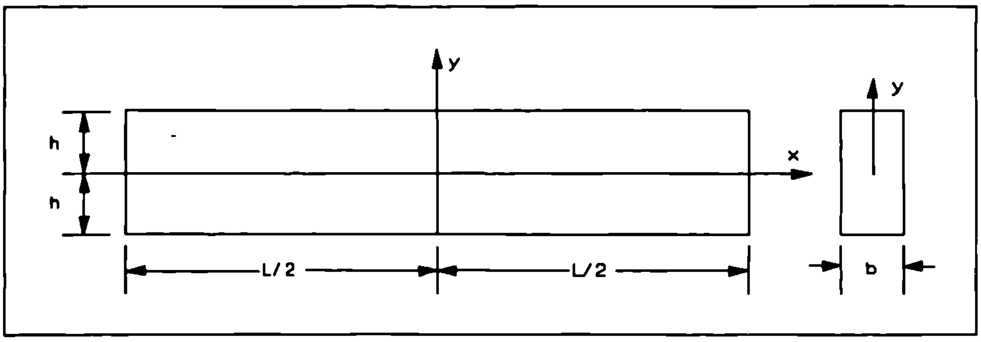

Figure 3.8: General Beam with Y-Axis Thermal Gradient

The temperature gradient for this specific rectangular beam is:

$$T = T(y) = \frac{y}{4} \tag{3.3}$$

The analytic solution for the *u* and *v* displacements of this problem are given by [Boley and Weiner (1967)]:

$$\begin{aligned} u &= \frac{x}{E}\left[\frac{(bN_T)}{A} + \frac{y}{I}(bM_T)\right] \\ v &= -\frac{(bM_T)}{2EI}x^2 - \frac{\nu}{E}\left[\frac{(bN_T)}{A}y + \frac{y^2}{2I}(bM_T)\right] + \alpha(1+\nu)\int_0^y T\,dy \end{aligned} \tag{3.4}$$

Where the area, *A*, is *2bh* and the second moment of area, *I*, of the cross section is

$2h^3b/3$. N_T and M_T are given by the following relationships.

$$N_T = \alpha E \int_{-h}^{h} T \, dy$$
$$M_T = \alpha E \int_{-h}^{h} Ty \, dy \qquad (3.5)$$

For this specific thermal beam when $h=100$, $b=1$, $l=1000$ with the material properties and temperature defined earlier, N_T reduces to 0. Using all the information known in equation 3.4, the u and v displacements can be found at the point A in Figure 3.7. The analytical solution at A is u =- 125mm and v = -300mm.

The expected displaced mesh is shown in Figure 3.9.

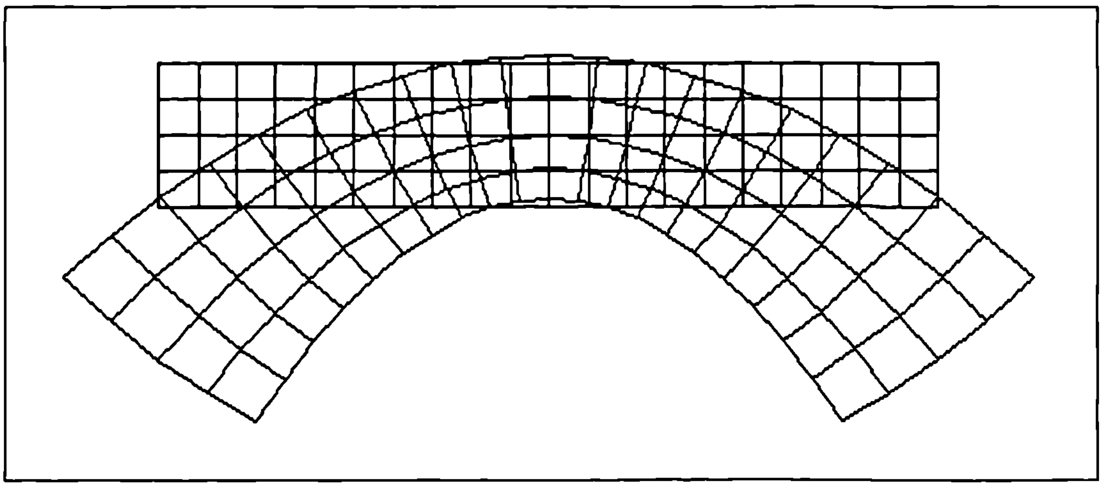

Figure 3.9: Displaced Thermal Beam

3.2.3 Finite Element Results

Using the IFECS package comparable finite element code results for the displacement at point A in Figure 3.7 were recorded along with the time taken. The displacement results for the thermal beam can be seen in Table 3.11. The triangular mesh used for the three different mesh sizes can be seen in Appendix B, Figures B.4-B.6. Figure 3.3 shows the 33 node mesh.

Number of Nodes	displacement at A		Time for solution (s)
	u (mm)	v (mm)	
33	-72.9	-168	7
105	-104.6	-249	36
369	-118.8	-285	195

Table 3.11: Finite Element Results - Thermal Problem

3.2.4 CV-UM Results

Various meshes differing in type and size were used with the control volume unstructured mesh code to test the accuracy of the algorithm as in the cantilever example in 3.1. The displacements and solution time were compiled in tables for the varying tolerances and relaxation parameters used.

3.2.4.1 Quadrilaterals

The quadrilateral mesh used is the same as the mesh used in the quadrilateral case for the cantilever example, Figure 3.4. The three different sized meshes used are shown in detail in Appendix B, Figures B.1-B.3. The displacement results were collected along with the time taken for different relaxation parameter values and tolerances. Tables 3.12-3.14 detail the quadrilateral mesh results for the thermal beam. Graphs showing the variation in global iterations required for a particular relaxation parameter are displayed in Appendix B, Figures B.22-B.25. From the 369 node mesh displacement results in Table 3.14, the u displacement is -124.538mm and the v displacement -298.929mm. The results are very close to the analytical solution, detailed in section 3.2.2, and are much better than the finite element results with triangular elements.

3.2.4.2 Triangles

The displacement results for the triangular mesh can be seen in Tables 3.15-3.17. The mesh used is the same as for the finite element results and can be seen in Appendix B, B.4-B.6. The value of the relaxation parameter and tolerance were altered to see the effect on the displacement results when using the control volume unstructured mesh code. Appendix B, Figures B.26-B.29, illustrate for the triangular mesh, the variation in global iterations required for a particular relaxation parameter before the set tolerance is reached. Table 3.17 detailing the 369 node triangular mesh results, suggests values for the *u* and *v* displacement results of -120.173mm and -288.561mm respectively. These results are not as accurate as the quadrilateral results but are more accurate than the finite element triangular mesh results.

3.2.4.3 Mixed Mesh

The mixed mesh used for the cantilever beam is used here for the thermal beam, shown in Figure 3.5 and Appendix B, Figures B.7-B.9. Altering the tolerance and the value of the relaxation parameter the displacements were noted as shown in Table 3.18-3.20. The consequences of using a particular relaxation parameter, for the three mixed meshes, on the number of global iterations used are seen in Figures B.30-B.33 in Appendix B. From the mixed mesh results with 369 nodes in Table 3.20 the *u* and *v* displacements are found to be -122.915mm and -295.374mm respectively, values between the triangular and quadrilateral element results.

Tolerance = 0.01, u & v displacements measured at Point A				
Relaxation(ω)	Time (s)	Iterations	u disp. (mm)	v disp (mm)
1.0	15.6602	26	-113.333	-266.069
1.2	12.0898	20	-115.805	-274.314
1.5	7.52734	12	-118.953	-284.523
1.7	7.80078	13	-121.750	-291.601
1.9	18.2422	32	-120.732	-290.110

Tolerance = 0.001, u & v displacements measured at Point A				
Relaxation(ω)	Time (s)	Iterations	u disp. (mm)	v disp (mm)
1.0	27.9141	47	-119.401	-285.346
1.2	20.3281	34	-119.724	-286.414
1.5	10.3828	17	-120.057	-287.505
1.7	12.4180	21	-120.184	-287.782
1.9	28.7383	51	-120.511	-289.226

Tolerance = 0.0001, u & v displacements measured at Point A				
Relaxation(ω)	Time (s)	Iterations	u disp. (mm)	v disp (mm)
1.0	41.3750	70	-120.118	-287.625
1.2	28.5156	48	-120.142	-287.706
1.5	13.9023	23	-120.183	-287.835
1.7	15.2188	26	-120.185	-287.836
1.9	50.1094	89	-120.190	-287.827

Table 3.12: Thermal Beam Results - 33 Nodes and Quadrilateral Elements

Tolerance = 0.01, u & v displacements measured at Point A				
Relaxation(ω)	Time (s)	Iterations	u disp. (mm)	v disp (mm)
1.0	58.5703	30	-115.009	-269.328
1.2	45.2734	23	-117.634	-278.112
1.5	30.1641	15	-121.473	-290.722
1.7	30.8789	16	-124.014	-297.976
1.9	87.9102	50	-121.636	-288.933

Tolerance = 0.001, u & v displacements measured at Point A				
Relaxation(ω)	Time (s)	Iterations	u disp. (mm)	v disp (mm)
1.0	107.855	56	-122.506	-293.232
1.2	77.5273	40	-122.814	-294.258
1.5	43.4063	22	-123.256	-295.698
1.7	49.0117	26	-123.526	-296.136
1.9	131.430	75	-123.446	-296.136

Tolerance = 0.0001, u & v displacements measured at Point A				
Relaxation(ω)	Time (s)	Iterations	u disp. (mm)	v disp (mm)
1.0	159.008	83	-123.360	-295.955
1.2	111.758	58	-123.396	-296.071
1.5	56.7578	29	-123.435	-296.214
1.7	59.7227	32	-123.464	-296.274
1.9	168.734	97	-123.441	-296.192

Table 3.13: Thermal Beam Results - 105 Nodes and Quadrilateral Elements

Tolerance = 0.01, u & v displacements measured at Point A				
Relaxation(ω)	Time (s)	Iterations	u disp. (mm)	v disp (mm)
1.0	261.922	31	-115.330	-269.614
1.2	204.672	24	-118.264	-279.374
1.5	145.770	17	-122.504	-293.198
1.7	141.758	18	-123.766	-298.230
1.9	365.879	55	-123.361	-293.149

Tolerance = 0.001, u & v displacements measured at Point A				
Relaxation(ω)	Time (s)	Iterations	u disp. (mm)	v disp (mm)
1.0	492.141	59	-123.558	-295.801
1.2	353.078	42	-123.860	-296.806
1.5	203.957	24	-124.311	-298.276
1.7	182.801	24	-124.556	-298.930
1.9	626.813	94	-124.645	-299.244

Tolerance = 0.0001, u & v displacements measured at Point A				
Relaxation(ω)	Time (s)	Iterations	u disp. (mm)	v disp (mm)
1.0	721.484	87	-124.454	-298.652
1.2	509.012	61	-124.494	-298.783
1.5	270.824	32	-124.538	-298.929
1.7	245.492	33	-124.543	-298.943
1.9	834.398	126	-124.586	-299.104

Table 3.14: Thermal Beam Results - 369 Nodes and Quadrilateral Elements

Tolerance = 0.01, u & v displacements measured at Point A				
Relaxation(ω)	Time (s)	Iterations	u disp. (mm)	v disp (mm)
1.0	14.2852	21	-80.8676	-186.580
1.2	11.0430	16	-82.3853	-191.553
1.5	7.14453	10	-84.2108	-196.913
1.7	11.3711	17?	-84.6518	-197.648
1.9	29.2305	46	-83.9004	-196.641

Tolerance = 0.001, u & v displacements measured at Point A				
Relaxation(ω)	Time (s)	Iterations	u disp. (mm)	v disp (mm)
1.0	24.5078	37	-84.1223	-196.516
1.2	17.4180	26	-84.2710	-197.007
1.5	9.72656	14	-84.5079	-197.634
1.7	13.8477	21	-84.4015	-197.261
1.9	39.0117	62	-84.4459	-197.363

Tolerance = 0.0001, u & v displacements measured at Point A				
Relaxation(ω)	Time (s)	Iterations	u disp. (mm)	v disp (mm)
1.0	34.7813	53	-84.4648	-197.537
1.2	23.8477	36	-84.4802	-197.585
1.5	11.5938	17	-84.5042	-197.651
1.7	18.2422	28	-84.5156	-197.672
1.9	56.9258	91	-84.5026	-197.652

Table 3.15: Thermal Beam Results - 33 Nodes and Triangular Elements

Tolerance = 0.01, u & v displacements measured at Point A				
Relaxation(ω)	Time (s)	Iterations	u disp. (mm)	v disp (mm)
1.0	62.4180	28	-102.542	-239.442
1.2	47.3633	21	-104.561	-246.255
1.5	32.3086	14	-107.908	-257.268
1.7	33.2422	15	-110.042	-262.350
1.9	112.910	56	-108.434	-256.899

Tolerance = 0.001, u & v displacements measured at Point A				
Relaxation(ω)	Time (s)	Iterations	u disp. (mm)	v disp (mm)
1.0	111.703	51	-108.522	-258.407
1.2	81.7031	37	-108.836	-259.447
1.5	45.3281	20	-109.147	-260.499
1.7	53.2422	25	-109.340	-260.965
1.9	167.582	83	-109.287	-260.831

Tolerance = 0.0001, u & v displacements measured at Point A				
Relaxation(ω)	Time (s)	Iterations	u disp. (mm)	v disp (mm)
1.0	165.223	76	-109.229	-260.639
1.2	116.156	53	-109.259	-260.740
1.5	58.5195	26	-109.290	-260.838
1.7	69.8359	33	-109.301	-260.857
1.9	210.219	105	-109.304	-260.866

Table 3.16: Thermal Beam Results - 105 Nodes and Triangular Elements

Tolerance = 0.01, u & v displacements measured at Point A				
Relaxation(ω)	Time (s)	Iterations	u disp. (mm)	v disp (mm)
1.0	286.922	30	-111.237	-260.134
1.2	231.922	24	-114.651	-271.388
1.5	166.703	17	-118.430	-283.682
1.7	161.098	18	-120.471	-291.596
1.9	501.098	63	-120.056	-287.682

Tolerance = 0.001, u & v displacements measured at Point A				
Relaxation(ω)	Time (s)	Iterations	u disp. (mm)	v disp (mm)
1.0	533.898	57	-119.213	-285.505
1.2	386.371	41	-119.549	-286.621
1.5	231.484	24	-119.989	-288.055
1.7	246.594	28	-120.169	-288.733
1.9	617.817	89	-119.922	-287.480

Tolerance = 0.0001, u & v displacements measured at Point A				
Relaxation(ω)	Time (s)	Iterations	u disp. (mm)	v disp (mm)
1.0	787.145	85	-120.093	-288.289
1.2	550.496	59	-120.125	-288.397
1.5	306.043	32	-120.173	-288.561
1.7	315.441	36	-120.200	-288.643
1.9	954.613	125	-120.164	-288.512

Table 3.17: Thermal Beam Results - 369 Nodes and Triangular Elements

Tolerance = 0.01, u & v displacements measured at Point A				
Relaxation(ω)	Time (s)	Iterations	u disp. (mm)	v disp (mm)
1.0	12.3086	24	-99.9573	-232.336
1.2	10.1641	19	-102.391	-240.292
1.5	6.42969	11	-104.975	-248.511
1.7	6.75781	12	-106.579	-252.521
1.9	17.2500	36	-105.232	-248.298

Tolerance = 0.001, u & v displacements measured at Point A				
Relaxation(ω)	Time (s)	Iterations	u disp. (mm)	v disp (mm)
1.0	21.5352	44	-105.281	-248.974
1.2	15.9883	32	-105.554	-249.860
1.5	8.73438	16	-105.854	-250.803
1.7	11.5938	21	-105.984	-251.230
1.9	25.5508	55	-105.540	-249.388

Tolerance = 0.0001, u & v displacements measured at Point A				
Relaxation(ω)	Time (s)	Iterations	u disp. (mm)	v disp (mm)
1.0	31.1523	65	-105.860	-250.782
1.2	22.0898	45	-105.883	-250.857
1.5	10.5508	20	-105.913	-250.954
1.7	14.2852	29	-105.931	-251.007
1.9	40.1094	88	-105.910	-250.932

Table 3.18: Thermal Beam Results - 33 Nodes and Mixed Elements

Tolerance = 0.01, u & v displacements measured at Point A				
Relaxation(ω)	Time (s)	Iterations	u disp. (mm)	v disp (mm)
1.0	56.5391	29	-109.841	-257.117
1.2	45.8242	23	-113.036	-267.701
1.5	32.7500	15	-116.467	-278.979
1.7	37.0313	19	-118.012	-283.145
1.9	90.6055	51	-119.350	-286.369

Tolerance = 0.001, u & v displacements measured at Point A				
Relaxation(ω)	Time (s)	Iterations	u disp. (mm)	v disp (mm)
1.0	104.285	55	-117.206	-280.650
1.2	74.8906	39	-117.482	-281.580
1.5	43.5156	22	-117.929	-283.016
1.7	51.5938	25	-118.154	-283.578
1.9	142.750	82	-118.176	-283.578

Tolerance = 0.0001, u & v displacements measured at Point A				
Relaxation(ω)	Time (s)	Iterations	u disp. (mm)	v disp (mm)
1.0	152.637	81	-117.990	-283.167
1.2	107.910	57	-118.029	-283.298
1.5	54.8359	28	-118.061	-282.400
1.7	59.8906	32	-118.087	-283.445
1.9	179.563	104	-118.093	-283.507

Table 3.19: Thermal Beam Results - 105 Nodes and Mixed Elements

Tolerance = 0.01, u & v displacements measured at Point A				
Relaxation(ω)	Time (s)	Iterations	u disp. (mm)	v disp (mm)
1.0	263.848	31	-113.955	-266.726
1.2	216.316	24	-116.831	-276.310
1.5	142.359	16	-120.683	-288.948
1.7	155.223	19	-122.090	-292.520
1.9	420.551	59	-123.362	-296.274

Tolerance = 0.001, u & v displacements measured at Point A				
Relaxation(ω)	Time (s)	Iterations	u disp. (mm)	v disp (mm)
1.0	482.855	58	-116.112	-292.035
1.2	353.461	42	-122.267	-293.269
1.5	206.320	24	-122.731	-294.770
1.7	386.320	29	-122.932	-295.350
1.9	579.559	83	-123.089	-295.838

Tolerance = 0.0001, u & v displacements measured at Point A				
Relaxation(ω)	Time (s)	Iterations	u disp. (mm)	v disp (mm)
1.0	713.898	87	-122.833	-295.031
1.2	512.855	62	-122.878	-295.182
1.5	271.371	32	-122.915	-295.296
1.7	281.043	36	-122.939	-295.374
1.9	784.176	114	-122.955	-295.442

Table 3.20: Thermal Beam Results - 369 Nodes and Mixed Elements

3.2.5 Comparison of Results

The control volume unstructured mesh results are seen to be more accurate than the finite element results depending on the tolerance and relaxation parameter chosen. Comparing the timings displayed in Tables 3.11-3.20 for the finite element code and the control volume unstructured mesh code on the same 386 machine, it is seen that the finite element results are faster. If the grid was refined further, increasing the number of elements and nodes greatly, it is expected that the difference in time taken to reach solution for the two algorithms would be closer.

As with the cantilever problem, the time taken, for the algorithm to reach convergence to a given tolerance, is greatly affected by the choice of relaxation parameter. If the tolerance is strict enough the solution will converge to the same displacement results regardless of relaxation parameter used. Appendix B contains graphs, Figures B.22-B.33, showing the effect of relaxation parameter chosen. A careful choice of relaxation parameter used for the larger meshes can greatly reduce the time taken to reach solution.

Studying the control volume unstructured mesh results it is observed that the thermal beam problem is much more suited to quadrilateral elements than triangular elements as was the cantilever example of section 3.1.2. Quadrilateral elements produce displacement results that are nearest the analytical results followed by the mixed element results then the triangular element results.

3.3 Example 3: Cusp Problem

For this problem the typical dimensions of a cusp tooth were used. The cusp consists of three layers of material as seen in Figure 3.10. The problem shows how the control volume unstructured mesh algorithm can handle multi-material problems and general unstructured geometries. A typical node on one of the two material boundaries is surrounded by elements of differing materials. A pressure is applied to the top boundary of the cusp tooth simulating mastication.

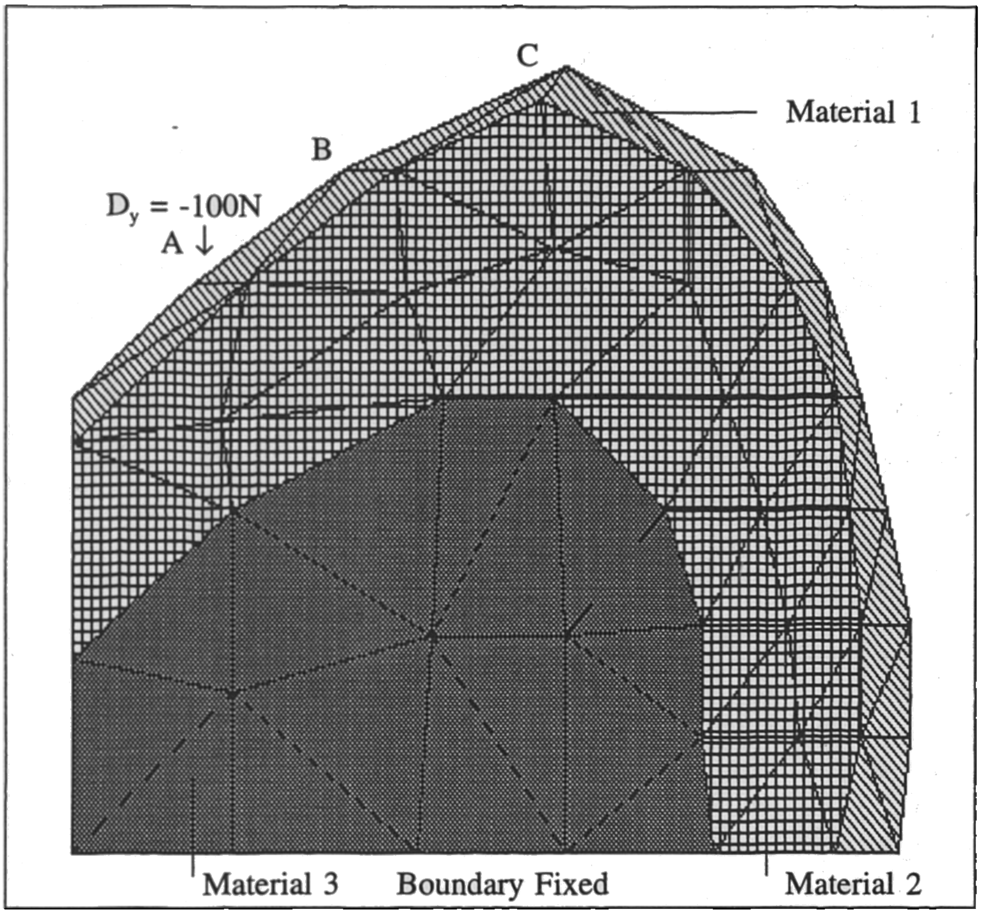

Figure 3.10: Cusp Initial Problem Description

The cusp tooth has a force applied to point A as displayed in Figure 3.10 and the assumption of plane stress is used when obtaining the resulting nodal displacements.

3.3.1 Problem Specification

The cusp had a maximum width of 6.8 mm and a maximum height of 6.9 mm. The material properties for the Young's Modulus, Poisson's ratio and the coefficient of thermal expansion, which make up the three different layers of the cusp are shown in Table 3.21.

Material	Young's modulus, E N/mm^2	Poisson's ratio	Coefficient of Thermal Expansion, $°C^{-1}$
1	2,650,000	0 3	0.0
2	4,000,000	0.3	0.0
3	2,650,000	0.3	0.0

Table 3.21: Cusp Material Properties

The coefficient of thermal expansion does not alter the resulting displacements of this problem as temperature effects are not included in the example.

3.3.2 Finite Element Results

The unstructured triangular mesh used for the cusp is displayed in Figure 3.11, and consists of 45 nodes. The displacements due to the force applied were found using the finite element code IFECS. The finite element displacement results at the points A, B and C as marked in Figure 3.10 can be seen in Table 3.22.

Points	Displacement($x10^{-5}mm$)	
	u	v
A	-4.085	-6.825
B	-4.923	-3.741
C	-5.803	-1.191

Table 3.22: Finite Element Cusp Problem Results

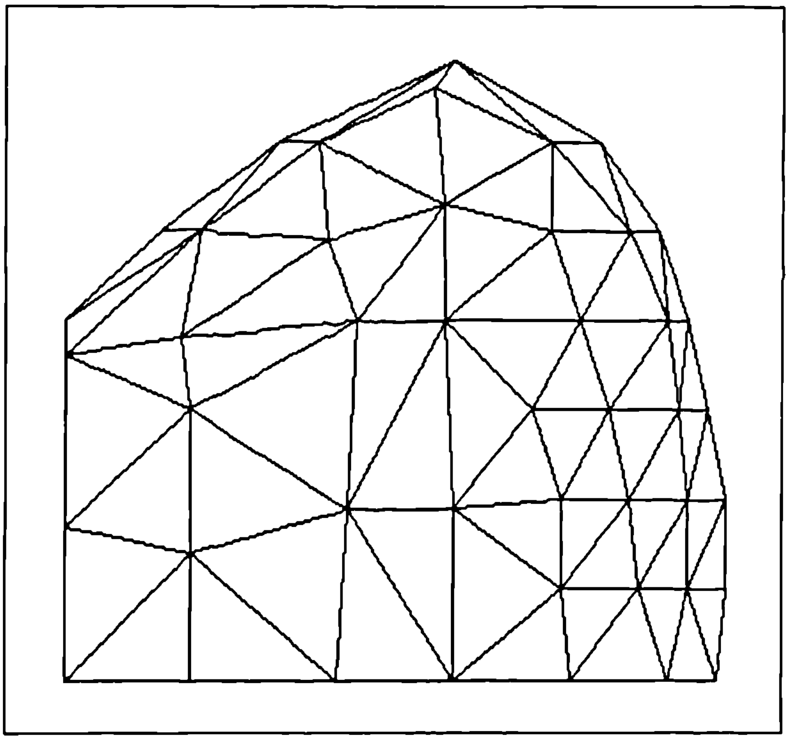

Figure 3.11: Cusp Triangular Element Mesh

Figure 3.12 shows the displaced mesh overlaying the original mesh with the displacements magnified by a factor of 10,000.

3.3.3 CV-UM Results

The 45 node unstructured Cusp mesh was used with the control volume unstructured mesh code to obtain the displacements due to the applied stress. Results were collected for different values of tolerance and relaxation parameter. Two different meshes were used, one consisting of triangular elements and the other a mixture of quadrilateral and triangular elements.

3.3.3.1 Triangles

The triangular mesh used with the unstructured mesh code was the same as the mesh used for the IFECS finite element program as shown in Figure 3.11 consisting of 69 triangular elements. Tables 3.23 to 3.25 show the displacements calculated at the nodes A, B, and C using the control volume unstructured mesh code for different tolerances and relaxation parameters. Figure 3.12 shows the displaced mesh overlaying the original mesh with the displacements magnified by a factor of 10,000.

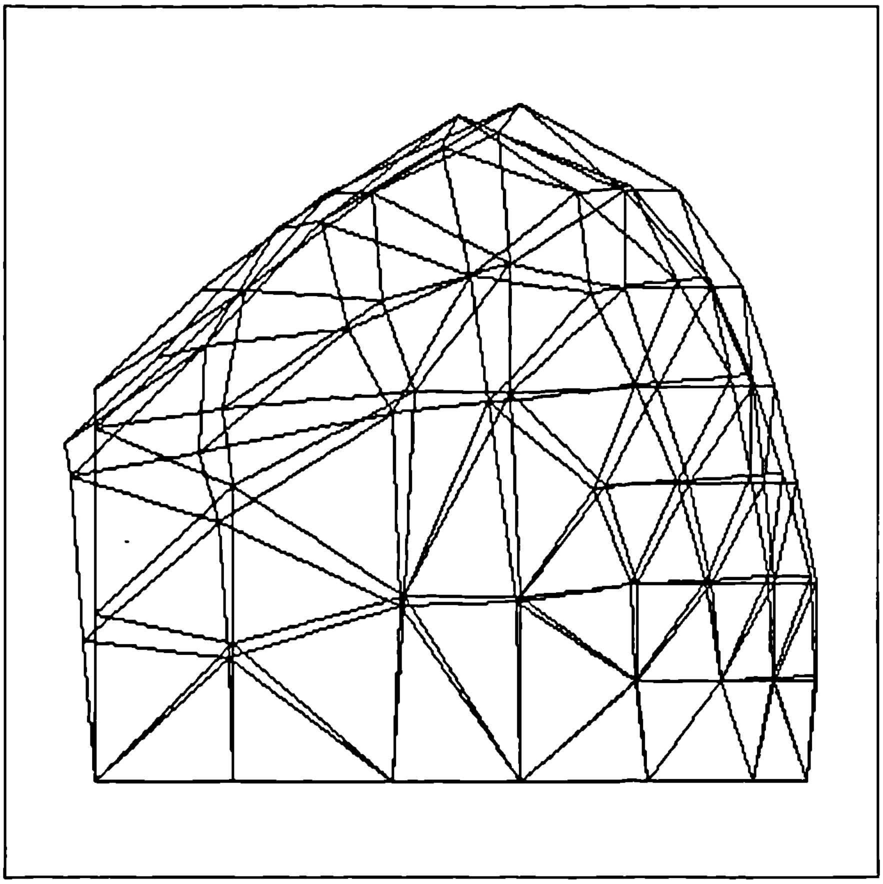

Figure 3.12: Cusp Displacements
(x 10,000)

3.3.3.2 Mixed Mesh

The 45 node triangular mesh displayed in Figure 3.11 was altered, where possible, to create quadrilateral elements that did not affect the position of the nodal coordinate points. The resulting mixed mesh is seen in Figure 3.13, element boundaries still border the material boundaries so the same material boundaries are conserved. The control volume unstructured mesh algorithm was tested on this mixed mesh in the same fashion as the triangular mesh. The displacement results for various relaxation parameter values and tolerances are shown in Tables 3.26 to 3.28.

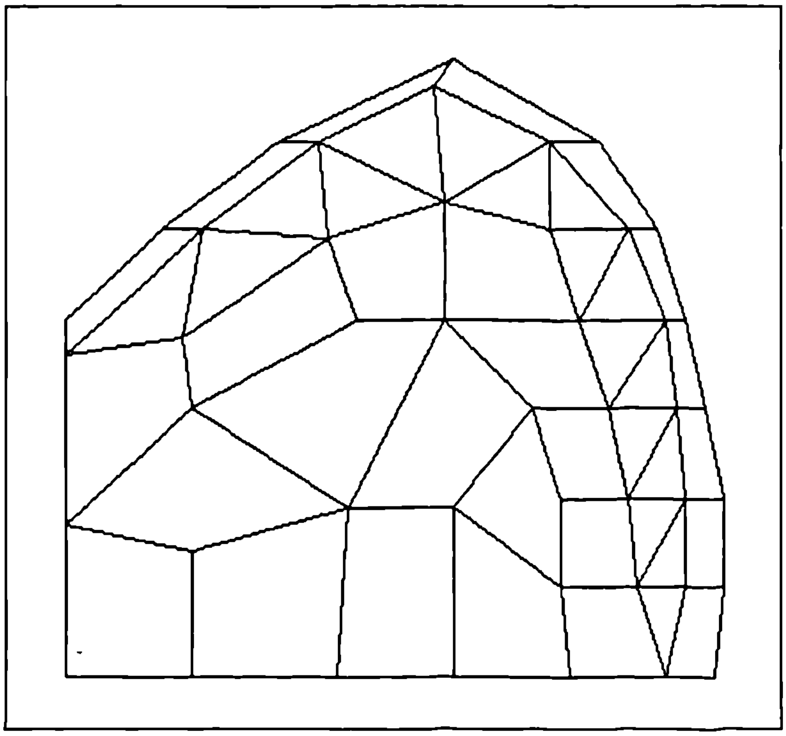

Figure 3.13: Cusp Mixed Element Mesh

3.3.4 Comparison of Results

The finite element results and the triangular control volume unstructured mesh results are virtually indistinguishable. The mixed mesh results vary a fraction from the others but are not necessarily incorrect as an analytical solution to the problem is not available. From the results of Tables 3.23-3.28 it is clearly seen that the correct choice of relaxation parameter used can greatly influence the time taken for the algorithm to reach a converged solution, though the displacement values only slightly differ.

Tolerance = 0.01, Displacements measured at Points A, B, C (10^{-5}mm)								
relaxation (ω)	time (s)	iterations	Point A		Point B		Point C	
			u	v	u	v	u	v
1.0	10.38	10	-4.0482	-6.8074	-4.8748	-3.7307	-5.7410	-1.1942
1.1	8.68	8	-4.0538	-6.8123	-4.8821	-3.7347	-5.7502	-1.1950
1.3	6.92	6	-4.0994	-6.8284	-4.9410	-3.7450	-5.8203	-1.1893
1.5	9.39	9	-4.1099	-6.8331	-4.9491	-3.7493	-5.8401	-1.1861
1.7	14.12	15	-4.1076	-6.8265	-4.9495	-3.7411	-5.8164	-1.1862
1.9	38.84	47	-4.1345	-6.8412	-4.9924	-3.7533	-5.8658	-1.1865

Table 3.23: Cusp Problem Results
Triangular Mesh, Tolerance = 0.01

Tolerance = 0.001, Displacements measured at Points A, B, C (10^{-5}mm)								
relaxation (ω)	time (s)	iterations	Point A		Point B		Point C	
			u	v	u	v	u	v
1.0	13.79	14	-4.0803	-6.8225	-4.9167	-3.7411	-5.7949	-1.1913
1.1	12.09	12	-4.0831	-6.8240	-4.9203	-3.7421	-5.7996	-1.1911
1.3	8.57	8	-4.0856	-6.8249	-4.9237	-3.7427	-5.8036	-1.1909
1.5	12.75	13	-4.0849	-6.8249	-4.9227	-3.7429	-5.8024	-1.1906
1.7	20.44	23	-4.0828	-6.8243	-4.9211	-3.7425	-5.8005	-1.1907
1.9	63.19	78	-4.0847	-6.8245	-4.9223	-3.7427	-5.8022	-1.1908

Table 3.24: Cusp Problem Results
Triangular Mesh, Tolerance = 0.001

Tolerance = 0.0001, Displacements measured at Points A, B, C (10^{-5}mm)								
relaxation (ω)	time (s)	iterations	Point A		Point B		Point C	
			u	v	u	v	u	v
1.0	18.07	19	-4.0848	-6.8246	-4.9226	-3.7425	-5.8024	-1.1909
1.1	14.61	15	-4.0849	-6.8247	-4.9227	-3.7426	-5.8026	-1.1909
1.3	10.99	11	-4.0853	-6.8248	-4.9232	-3.7427	-5.8032	-1.1909
1.5	15.16	16	-4.0850	-6.8247	-4.9229	-3.7426	-5.8028	-1.1909
1.7	25.99	30	-4.0853	-6.8248	-4.9233	-3.7427	-5.8033	-1.1908
1.9	80.86	100	-4.0850	-6.8247	-4.9228	-3.7426	-5.8028	-1.1908

Table 3.25: Cusp Problem Results
Triangular Mesh, Tolerance = 0.0001

Tolerance = 0.01, Displacements measured at Points A, B, C (10^{-5}mm)								
relaxation (ω)	time (s)	iterations	Point A		Point B		Point C	
			u	v	u	v	u	v
1.0	9.29	10	-3.8140	-7.4086	-4.6847	-3.7873	-5.5336	-1.2922
1.1	7.80	8	-3.8190	-7.4123	-4.6920	-3.7906	-5.5431	-1.2911
1.3	6.27	6	-3.8710	-7.4297	-4.7592	-3.8010	-5.6262	-1.2841
1.5	8.35	9	-3.8461	-7.4216	-4.7326	-3.8006	-5.5997	-1.2852
1.7	13.13	16	-3.8890	-7.4360	-4.7790	-3.8028	-5.6492	-1.2850
1.9	37.09	51	-3.8298	-7.4120	-4.7249	-3.7965	-5.5744	-1.2852

Table 3.26: Cusp Problem Results
Mixed Mesh, Tolerance = 0.01

Tolerance = 0.001, Displacements measured at Points A, B, C (10^{-5}mm)								
relaxation (ω)	time (s)	iterations	Point A		Point B		Point C	
			u	v	u	v	u	v
1.0	13.18	15	-3.8478	-7.4231	-4.7293	-3.7967	-5.5915	-1.2871
1.1	10.88	12	-3.8488	-7.4236	-4.7304	-3.7970	-5.5930	-1.2870
1.3	8.52	9	-3.8507	-7.4243	-4.7329	-3.7935	-5.5961	-1.2867
1.5	11.15	13	-3.8495	-7.4241	-4.7315	-3.7970	-5.5947	-1.2867
1.7	18.07	23	-3.8503	-7.4239	-4.7326	-3.7978	-5.5958	-1.2864
1.9	52.80	74	-3.8474	-7.4236	-4.7296	-3.7967	-5.5925	-1.2869

Table 3.27: Cusp Problem Results
Mixed Mesh, Tolerance = 0.001

Tolerance = 0.0001, Displacements measured at Points A, B, C (10^{-5}mm)								
relaxation (ω)	time (s)	iterations	Point A		Point B		Point C	
			u	v	u	v	u	v
1.0	16.32	19	-3.8505	-7.4243	-4.7327	-3.7974	-5.5960	-1.2867
1.1	13.24	15	-3.8507	-7.4243	-4.7329	-3.7974	-5.5962	-1.2867
1.3	9.23	10	-3.8507	-7.4244	-4.7329	-3.7974	-5.5962	-1.2867
1.5	13.29	16	-3.8510	-7.4245	-4.7333	-3.7975	-5.5968	-1.2867
1.7	24.29	32	-3.8511	-7.4245	-4.7334	-3.7975	-5.5968	-1.2867
1.9	70.05	99	-3.8511	-7.4245	-4.7333	-3.7975	-5.5968	-1.2867

Table 3.28: Cusp Problem Results
Mixed Mesh, Tolerance = 0.0001

3.4 Example 4: Stress Concentration at a Hole

This example tests whether, once the displacements have been obtained by the control volume unstructured mesh algorithm, the correct stresses can be obtained. A flat square plate, Figure 3.14, is subjected to a uniform tensile stress σ, at the top and bottom edges of the plate. At the centre of the plate is a small circular hole. The thickness of the plate is assumed to be sufficiently small so that the plane stress approximation is applicable.

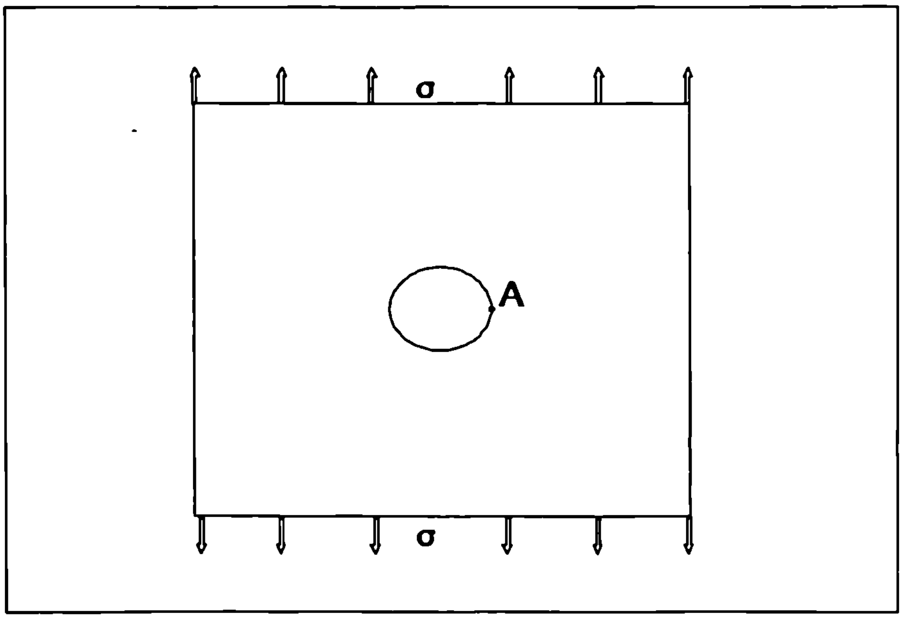

Figure 3.14: Square Plate with a Central Hole

3.4.1 Problem Specification

The plate has a width and height of 200 mm and the diameter of the hole is 10 mm. There is a tensile stress applied to the top and bottom surfaces of 1,000N/mm^2. Only one quarter of the plate need be considered for solution because of the symmetry of the problem. The Young's modulus for the plate was taken as 210,000 N/mm^2 and the Poisson's ratio was 0.25. Figure 3.15 shows the quarter of the square plate with the initial conditions.

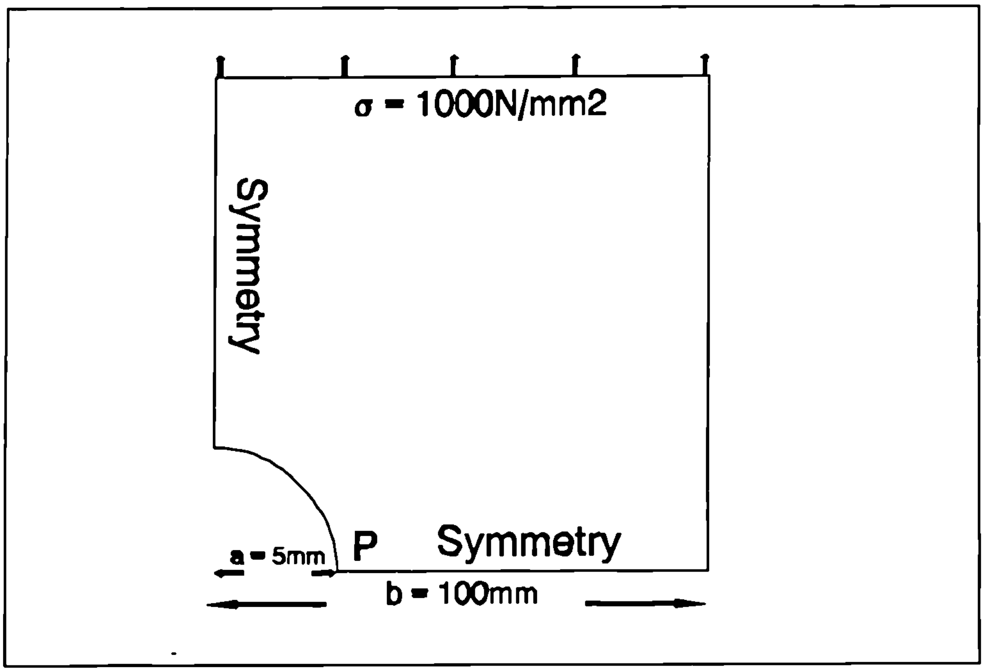

Figure 3.15: Plate with Hole Initial Conditions

3.4.2 Analytical Results

The hole at the centre of the plate causes local concentrations of stresses, the maximum stress being at x = +a (and -a), y = 0, the point P in Figure 3.15. The analytical solution for the stress at A in Figure 3.14, P in Figure 3.15, is $\sigma_{yy} = 3\sigma$ [Fenner (1986)], where in this case the stress concentration factor is three. The width of the plate is much larger than the diameter of the hole so the stresses diminish rapidly with distance from the hole to the values they would have in its absence. With a tensile stress of 1,000N/mm^2 applied at the top edge of the plate and at the bottom edge of the plate, this gives the analytical stress at point A of 3,000N. The displaced elongated mesh for the top right quadrant is shown in Figure 3.16.

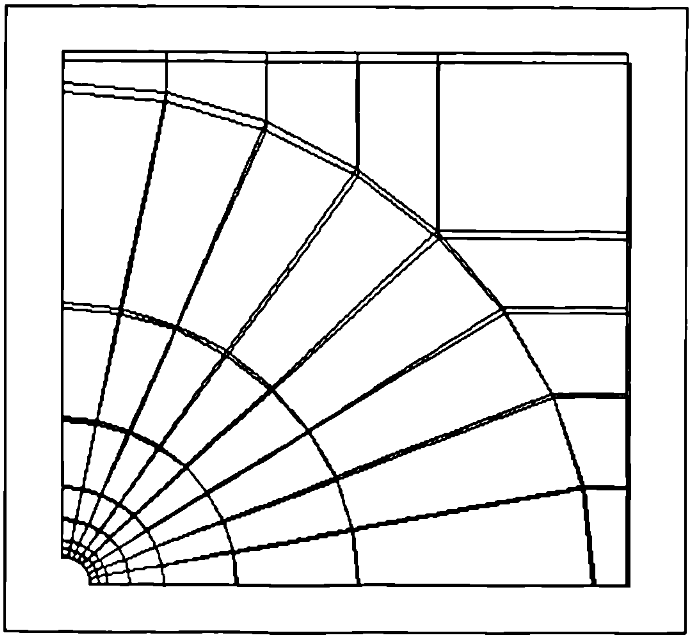

Figure 3.16: Displaced Plate with Hole (Displacements x4)

3.4.3 Finite Element Results

The finite elements code IFECS was used with the triangular mesh shown in Figure 3.17 to obtain results for the stress at point A in Figure 3.14. The stress at point A was found to be 2379.94 N/mm^2, giving a stress concentration factor of 2.380.

3.4.4 CV-UM Results

The 83 node unstructured plate mesh was used with the control volume unstructured mesh code. The results were collected for different values of the tolerance and relaxation parameter. Two meshes were used to obtain a solution to the problem the first a triangular mesh, *the same as used with the finite element code, and the second a* quadrilateral mesh.

3.4.4.1 Triangles

The triangular mesh shown in Figure 3.17 was used to obtain the stress results at point A in Figure 3.14. The results were collected and tabulated for different values of the relaxation parameter and tolerance, as shown in Table 3.30. The stress, σ_{yy}, calculated at point A is 2717.7N/mm^2, which is substantially closer to the analytical solution than the finite element triangular mesh solution obtained in section 3.4.3

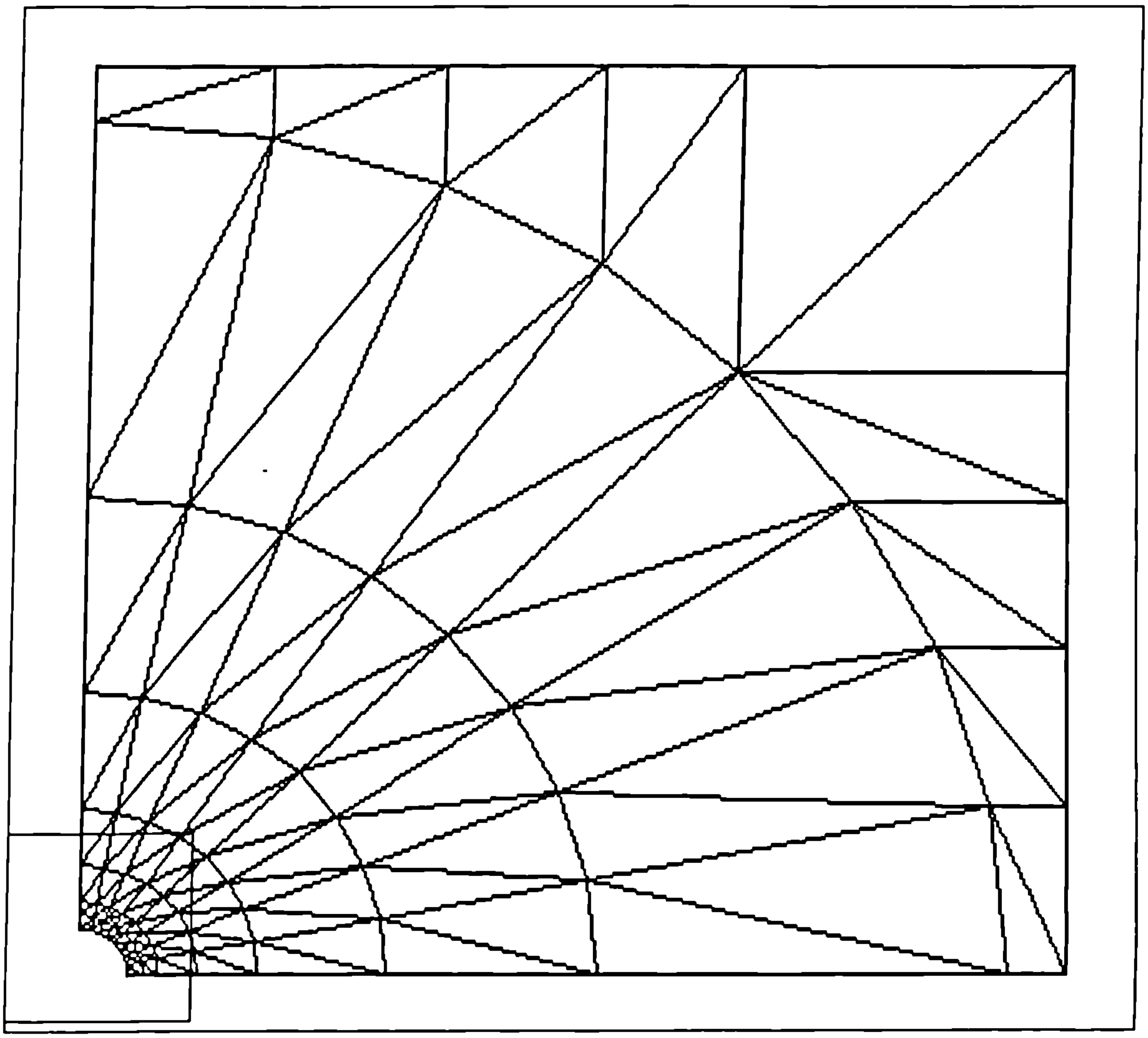

Figure 3.17: Plate with Hole Triangular Mesh

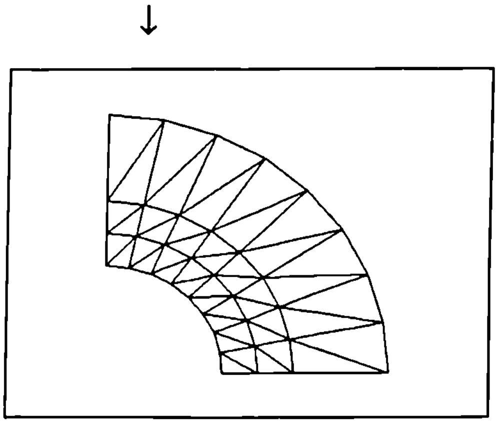

Detail of Figure 3.17

3.4.4.2 Quadrilaterals

A mesh consisting of quadrilaterals was designed for the plate so that the nodal coordinate points were the same as for the triangular mesh and is seen in Figure 3.18. The stress, σ_{yy}, at the point A in Figure 3.14 was collected and tabulated for a variety of tolerances and relaxation parameter values. The results can be seen in Table 3.31, where the stress, σ_{yy}, obtained is 2234.3N/mm^2 a value less accurate than the triangular mesh results.

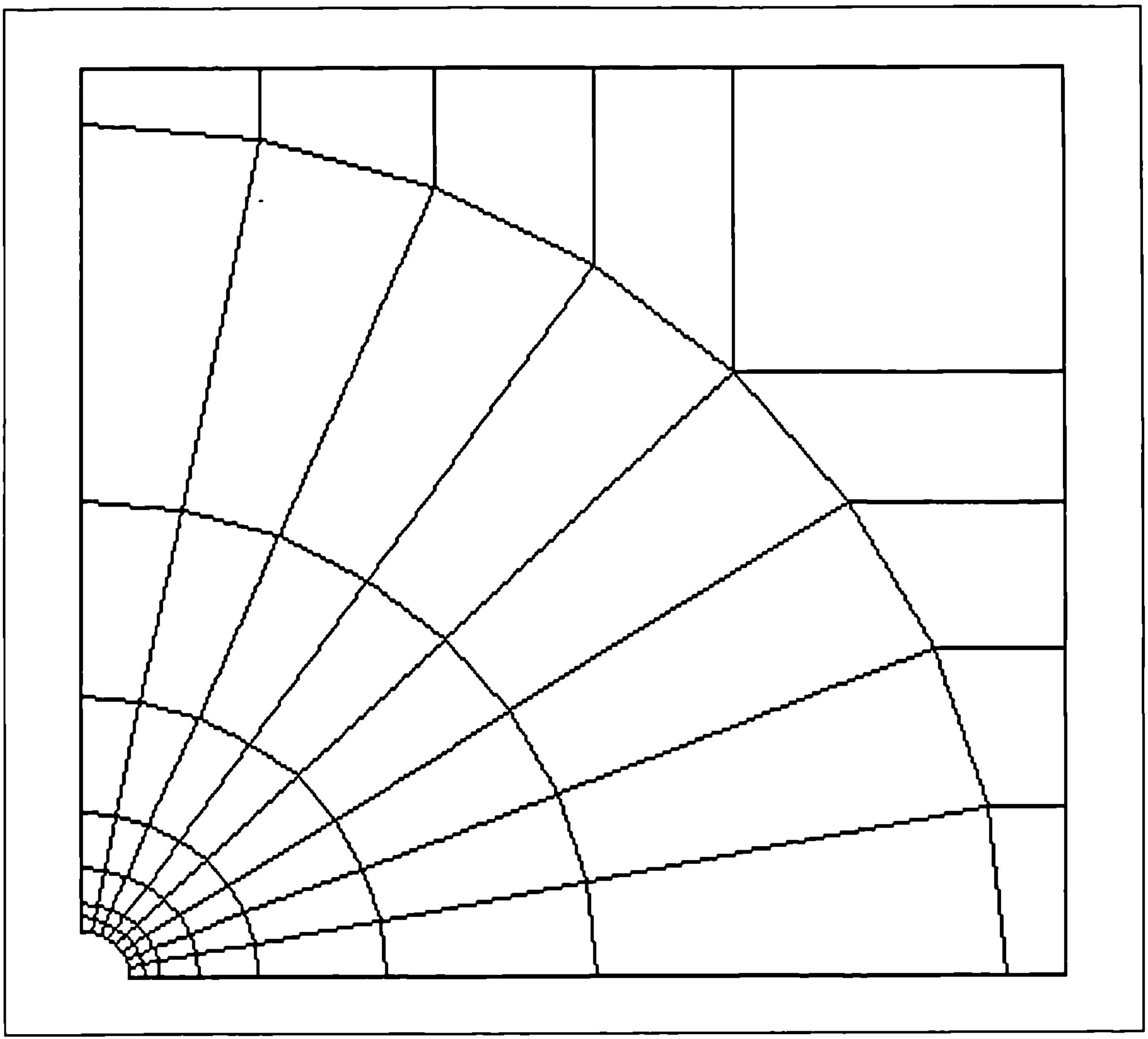

Figure 3.18: Quadrilateral Mesh for Plate with Hole

3.4.5 Comparison of Results

Table 3.29 shows the summarised stress concentration factors for the plate with a hole obtained using IFECS and the control volume unstructured mesh code.

Stress Concentration factor	analytic	finite element	CV-UM code	
			triangles	quadrilaterals
	3	2.380	2.717	2.234

Table 3.29: Hole Problem Stress Concentration Factors

The stress solution nearest to the analytical solution is the triangular control volume unstructured mesh case. The finite element stress concentration factor is just greater than the quadrilateral element control volume unstructured mesh stress concentration factor. The reason the triangular elements perform so much better for this case could be because the stresses are obtained at the element centres and then approximated at the nodes. For the triangular case there are twice as many elements and the element centres are much nearer the point A where the stresses are to be obtained.

Tolerance = 0.01, Stress measured at Point A (N/mm^2)			
relaxation (ω)	time (s)	iterations	Y-stress (σ_{yy})
1.0	12.47	6	2713.8
1.1	12.42	6	2715.9
1.3	13.84	7	2717.3
1.5	19.95	11	2720.0
1.7	33.35	20	2715.9
1.9	92.53	61	2709.7

Tolerance = 0.001, Stress measured at Point A (N/mm^2)			
relaxation (ω)	time (s)	iterations	Y-stress (σ_{yy})
1.0	17.20	9	2717.5
1.1	15.61	8	2717.6
1.3	16.92	9	2717.5
1.5	25.99	15	2717.8
1.7	43.46	27	2718.2
1.9	124.12	83	2716.4

Tolerance = 0.0001, Stress measured at Point A (N/mm^2)			
relaxation (ω)	time (s)	iterations	Y-stress (σ_{yy})
1.0	25.16	14	2717.7
1.1	21.92	12	2717.7
1.3	22.97	13	2717.7
1.5	36.43	22	2717.8
1.7	63.84	41	2717.7
1.9	197.42	134	2717.7

Table 3.30: Hole Problem Stress results with Triangular mesh

Tolerance = 0.01, Stress measured at Point A (N/mm^2)			
relaxation (ω)	time (s)	iterations	Y-stress (σ_{yy})
1.0	10.71	6	2231.2
1.1	10.61	5	2233.1
1.3	11.70	7	2234.3
1.5	16.92	11	2234.5
1.7	28.13	20	2235.4
1.9	79.34	63	2227.9

Tolerance = 0.001, Stress measured at Point A (N/mm^2)			
relaxation (ω)	time (s)	iterations	Y-stress (σ_{yy})
1.0	13.30	8	2233.9
1.1	13.24	8	2234.2
1.3	14.23	9	2234.2
1.5	21.70	15	2234.2
1.7	35.11	26	2233.7
1.9	107.91	87	2234.9

Tolerance = 0.00001, Stress measured at Point A (N/mm^2)			
relaxation (ω)	time (s)	iterations	Y-stress (σ_{yy})
1.0	21.37	14	2234.3
1.1	18.52	12	2234.3
1.3	19.39	13	2234.3
1.5	30.27	22	2234.3
1.7	51.76	40	2234.3
1.9	163.02	134	2234.3

Table 3.31: Hole Problem Stress Results with Quadrilateral Mesh

3.5 Example 5: Hollow Sphere with Temperature Variation

The hollow sphere has a radial temperature variation such that the inner radius of the sphere is cooler than the outer radius of the sphere. Figure 3.19 shows a section through a quadrant of the hollow sphere. The problem can be modelled using the axisymmetric assumptions and the resulting displacements from the temperature variation obtained.

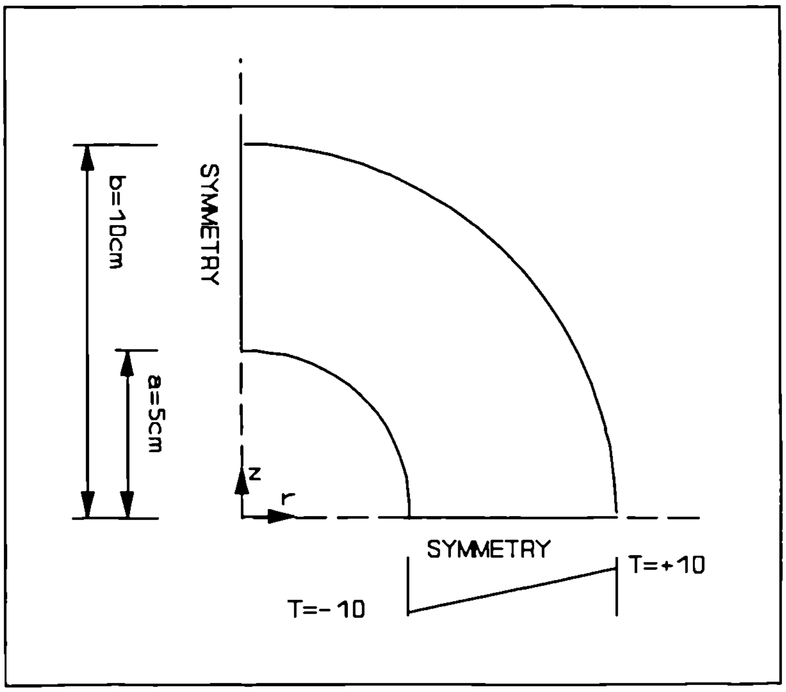

Figure 3.19: Thermal Hollow Sphere Section

3.5.1 Problem Specification

The inner radius, a, of the sphere is 5cm and the outer radius, b, 10cm as shown in Figure 3.19. The temperature at the inner radius is -10°C and increases to 10°C at the outer radius. The radial temperature variation for this problem can then be described by the function $T = T(r) = 4r - 30$, where $a \leq r \leq b$. The material has a Poisson's ratio, ν, of 0.25 and a coefficient of thermal expansion, α, is $0.01^{\circ}C^{-1}$.

3.5.2 Analytical Results

The analytical solution for the displacement and stresses of a hollow sphere with radial temperature variation can be found in Boley and Weiner (1967). The equation for the radial displacement is summarised below:

$$u(r) = \frac{\alpha}{(b^3 - a^3)}\left(\frac{1+\nu}{1-\nu}\right)\left[\frac{a^3}{r^2}\int_r^b Tr^2 dr + \frac{b^3}{r^2}\int_a^r Tr^2 dr + \frac{2(1-2\nu)}{(1+\nu)} r \int_a^b Tr^2 dr\right] \tag{3.6}$$

For the particular hollow sphere described in section 3.5.1 the equation reduces to:

$$u(r) = \frac{r^2}{60} - \frac{11r}{70} + \frac{250}{21r^2} \tag{3.7}$$

Where the radius, r, varies from a = 5cm the inner radius to b = 10cm the outer radius of the hollow sphere. The radial displacements can be seen in Figure 3.20 overlaying the original hollow sphere.

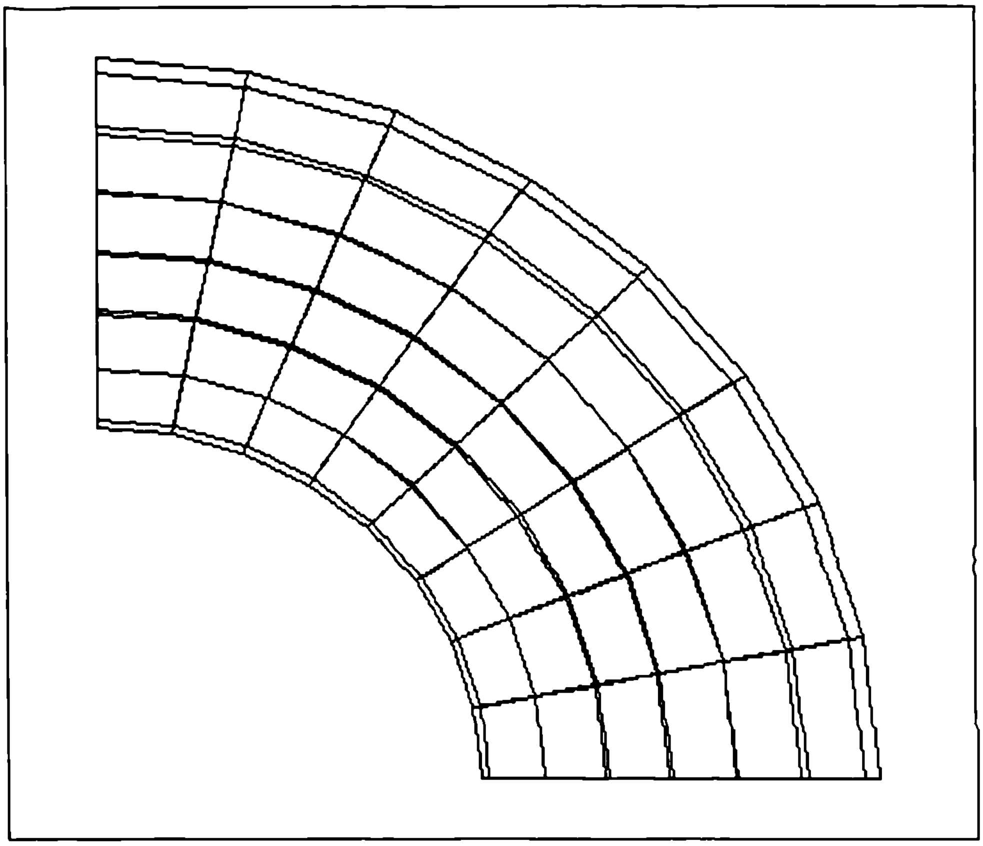

Figure 3.20: Thermally Displaced Sphere

3.5.3 CV-UM Results

Figure 3.21 shows the 48 element and 63 node mesh used with the control volume unstructured mesh code to obtain the displacement of the hollow sphere due to the radial temperature variation, using the axisymmetric option. The displacements were collected for each node and then approximated over the nine nodes in a given radius to obtain averaged values of the displacement for a particular radius. The displacements were averaged for radius values:- 5, 5.883, 6.666, 7.5, 8.333, 9.166 and 10cm. The results were collected and tabulated for various relaxation parameter values and tolerances as can be seen in Tables 3.32-3.35.

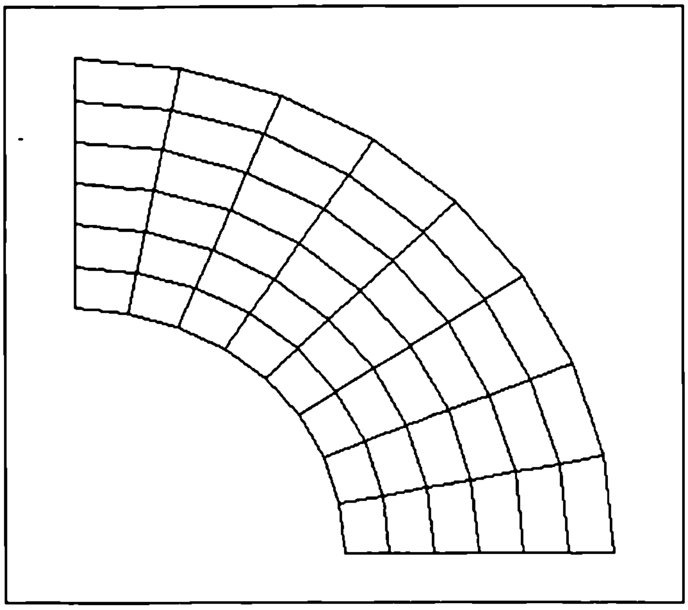

Figure 3.21: Sphere Quadrilateral Mesh

The control volume unstructured mesh code produces a displacement of 0.0978cm at the inner radius and 0.2111cm at the outer radius of the sphere. The thermal displaced hollow sphere is shown in Figure 3.20.

Tolerance = 0.01		Average Radial Displacement (cm)						
Relaxation (ϖ)	Iterations	r=5cm	r=5.883	r=6.666	r=7.5cm	r=8.333	r=9.166	r=10cm
1.0	8	0.0979306	-0.0063623	-0.0440064	-0.0334265	0.0159068	0.0985453	0.2112088
1,2	6	0.0978177	-0.0064322	-0.0441233	-0.0335483	0.0157785	0.0984144	0.2110796
1.5	12	0.0978085	-0.0064446	-0.0441238	-0.0335507	0.0157688	0.0983942	0.2110419
1.7	18	0.0975087	-0.006616	-0.0442573	-0.0336909	0.0156106	0.0982615	0.2108747
1.9	55	0.0975922	-0.0067239	-0.0444923	-0.0340038	0.0152562	0.0980213	0.2107578

Table 3.32: Thermal Hollow Sphere
Results Tolerance = 0.01

Tolerance = 0.001		Average Radial Displacement (cm)						
Relaxation (ϖ)	Iterations	r=5cm	r=5.883	r=6.666	r=7.5cm	r=8.333	r=9.166	r=10cm
1.0	11	0.0978251	-0.0064286	-0.0441055	-0.0335234	0.0158093	0.098449	0.2111118
1.2	7	0.0978064	-0.0064395	-0.0441221	-0.0335394	0.0157926	0.0984326	0.2110954
1.5	13	0.0977848	-0.0064638	-0.0441366	-0.0335473	0.015794	0.0984426	0.2111152
1.7	26	0.0978279	-0.0064228	-0.0441029	-0.0335163	0.0158166	0.0984567	0.211111
1.9	83	0.0978006	-0.006451	-0.0441439	-0.0335615	0.0157564	0.098387	0.2110482

Table 3.33: Thermal Hollow Sphere Results Tolerance = 0.001

Tolerance = 0.0001		Average Radial Displacement (cm)						
Relaxation (ϖ)	Iterations	r=5cm	r=5.883	r=6.666	r=7.5cm	r=8.333	r=9.166	r=10cm
1.0	14	0.0978121	-0.0064374	-0.0441177	-0.0335353	0.0157975	0.0984374	0.2111002
1.2	10	0.0978097	-0.0064392	-0.0441199	-0.0335374	0.0157953	0.0984353	0.2110981
1.5	17	0.0978122	-0.0064371	-0.0441187	-0.0335364	0.0157959	0.0984359	0.2110988
1.7	32	0.0978095	-0.0064392	-0.0441192	-0.0335365	0.0157965	0.0984368	0.2110984
1.9	106	0.0978042	-0.0064419	-0.0441233	-0.0335404	0.0157936	0.09843	0.2110958

Table 3.34: Thermal Hollow Sphere
Results Tolerance = 0.0001

3.5.4 Comparison of Results

Figure 3.22 display the analytical radial displacements for the hollow sphere along with the control volume unstructured mesh solution to the problem. The radial displacement results for the problem using the package MicroFIELD, (MFIELD), are also shown. MicroFIELD used a mesh containing the same number of elements, as shown in Figure 3.21, but each element had 8 nodes. From the displacements seen in Figure 3.22 the control volume unstructured mesh displacements are very close to the analytic solution. The MicroFIELD results are slightly better due to the 8 node elements. Grid refinement of the quadrilateral mesh used with the unstructured code would produce radial displacements nearer the analytic solution.

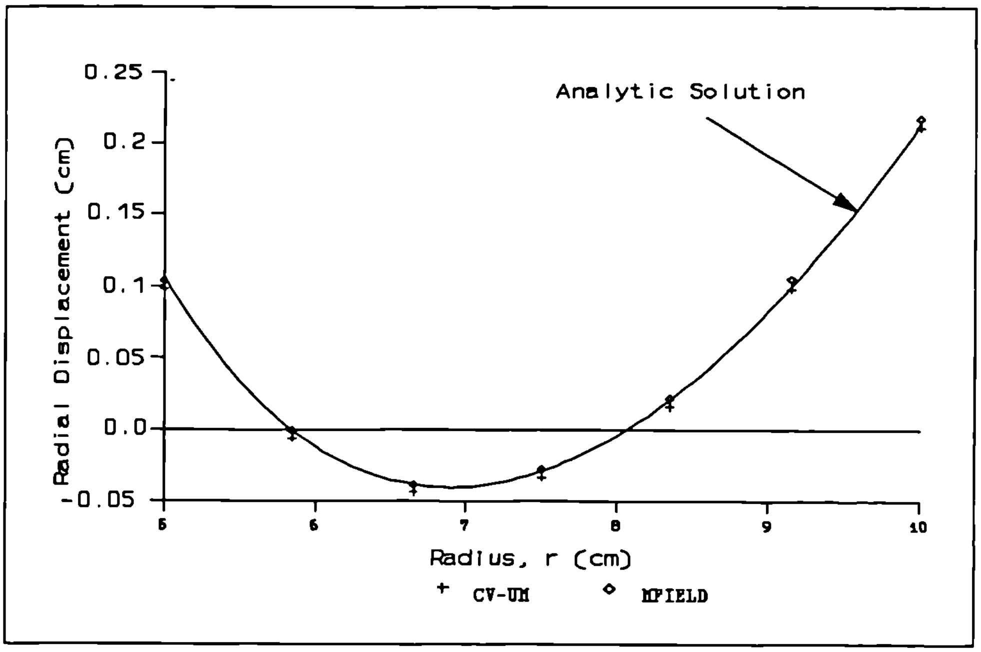

Figure 3.22: Thermal Hollow Sphere Displacements

Tables 3.32-3.34 indicate that a relaxation parameter value of 1.2 would produce a converged solution with the minimum number of global iterations.

3.6 Example 6: Thermal Sphere with Mechanical Loading

In this example the hollow sphere has an internal and external pressure applied at the inner and outer radii in addition to a radial thermal variation. Figure 3.23 shows a section through a quadrant of the sphere. The axisymmetric approximation is suitable for use when modelling this problem and obtaining the resulting radial displacements.

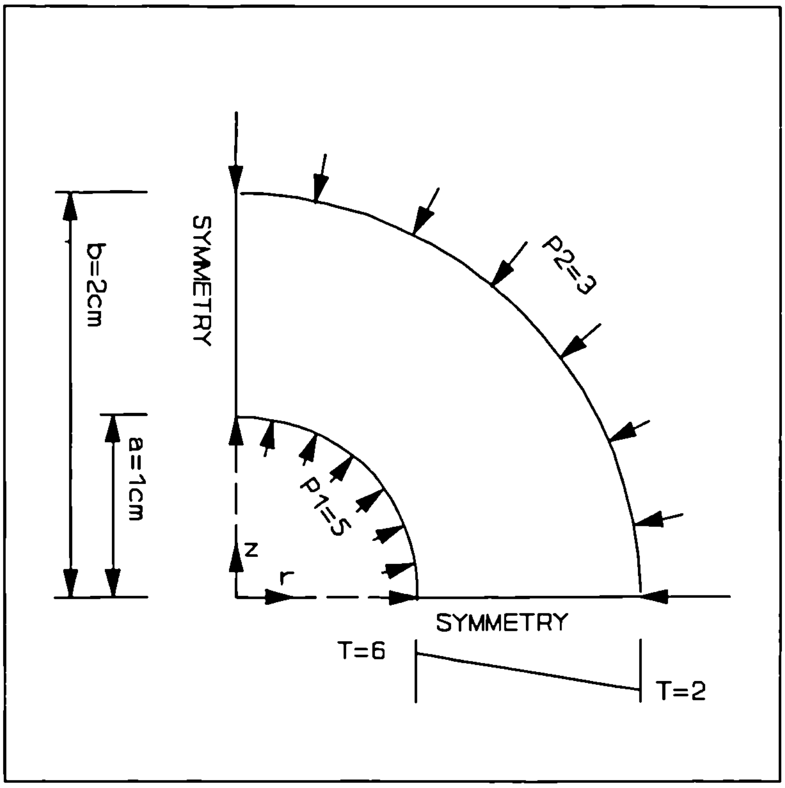

Figure 3.23: Hollow Sphere Section with Applied Pressures

3.6.1 Problem Specification

The geometry and initial conditions for the hollow sphere are the same as used by Bakr and Fenner (1983) when they modelled the example. The inner radius of the sphere, *a*, is 1cm and the outer radius, *b*, 2cm as shown in Figure 3.23. The inner radius is maintained at a temperature of 6°C and the outer radius 2°C. The pressure applied at the inner radius is 5N/cm^2 and at the outer radius the pressure applied is 3N/cm^2. The material properties used have values 1.0N/cm^2 for Young's modulus, 0.3 for Poisson's ratio and 0.02°C^{-1} for the coefficient of thermal expansion.

3.6.2 Analytical Results

The analytical results for this example are given by Bakr and Fenner (1983). The radial displacement at the inner radius is 0.4629cm and the radial displacement at the outer radius is -1.6743cm. These two results indicate the sphere has somehow turned inside out. Figure 3.24 shows the displaced hollow sphere with the displacements produced by the control volume unstructured mesh algorithm, showing the outer radius of the sphere has become the inner radius of the sphere and the inner radius of the sphere is now the outer radius.

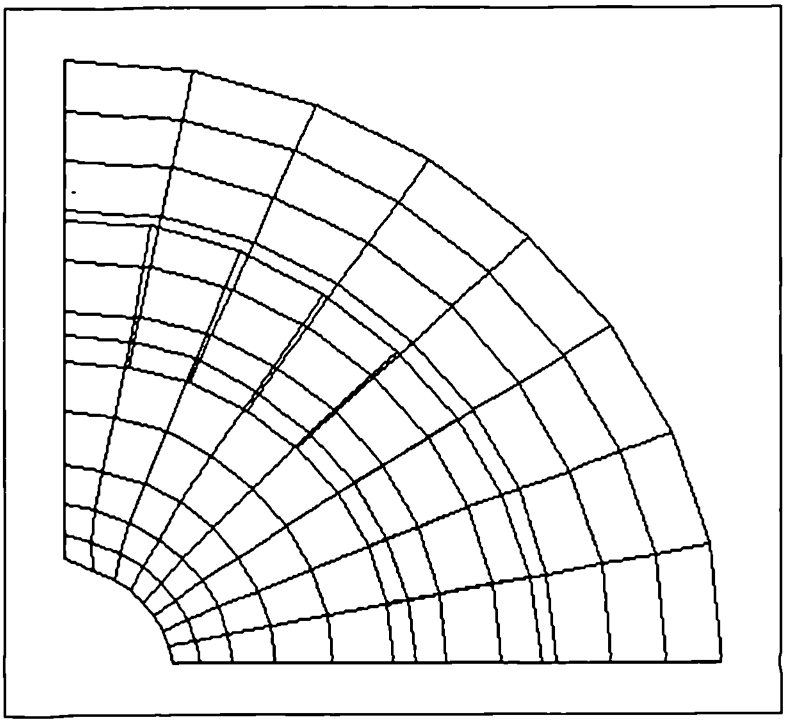

Figure 3.24: Thermally and Mechanically Displaced Sphere

3.6.3 CV-UM Results

Figure 3.21 shows the quadrilateral mesh with 48 elements and 63 nodes used with the control volume unstructured mesh code. The radial displacements resulting from the radial thermal temperature variation and the applied pressures were obtained, using the axisymmetric option, for various relaxation parameter values and tolerances. The radial displacements were averaged over the nine nodes that had the same radius and the values were tabulated in Tables 3.35-3.37. The control volume unstructured mesh code produces a displacement of 0.4528cm at the inner radius and -1.68cm at the outer radius.

Tolerance = 0.01		Average Radial Displacement (cm)						
Relaxation (ϖ)	Iterations	r=1cm	r=1.167	r=1.333	r=1.5cm	r=1.667	r=1.833	r=2cm
1.0	8	0.450316	0.0992714	-0.5192774	-0.863941	-1.162362	-1.431462	-1.682071
1.2	6	0.4518983	0.0977154	-0.517766	-0.862503	-1.160989	-1.430193	-1.680941
1.5	10	0.4534333	0.0964528	-0.5164783	-0.8612057	-1.159704	-1.428691	-1.679126
1.7	17	0.4538462	0.0962009	-0.5159863	-0.8606636	-1.159438	-1.428344	-1.678521
1.9	54	0.4513065	0.0987412	-0.5176917	-0.8609698	-1.159686	-1.428764	-1.680793

Table 3.35: Hollow Sphere Results
Tolerance = 0.01

Tolerance = 0.001		Average Radial Displacement (cm)						
Relaxation (ϖ)	Iterations	r=1cm	r=1.167	r=1.333	r=1.5cm	r=1.667	r=1.833	r=2cm
1.0	12	0.4526508	0.0970847	-0.5170828	-0.8618418	-1.160354	-1.429531	-1.680219
1.2	8	0.4528264	0.0969247	-0.5169216	-0.8616908	-1.160216	-1.429402	-1.680102
1.5	13	0.4528481	0.0968985	-0.5168563	-0.8615853	-1.160062	-1.429205	-1.679842
1.7	25	0.4527482	0.0969859	-0.5169658	-0.8617491	-1.16028	-1.429469	-1.68016
1.9	77	0.4526119	0.0970761	-0.5170493	-0.8618131	-1.160205	-1.429421	-1.680093

Table 3.36: Hollow Sphere Results
Tolerance = 0.001

Tolerance = 0.0001		Average Radial Displacement (cm)						
Relaxation (ϖ)	Iterations	r=1cm	r=1.167	r=1.333	r=1.5cm	r=1.667	r=1.833	r=2cm
1.0	15	0.4528008	0.0969532	-0.516944	-0.8617084	-1.160226	-1.429409	-1.6801
1.2	10	0.4528253	0.096932	-0.5169224	-0.8616877	-1.160206	-1.429389	-1.680081
1.5	16	0.4527968	0.0969493	-0.5169377	-0.8616476	-1.160211	-1.429387	-1.68008
1.7	32	0.4528251	0.0969301	-0.5169215	-0.8616884	-1.160205	-1.42939	-1.680083
1.9	100	0.4528151	0.0969476	-0.516941	-0.861704	-1.160229	-1.429406	-1.6801

Table 3.37: Hollow Sphere Results
Tolerance = 0.0001

3.6.4 Comparison of Results

Radial displacement results for the problem were collected using the MicroFIELD package. The same number of elements and mesh were used, but the elements consisted of eight nodes. The resulting MicroFIELD radial displacements are shown in Table 3.38 (MFIELD), along with the control volume unstructured mesh results, the analytical results and the boundary integral equation (BIE) results from Bakr and Fenner (1983).

Radial Displacements (cm): CV-UM, MFIELD - Averaged Values. Exact, BIE - [Bakr and Fenner (1983)]				
radius, r(cm)	CV-UM	Exact	BIE	MFIELD
1.000	0.4528253	0.4629	0.4626	0.4554399
1.167	-0.096932	-0.0899	-0.0899	-0.0899009
1.333	-0.5169224	-0.5122	-0.5117	-0.5084117
1.500	-0.8616877	-0.8586	-0.8582	-0.8504378
1.667	-1.160206	-1.1580	-1.1574	-1.146567
1.833	-1.429389	-1.4266	-1.4254	-1.413576
2.000	-1.680081	-1.6743	-1.6744	-1.660208

Table 3.38: Comparison of Displacements for Hollow Sphere

The boundary integral equation results are the closest to the analytical results, where Bakr and Fenner (1983) used curved boundary elements. The control volume unstructured mesh displacements are fairly close to the analytic displacements, grid refinement would produce more accurate radial displacement results.

3.7 Conclusions

The six examples included in this chapter have demonstrated the suitability of the control volume unstructured mesh algorithm to the application of solid mechanics problems. The cantilever problem in section 3.1 illustrates the algorithms capacity for treating applied stresses and fixed displacements as initial conditions. The beam that has a temperature variation through it in section 3.2 shows thermal problems can be solved efficiently using the control volume unstructured mesh algorithm. The algorithm can efficiently manage meshes with various elements such quadrilaterals, triangles or both. The type of mesh used can then be altered for each specific problem considered. It was shown that rectangular beams are more suited to quadrilateral elements, with the triangular element mesh results very similar to the finite element results. The plate with a circular hole in section 3.4 produces stresses more closely resembling the analytical results when triangular elements are used.

Multi-material problems such as the cusp in section 3.3 are easily catered for in the control volume unstructured mesh algorithm. The cusp triangular mesh displacement results agree with the finite element displacement results. Examples 3.5 and 3.6 show the capability of the algorithm to manage axisymmetric problems with thermal and mechanical loading. The results produced are very close to the analytical solutions for the problems and require no extra computational effort.

The time for convergence at present is slower than the finite element counterparts but with the inclusion of improved algorithms, such as more efficient solvers, it is hoped the speed will improve. From the results showing the variation in global iterations with respect to the relaxation parameter chosen, a clear pattern is seen showing that the most efficient relaxation parameter for individual problems stays the same regardless of tolerance and mesh refinement. The optimum relaxation parameter to be used with a specific problem can be calculated using the spectral radius of the system matrix formed with the coefficients of neighbouring nodes [Smith (1975)].

Chapter 4

Friction at Boundaries

Frictional forces act along the common surface between two bodies in such a direction as to oppose the relative movement of the two bodies. This chapter briefly describes the existing theories of friction established over hundreds of years and more recently. The classic laws of friction are then included as a boundary condition into the two-dimensional stress-strain code, described previously in Chapters 3 and 2. The two bodies are assumed to be in full contact, so that a complicated contact algorithm is not considered for inclusion and so will not affect the friction boundary displacements. A simple block is used to test the friction algorithm for a variety of surface angles then a silica brick example is tested with various mesh sizes.

4.1 Definition of Friction

Detailed descriptions of the history of the theories of friction can be found in papers such as Martins, Oden and Simoes (1990), Oden and Martins (1985), Curnier (1984) and Tabor (1981). It is stated that friction theory has received only episodic attention over the years whereas the similar plasticity phenomena has advanced much further [Curnier, (1984)]. Over the last decade the advancement in the solution of contact problems by means of variational inequalities means that more sophisticated friction models are required. It is not the purpose of this chapter to suggest new theories of friction, but it is meant to include an existing generally accepted friction theory into the stress-strain code described previously. The classic laws of friction are summarised along with more recent theories of the friction phenomena. A few examples are given for numerical friction prediction methods.

4.1.1 Classic Laws of Friction

According to Tabor (1981), Charles Augustin Coulomb established the basic laws of friction about one hundred years after Amonton's 1699 ideas on friction. Figure 4.1 shows a free-body diagram for a block resting on a flat surface.

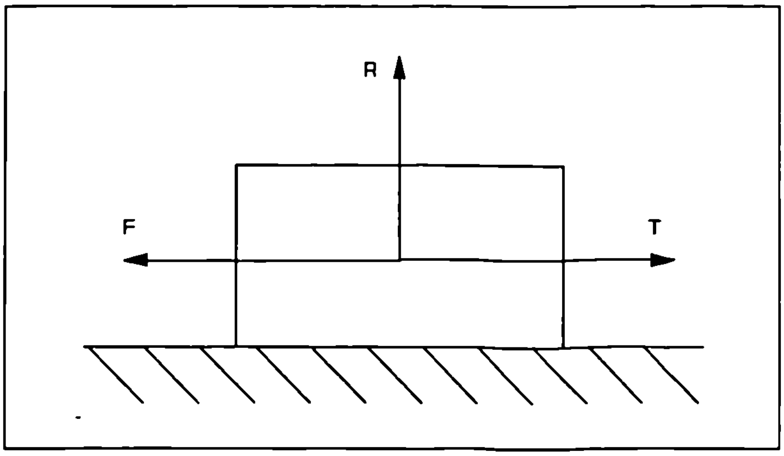

Figure 4.1: Frictional Forces

When the two bodies in contact are subjected to an applied force, *T*, which tends to produce relative sliding motion, frictional forces, *F*, develop on the interface that tend to oppose the motion. Forces *F* and *T* act in opposite directions with *F* less than or equal to *T*.

The classic friction laws as given by Oden and Martins (1985) are given by:-

(i) The frictional force, at onset of sliding and during sliding, is proportional to the normal contact force

$$|F| = \mu R \tag{4.1}$$

The coefficient of proportionality, μ, is known as the coefficient of friction. Often two values of μ are quoted: the coefficient of static friction that applies to the onset of sliding and the coefficient of kinetic or dynamic friction that applies during sliding.

(ii) The coefficient of friction is independent of the apparent area of contact.

(iii) The static friction coefficient is usually greater than the kinetic coefficient.

(iv) The coefficient of kinetic friction is independent of the sliding velocity.

A surface is said to be 'smooth' and frictionless when $\mu = 0$ or 'rough' and frictional when $\mu > 0$. When the force is applied at the friction boundary there are two possible outcomes, either

$$F \leq \mu R \tag{4.2}$$

and the boundaries of the connecting objects will 'stick' together, or

$$F = \mu R$$

and the object with the force applied to it will 'slip' against the other object. This applies to static friction at the onset of sliding. Examples for values of the coefficient of friction, are 0.2-0.5 for wood on wood and 0.2-0.6 for wood on metals. Other values can be obtained from engineering data books [Munday and Farrar (1986)].

4.1.2 Recent Theories of Friction

Coulomb suggested that the asperities on the surfaces of the two connecting bodies were responsible for the coefficient of kinetic friction often being less than the coefficient of static friction. Tabor (1981) wrote that the main weakness with the coulomb roughness model was that it was basically non dissipative. The terminology of 'rough' and 'smooth' surfaces is still used though known to be a false correlation and completely discredited. The Coulomb law for perfect friction covers a restricted range of tribological situations.

Tabor (1981) lists three basic elements of friction in unlubricated solids as:-

i) The area of true contact between the sliding surfaces.

ii) The type of strength of bonding that is formed at the interface where sliding occurs.

iii) The way in which the material in and around the contact regions is sheared and ruptured during sliding.

This is a substantially different theory from the classic laws of friction in section 4.1.1 for the friction phenomena and the most widely accepted in recent decades [Oden and Martins (1985), Tabor (1981)]. The friction coefficient can be given as a sum two components resulting from adhesion and ploughing.

Oden and Martins (1985) explain that there are cases when the classic laws labelled (i) and (ii) in section 4.1.1, often known as Amonton's laws, are not true. Section 4.1.1 number (iii) is intimately associated with the stick-slip phenomena referred to in later sections. The fourth law of section 4.1.1 is now known to be invalid as a large volume of experimental data has shown the variation of the friction coefficient with the sliding velocity [Oden and Martins (1985)].

More recent theories of friction with more details can be found in Oden and Martins (1985) and Martins, Oden and Simoes (1990). Curnier (1984) proposes a general theory of friction inspired from the field of plasticity, restricted to moderate amounts of slip with a contact impenetrability condition included as a by-product.

4.1.3 Friction Algorithms in Use

Oden and Martins (1985) use a finite element semi explicit model with a central difference scheme to test the friction methods. Their preliminary numerical results show promising simulations which correspond experimentally. Close cooperation is needed between experimentalists and numerical analysts for a thorough test of friction models.

Moscardini (1985) implements the Coulomb law of perfect friction in a finite element code INFESA. The iterative results initially produced the stick-slip boundary displacements expected. The resulting stresses along the friction boundary were re-input as the boundary forces, but the 'slip' point on the friction boundary rose steadily so that all the nodes on the boundary became fixed. A finer grid was suggested as a possible solution to the problem.

A formulation for finite element simulation of frictional contact is proposed by Saran and Wagoner (1991a), (1991b) for industrial forming processes. The model has to contend with non-linearities caused by large strains and plastic flow plus the complex boundary conditions concerning frictional contact. The convergence of two methods was compared for the solution of a flat sheet of metal under plane strain conditions subject to the application of a cylindrical punch. The method using the linearised friction-contact equations failed to converge. Whereas the method where the complete set of governing equations were linearised was found to have a quadratic rate of asymptotic convergence.

An elasto-plastic finite element unilateral contact analysis by Hrycaj, Cescotto and Oudin (1991) with friction used an incremental non-associated plastic constitutive equation. Katona (1983) uses a simple interface element to simulate contact friction interaction between two bodies, implemented in a standard finite element program. The two applications presented and tested with friction coefficient values ranging from infinity, bonded, to zero, free, produced converged solutions. Katona (1983) states that some cases not presented did not converge due to the interface being borderline between a small compressive normal force and a small normal gap, but the lack of convergence was generally inconsequential with regard to the overall solution.

Ibrahimbegovic and Wilson (1992) use a model that contains a regularised form of the Coulomb friction law, which stems from an analogy of friction and plasticity phenomena. The frictional contact model is capable of treating both dynamic and quasistatic problems without reduction of the coefficient of friction from static to kinematic.

The Signorini problem with Coulomb's law of friction is considered by Haslinger (1992). The existence of a solution is determined using a finite element approximation of mixed type. Klarbring and Björkman (1992) formulate a model for large displacement contact problems with friction. Contact with a classical formulation of Coulomb's friction law is used in variational form. A transformation to a non-orthogonal coordinate system at each contact point is assessed by Runesson, Klisinski and Larsson (1993) for a novel implementation of the stick-slip law. The introduction of regularisation to overcome convergence problems is not used with this method of solution of Signorini's problem.

Important factors in tribology - the study of friction, wear and lubrication, are the magnitude and distribution of surface temperatures generated by one body sliding against another. Vick, Furey and Foo (1991) developed a boundary integral equation method with a moving Green's function to solve the problem of frictional heating. The method produced accurate results and was unconditionally stable. Boundary elements were used by Takahashi and Brebbia (1988) to provide a flexibility approach for contact problems with and without friction.

Various numerical procedures have been used with varying degrees of success to solve frictional problems. The major problem, especially with the finite element programs is a lack of convergence of the solution. Linearisation appears to be an option that can be used, though the success of this is not guaranteed.

4.2 Implementation in CV-UM code

An algorithm is developed from Coulomb's perfect law of friction for implementation into the control volume unstructured mesh stress-strain code.

From equation 4.1 the forces (N) can be divided by the area over which they are applied to obtain the stresses (N/m^2). In the case of two-dimensional elasticity the forces are divided by the distance, *Ds*, as seen in Figure 4.2.

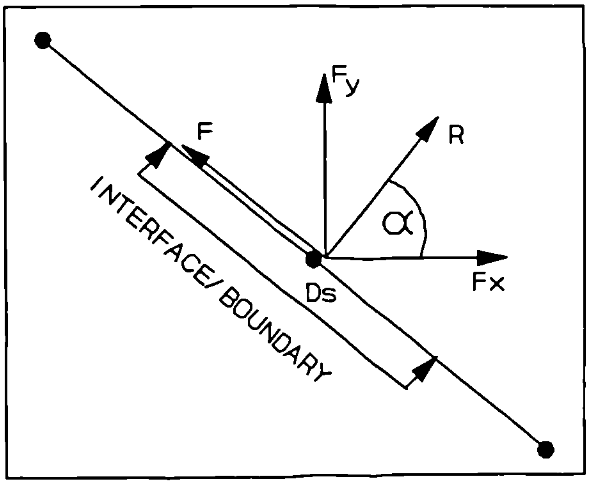

Figure 4.2: Applied Frictional Forces

The friction condition becomes:-

$$\frac{F}{Ds} = \mu \frac{R}{Ds} \tag{4.3}$$

$$\rightarrow \quad S_S = \mu \, S_N$$

The equation now relates the shear stress, S_S, to a proportion of the normal stress, S_N. The two conditions for the stick-slip friction law are seen in equation 4.4 and the stresses shown in Figure 4.3.

$$\begin{array}{ll} S_S < \mu\ S_N & \textit{stick} \\ S_S = \mu\ S_N & \textit{slip} \end{array} \tag{4.4}$$

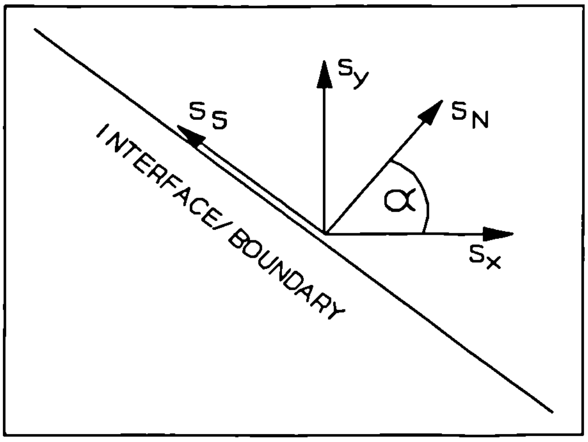

Figure 4.3: Frictional Stresses

The normal and shear stresses can be resolved into components parallel to the coordinate directions as shown in equation 4.5.

$$\begin{aligned} S_N &= S_x l + S_y m \\ S_S &= S_x m - S_y l \end{aligned} \tag{4.5}$$

where S_x and S_y are the components in the coordinate directions. The direction cosines l and m are defined as: $l = \cos\alpha$ and $m = \sin\alpha$, where α is the angle between the normal S_N and the x-axis as shown in Figure 4.3

The components S_x and S_y can be defined in terms of the stresses σ_{xx}, σ_{yy} and σ_{xy} [Fenner (1986)] shown in equation 4.6 for the two-dimensional case. The stresses σ_{xx}, σ_{yy} and σ_{xy} at the nodes are approximated values from the element stresses obtained in the control volume unstructured mesh stress-strain code.

$$\begin{aligned} S_x &= \sigma_{xx} l + \sigma_{xy} m \\ S_y &= \sigma_{yy} m + \sigma_{xy} l \end{aligned} \tag{4.6}$$

It is possible to rewrite the coordinate stresses S_x and S_y in terms of the normal and shear stresses as seen in equation 4.7

$$\begin{aligned} S_x &= S_N l + S_S m \\ S_y &= S_N m - S_S l \end{aligned} \tag{4.7}$$

Resolving the forces F and R into the axis directions or multiplying equation 4.7 by the distance, Ds, results in

$$\begin{aligned} S_x Ds &= Ds(S_N l + S_S m) & & F_x = Rl + Fm \\ & & or & \\ S_y Ds &= Ds(S_N m - S_S l) & & F_y = Rm - Fl \end{aligned} \tag{4.8}$$

The forces applied at the boundaries in the axis directions can be defined in terms of the stresses

$$\begin{aligned} F_x &= Ds(S_N l + S_S m) \\ F_y &= Ds(S_N m - S_S l) \end{aligned} \tag{4.9}$$

For the slip condition of friction as in equation 4.4, equation 4.9 is modified as follows:

$$\begin{aligned} \boldsymbol{F_x} &= \boldsymbol{Ds.S_N(l + \mu m)} \\ \boldsymbol{F_y} &= \boldsymbol{Ds.S_N(m - \mu l)} \end{aligned} \tag{4.10}$$

The normal stress, S_N, can be calculated using equations 4.5 and 4.6. When a slip friction boundary point is defined then the forces F_x and F_y are prescribed at the boundary. If the boundary is a fixed friction node then the point is defined as a fixed node. As the contact at the friction interface is fixed the relative displacement u' in the x'-axis direction as shown in Figure 4.4 will be zero.

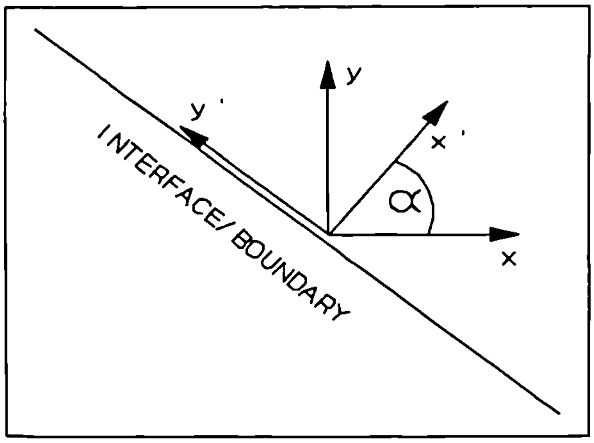

Figure 4.4: Coordinate Systems

The relative displacements u' and v' can be defined in terms of the displacement u and v seen in equation 4.11.

$$u' = lu + mv$$
$$v' = lv - mu \tag{4.11}$$

When u' is zero, $l.v = m.u$, so if the u displacement is obtained using the applied force F_x then the displacement v can be determined from $v = u.m/l$ and vice versa.

4.2.1 Stick-Slip Friction Algorithm

The stick-slip friction algorithm to be included in the two-dimensional stress-strain code is illustrated in Figure 4.5. For each node on a friction interface the direction cosines l and m are calculated followed by the frictional forces acting at the node if the relative v displacement is positive.

4.2.2 Solution Procedure

Figure 4.6 shows the inclusion of the friction algorithm, as displayed in Figure 4.5, in the control volume unstructured mesh stress-strain code. The slip routine is accessed after the u and v displacements have been obtained for a particular iteration, the boundary conditions at the friction boundary are then altered if necessary for the next iteration. For each new global iteration the system matrices for u and v, containing the coefficients, are recreated to allow for the altered boundary conditions on the friction interface predicted by the friction algorithm.

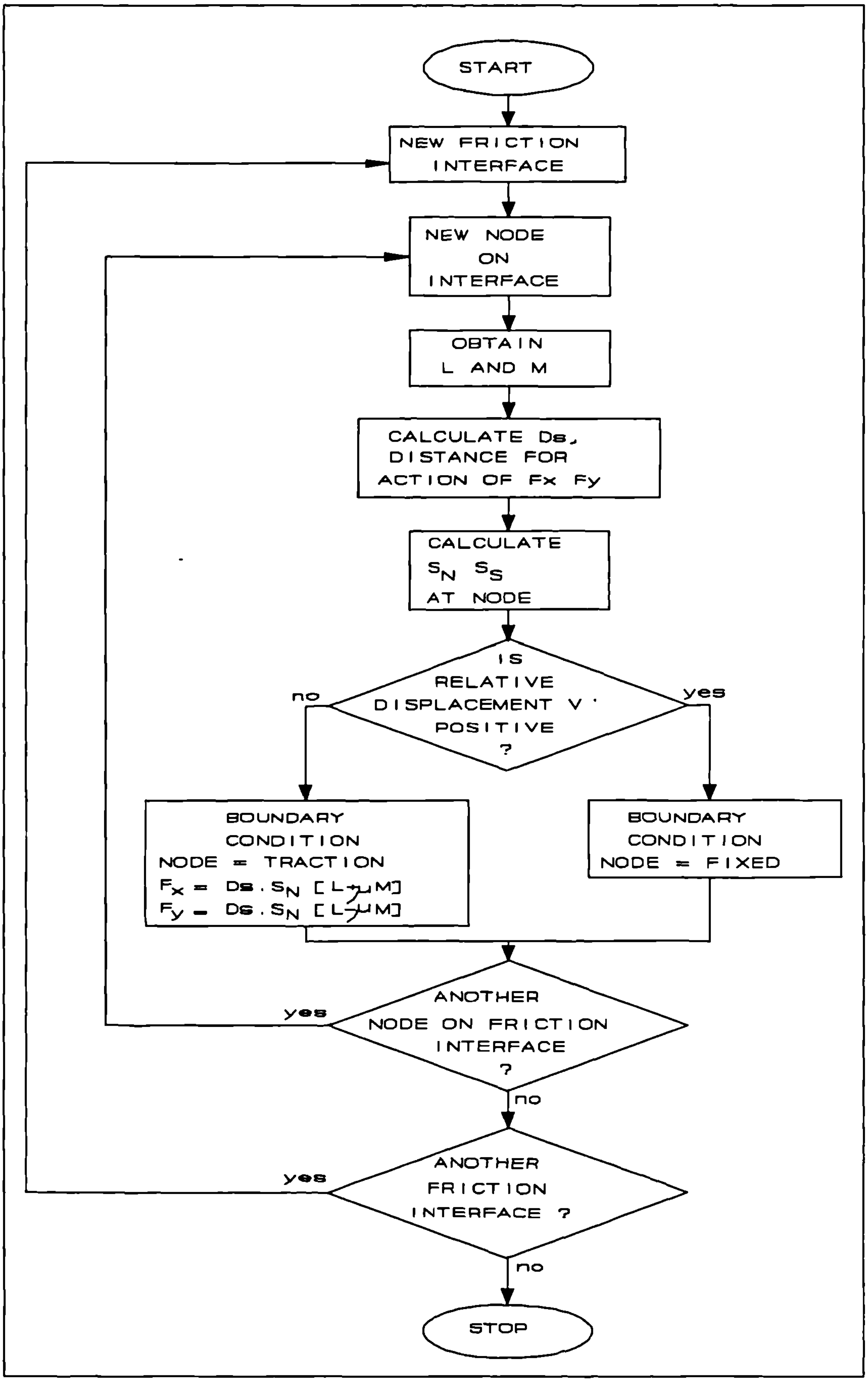

Figure 4.5: Friction Algorithm

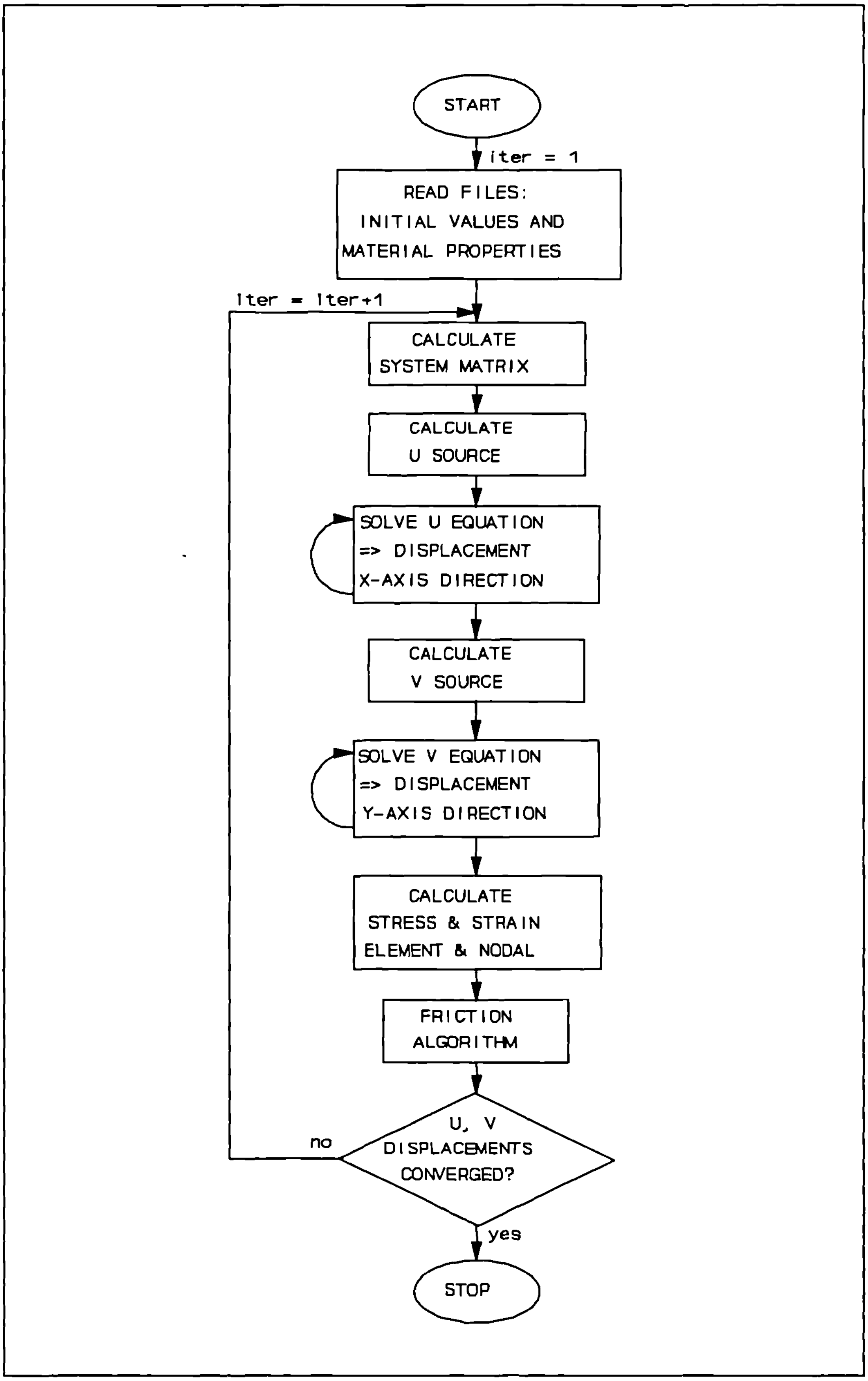

Figure 4.6: Solution Procedure with Friction Algorithm

4.2.3 Test Results

The two-dimensional friction code was applied to simple test blocks. A square block with two adjacent sides fixed, a third connecting side has a uniform force applied normal to it and the final edge, the friction boundary, is in contact with another object as in Figure 4.9. The resulting displacements along the friction boundary were computed, and the *u* and *v* displacement residuals were found not to converge. The residuals would oscillate about certain small values as shown in Figure 4.7.

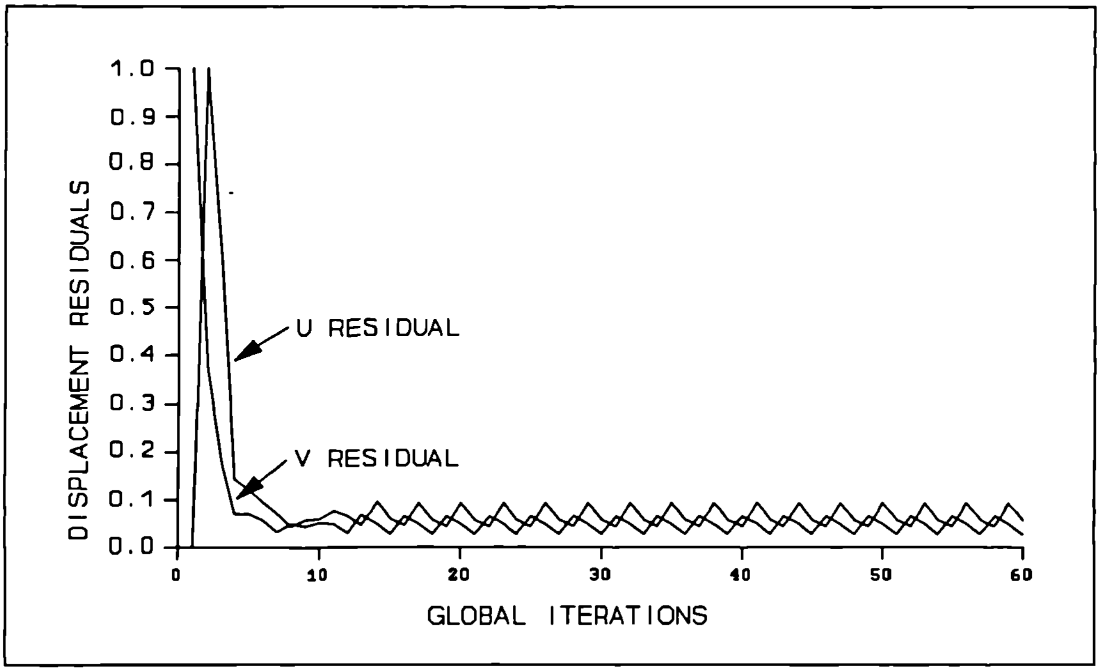

Figure 4.7: Displacement Residuals for Algorithm with Friction no Source Linearisation

4.2.4 Linearisation of Source

To solve the problem of oscillating residuals the source terms for the *u* and *v* displacements were linearised [Patankar (1980)]. During an iteration the equations for the displacement *u* or *v* obtained are in the form shown in equation 4.12, where the value of the displacement at a point depends on the displacements at the surrounding points.

$$a_p \phi_p = \sum a_{nb} \phi_{nb} + b_p \qquad (4.12)$$

Where ϕ represents either the u or v displacement. To linearise the source term b_p the transformation in equation 4.12 is used

$$b_p = Sc - \phi_p \, Sp \tag{4.13}$$

where

$$Sp = \left| \frac{b_p}{\phi_p^{old}} \right|$$

$$Sc = 2\, b_p \qquad if \quad \frac{b_p}{\phi_p^{old}} \quad is\ positive \tag{4.14}$$

$$Sc = 0 \qquad if \quad \frac{b_p}{\phi_p^{old}} \quad is\ negative$$

The equation solved for u or v then becomes:-

$$(a_p + Sp) \, \phi_p = \sum a_{nb} \phi_{nb} + Sc \tag{4.15}$$

4.2.5 Revised Solution Procedure

Figure 4.8 shows the revised solution procedure. The difference between this and the original solution procedure is that after the right hand sides of a particular displacement equation have been obtained they are then linearised.

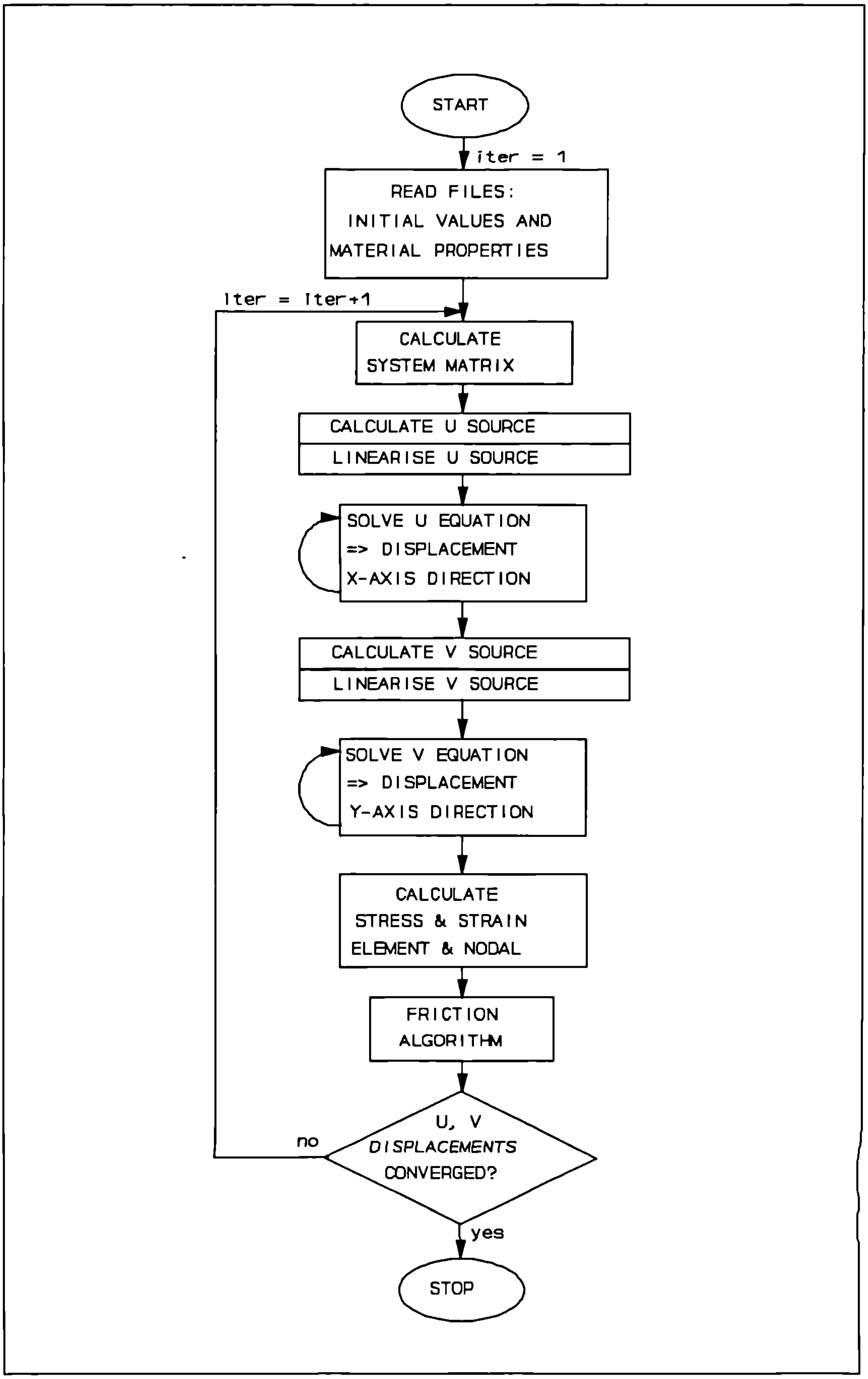

Figure 4.8: Revised Solution Procedure with Friction Algorithm

4.3 Example 1: Simple Block

A square block is used as a simple test for the friction boundary condition routine. The block is fixed along the left edge and bottom edge so that it cannot move in any direction. Along the right edge of the block the friction boundary condition is applied simulating the block in contact with another object. The top edge of the block has a pressure applied. An arbitrary value for the coefficient of friction is used initially and the effect along the right edge of the block noted. The displacements along this edge are compared to the displacements along the edge if the coefficient of friction was zero and free to move along the edge of the neighbouring object. Various values of the coefficient of friction are used to see the general effect this has on the displacement along the friction boundary. The coefficient of friction is then kept constant at the original value while the angle of the block is rotated and the relative displacements along the friction boundary noted.

4.3.1 Problem Specification

The arbitrary square block is taken to be 10cm by 10cm as shown in Figure 4.9. The left edge and the bottom edge are completely fixed.

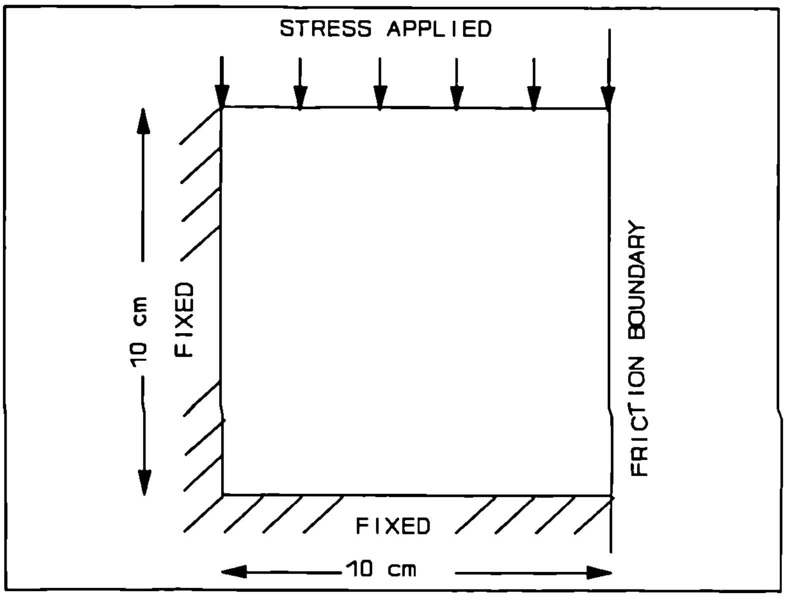

Figure 4.9: Initial block

The right edge is the friction boundary, which is in contact with the edge of another object and initially has an arbitrary coefficient of friction value of 0.6. The stress applied along the top edge is -2,000N/cm^2. The block has a Poisson's ratio of 0.4, a Young's modulus of 50,000N/cm^2 and the coefficient of thermal expansion is 0.0001°C^{-1}.

Figure 4.10 shows the quadrilateral mesh used with the control volume unstructured mesh code, where each element has area 1cm^2. The node numbers along the friction boundary are shown for reference when displaying the displacement results.

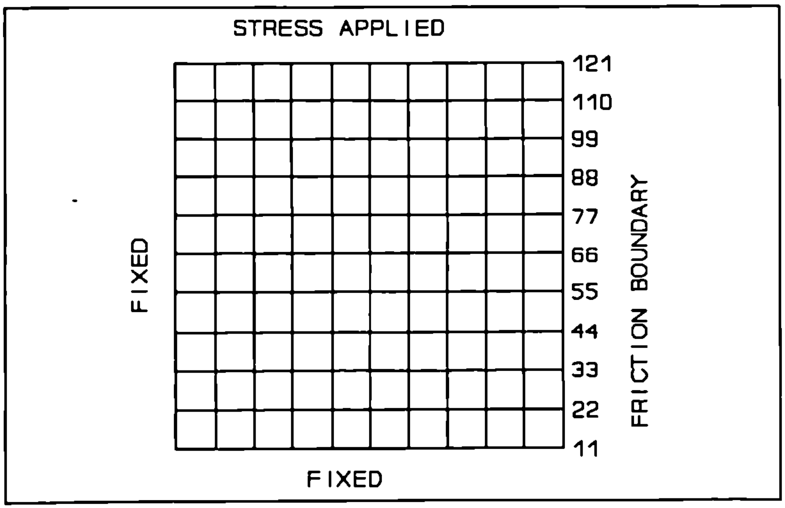

Figure 4.10: Simple Friction Block Mesh

4.3.2 Friction Results

The control volume unstructured mesh code was used to solve the square block problem. An arbitrary tolerance of 0.0001 was used for the nodal displacement residuals of the block. The residuals for the first 60 global iterations of the *u* and *v* displacements are shown in Figure 4.11. After 500 iterations the required tolerance had still not been reached and the displacements were seen to oscillate slightly in similar fashion to the residuals displayed in Figure 4.11.

Figure 4.12 shows the displaced mesh overlaying the original mesh of the square block.

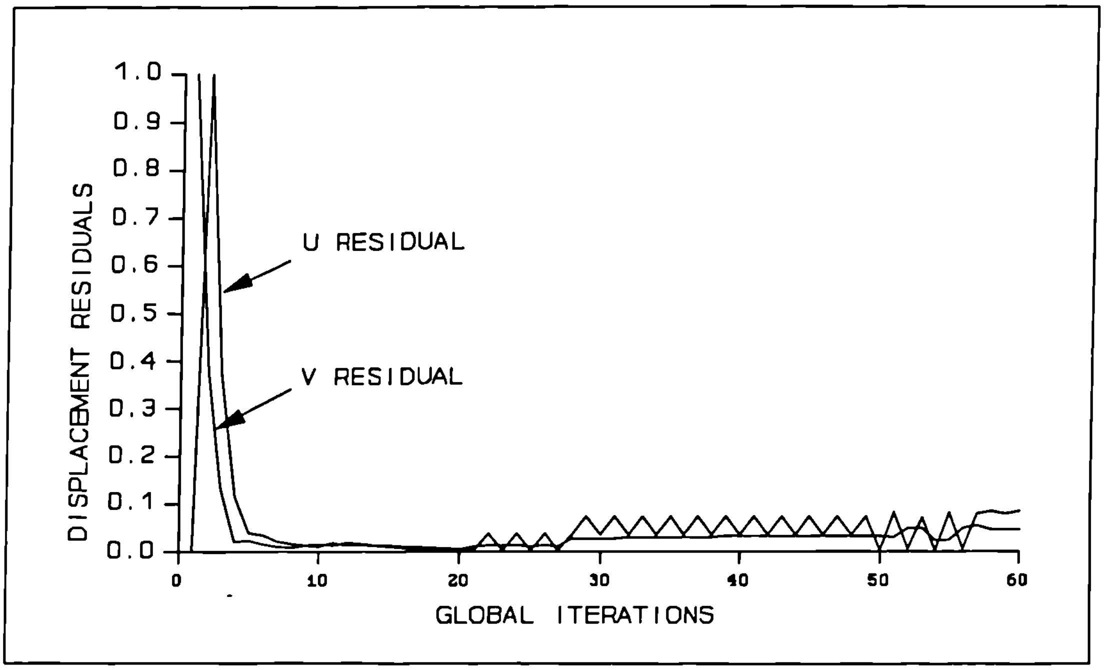

Figure 4.11: Displacement Residuals of Block with Source Linearisation

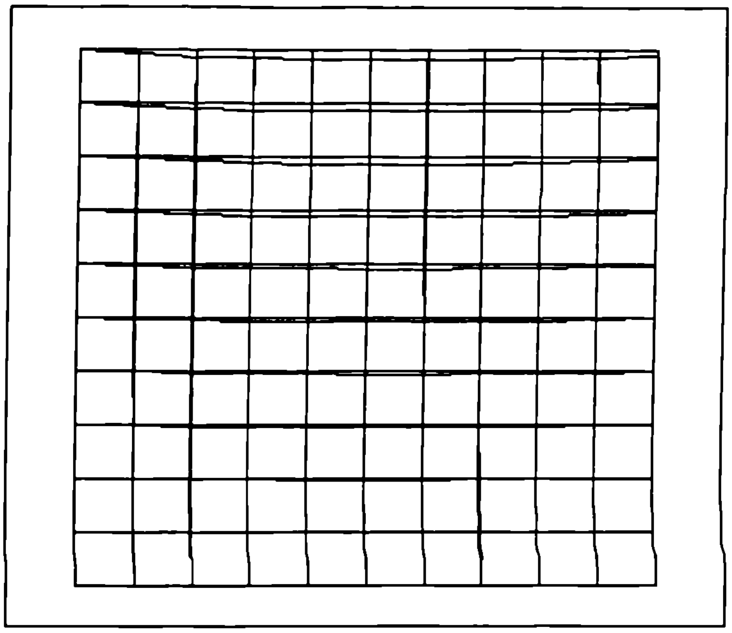

Figure 4.12: Simple Block Displacements

Looking at the *v* displacement along the friction boundary in more detail the nonlinear properties of the frictional contact can be seen. Figure 4.13 shows the displacement along the frictional boundary with a value of 0.6 for the coefficient of friction and compares these to the displacement of the edge if the contact surface was completely smooth.

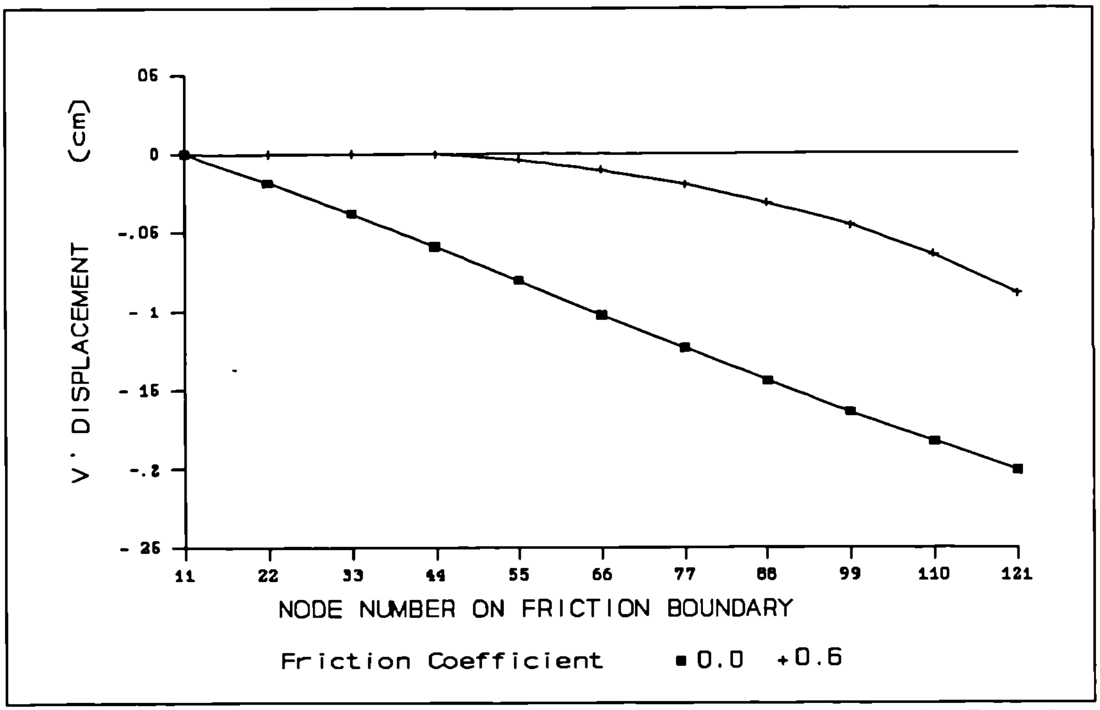

Figure 4.13: The Graph of Displacement at Nodes on Friction Boundary

When the contact surface is completely smooth and the coefficient of friction between the two surfaces is zero, the displacement obtained along the boundary is linear as seen in Figure 4.13. When friction is present the displacement is found to be nonlinear with nodes below a certain point 'sticking' and the nodes the other side 'slipping'.

To investigate the effect of the coefficient of friction, the value along the friction boundary was altered and the associated displacements obtained. Values for the coefficient between 0 and 2 were used. The tolerance for the displacement residuals was kept at 0.0001 and the simulation for each case was allowed a maximum of 500 global iterations. Again the solution did not reach the required tolerance, but the residuals were seen to oscillate slightly and not diverge.

Figure 4.14 shows how varying the value of the coefficient of friction between the two surfaces alters the displacements of the nodes along the friction boundary. The node that divides the stick or slip parts on the friction boundary is seen to move along the boundary as the friction coefficient is altered.

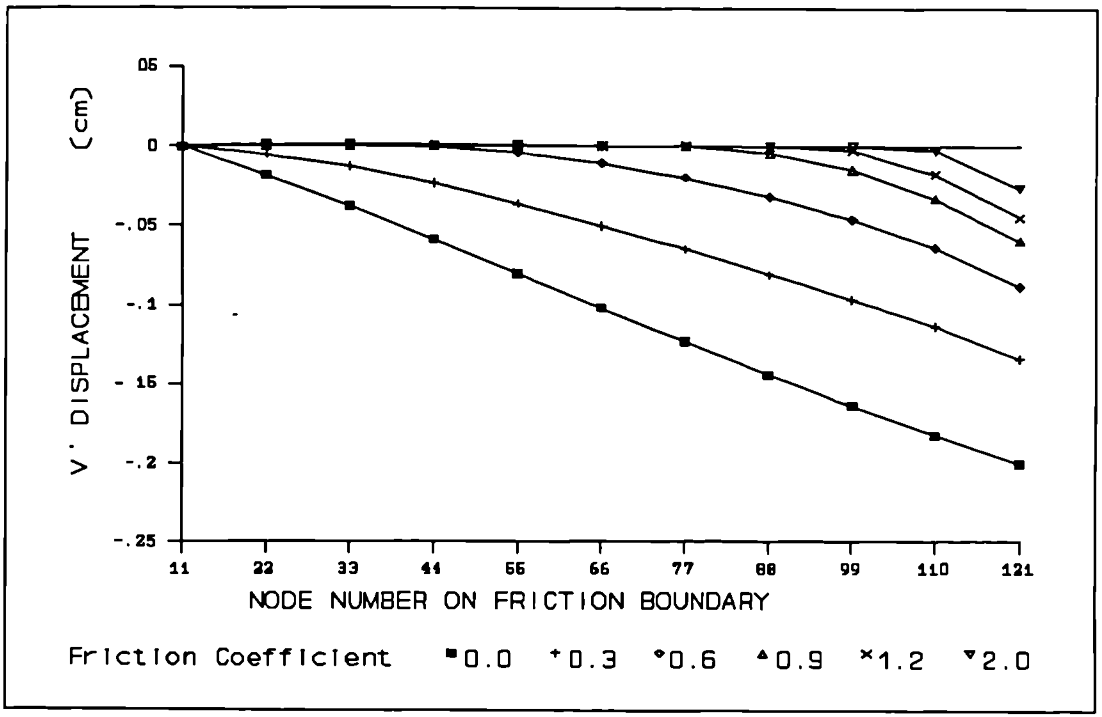

Figure 4.14: The Graph of Displacement at Nodes on Friction Boundary for Various Coefficients of Friction

4.3.3 Rotation of Block

To test the friction algorithms capacity for general boundaries the square block was rotated 30 degrees. The other properties were kept the same so that the relative v displacements, the tangential displacements, along the friction boundary could be compared with the v displacements of the original block. Figure 4.15 shows the initial block rotated 30 degrees, the two edges fixed in the previous example are still fixed and the top boundary has the same normal pressure applied.

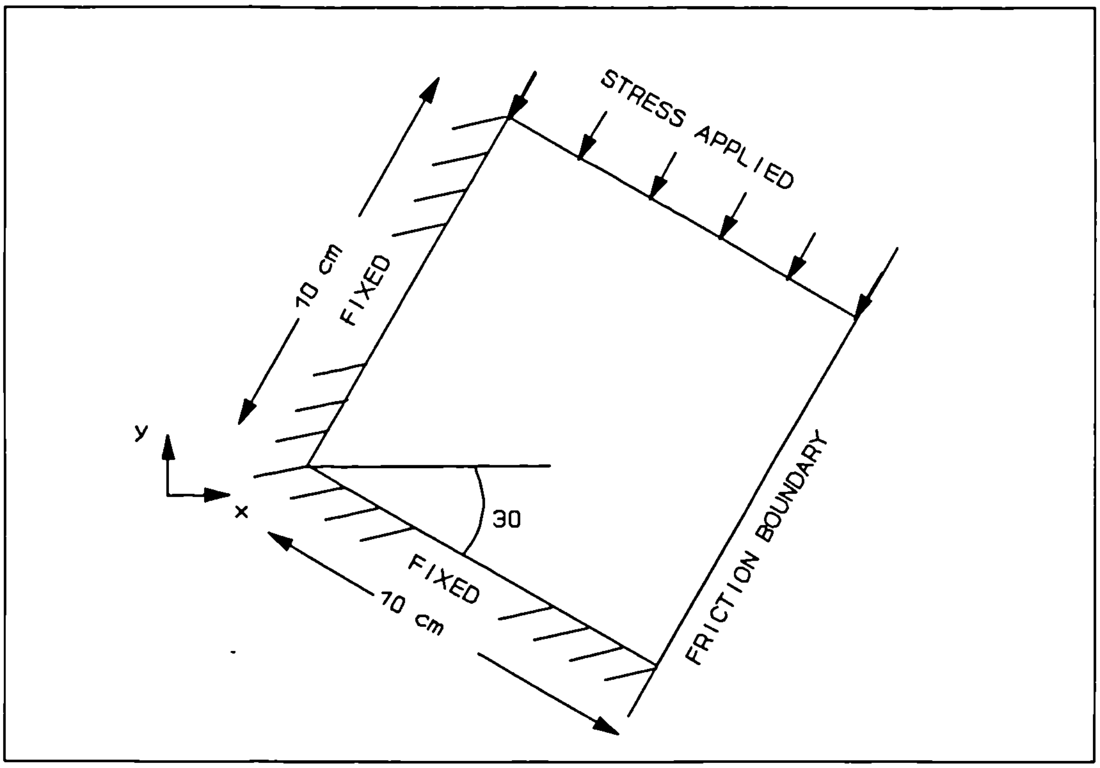

Figure 4.15: Simple Block Rotation of 30 degrees

The solution for the displacements was considered to have converged when the required tolerance of 0.0001 was reached as in the non rotated case or the maximum 500 global iterations were reached. Again the maximum of 500 global displacement iterations were reached and the required tolerance was not obtained. Figure 4.16 shows the oscillating *u* and *v* displacement residuals when the global iterations vary from 200 to 400 inclusive.

Figure 4.17 shows the displacements of the rotated block when a value of 0.6 was used for the coefficient of friction between the contact surfaces after 500 displacement iterations.

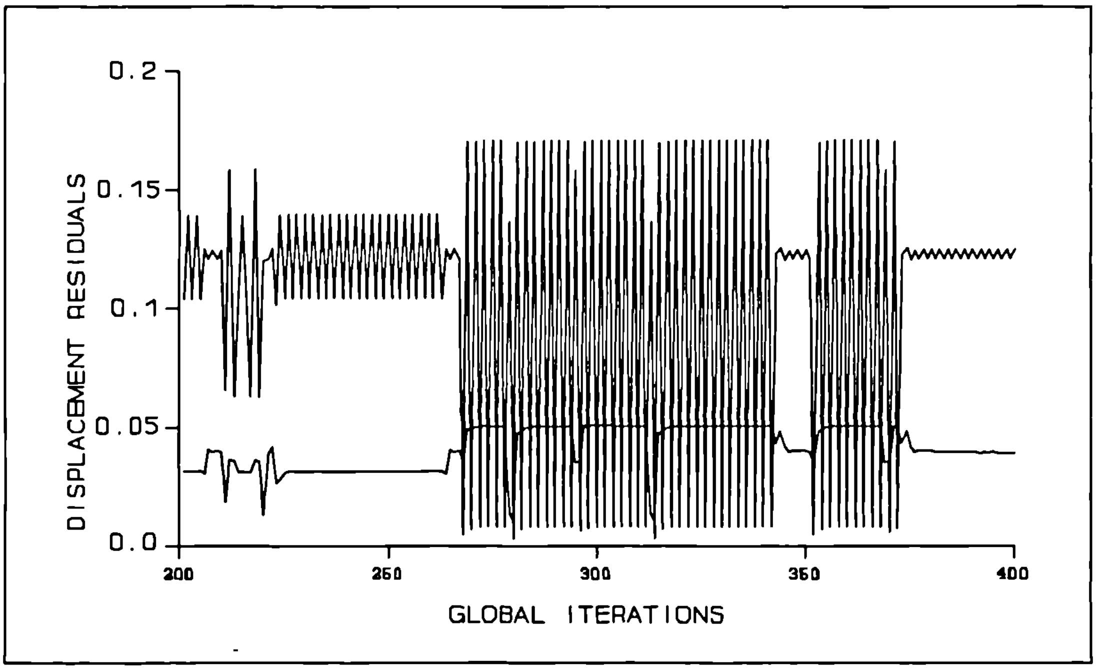

Figure 4.16: Displacement Residuals for Block Rotated 30 Degrees

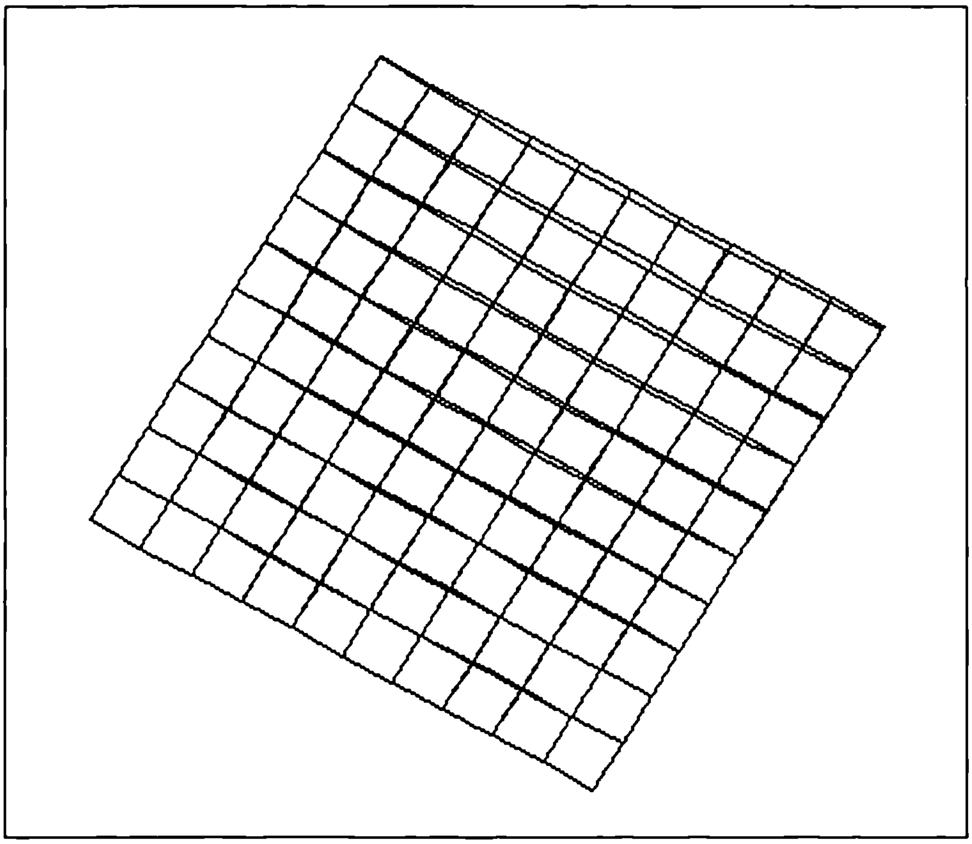

Figure 4.17: Displacements of Simple Block Rotated 30 Degrees

4.3.4 Comparison Results for Different Angles

To test completely the generality of the friction algorithm, the block was rotated between -90 and 90 degrees, and displacement results collected every 15 degrees. The results for the relative *v* displacement at node 110 are shown in Table 4.1. An arbitrary convergence tolerance of 0.0001 was used for the displacement calculations but in all cases the maximum number of global iterations, 500, was reached before the required tolerance was obtained.

Block Rotation degrees	v' Displacement (cm) at 110
-90	-0.0642251
-75	-0.0617375
-60	-0.0592075
-45	-0.0746322
-30	-0.0697129
-15	-0.0667230
0	-0.0642406
15	-0.0620162
30	-0.0593366
45	-0.0562012
60	-0.0695469
75	-0.0665926
90	-0.0641351

Table 4.1: Relative v Displacements on Friction Boundary for Rotated Blocks

For the friction algorithm to be general for all angles, the relative *v* displacement at node 110 for the various cases shown in Table 4.1 should be the same. From the Table it is seen that there is some variation. Figure 4.18 shows more clearly that the variation appears not to be random but actually there is a cyclic pattern. This small variation can be explained by the method of obtaining the stresses at the nodes. The stress calculations originally obtain values at the centre of the elements from the displacements calculated at the nodes. These element stresses are then approximated to obtain the nodal stresses. Where a node is surrounded only by one element, for example at the corner of the block, then the stress at this node is taken to be the stress at the element centre. Similar discrepancies occur for boundary nodes surrounded by two elements.

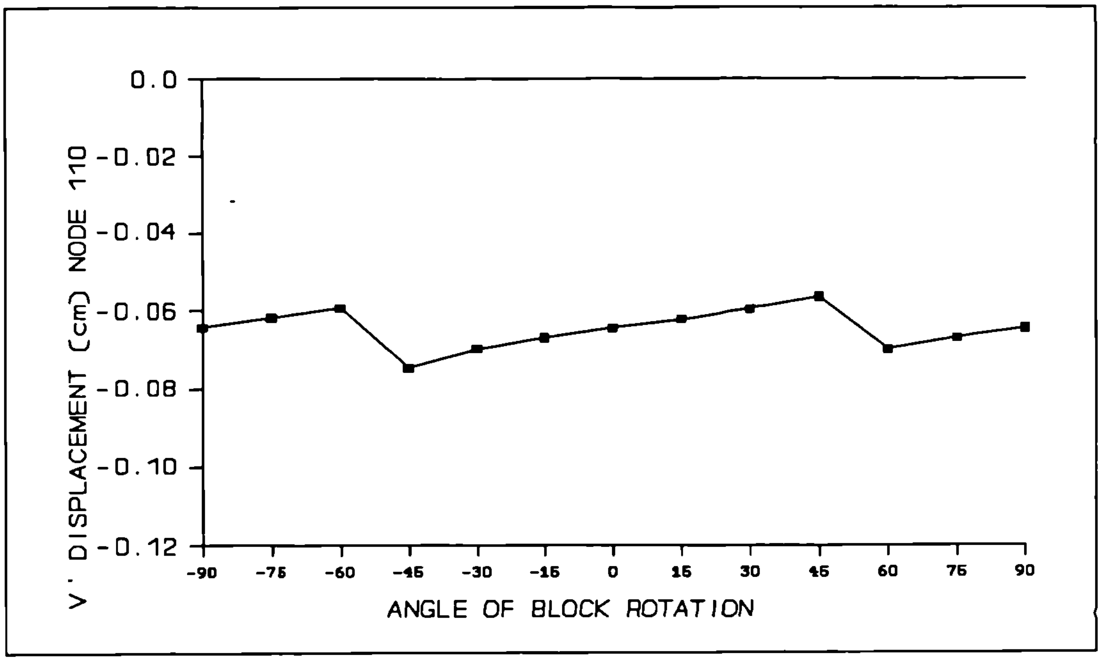

Figure 4.18: Graph of Relative v Displacements for Block Rotations

Another explanation emanates from the choice of F_x and F_y for the frictional force applied at the slip nodes on the friction boundary. If F_x is used for the solution of the u displacements then the v displacement is fixed along the interface line. Similarly if F_y is used then u is fixed. Whether to us F_x or F_y is dependent on the angle of the boundary, so errors can result as the fixing of the other displacement is an approximation.

4.4 Example 2: Silica Problem

This example was originally considered for solution by Moscardini (1985). Silica shapes that are often large and complex are manufactured for coke oven construction. Moscardini (1985) explains that the principle production procedures have not changed since the 1930's, but the acceptance standards have become increasingly stringent. There are two stages of production for the silica shapes, a pressing stage followed by a firing stage. The green shape needed for firing is produced by placing silica material into a mould and applying high pressures. The pressing stage can itself be divided into two phases. The early phase is when the silica material is initially rearranging itself and increasing in density. The later phase when little compaction occurs most of the particle bonds will be established. The material recovers its shape after pressing and so it is assumed to behave in an elastic fashion. During the second phase of the pressing stage frictional forces occur between the mould wall and the silica, it is these forces that are to be modelled in this section. Figure 4.19 shows a section through the silica and mould with the compressive forces acting on the top boundary of the silica. The friction effects act on the side mould and silica interface walls during this compression.

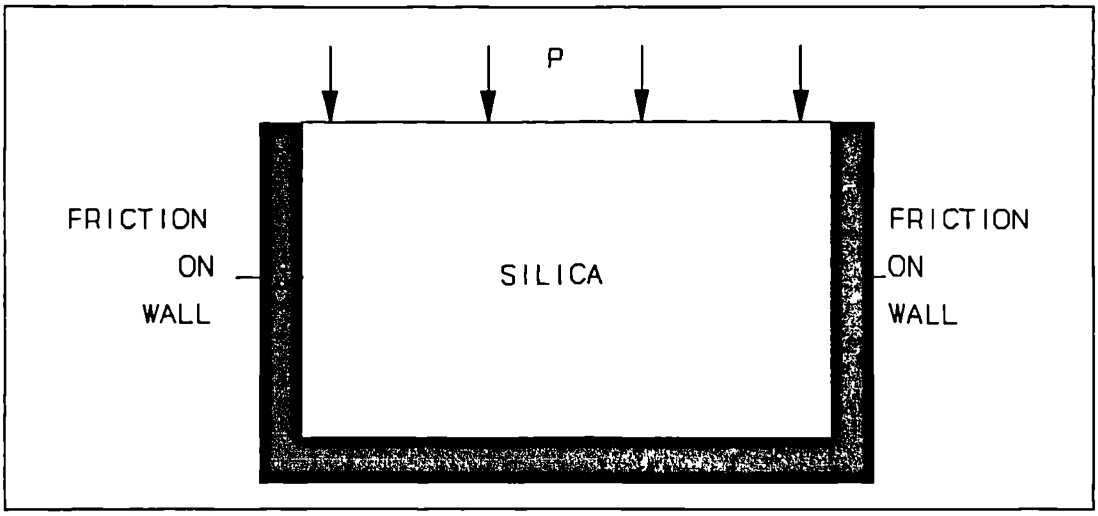

Figure 4.19: Initial Silica Conditions

4.4.1 Problem Specification

A typical section through a silica brick as in Figure 4.19 is 30cm long by 10cm high. As a result of the symmetry of the problem, only half the brick need be considered for modelling. Using a mesh of 1cm^2 quadrilateral elements, as shown in Figure 4.20, produces 176 nodes, the same mesh that Moscardini (1985) used. Figure 4.20 shows the numbers of the nodes along the right friction boundary for reference in the results section. The left edge is the symmetry boundary where the nodes are free to move in the y-axis direction but essentially fixed in the x-axis direction. The mould for the silica brick need not be modelled as on both connecting boundaries, the bottom fixed boundary and the right friction boundary, are assumed to be in full contact with the mould.

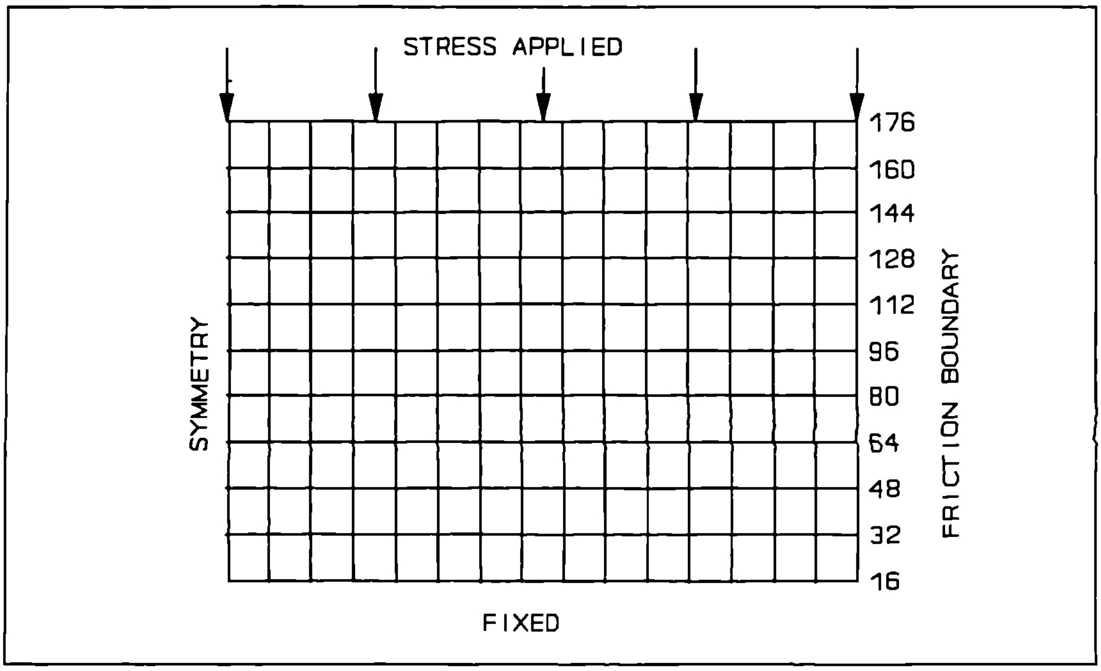

Figure 4.20: Silica Mesh and Boundary Conditions

The compressive stress, P equal to 4,000 N/cm^2, is applied along the top edge of the brick. The silica at the second phase of the pressing stage is considered to have a Young's modulus of 50,000 N/cm^2 and a Poisson's ratio of 0.4 [Moscardini (1985)]. The coefficient of friction used is 0.6.

4.4.2 CV-UM Results

The control volume unstructured mesh code was used to solve the silica problem with the mesh shown in Figure 4.20. A refined mesh as shown in Figure 4.21, where each element is 0.25cm^2 and there were 651 nodes, was also used to obtain a solution to the problem.

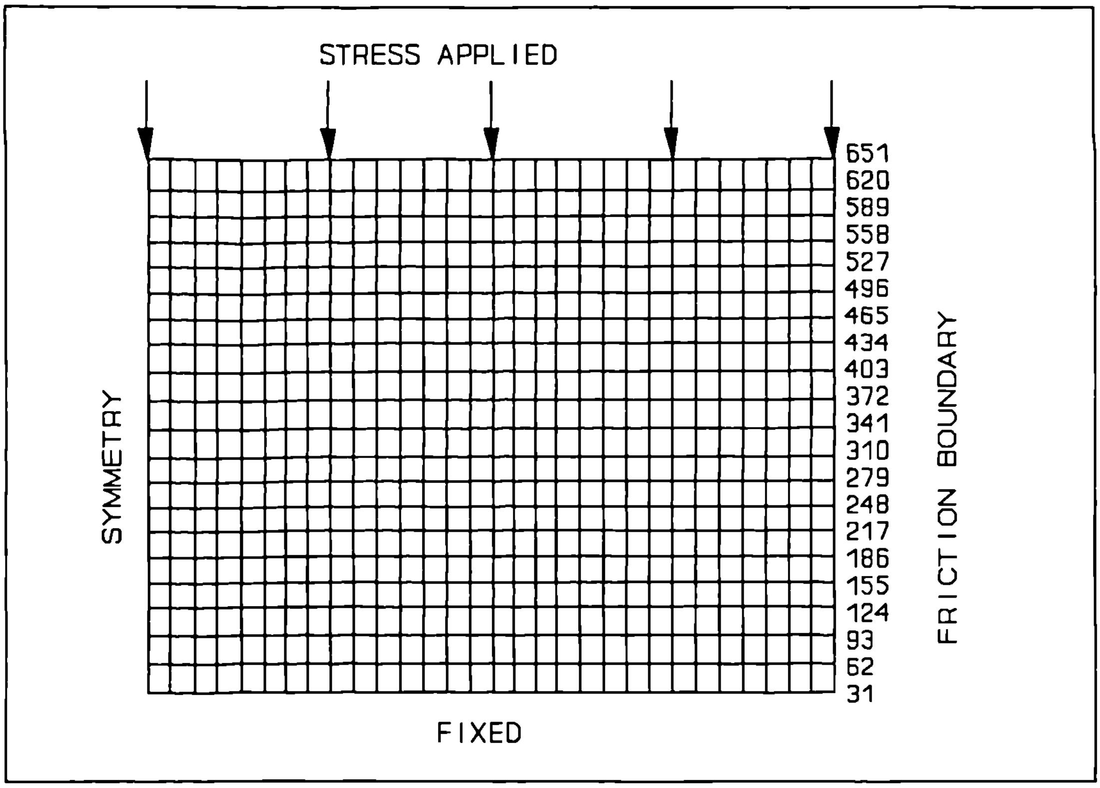

Figure 4.21: Refined Silica Mesh

Figure 4.22 shows the displaced mesh overlaying the original mesh for the silica brick. The effect of the friction between the brick and the mould can be seen along the right edge, where the silica brick has not compacted as much as the centre of the brick at the left edge of the mesh.

The maximum 500 global displacement iterations were used to obtain the displaced mesh for both the 176 node mesh and the refined mesh.

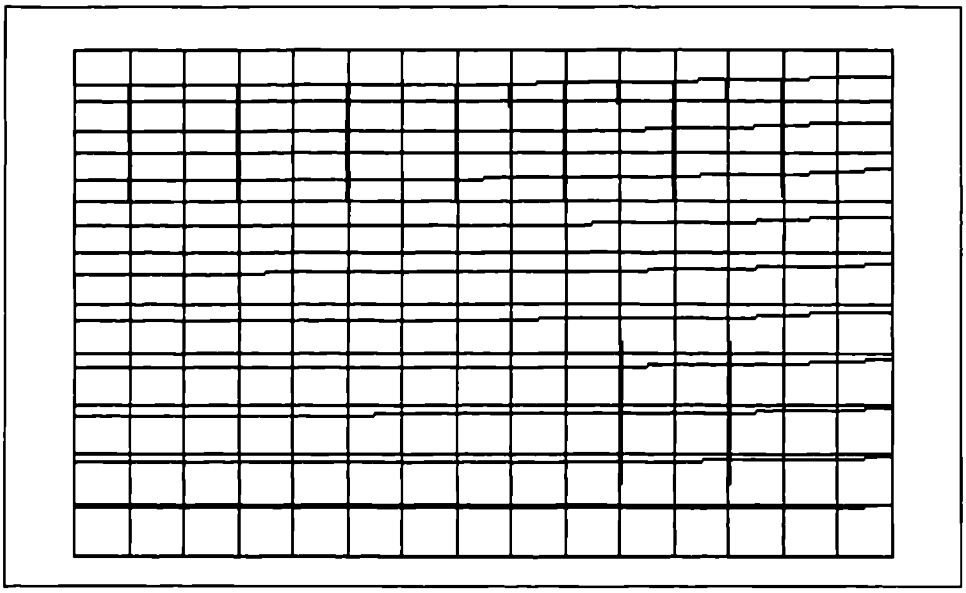

Figure 4.22: Silica Problem Displaced Mesh

The displacement along the friction boundary for the original mesh and the refined mesh can be seen in Figure 4.23. When the coefficient of friction is zero and linear displacements result along the friction boundary both meshes are seen to produce the same expected displacements.

When the coefficient of friction is 0.6, the node marking the stick and slip border is approximately the same for the 176 node case and the refined 651 node mesh. The results differ slightly towards the top of the silica brick, possibly due to the approximation of the stresses at the nodes from the element stresses. The refined mesh should produce more accurately the nodal stresses and so the frictional stresses for the two cases will vary resulting in slight variations on the displacements along the friction boundary.

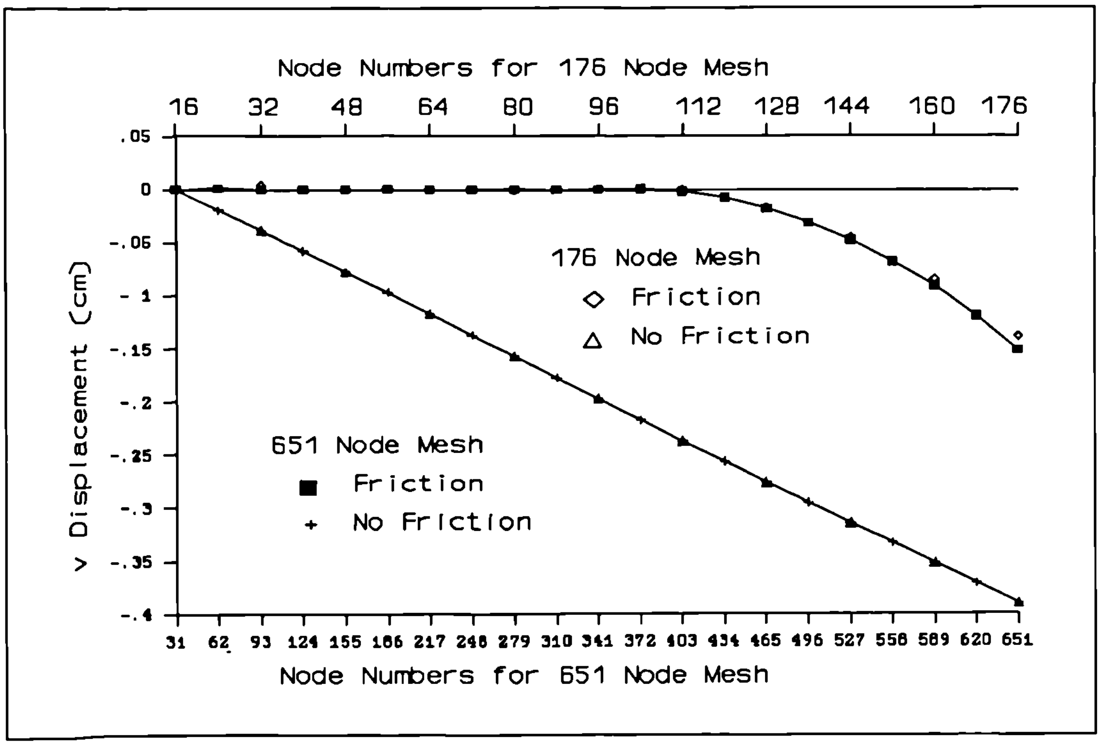

Figure 4.23: Graph of Displacement along Friction Boundary

4.4.3 Comparison with other Results

With the silica problem as specified previously, Moscardini (1985) found that the slip point, the node bordering the edge of the stick and slip regions of the friction boundary, was about 5 to 6 cm from the bottom of the silica brick. Moscardini (1985) when using the results further in the iterative algorithm found the slip point rose steadily and did not converge. The results obtained with the friction algorithm in this chapter, shown in Figure 4.23, suggest that the slip point is close to node 112 for the initial 176 node mesh in Figure 4.20. For the refined mesh in Figure 4.21 suggests the slip point is between nodes 372 and 403. Both meshes produce similar results for the slip point, which is predicted to be approximately 4.5 to 6 cm from the bottom of the silica brick. A finer grid could produce more accurate displacement results that might narrow the slip point interval further.

4.5 Conclusions

The inclusion of the nonlinear friction algorithm into the two-dimensional control volume unstructured mesh code resulted in non-convergence of the displacement residuals. In section 4.1.3 it was seen that often numerical procedures that include friction models have convergence problems. In this instance the residuals did not diverge, but oscillated over a small range and it was found that linearising the source term only made the range of the oscillations smaller. A future friction algorithm could be developed to avoid this problem altogether.

Ignoring the problem from the residuals, the results for the displacements produced along the friction boundary are very encouraging. The nonlinear aspects of the boundary condition are clearly seen when comparisons are made between interfaces with and without friction. Comparing the results of the silica problem with other simulation results found the results are in good agreement. Using a refined mesh for the problem produces a stick-slip point in the same region as the original mesh.

When the small block is rotated and the displacements compared along the friction boundary it appears that there is some variation of the relative displacements. There are two possible explanations for this effect. The first could be due to the way the stresses are approximated at the nodes from the element stresses. The second reason could be associated with the choice of frictional forces at the slipping points on the interface. As explained earlier in the chapter one friction force is applied to either the u or v displacements and the other displacement is fixed so that the node only moves along the friction boundary. The introduction of contact routine may avoid the second reason effecting the varying displacements for the rotated block.

Chapter 5

Application to Castings

The two-dimensional deformation code has been integrated and coupled with an existing two-dimensional control volume unstructured mesh solidification code. The fully coupled code modelling fluid flow, heat transfer, solidification, deformation and stress development, is then applied to the casting process and an example of a casting simulation detailed. The author believes that this is the first time that such a physically comprehensive analysis of the casting process has been performed.

5.1 The Casting Process

There are many variations of the casting process listed and described in numerous books [Campbell (1991), Higgins (1989)]. In some cases the mould may be of a simple shape giving rise to an ingot which is subsequently shaped plastically by forging, rolling or extrusion. Sand casting involves casting the molten metal into a sand mould of the desired shape. The resulting casting requires cleaning and light machining to reach the required measurements. Other casting processes that produce castings closer to the required shape include investment casting and permanent mould casting.

Consider the mould for a simple sand casting as shown in Figure 5.1. In this case the mould is made in two halves called the cope and the drag. The cope covers the drag and the connecting surface is the parting surface. The cope and drag are secured into the correct location using the pins on the drag and the lugs on the cope. The function of the runner is to admit the molten metal into the mould cavity through the in gate. The feeder (or riser) provides, if necessary, a reservoir of molten metal to feed back into the casting as it solidifies and shrinks.

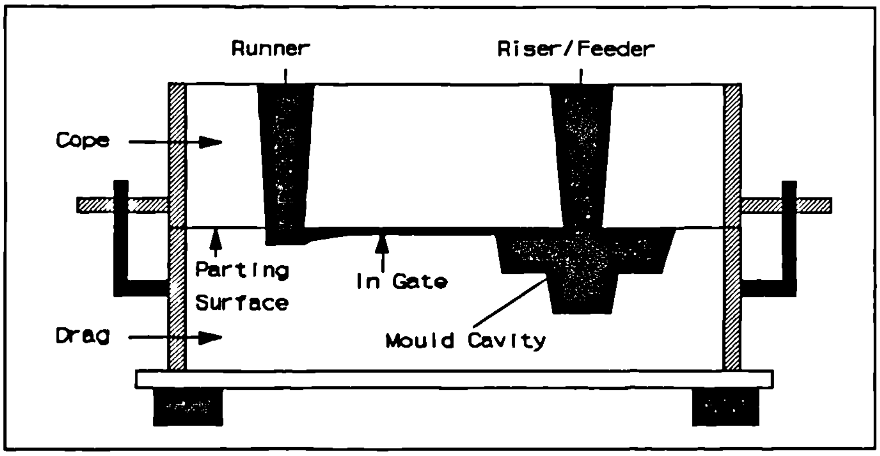

Figure 5.1: Sand Casting Mould Section

The mould is filled with molten metal, heat transfer occurs so that the casting solidifies and deforms residual stresses forming in the solidified regions. At present mould filling is generally modelled numerically using finite difference or finite volume schemes. The finite volume technique is an established method for fluid flow though more recently finite element methods have also been used. Finite element methods have generally been used for thermal and stress analysis with finite difference and control volume schemes being the popular choice for solidification modelling. In the past there has been a lack of integration in the modelling of the different phenomena. Chow (1993) has developed a fully integrated control volume-unstructured mesh code solving for fluid flow, heat transfer and solidification which in this chapter is coupled with the control volume-unstructured mesh code explained previously.

Adams et al. (1992) detail the requirements for a casting modelling system in the UK, to consist of a foundryman's interface for a particular casting process, the casting modelling framework software, integrated flow, solidification, thermal analysis and stress analysis programs, a materials database and a database of model and project files. The current time consuming and costly trial and error methoding approach of the foundryman will be replaced by a consistent and repeatable numerical procedure run rapidly and interactively on a computer, enabling reduction in lead times and costs.

5.2 Software for Casting Simulation

Computer modelling of casting process promises considerable benefits for the methoding process. Casting software is important for reduction in costs of castings. The aim is to reduce the lead time for casting production. At present with existing numerical casting software there is often a technical gulf between foundry users and researchers, little effort has been applied to make them usable by the foundry engineer [Butlin and Nutbourne (1993)].

In the U.S.A much money has been devoted to casting modelling, computer codes produced include PREDICT and PROCAST. Typically finite element packages that have concentrated on the simulation of particular physical problems. PROCAST uses a finite element mesh and has a built in two-dimensional quadrilateral and triangular mesh generator besides the capacity to read in meshes from various finite element packages such as ANSYS.

From Europe such packages as MAGMASOFT and SIMULOR have been produced though again they are limited in scope and performance. Finite difference based, limited in geometry coverage and typically only represent filling, heat transfer and solidification aspects of the casting process. MAGMASOFT uses an orthogonal cell mesh to represent heat dissipation and solidification. Fedelich, Mathiak and Deisenroth (1992) conclude, after using MAGMASOFT to simulate mould filling and cast solidification of a low pressure die casting process, that a stress/strain analysis of the cast would give additional valuable information concerning contact zones and air gap formation. MAGMASOFT is used to simulate the mould filling and solidification of a high pressure die casting example coupled, though not in a fully integrated sense, with a three-dimensional finite difference method technique for the thermoelastic equations using a staggered grid [Hattel, Hansen and Hansen (1993)]. SIMULOR was presented for the first time at the GIFA '89 exhibition. It provides a three-dimensional simulation of metal filling and solidification in a mould, but no deformation or stress prediction.

Other countries such as Japan have established casting modelling software such as the computer code CASTEM. The three-dimensional finite element code calculates the solidification sequence and temperature distribution in real time but does not calculate the metal flow or the internal stresses.

An empirical based code SOLSTAR from FOSECO is available in the U.K. that has an acceptable user friendly interface and is in use in many Foundries in the U.K and world wide. SOLSTAR does not attempt to model the fundamental physics underlying the casting process. SOLSTAR has been described as an "empirical finite difference" code [Preddy (1993)], that compares the temperature of a cube to the temperatures of the 26 surrounding cubes and essentially obtains a solidification sequence. Another code used by the foundry industry is FEEDERCALC, a simple code that enables the foundry engineer to decide on the requirements of the casting with respect to feeders, chills and insulating sleeves. Methoding packages used in the foundry industry do provide useful tools for designing castings with risers and chills as necessary, but for more detailed prediction of defects these packages become too generalised and the need for mathematical models arises [Hogg (1991)].

According to Adams (1993), the lessons learned during the evolution of structural analysis 15-20 years ago should enable the exploitation of casting modelling to be accelerated. Full benefits of process modelling will not be achieved unless the process can be operated by the foundry engineer, though it must not be seen as a means for making the skills of the foundryman redundant.

Bellet, Bay, Brioist and Chenot (1992) have developed a three-dimensional finite element model for the thermomechanical phenomena occurring during the solidification and cooling of cast products. The mould is assumed to be rigid for the deformation calculations. Rather than use coincident nodes at domain interfaces the thermal boundary conditions are modelled by contact thermal resistances.

Other techniques for casting software include the use of an intelligent knowledged based system. Upadhya, Paul and Hill (1993) use empirical heuristics for the design of runners, sprue and gates. Chvorinov's rule, as explained in Chapter 6, is used to aid the design and positioning of the risers. A knowledge-based expert system called EXCAST is used by Natarajan, Chu and Kashyap (1989) in order to facilitate the design and manufacturing of casting components. The global casting soundness is predicted using an efficient geometry based simulation method modelling the solidification process. Research is under way to develop a model-based knowledge system for casting design and manufacturability assessment which integrates a commercial computer aided design (CAD) package, a database management system, and design algorithms within a frame-based knowledge engineering environment [Bradley, Adams, Gadh and Mirle (1993)]. ALEXSYS is a prototype expert system designed for use in the aluminium high pressure die-casting industry. [Webster and Weller (1993)]. The system was designed to reflect the sub-sets of knowledge within the foundry. Webster and Weller (1993) conclude that the most important factor in constructing a worthwhile expert system would seem to be the cooperation and enthusiasm of the expert(s), and in order to gain this there may have to be sacrifices with regards to pure knowledge engineering theory. Cowell, Knight and Preddy (1993) aim to produce a computer based system capable of giving advice on methoding design, to produce a geometric feature analysis tool, capable of representing features of importance to casting design and to produce a database of example cases. Unlike other researches in the field, Cowell, Knight and Preddy (1993) propose to include the modulus model at the initial shape construction stage using a geometric design-by feature.

With the development of faster computers and use of parallel processing, the use of numerical techniques for the physical phenomena of the casting process increasing speed and efficiency will produce casting software capable of competing with existing methoding casting software. The full casting software could involve computer aided design tools for methoding the casting design followed by numerical models for casting simulation and testing. [Cross (1993)] The use of fully automatic mesh generation facilities and mesh decomposition algorithms needs to be available for the numerical simulation of the casting.

5.3 Fundamental Equations for Casting Process

The physical phenomena of the casting process to be included in the casting software developed in this chapter include:- fluid flow, heat transfer, solidification and stress analysis. The differential equation governing the conservation of momentum for a two-dimensional cartesian coordinate system for an incompressible fluid can be written as [Chow (1993)]:

$$\begin{aligned} \frac{\partial(\rho u)}{\partial t} + \nabla.(\rho \underline{V} u) &= \nabla.(\mu \nabla u) - \frac{\partial p}{\partial x} + S_u \\ \frac{\partial(\rho v)}{\partial t} + \nabla.(\rho \underline{V} v) &= \nabla.(\mu \nabla v) - \frac{\partial p}{\partial y} + S_v \end{aligned} \qquad (5.1)$$

where μ is the viscosity, ρ the material density, p the pressure, $\underline{V}$ the resultant velocity, S_u and S_v are the sources for the x and y direction respectively. The u and v are the cartesian velocity components in the respective directions. For mass conservation in the flow field an additional equation, the continuity equation, needs to be satisfied

$$\frac{\partial \rho}{\partial t} + \nabla.(\rho \underline{V}) = 0 \qquad (5.2)$$

The general conservation of energy equation can be expressed as:

$$\frac{\partial(\rho h)}{\partial t} + \nabla.(\rho \underline{V} h) = \nabla.(k\nabla(h/c)) + S_h \qquad (5.3)$$

where h is the specific enthalpy, c the specific heat , k the thermal conductivity and S_h the source term for the volumetric rate of heat generation. Chow (1993) developed a control volume unstructured mesh code to solve for fluid flow, heat transfer and solidification. The deformation equations used are those described in chapter 2, where the equilibrium equations apply to a particular cell for stress with body forces neglected.

$$\frac{\partial \sigma_{xx}}{\partial x} + \frac{\partial \sigma_{xy}}{\partial y} = 0$$
$$\frac{\partial \sigma_{xy}}{\partial x} + \frac{\partial \sigma_{yy}}{\partial y} = 0 \qquad (5.4)$$

The stresses resulting from the temperature change of a particular time step are summed to produce the overall stresses for the total simulation time. The discretised equations allow for non-linear elastic behaviour, in the form of temperature dependent material properties such as Young's modulus, E.

5.3.1 Metal/Mould Contact

At the start of the simulation, coincident nodes are used at the mould/cast interface. Here two nodes are defined as having the same coordinate point, but are associated with two different elements which may have different material definitions [Samonds, Lewis, Morgan and Symberlist (1985)]. Figure 5.2 shows an example of the coincident nodes at the mould/metal interface when the casting material has started to deform. At present the mould interface with the casting is prescribed as fixed for use with the simple contact routine.

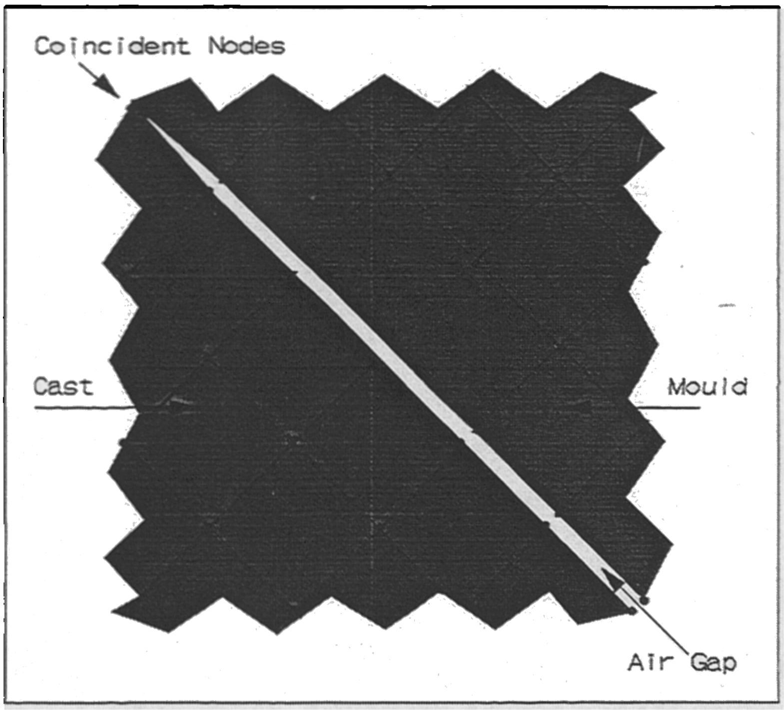

Figure 5.2: Coincident Nodes in Mould and Cast

5.3.2 Air Gap Formation

At the mould/cast interface a simple geometric routine calculates the size of the air gap. During the iterative procedure, for both the u and v displacements of the cast material, the deformation is checked to see if it is moving into the mould. If this is the case then the nodes moving into the mould are adjusted so that they lie on the mould boundary. This operation is carried out during the iterative solution procedure to ensure conservation of mass as all the other nodes feel the restricting effect of the mould. The casting placement is also adjusted to allow for gravity acting upon it.

Dantzig (1987) states that in foundry castings with sand moulds the size of the air gap is insignificant resulting from poor thermal conductivity in the sand making the gap minimal. The modelling experience of Bailey, Fryer, Cross and Chow (1993) has shown neglecting the gap distance can overestimate the cooling rate by 2%. Thomas, Samarasekera and Brimacombe (1986) predicting gap formation during continuous casting and Michalek, Kelly and Dantzig (1986) predicting gap formation in ingot casting use finite element techniques with essentially an empirical method for gap formation.

The usual procedure for thermal modelling is to assume a convective heat transfer expression at the interface [Lewis and Roberts (1987)]:

$$\frac{\partial T}{\partial n} = h_{eff}(T_{metal} - T_{mould}) \qquad (5.5)$$

where the effective heat transfer coefficient, dependent on the gap distance, is given by [Michalek, Kelly and Dantzig (1986)]:

$$h_{eff} = \frac{k_{gap}}{\Delta_{gap}} \qquad (5.6)$$

where k_{gap} is the thermal conductivity of the gap medium, assumed to be air, and Δ_{gap} is the gap distance. The effective heat transfer coefficient, h_{eff}, is initially 3000W/m^{2o}K when there is a zero gap distance.

5.4 Solution Procedure for 2D code - UIFS

The two-dimensional stress-strain code, explained in chapter 2, has been coupled with the two-dimensional thermal convection, heat transfer and solidification code, from Chow (1993), involving the equations shown in section 5.3. The control volume unstructured mesh fluid solidification code termed an irregular control volume method uses a cell centred approach for determination of results, whereas the deformation algorithm is vertex based. The same mesh is used for all parts of the fully coupled code and data transfer between the FORTRAN 77 subroutines is simple without the need for data conversion routines.

Figure 5.3 shows diagrammatically how two procedures are coupled together in the same code. At the start of the program the run information is read in from a file containing such information as tolerance values, relaxation parameters, debug options and restart switch. The initial problem specific data such as material and thermal properties, coordinate points, boundary conditions and element topology, are read in from various files. If the program is being used to continue a previous simulation then a restart file is read in otherwise initial properties and conditions are set and the simulation time defined as zero. The flow-solidification loop is then started, the thermal convection in the molten metal is obtained followed by the enthalpy calculations. The temperature material properties are updated along with the liquid-fraction information. If convergence has not been reached the program continues with another iteration of the flow-solidification section. Once a converged solution is obtained the stress module is entered. With the temperature changes obtained in the previous section the deformation of the solidified parts of casting are found, and the resulting stresses are calculated in the casting using an additive model. Details about the air gap size between the casting and the mould enable the heat transfer coefficient at the mould/metal interface to be altered accordingly. If the required number of time steps has not been reached the next time step calculations begin otherwise the program dumps the results to various files for use with post processing facilities. The fully coupled two-dimensional code is identified as UIFS, where UIFS stands for Unstructured Integrated Fluids and Solids.

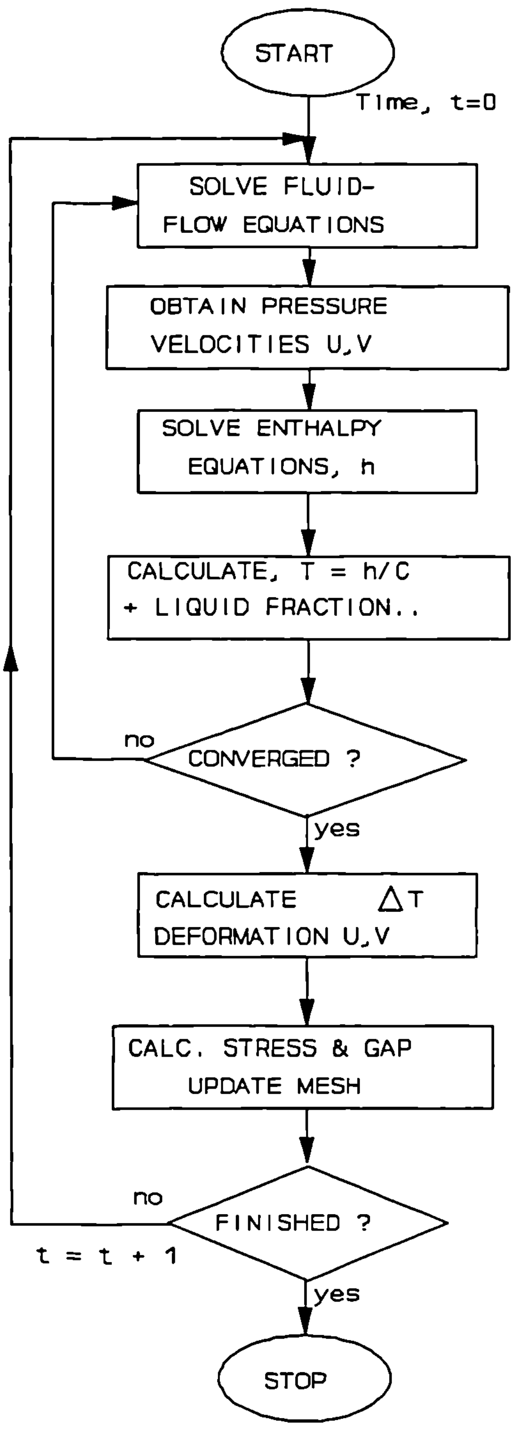

Figure 5.3: Coupled Heat Transfer/Deformation Algorithm - UIFS

5.5 Example: T-Bar Casting

This example models the solidification of a section through a simple T-bar casting with numerous curved boundaries in a sand mould. The results are monitored during solidification using the fully coupled fluid flow solidification code with the stress-strain equations. The prediction of an air gap forming between the casting and the mould, as the casting solidifies and deforms, is also noted. The solidification results are also monitored with the deformation algorithm switched off, and hence no air gap formation, to see the effect on the solidification time.

5.5.1 Problem Specification

The side view of the T-bar casting is shown in Figure 5.4, the casting has a diameter of 50cm and a maximum height of 14cm. Due to the symmetry of the problem only half the casting need be modelled.

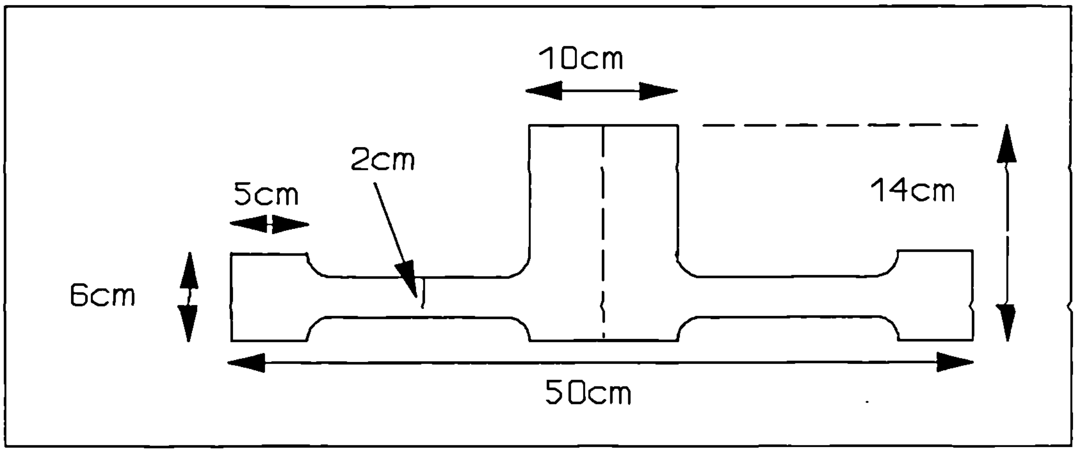

Figure 5.4: T-Bar Casting - Side View

Figure 5.5 shows the casting section to be modelled using the coupled code, with the appropriate boundary conditions noted. The left boundary is the symmetry plane for all aspects of the simulation. The top boundary of the casting is considered insulated by the fluid flow and solidification parts of the code and free to move in the deformation part of the code. All boundary nodes of the mould are at present described as fixed. The boundary of the mould and air is defined as having a ambient temperature of 25°C and the mould/metal boundary is defined using coincident nodes. No filling module is as yet coupled with the two-dimensional code so the mould is assumed to be completely filled at the start of the solidification simulation.

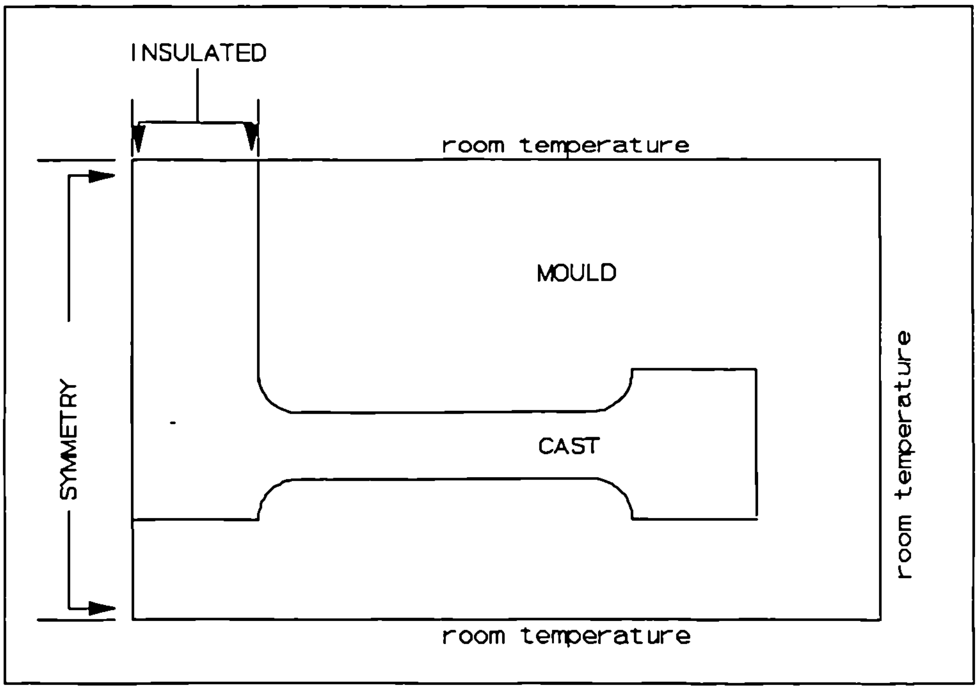

Figure 5.5: T-Bar Casting - Initial Conditions

The solidification is modelled using the alloy A-357. Table 5.1 shows the thermal properties A-357 [Moosbrugger and Berry (1986)] and approximate elastic properties used in the solidification simulation.

The casting has curved boundaries that are modelled using triangular elements. A two-dimensional mesh consisting of triangular elements was generated by Lawrence (1993) for this specific two domain problem. The resulting mesh consisted of 1099 vertices and 2068 elements. To allow for the coincident nodes at the mould/metal interface extra nodal points were defined so the total number of nodes increased to 1195. Figure 5.6 shows the initial triangular mesh with coincident nodes at the mould/metal boundary.

	Moulding Sand	Alloy
Conductivity (W/m°C)	0.84	187.0
Specific Heat Capacity (J/kg°C)	1,120.0	1,050.0
Density (kg/m^3)	1,682.0	2,670.0
Viscosity (kg/ms)	0.00181	0.00181
Young's Modulus (N/m^2)	21×10^{10}	12×10^{10}
Poisson's Ratio	0.0	0.29
Coefficient of Thermal Expansion (°C^{-1})	0.0	0.00012
Latent Heat Coefficient (J/kg)	-	432,600.0
Solidus Temperature (°C)	-	613.0
Liquidus Temperature (°C)	-	660.0
Initial Temperature (°C)	25.0	700.0

Table 5.1: Casting - Thermal and Elastic Properties

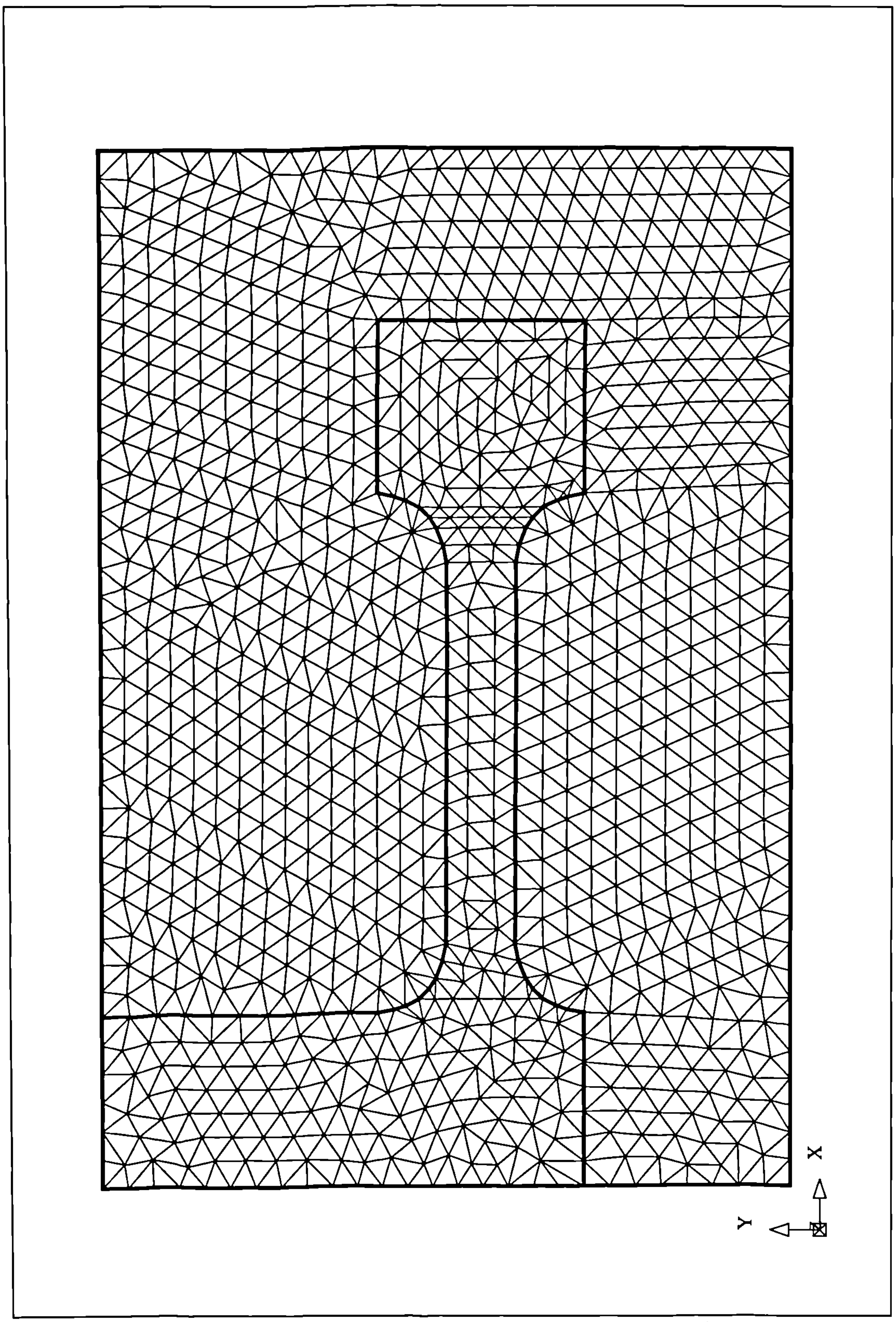

Figure 5.6: T-Bar Casting - Initial Mesh

5.5.2 UIFS Results

Solidification results were collected using the coupled thermal solidification stress code. Firstly the results were collected with the deformation algorithm switched on then the solidification results were collected without the deformation of the casting taken into account. A time step of 2 seconds was used for the simulation of the casting solidifying.

Figure 5.7 shows the fluid flow pattern after the first 10 seconds of computation including the deformation prediction.

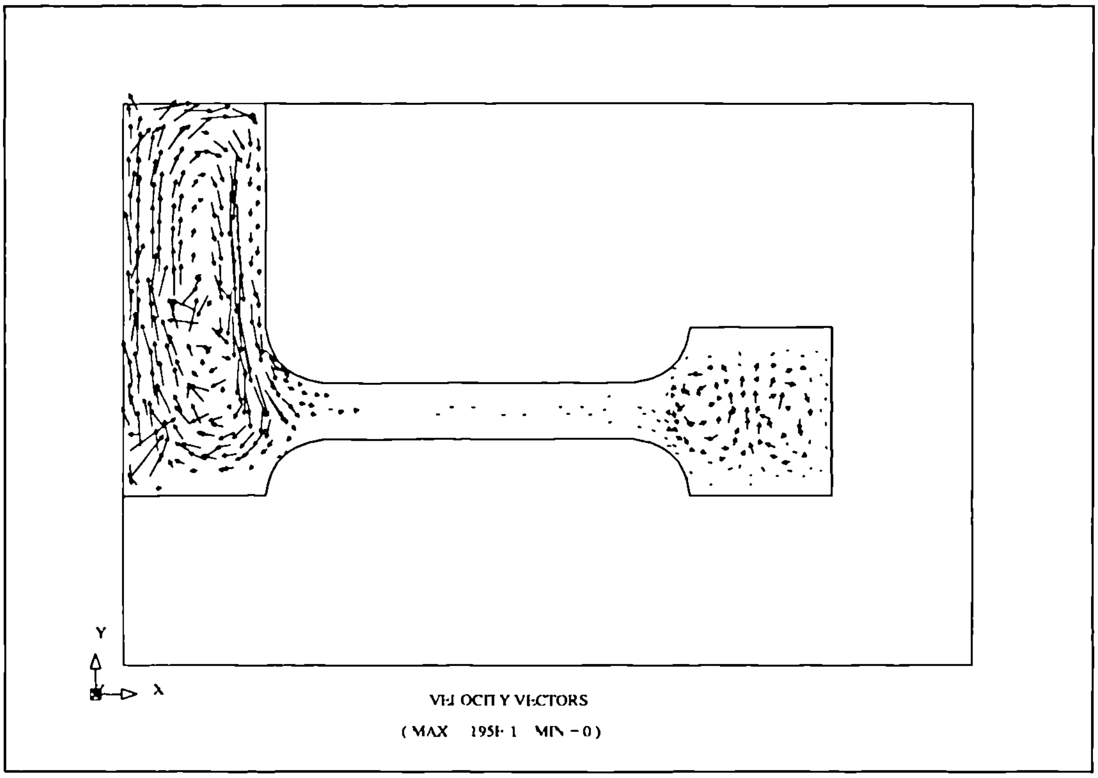

Figure 5.7: T-Bar - 10 second - Fluid Flow Results

Figures 5.8-5.10 show intermediate results of 5, 15 and 25 minutes respectively when the casting is allowed to solidify and the deformation and corresponding stresses are also noted. Each figure displays the liquid fraction, the temperature, the fluid flow and the effective stress present. Other results such as the density or enthalpy could be monitored. The figures show the bridging that occurs during the solidification, two separate flow patterns are seen. The modulus of the T-bar would indicate that the thin section would freeze first as is seen in Figure 5.8. The first stresses then develop in this region before the rest of the T-bar is solid. 15 minutes into the solidification, Figure 5.9 shows that only the centre of the T-bar is left to freeze. Maximum stresses can now be found at the mould metal interface at the larger solidified section. The corresponding stresses resulting in the mould are not modelled at present. Figure 5.10 shows that after 25 minutes only a mushy part at the centre of the T-bar is left to freeze.

The T-bar is completely solidified 34 minutes into the simulation, the resulting stresses in the T-bar are shown in Figure 5.11. The maximum stress is seen where the large section of the T-bar is pulled against the mould as the casting contracts. Due to the deformation and contraction of the casting, an air gap at the mould/cast interface can clearly be seen at the right boundary of the T-bar. The deformation at the top of the casting can also be seen, though they are quite small. The stresses of interest in the casting are obtained but the resulting stresses formed in the mould due to the casting and temperature effects are not yet monitored.

The stresses predicted are larger than they should be because of the elastic model used, rather than a visco-plastic model, though the *deformation predicted is correct.*

The intermediate casting simulation results predicted when the deformation of the casting is not calculated are shown in Figure 5.12. At 25 minutes into the solidification the temperature contours are clearly different at the far end of the casting due to the lack of air gap prediction so the casting cools faster.

It was found that when the deformation of the casting was neglected the simulation predicted the casting would take approximately two minutes less time to become completely solid than with the deformation prediction. This is due to the lack of air gap prediction and so the heat transfer coefficient calculations at the mould/metal interface will be incorrect in the simulation when the deformation is not predicted. The maximum temperature of the casting at 34 minutes was 2°C greater than results when the displacements were calculated.

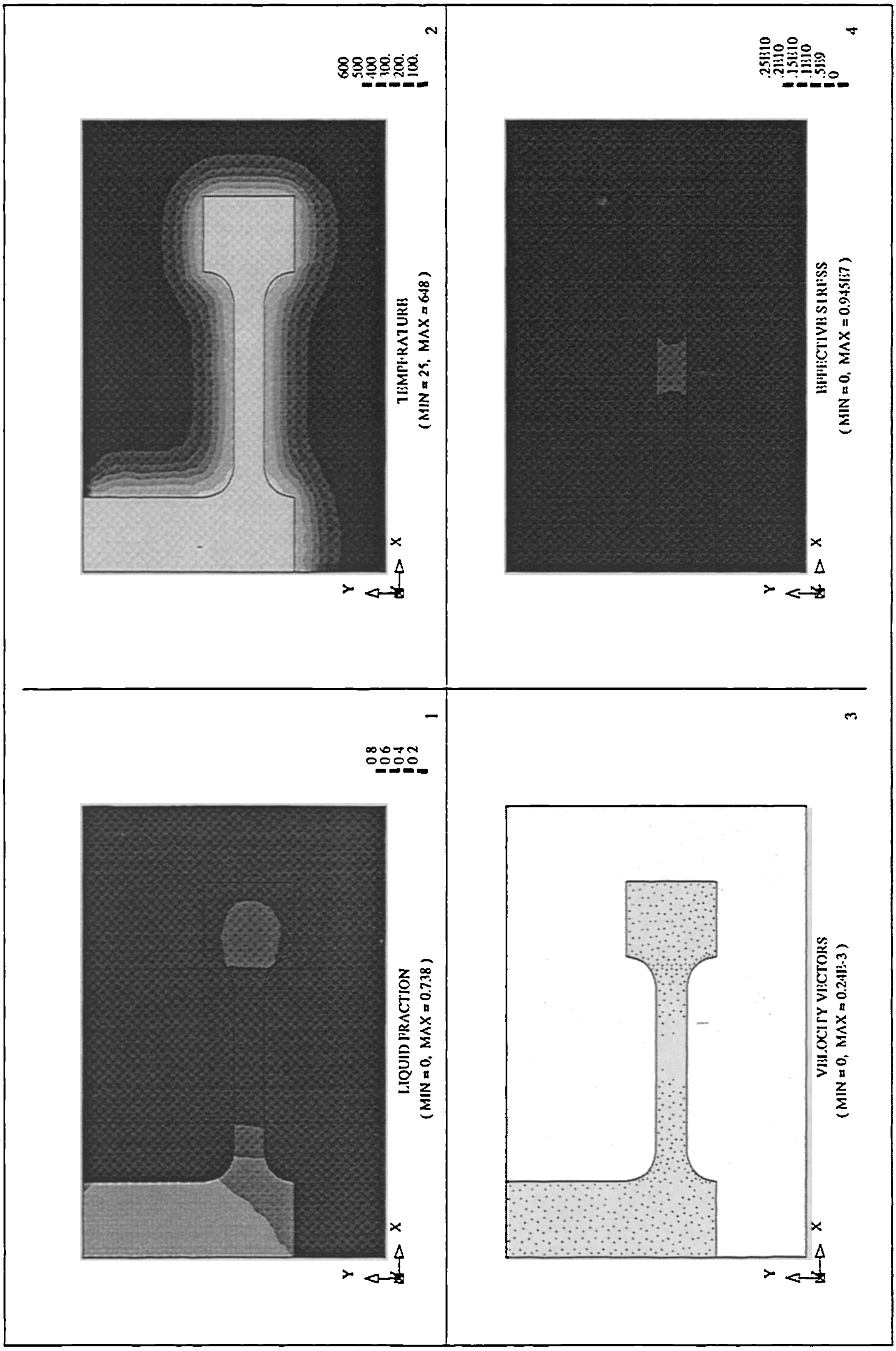

Figure 5.8: T-Bar Casting - Intermediate Results 5 Minutes

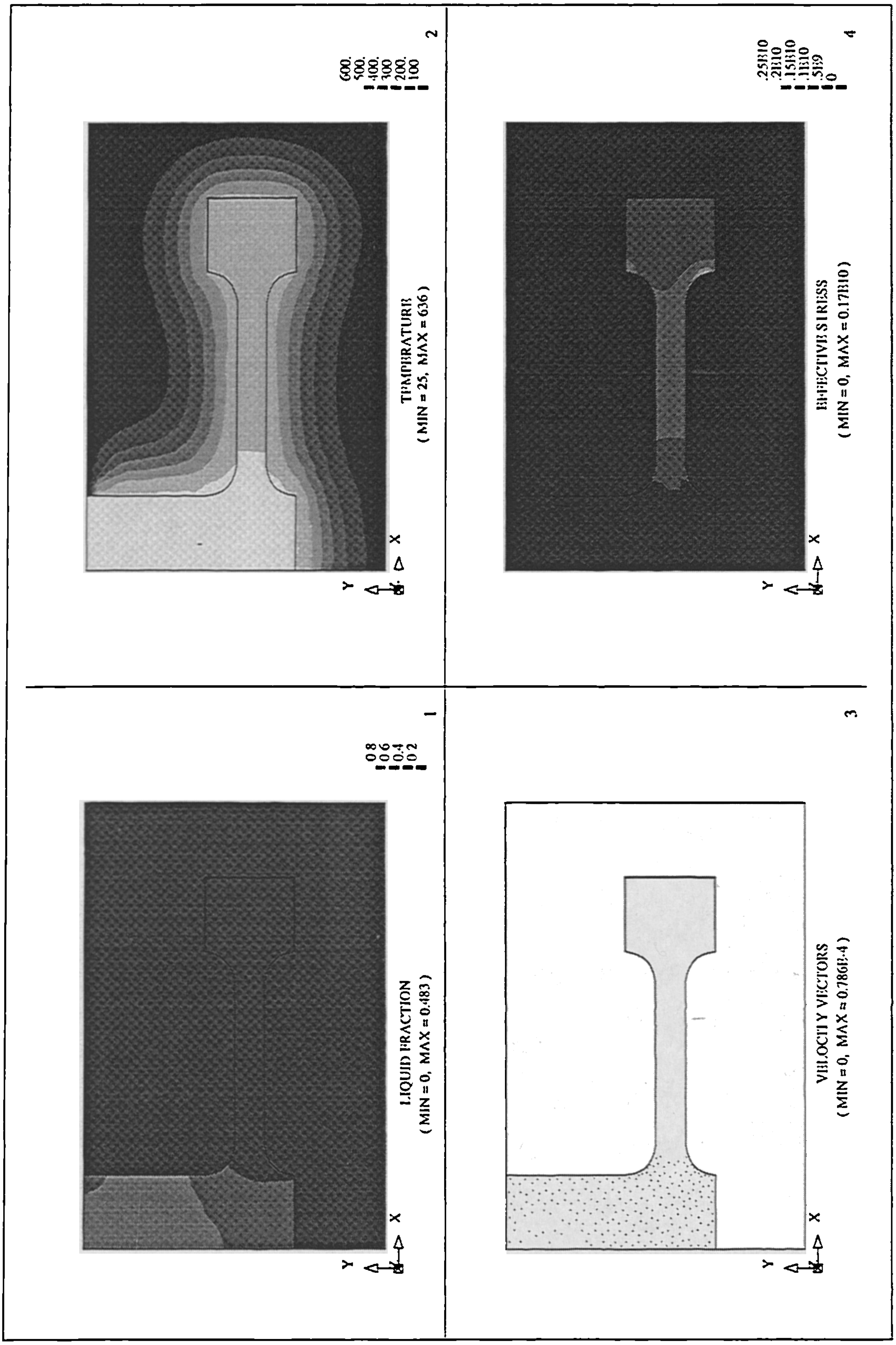

Figure 5.9: T-Bar Casting - Intermediate Results 15 Minutes

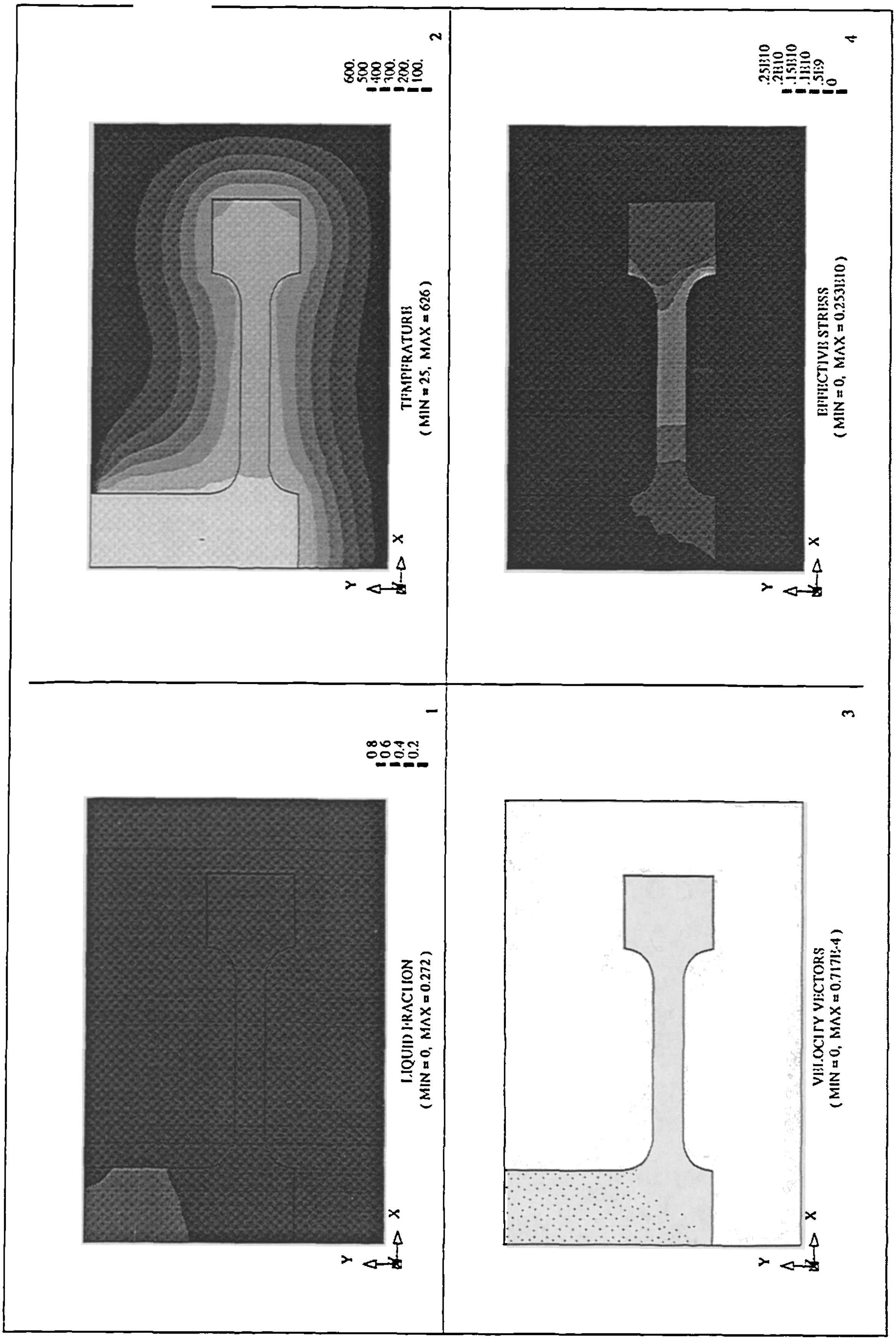

Figure 5.10: T-Bar Casting - Intermediate Results 25 Minutes

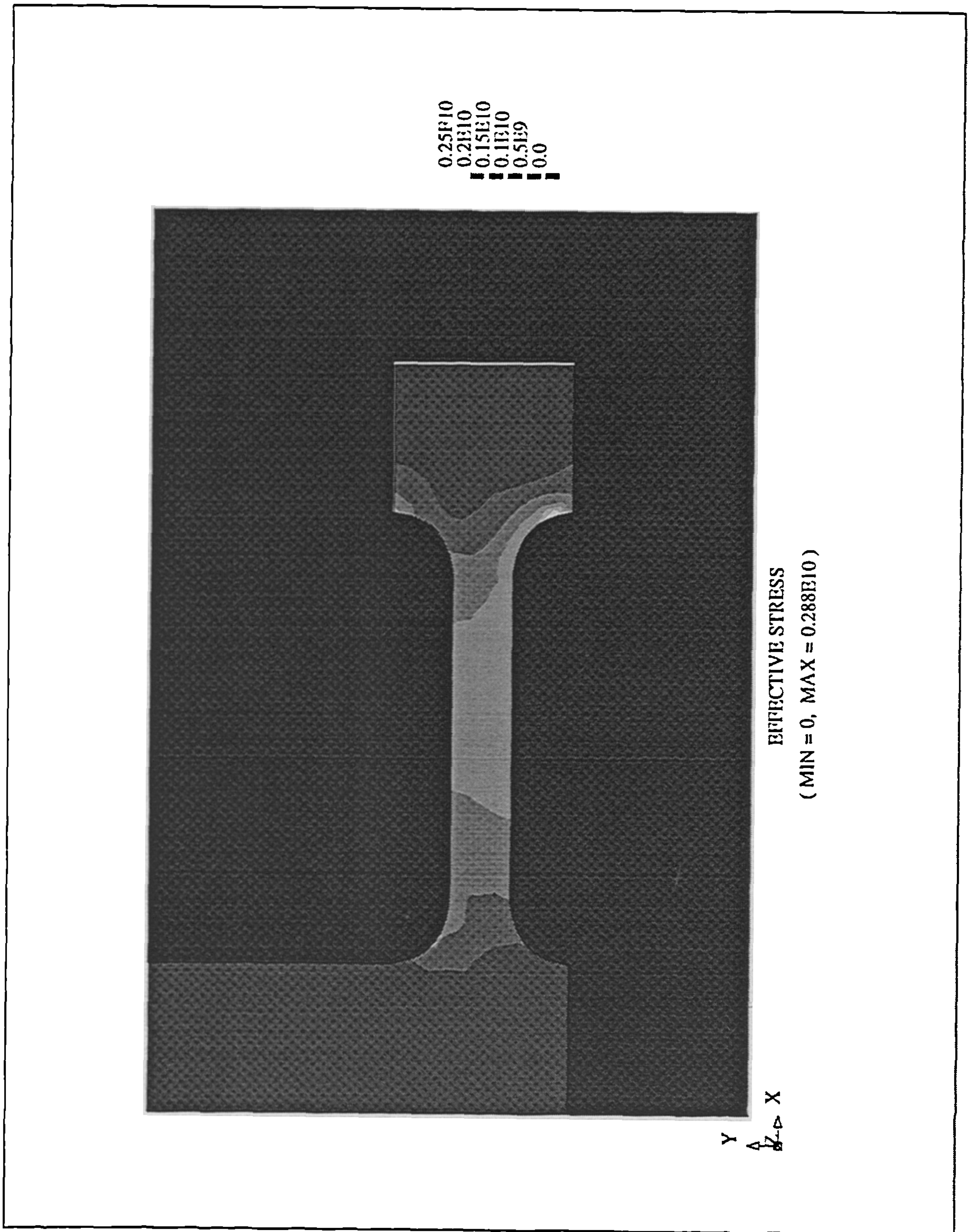

Figure 5.11: T-Bar - Final Stress Results - 34 Minutes

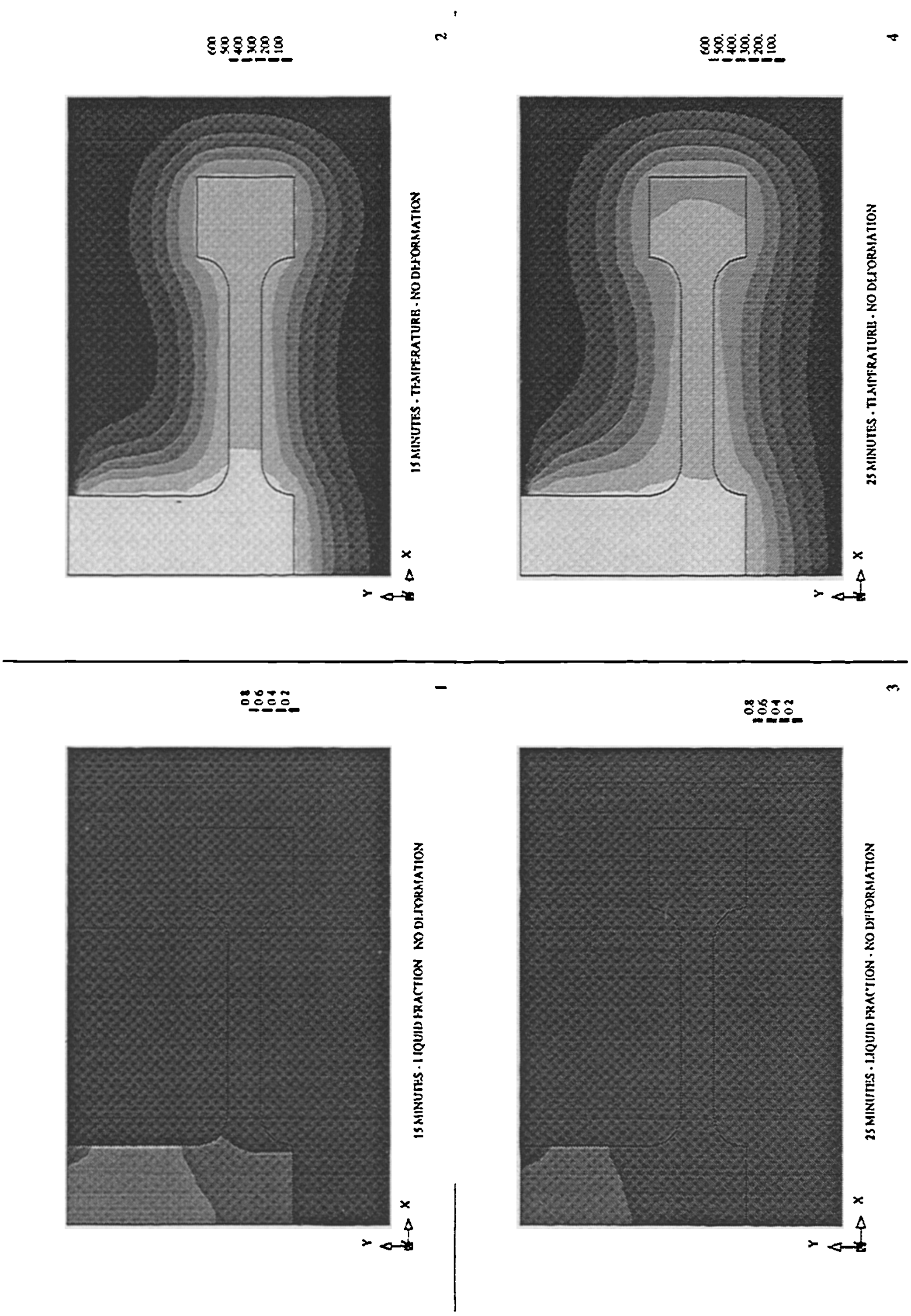

Figure 5.12: T-Bar Casting - Intermediate Results - No Deformation

5.6 Conclusions

The two-dimensional control volume unstructured mesh procedure for solid mechanics has coupled together with *the two-dimensional fluid flow solidification procedure very* well. Both procedures were based on very similar algorithms which aided the link forming the fully coupled and integrated casting code. The T-bar example results from section 5.5 show results generated simultaneously during the casting solidification simulation. The temperature changes as the casting cools and solidifies causes the solidified casting to deform. The deformed casting may cause an air gap formation at the mould/casting interface. The air gap will influence the effective heat transfer coefficient at the mould/casting interface. The change in the effective heat transfer coefficient will change the amount of heat lost through the mould walls for a particular time step hence the deformation of the casting will vary accordingly. For a computer program to effectively model the solidification of a casting it is important to include as many casting physical phenomena as possible. It was shown that if the deformation calculations are neglected then the simulation will cool the casting to quickly. Bailey, Fryer, Cross and Chow (1993) show a cooling rate for a casting that was overestimated by 2% when the displacement calculations were not used. The code introduced here includes the physical phenomena of thermal convection, heat transfer, solidification, deformation, stress calculations and air gap formation. Further work might include a mould filling module coupled with heat transfer and solidification.

The contact between the mould and the casting though effective is not complete. The casting movement is restricted by the mould and so stresses result in the casting. The force of the casting on the mould surface at present is not monitored, further work on the contact analysis can include this. Further work can include the conditions for visco-plasticity or visco-elasticity when the stress-strain relationships are non-linear.

Chapter 6

Porosity Formation

Porosity prediction is very important for the modelling of sound castings. If shrinkage porosity can be predicted before the casting is made it can save material, energy and time. This chapter briefly describes what is meant by porosity with respect to castings and details some of the existing methods of porosity prediction and examples of usage. A new porosity prediction method is derived that uses information from the deforming casting. The inclusion of the porosity algorithm into the control volume unstructured mesh heat transfer and deformation code is then tested with various examples.

6.1 Porosity Definition

Gas evolution and solidification shrinkage are the two major sources of possible porosity formation in solidifying metals, acting frequently simultaneously. The porosity is formed in various locations of the casting and can be either macroscopic or microscopic.

6.1.1 Gas Evolution

Gas evolution occurs during solidification as gases are generally more soluble in liquid metals than in solids [Kubo and Pehlke (1986)]. Two events can influence gas evolution. Firstly, the decrease in solubility on phase transformation and secondly the liquid phase is continuously enriched in the gaseous component as the solid is formed and then rejects the solute species to the liquid. Examples include hydrogen in aluminium alloys and carbon monoxide, a compound gas, in iron alloys. Foundry techniques exist to reduce such gases before casting to alleviate the gas evolution in the casting during solidification [Viswanathan, Sikka and Brody (1992)].

6.1.2 Solidification Shrinkage

As the metal in the casting freezes there is generally an increase in the density resulting in a reduction in volume. This occurrence is a primary source of porosity formation in solidifying castings. It is known that when the metal transforms from the liquid to solid state the volumetric shrinkage can range from 3-10% [Kubo and Pehlke (1986)], with 5-8% typical of most cast alloys. Porosity formation as a result of the shrinkage process can be aided by incorrectly fed castings. As the casting freezes the porosity formed can be macroscopic or microscopic depending on the alloy.

6.1.3 Macroporosity

Macroporosity, as the name suggests, is the presence of relatively large voids in the casting. Figure 6.1 shows a region of a casting that has been poorly fed. The residual liquid is presently cut off from the reservoir of liquid metal stored in the feeder. Due to the nature of the alloy, short freezing range and low thermal conductivity, a high thermal gradient results between centre and edge of casting. This skin freezing nature results in macroscopic porosity forming as the remaining residual liquid in the casting solidifies. A section through a casting suffering from macroporosity will reveal holes visible without enlargement.

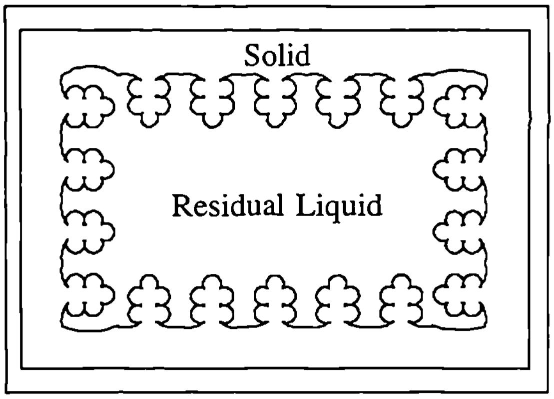

Figure 6.1: Skin Freezing Alloy

6.1.4 Microporosity

An alloy with a long freezing range and a high thermal conductivity, when solidifying, will typically produce microporosity. The low thermal gradient is responsible for the mushy freezing that takes place as shown in Figure 6.2. To feed the solidification shrinkage the liquid metal has to be brought through the complicated interdendritic channels that result from the mushy freezing. The resistance of the residual liquid to flow in the mushy zone enables microscopic porosity to form between the dendrite arms. A section through a casting with microporosity will reveal the defect when viewed with the aid of a microscope.

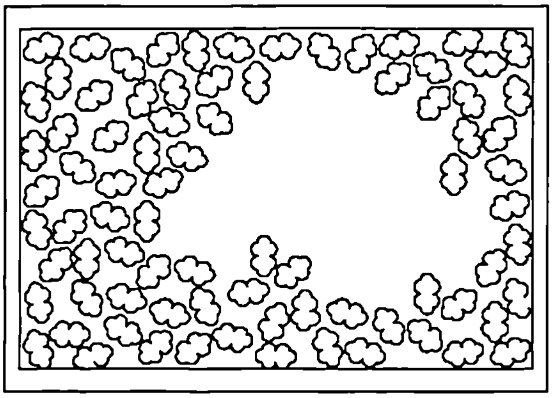

Figure 6.2: Mushy Freezing Alloy

6.1.5 Porosity Location in Castings

Figure 6.3 shows location of possible porosity features obtained in a typical casting. To allow for the volumetric shrinkage in the casting a reservoir of liquid stored in the feeder is used to feed the casting. More information on the various methods of feeding that take place during the solidification of the casting can be found in various books and papers [Campbell (1991), (1969), Kubo and Pehlke (1986), (1985)], but will not be discussed here. As a result of the loss of liquid from the feeder on freezing a shrinkage pipe will form in the feeder, or a shrinkage cavity if the top is sealed by the solidified metal. In the foundry such things as exothermic powders can be used on top of the feeder, where suitable, to stop the bottom of the shrinkage pipe from reaching as far as the casting. Progressive freezing ensures the casting freezes before the riser. If for some reason the riser freezes before the casting has finished solidifying then a hot spot will form in the casting. A hot spot is a section of casting that is cut off from the feeder and so the reservoir of liquid stored in the riser cannot feed the casting as it solidifies further. As the residual liquid in the casting then freezes macroporosity could then result. This porosity is often known as centreline shrinkage because of the usual location. Throughout the casting, depending on the alloy, microporosity may be present due to impedance of fluid flow through the interdendritic channels as the alloy solidifies. Layer porosity may form along an isobaric surface in the casting [Campbell (1991), (1968c)]. It has been observed in many different cast alloys including copper and aluminium. It is initiated, in the mushy/pasty zone, when the hydrostatic tension reaches a critical level, a pore nucleates then the layer porosity continues along the isothermal and isosolid surface reducing the hydrostatic tension.

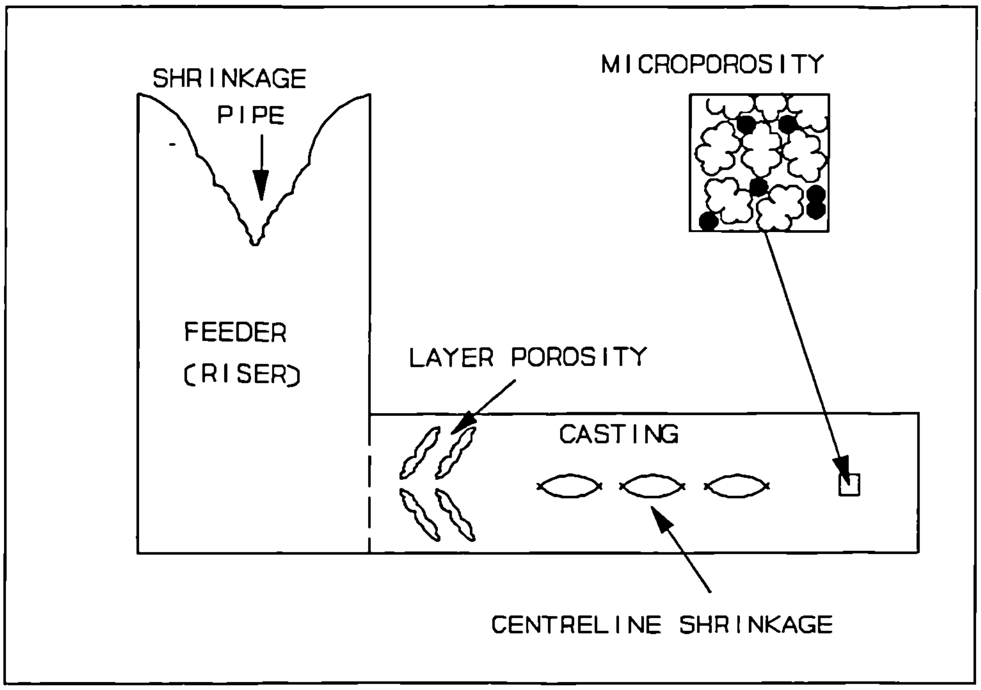

Figure 6.3: Porosity Location

6.1.6 Pore Nucleation

The mechanisms for pore nucleation have been studied in much detail [Campbell (1967), (1968a), (1968b), (1969)] and a conclusion reached that the homogeneous nucleation of pores by shrinkage is seen as impossible. The stress in the liquid is too small by at least an order of magnitude, so in the absence of assistance from gas, some form of heterogeneous or non-nucleation process must be responsible for the creation of pores in unfed regions of castings. If no suitable nucleous is present no pore will form and the casting will be sound [Campbell (1991)]. It is often stated that in principle it is feasible to obtain sound castings without additional supplies of feed liquid to make up for the solidification contraction.

For the porosity prediction method defined in this chapter, in the absence of gas evolution, the assumption is made that some heterogeneous nuclei are present to enable the porosity to form that is normally observed in castings.

6.2 Existing Methods for Porosity Prediction

As the casting solidifies and volumetric shrinkage follows, extra liquid metal is fed to the casting from the attached feeder. The dimensions and positions of the feeders are very important to ensure the soundness of the solidified casting. Progressive freezing is required where the furthest point in the casting from a particular feeder freezes first and then finally the feeder itself freezes. The modulus for each component or junction of the casting and each feeder are calculated as appropriate. The modulus is equal to the volume-to-area ratio. As long as the modulus values increase from casting to feeder, progressive freezing should result and so facilitate the production of a sound casting.

Following on from this technique, so called Modulus Methods [Hansen and Sahm (1988)] have been developed that incorporate the modulus into a criterion for porosity prediction. The well known *Chvorinov's rule relates the solidification time of the riser* or casting to the square of its volume-to-area ratio [Viswanathan, Sikka and Brody (1992)]. Although the rule aims to ensure the feeder retains liquid longer than the casting, the shape of the casting is not taken into account. Different shapes having the same modulus show different solidification characteristics [Hansen and Sahm (1988)] and for this reason the rule is therefore a rough approximation where safety factors should be introduced.

Since the 1960's numerical methods have been used to simulate the solidification sequence in castings. With the advent of faster computers and faster algorithms, greater consideration of criteria functions has been to enable better prediction of deformation defects. There are now various methods that can to some extent predict shrinkage porosity [Hansen and Sahm (1988)].

Temperature isotherms can be obtained from numerical heat transfer models. The plots of the freezing isotherms indicate possible shrinkage porosity if there is bridging, resulting in a hot spot that cannot be fed. Figure 6.4 shows a casting where no bridging of the isotherms occurs, and the casting should be sound, and a casting where bridging results and the casting may have shrinkage porosity. This obvious method gives a good estimate of shrinkage porosity, but sometimes even if the isotherms do not cross shrinkage has still been present in the final casting [Viswanathan, Sikka and Brody (1992)].

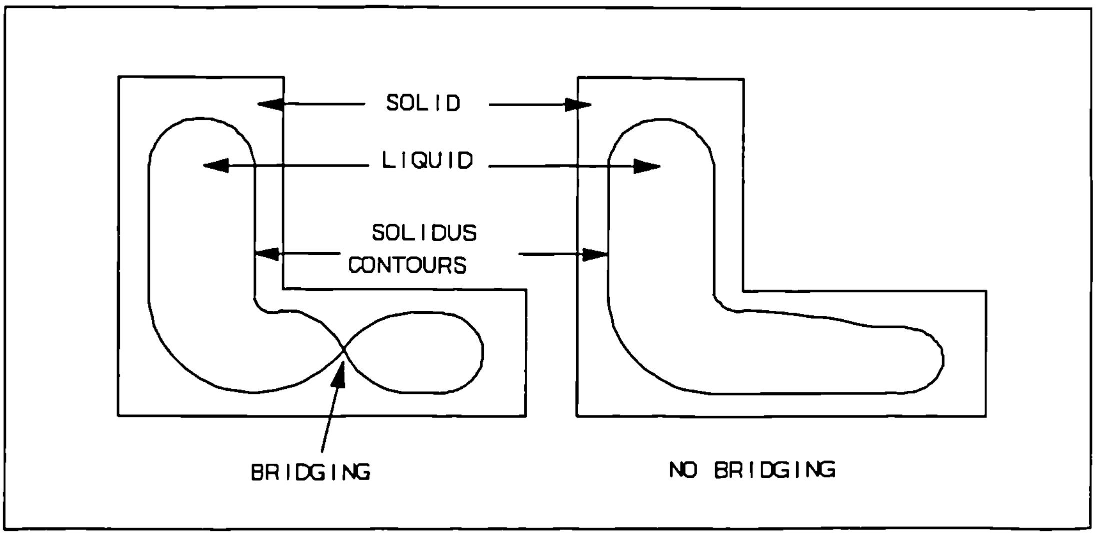

Figure 6.4: Temperature Isotherms

It was noticed [Pellini (1953)], that the magnitude of the temperature gradient, G °C/m, at the solidus temperature correlated well with the formation of centreline shrinkage porosities in castings of similar shapes. Unfortunately, the value of G needed to feed a plate is about 5-10 times smaller than for a bar. A suggested improvement on this parameter [Niyama et al. (1982)] introduces the 'Niyama' criterion, where the temperature gradient is divided by the square of the cooling rate, R. If $G/\sqrt{R}$ is greater than some critical value then the casting is said to be sound, else some shrinkage porosity is present. Both terms should be determined at the solidus temperature.

The Niyama criterion is widely used, though not based on any real physical understanding of porosity. Ryan et al. (1993) used solidification simulations to solve recurring shrinkage porosity problems with a large (21,000 kg pour weight) rudder hub steel casting. The RaRiD/CASTST code used with the criterion function has proved useful in designing a mould that showed improvements on the shrinkage porosity levels. Dalin et al. (1992) evaluate the shrinkage present in castings using the Niyama criterion in an effort to reduce both costs and adjustment times for casting production. The Niyama criterion is included in the SIMULOR code for predicting macroshrinkage, but for microshrinkage an alloy specific criteria function is used [Rigaut et al. (1993)]. The Niyama criterion proves to be very useful for predicting shrinkage porosity, but does not account for the fact that the critical value of G of a bar differs at the feeder end and at the opposite end [Hansen and Sahm (1988), Pellini (1953)].

Criteria functions for porosity prediction are also of the form of pressure or pressure related parameters, often Darcy law models are being used [Ampuero, Hoadley and Rappaz (1991)]. Various other models are in use such as a feeding criteria in the MAGMASOFT^{TM} code [Lipinski, Schaefer and Flender (1993)] and an interdendritic flow based model which makes use of the friction drag within the feeding system [Huang et al. (1993)].

Recent work has seen the advocation for process maps where the casting processes and alloy types are divided into four groups with a different criterion selected for each group [Viswanathan, Sikka and Brody (1993), (1992), Brody, Viswanathan and Stoehr (1991), Viswanathan (1990)].

A critical review of solidification models which included a section on shrinkage [Stefanescu (1993)], stated that the models proposed to date address the principal macro-aspects but ignore the complicated aspects related to pore nucleation. Physical models that include pore nucleation concepts may take too long to produce results and require more physical information before results produced are correct. The foundry engineer aims to produce results fairly quickly, generally the models in use achieve this and are also relatively easy to use.

6.3 Porosity Prediction with UIFS

Consider a section of a solidifying sphere shown in Figure 6.5. As the outside of the sphere cools and solidifies, the solid part reduces in volume. It is suggested here that the solid part is able to contract away from the remaining liquid at the centre of the sphere. The assumption is made that either the critical hydrostatic tension in the liquid is exceeded or heterogeneous nucleation occurs and a pore will form developing to the size of the liquid deficit. A short freezing range alloy would result in macroporosity and a long freezing range alloy would produce microporosity in the mushy zone on solidification. The method is based upon two equations:- mass and density.

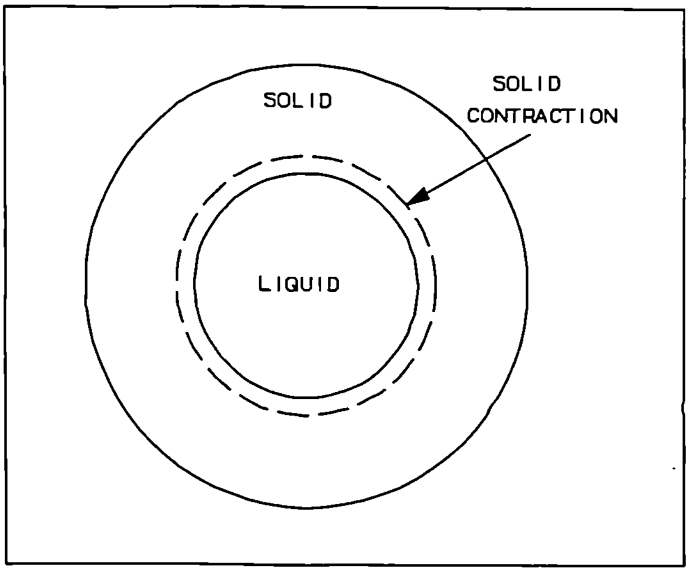

Figure 6.5: Section Through a Solidifying Sphere

The mass of a particular control volume must be the same before and after the deformation has taken place. This results in the mass equation shown as equation 6.1, the left hand side representing the post deformation values and the right hand side the parameter values before deformation.

$$\rho_n A_n \Phi_n = \rho_o A_o \Phi_o \tag{6.1}$$

Where ρ is the density of the element concerned and A the area for the two dimensional case. Φ represents the porosity values of the element. The subscript n represents the new time step values after deformation and subscript o the old time step values before deformation.

The moving of mass from one element to the next is not allowed. At present the effect of gravity and fluid flow to feed an element are not included. Porosity formed in one element is unable to move to another element.

The second equation concerns the density of the elements. If porosity is present in a liquid element then the density of the element is a function of the void density and the liquid metal density, as shown in equation 6.2.

$$\rho_n = \Phi_n \rho_m + (1-\Phi_n)\rho_v \tag{6.2}$$

Where m represents the material properties and v the void properties, the void density in this case is assumed to be that of air. The density of the liquid metal is kept constant though the solidified metal does vary in density, due to programming constraints.

The two equations can be combined and rearranged solving for the latest porosity values, which results in equation 6.3. The right hand side of equation 6.3 consists of only old previous time step values or known values so therefore the porosity of a particular liquid element can be obtained for the current time step.

$$\Phi_n = \frac{-\rho_v + \sqrt{\rho^2_v + 4(\rho_m - \rho_v)\rho_o \frac{A_o}{A_n}\Phi_o}}{2(\rho_m - \rho_v)} \tag{6.3}$$

The porosity variable Φ, because of the nature of equation 6.2, can only take values from 0 to 1. A value of 1 in any particular element indicates the element is solid and no porosity is present, a value of 0 indicates that the element is completely void of material. The porosity calculation using equation 6.3 only occurs in an element that is not solid, as in any solid element it is assumed that the porosity will not alter. After the porosity calculations have taken place the density of the element is altered to take into account the amount of porosity present.

This method takes advantage of the deformation calculation of the coupled heat transfer stress strain code. If the solid expands rather than contracts the process of porosity formation can be reversed. The porosity algorithm has been included into the coupled code as shown in Figure 6.6.

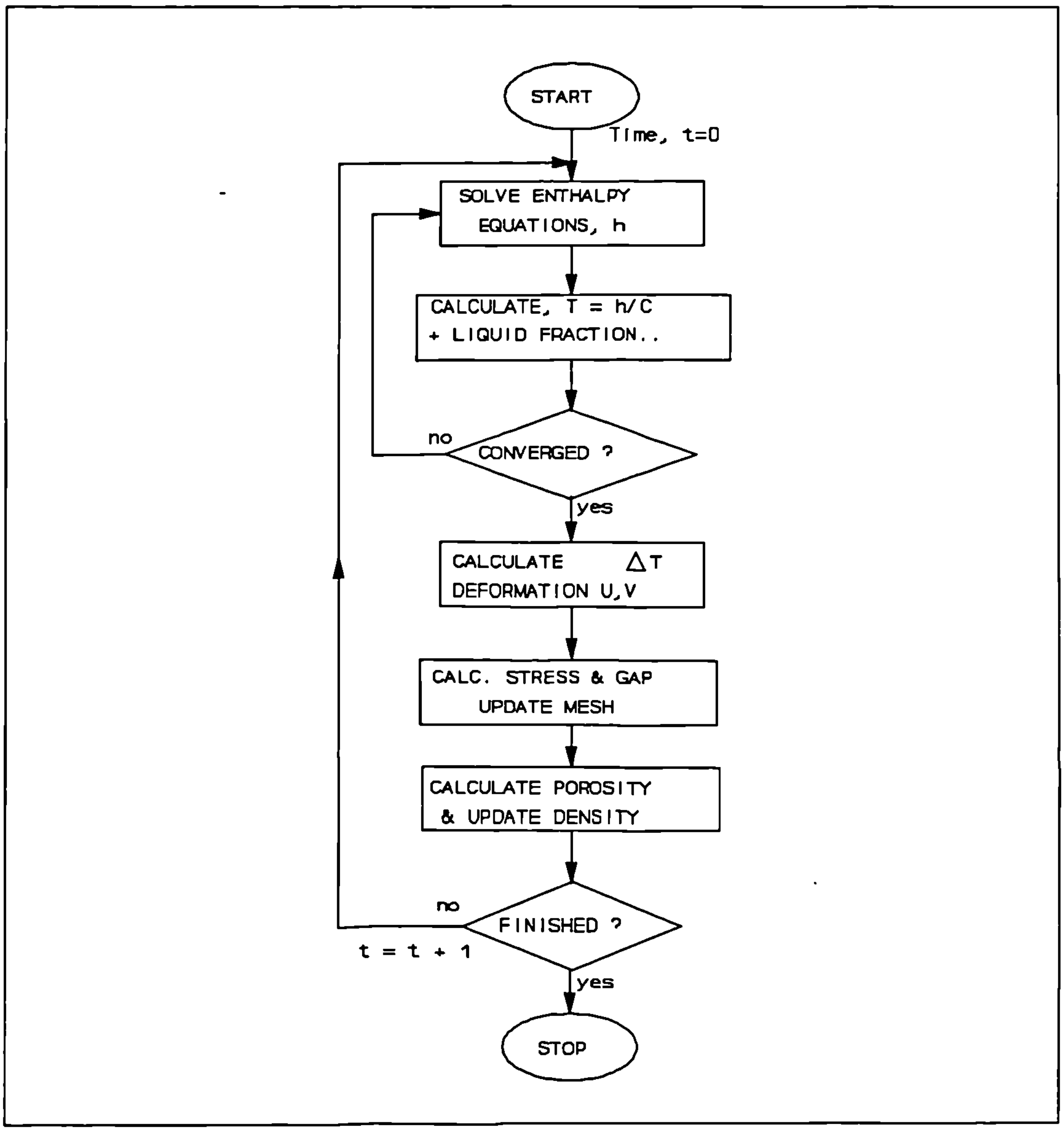

Figure 6.6: Solution Procedure with Porosity Calculations

6.4 Example 1: Simple Liquid Block

This example, though very simple and idealised, was designed as a basic test for the porosity prediction algorithm. It consists of a liquid metal block cooling and solidifying and, rather unrealistically, the block is not restrained anywhere. In effect gravity is not acting on the block. As the outer edges of the block cool and solidify intuition predicts the porosity will form in the centre of the block.

A diagram of the initial liquid metal block is seen in Figure 6.7, with initial dimensions 0.5m by 0.5m. The liquid metal is initially at a temperature of 1000°K and the boundaries in contact with a room temperature of 298°K. The metal has a liquidus and solidus temperature of 950°K, so a pure metal is simulated without a mushy zone.

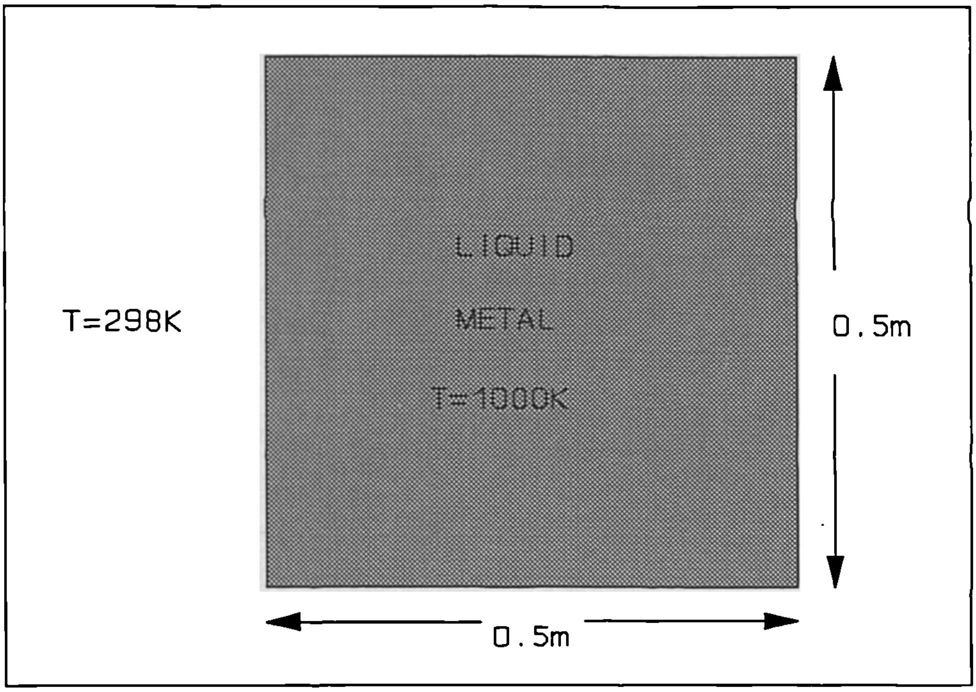

Figure 6.7: Initial Liquid Block

Table 6.1 shows a summary of the material properties used for the metal block. The value for the coefficient of thermal expansion has been increased so that clearly visible displacements will be produced as the block deforms.

Conductivity (W/m°K)	75
Specific Heat (J/kg°K)	500
Density (kg/m^3)	7,000
Latent Heat Coefficient	312,600
Poisson's Ratio	0.29
Young's Modulus	21x10^{10}
Coefficient of Thermal Expansion	0.001

Table 6.1: Pure Metal Material Properties

The mesh used for the liquid metal block is shown in Figure 6.8. The mesh consists of 625 quadrilateral elements of equal size and 676 nodes.

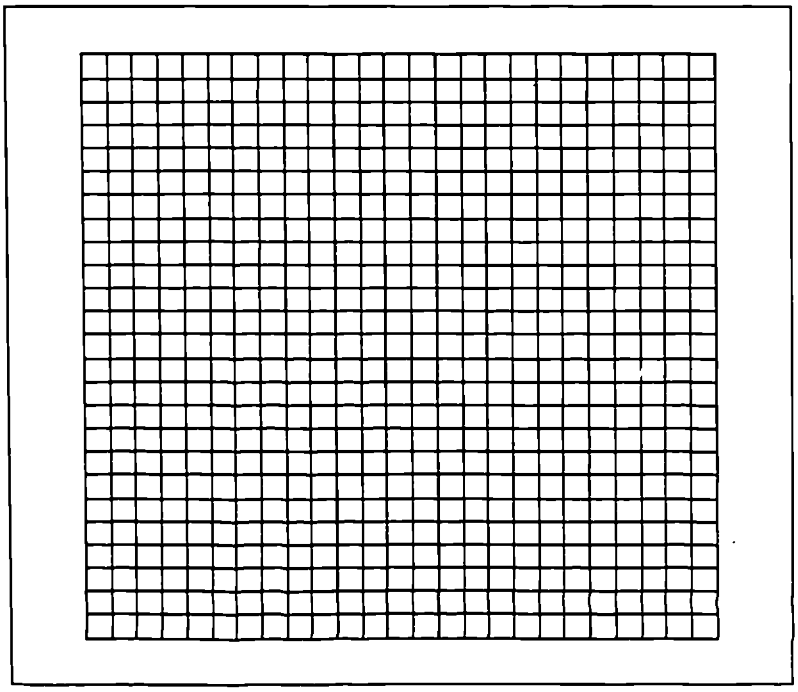

Figure 6.8: Initial Block Mesh

Using the coupled heat transfer and deformation code with the porosity algorithm, the liquid metal block was allowed to cool and solidify. Intermediate results, when the block is still partially liquid, can be seen in Figure 6.9.

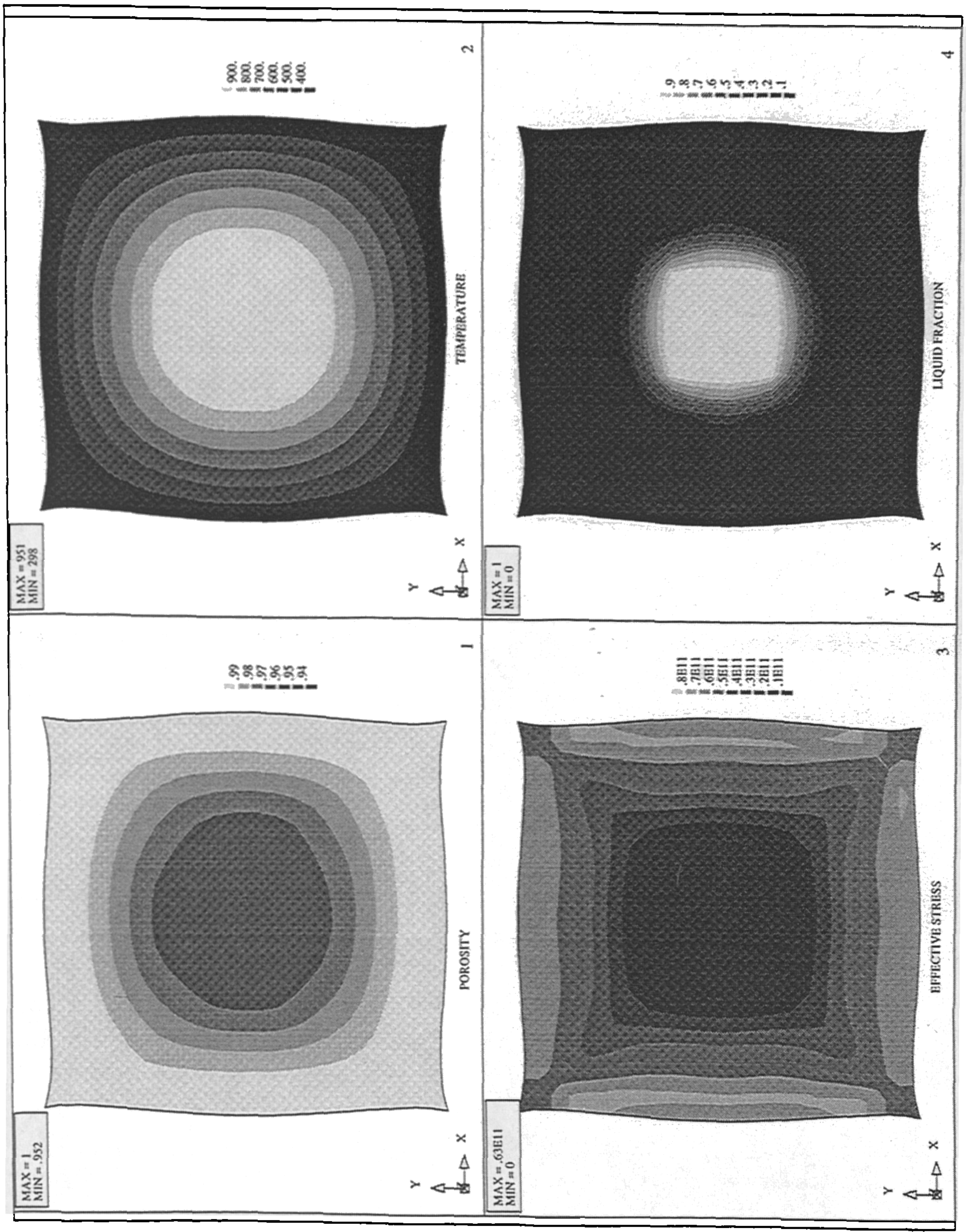

Figure 6.9: Block - Intermediate Results

Figure 6.9 displays, the temperature, liquid fraction, effective stress and porosity of the block, a few of the results available at any time step with the coupled code. The liquid fraction indicates the outer edges of the block have solidified leaving a liquid centre, which is consistent with the temperature distribution shown. The effective stress results show large values as a result of the elastic assumptions in the coupled code at present. The porosity results show the porosity is forming in the centre of the block where the block is still liquid. As there is no gravity acting on the block or fluid feeding effects, the porosity forms throughout the centre of the block. For the macroporosity that is expected of a pure metal, if gravity was present with feeding, the porosity would form nearer the top of the block.

The final porosity results, once the block has completely solidified, are shown in Figure 6.10. The maximum levels of porosity are obtained at the centre of the block where Φ has a minimum value of 0.936. Where a porosity value of an element is 1, this indicates the element is sound and no porosity is present. The porosity results are as expected from the porosity algorithm for such an example.

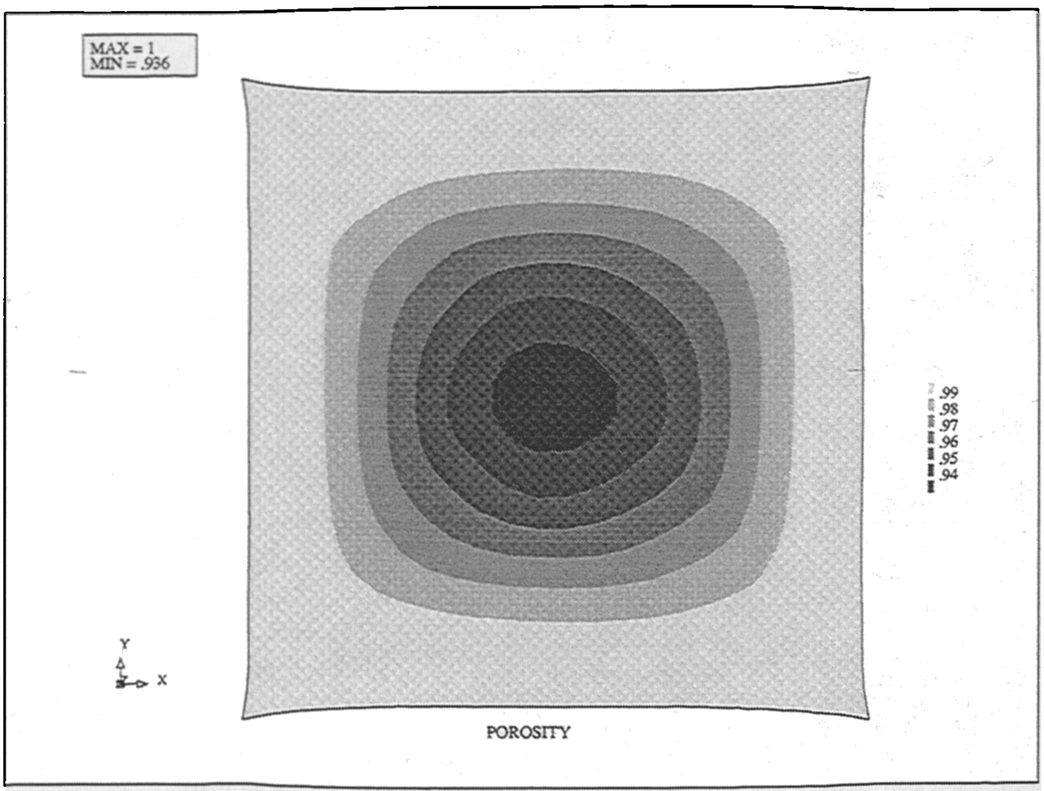

Figure 6.10: Block - Final Results

6.5 Example 2: L-Shape Problem

The geometry used for this example is section through an l-shape type casting with two feeders. The symmetry of the problem means that only half of the casting need be considered. The casting was designed taking into account none of the six rules of feeding [Campbell (1991)], so it is a suitable example for the porosity prediction algorithm. The casting section is seen in Figure 6.11 as a block 1m by 1m. The left hand boundary representing the symmetry plane.

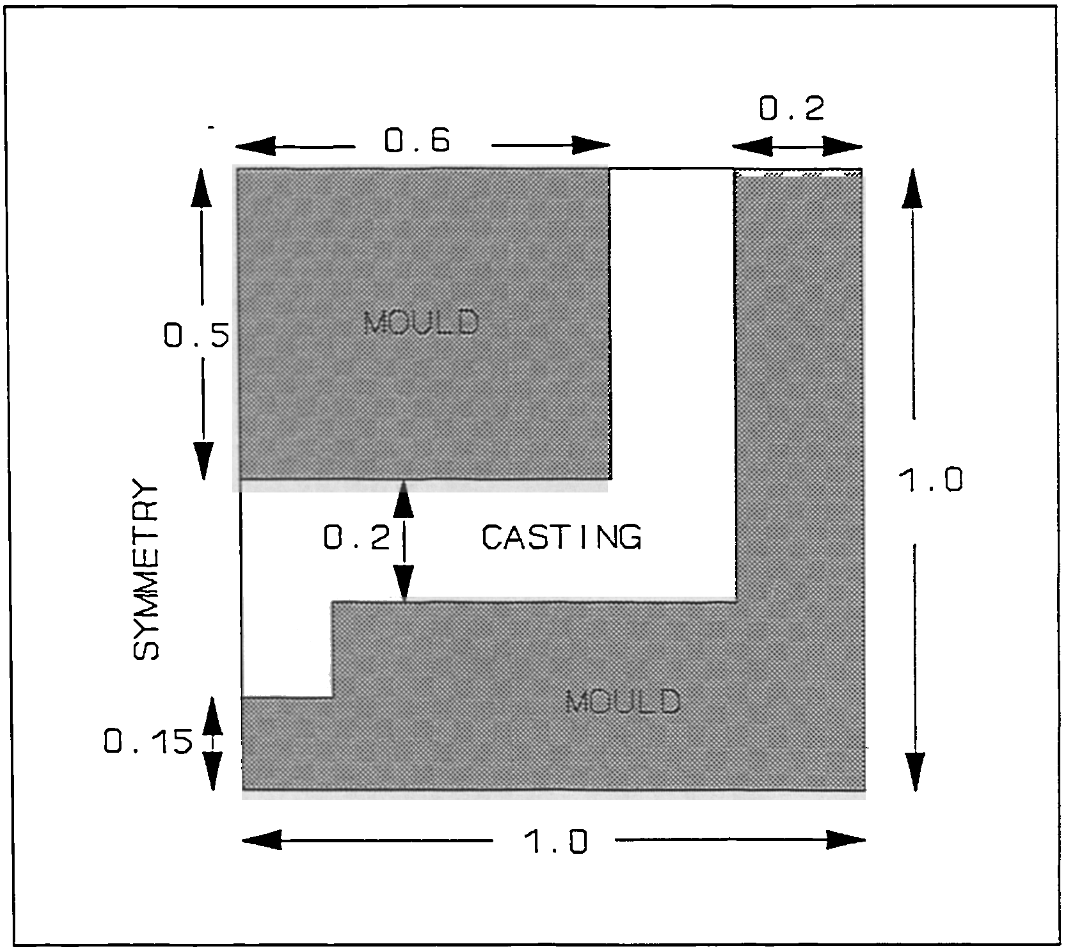

Figure 6.11: L-Shape - Initial Conditions

The liquid metal has an initial temperature of 1000°K and the mould a temperature of 298°K. The mould, though present, in this example only acts as a restriction to the casting. As the mould is completely rigid it defines where the casting can deform to.

The boundary at the top of the feeder is insulated, so heat is lost through the wall of the casting and the top of the feeder. The material properties for the metal are the same as for example 6.4 and are shown in Table 6.1. The metal has a liquidus and solidus temperature of 950°K as before. The l-shape mesh shown in Figure 6.12 has 400 elements and 498 nodes, with coincident nodes where the casting boundary meets the mould boundary.

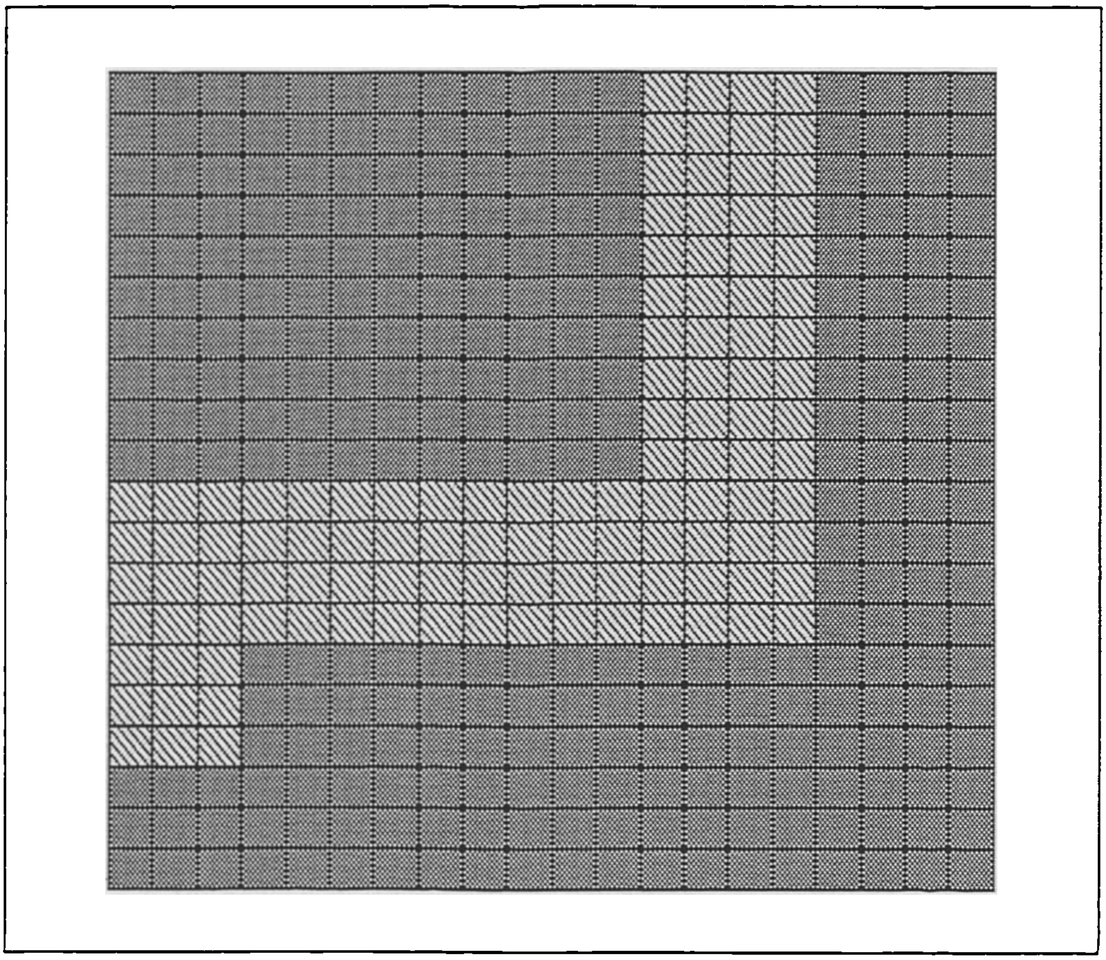

Figure 6.12: L-Shape - Mesh

The solidification and deformation code is used to obtain the porosity results when the l-shape cools. The results for 5, 10 and 16 minutes are displayed in Figures 6.13, 6.14 and 6.15 respectively.

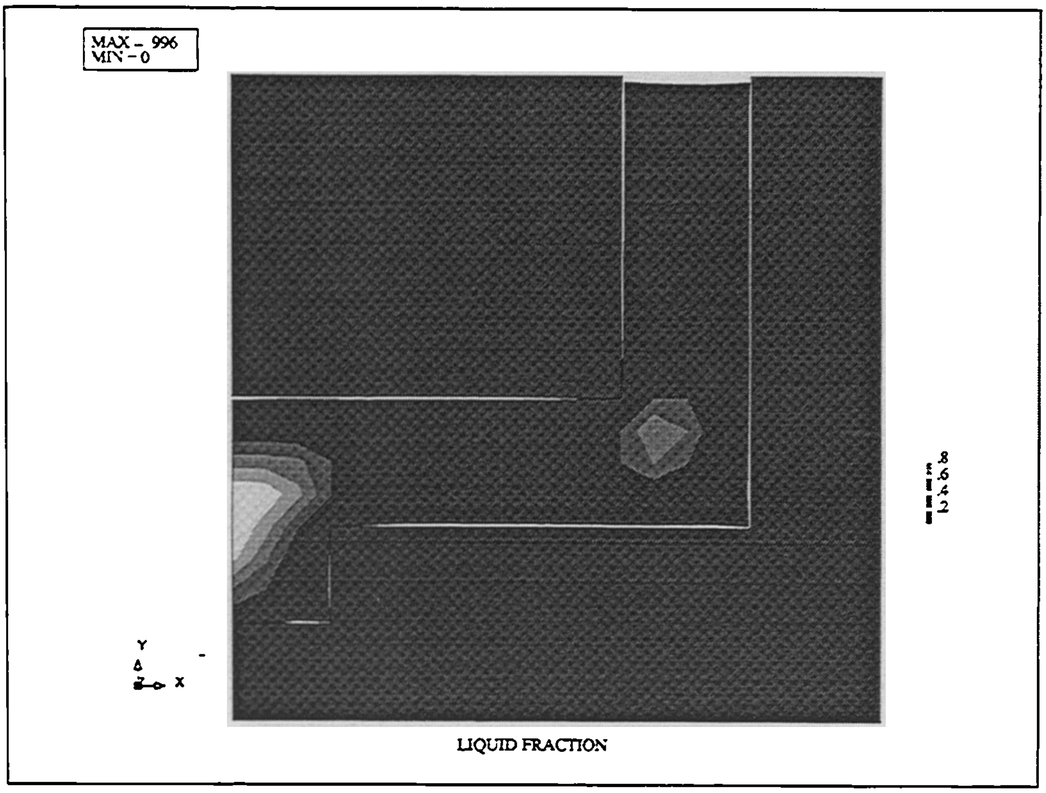

LIQUID FRACTION

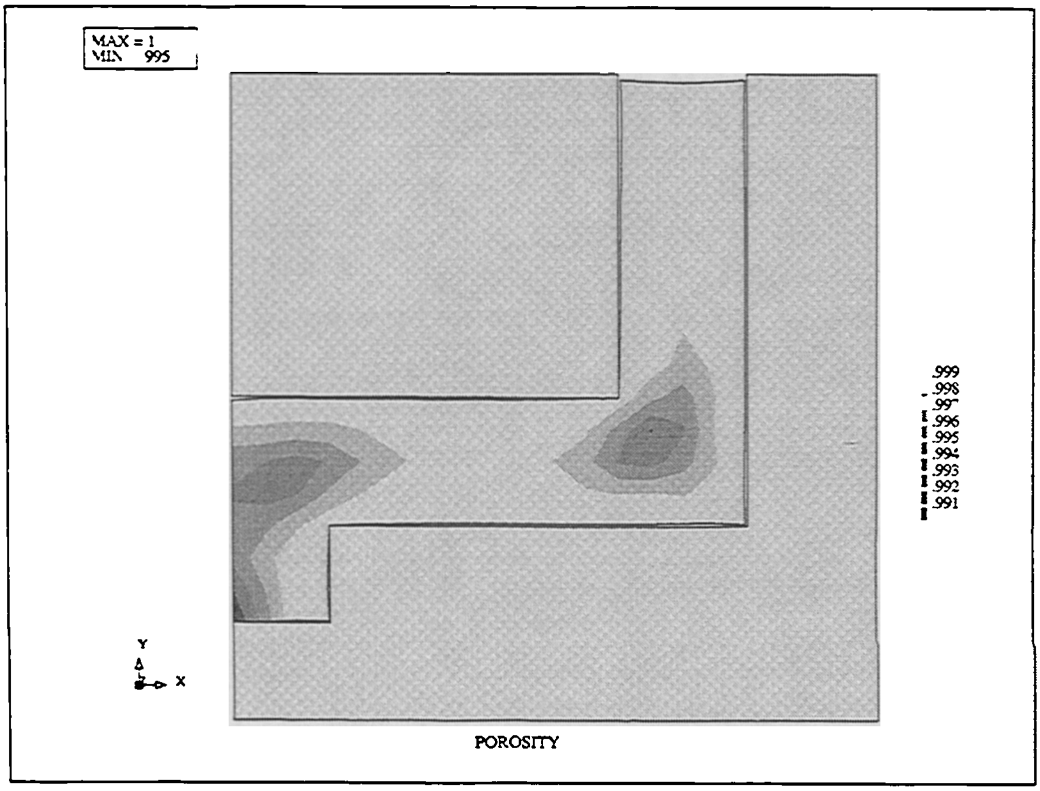

POROSITY

Figure 6.13: L-Shape - Results 5 Minutes

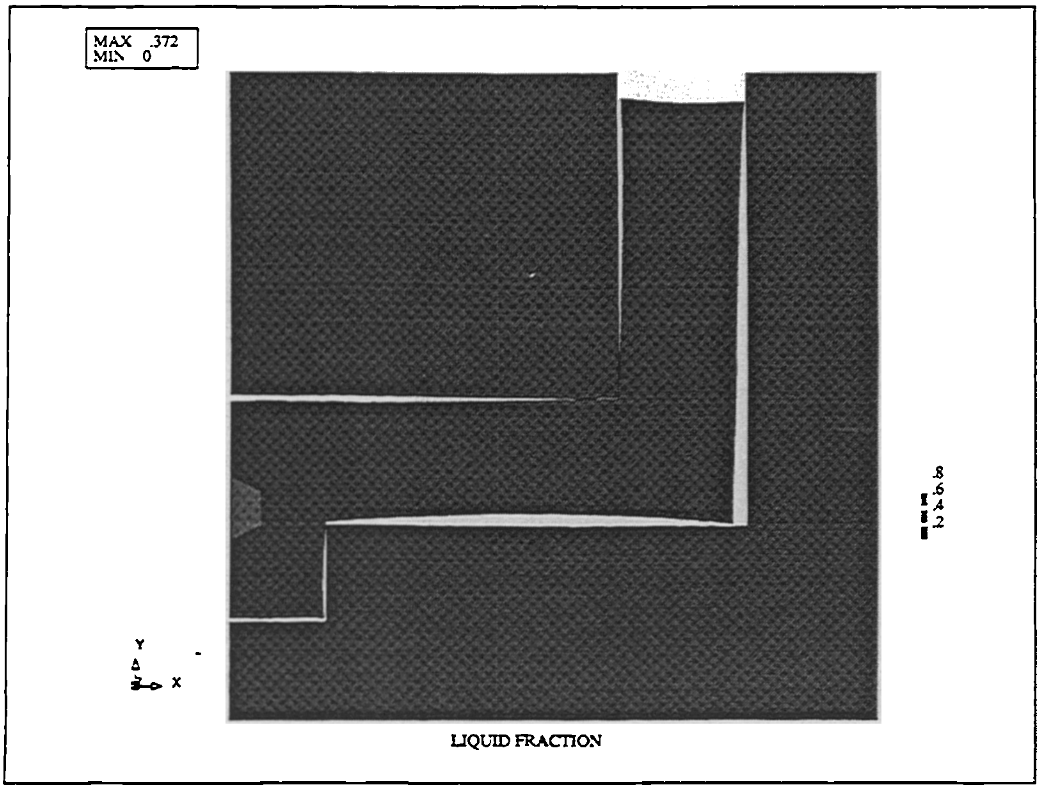

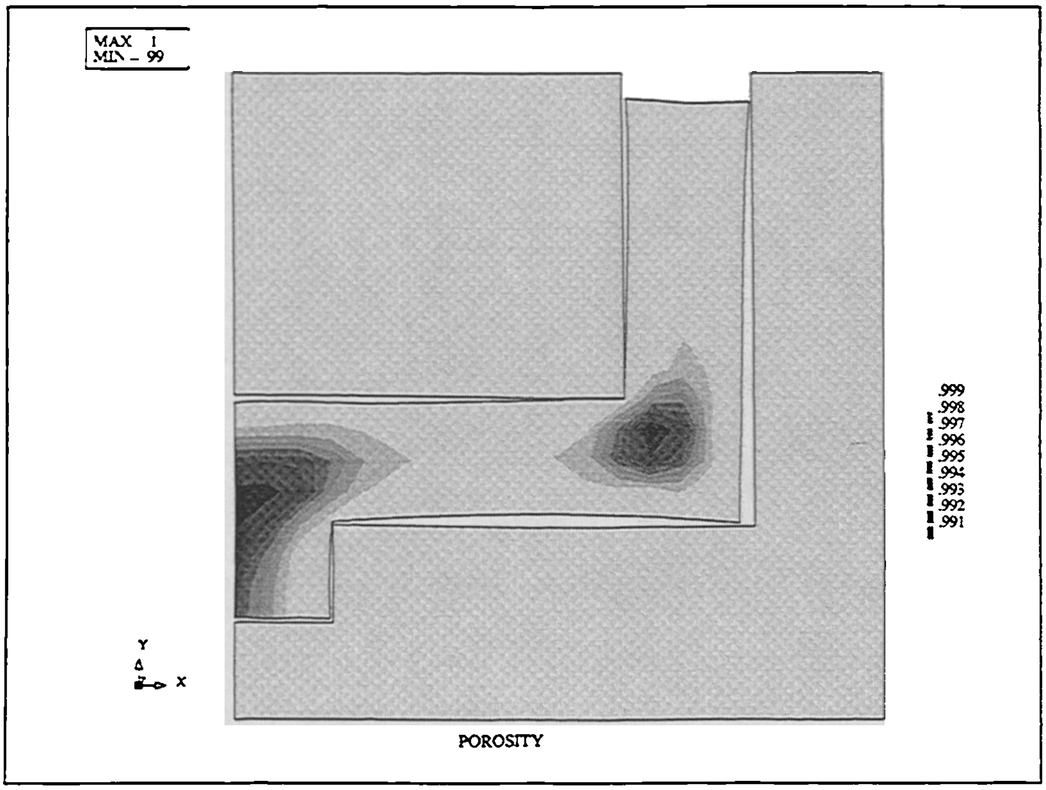

Figure 6.14: L-Shape - Results 10 Minutes

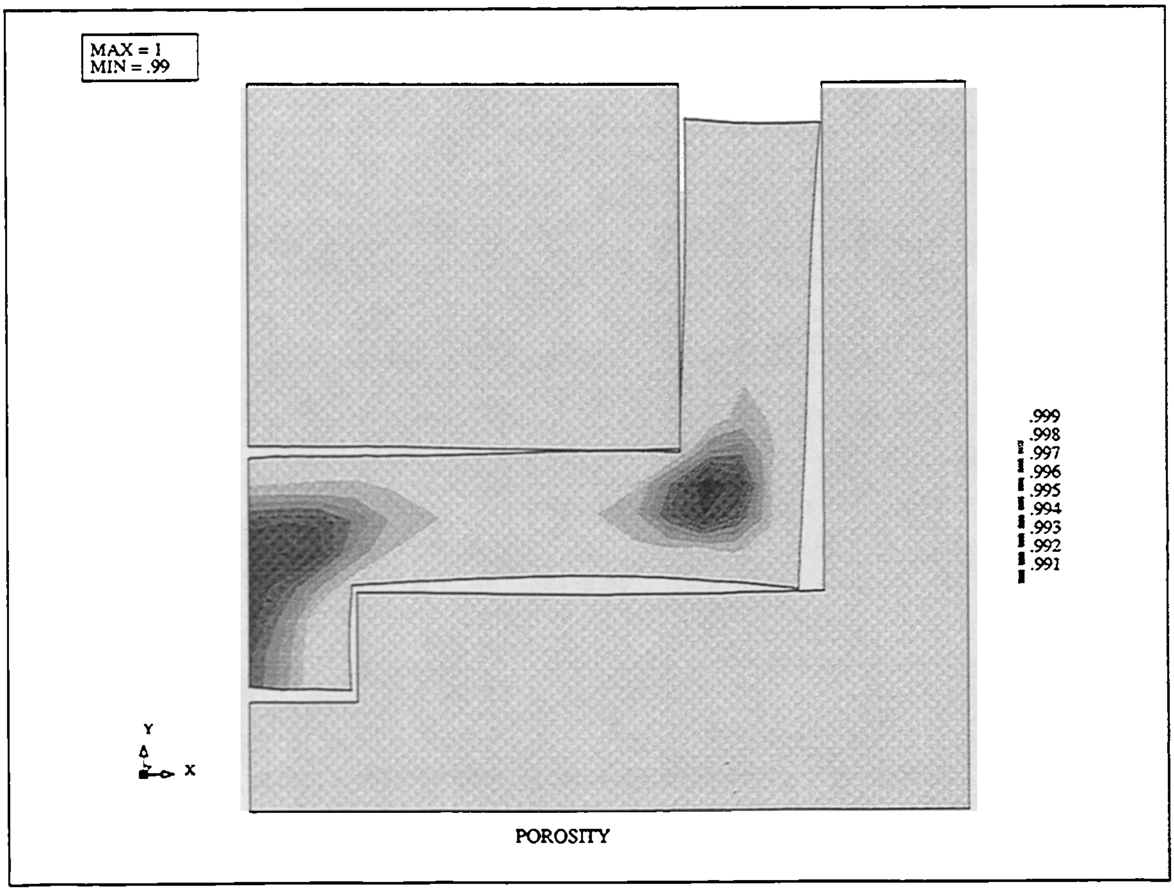

Figure 6.15: L-Shape - Final Results

Figure 6.13 shows the liquid fraction results and the porosity results after the l-shape has been solidifying for 5 minutes. The skin freezing nature of the metal and poor casting design have resulted in two distinct hot spots. The one at the centre of the casting and the other at the bottom of the feeder, which is where the porosity is forming. After 10 minutes, the results in Figure 6.14 indicate the only remaining liquid is at the centre of the casting and the porosity levels have increased in both hot spot areas. The deformation of the casting from the mould is now clearly visible. When the casting has finally solidified after 16 minutes, as shown in Figure 6.15, the maximum amount of porosity present in any element is 0.99 which translates to 1%. Looking at the casting design, if Chvorinov's modulus method had been applied the porosity predicted would be in the places shown in Figure 6.15 due to the volume-to-area ratio.

6.6 Example 3: Simple Casting

This example is based on an experiment carried out by ABEX Experimental Foundry. The solidification history of the experiment was recorded and compared to computed results using C.A.S.T. (Computer Aided Solidification Technique), a two and three, dimensional code [Walther (1987)]. The computer code C.A.S.T. has been used since the 1970's to gain knowledge of the solidification process. The experiment was intended to be useful to other computer simulation modellers as a benchmark. This problem compares the porosity found in the experimental plate and resulting from the Niyama criterion to the predictions obtained using the method stated in this chapter. The experiment consisted of a low alloy steel plate with a riser at one end. The casting is poured into a mould of silica sand with sodium silicate binder. The experiment also had a zircon blue wash applied to the inside surfaces of the cope and drag.

6.6.1 Problem Specification

The initial experiment was carried out in imperial units as detailed here. The plate was 24 inches long, 8 inches wide and 4 inches high. There was a riser at one end of the plate that had a diameter of 7 inches with a height of 14 inches above the base of the plate. The initial dimensions of the casting and riser are seen in Figure 6.16 side view and Figure 6.17 top view. A sleeve and topping compound were used to insulate the riser from the surrounding media as seen in Figure 6.18.

The ABEX experiment used a steel alloy, but the computer simulations by C.A.S.T. used 1% Cr steel. The thermal properties for the alloy were not easy to obtain so properties for the Cr steel were substituted as these were very similar. The 1% Cr steel properties are used here with the control volume unstructured mesh code and can be seen in Appendix C.1 imperial and metric. The density of the metal was kept constant for the liquid metal unlike in the C.A.S.T. simulation, but the density was allowed to vary in the solid elements. The thermal properties for the moulding sand can also be seen in Appendix C.2. The initial temperature of the steel was 1839°K (3310R) and it had solidus and liquidus temperatures of 1778°K (3200R) and 1744°K (3140R) respectively.

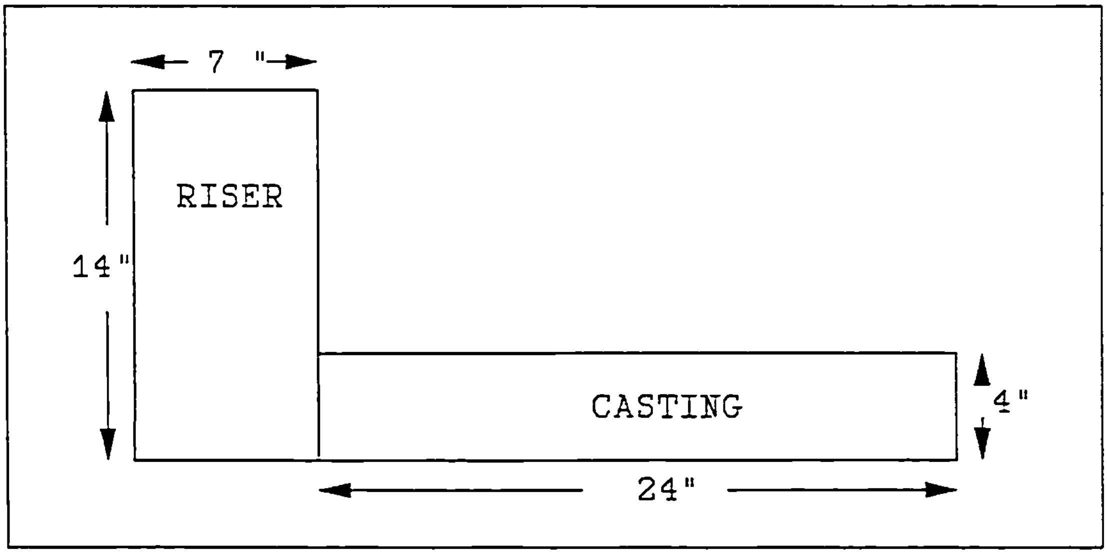

Figure 6.16: Simple Casting - Side View

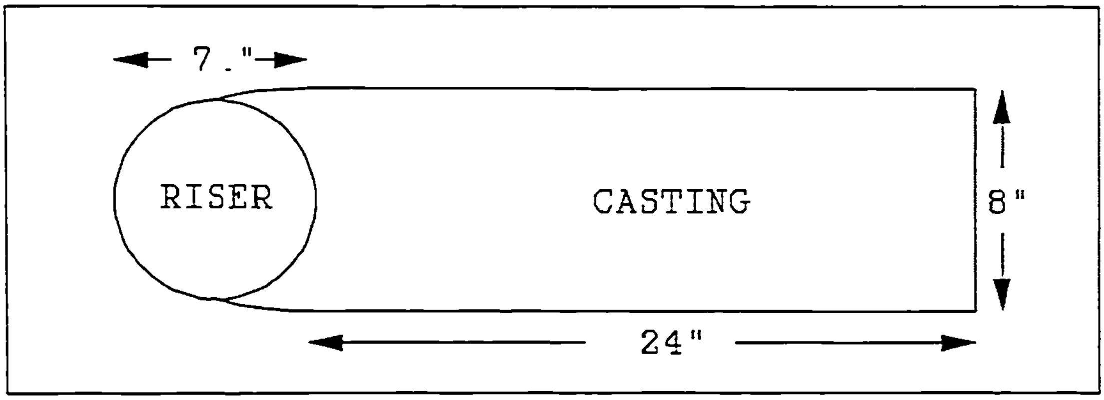

Figure 6.17: Simple Casting - Top View

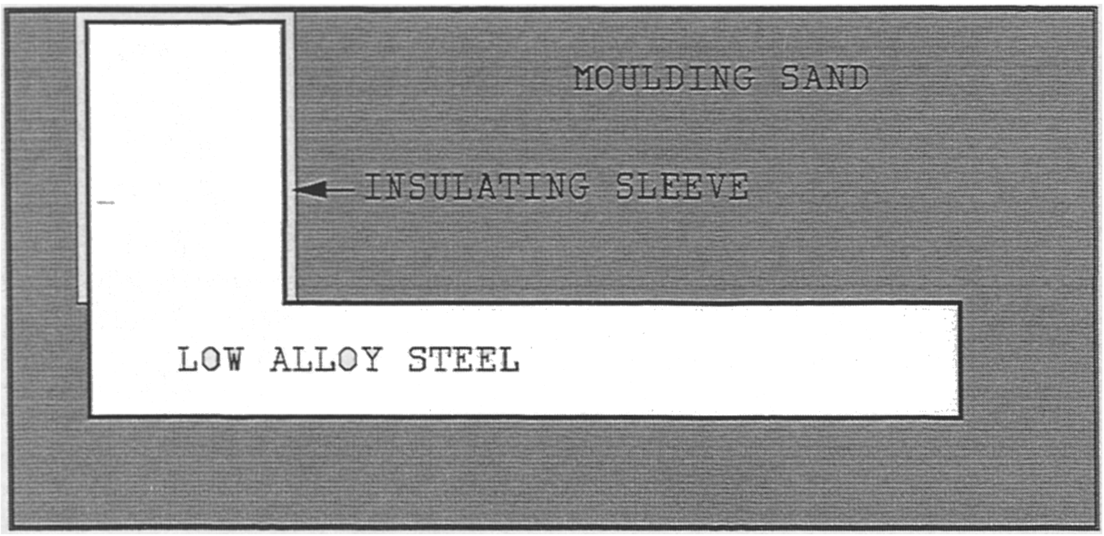

Figure 6.18: Simple Casting - Initial Conditions

The initial temperature of the insulating sleeve and moulding sand was 298°K (540R). For the insulating sleeve and riser topping conductivity, specific heat and density the constant values as used by Walther (1987) were used. These were 0.225 Btu/hr-ft-R, 0.32 Btu/lb-R and 50 lb/ft^3 respectively or in metric 0.3894168 W/mK, 1,339.759 J/kgK and 801 kg/m^3. For the modelling using the coupled solidification and deformation code the steel had a poisson's ratio of 0.29, a Young's modulus of 21x10^{10} and a coefficient of thermal expansion of 0.001. A section through the middle of the casting is used for the simulation. The mesh used to model the casting solidifying is the same as the for the C.A.S.T simulations [Walther (1987)] and is shown in Figure 6.19.

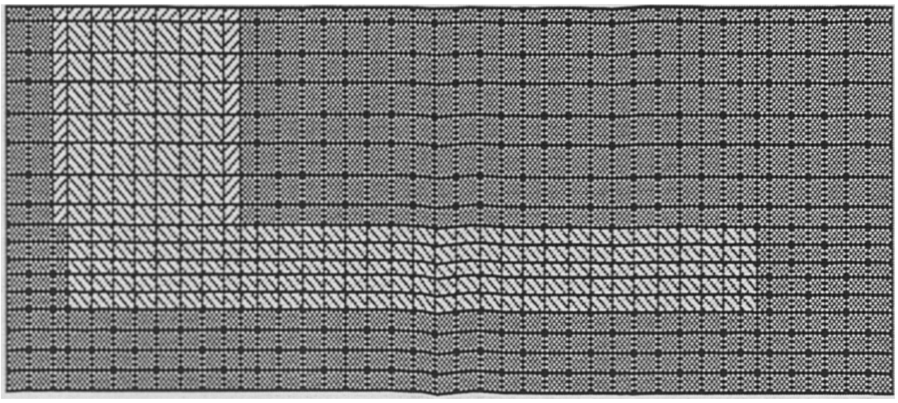

Figure 6.19: Simple Casting - Initial Mesh

The mesh has 714 elements, 23 for the insulating sleeve, 209 for the casting and the remaining 482 for the mould. There are 872 nodes in use, with coincident nodes where the casting boundary meets either the mould or the insulating sleeve. The heat transfer coefficient at the interface is dependent on the gap distance as in Chapter 5. As the casting cools the heat is dissipated through the surrounding mould and sleeve.

6.6.2 Experimental Results

From the ABEX experiment, the casting produced centreline shrinkage as indicated by the black dots along the plate shown in Figure 6.20. The C.A.S.T. program was also used with the Niyama criterion to produce porosity predictions, as shown in Figure 6.21. The C.A.S.T. predictions graded the porosity in three levels:- minor, moderate and major.

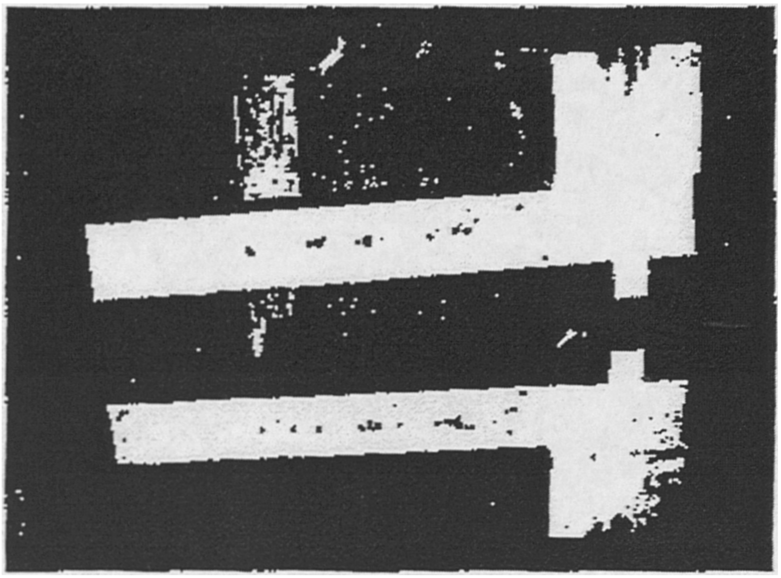

Figure 6.20: ABEX Experimental Results [Walther (1987)]

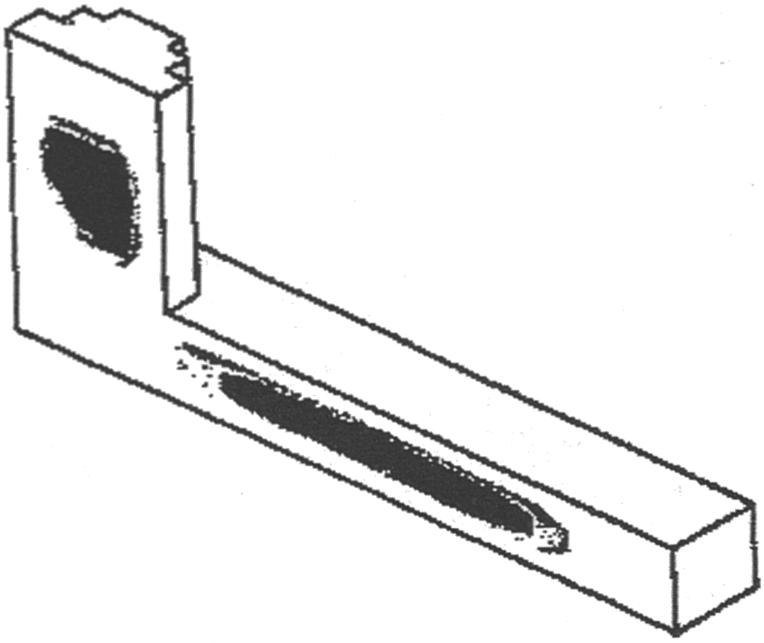

Figure 6.21: C.A.S.T. Porosity Predictions [Walther (1987)]

Generally if the Niyama criterion produced a porosity value of 1 then that particular element was said to be sound for this alloy. Figure 6.21 also shows the centreline porosity predictions. The darker regions being the areas of 'major' porosity and the areas encircling these the 'moderate' porosity.

6.6.3 UIFS Results

The casting solidification was simulated using the coupled solidification and deformation code. Various results were collected whilst the plate was solidifying.

Figure 6.22 show the liquid fraction results and porosity results after 20 minutes solidification time. From the liquid fraction results it is clear that most of the casting has now solidified, so progressive freezing is apparent. The porosity results indicate the development of centreline shrinkage along the plate.

After 40 minutes solidification time one small corner of the casting is still not completely solid, as shown in Figure 6.23. Further porosity formation has taken place in the plate nearer the join of the casting to the feeder and there is porosity predicted along the feeder edge.

The final results when the whole casting and feeder are solid, one hour and 20 minutes into the simulation, are shown in Figure 6.24. The porosity pattern has changed very little form the results at 40 minutes shown in Figure 6.23. A noticeable feature is the sub-surface porosity near the feeder in the casting section.

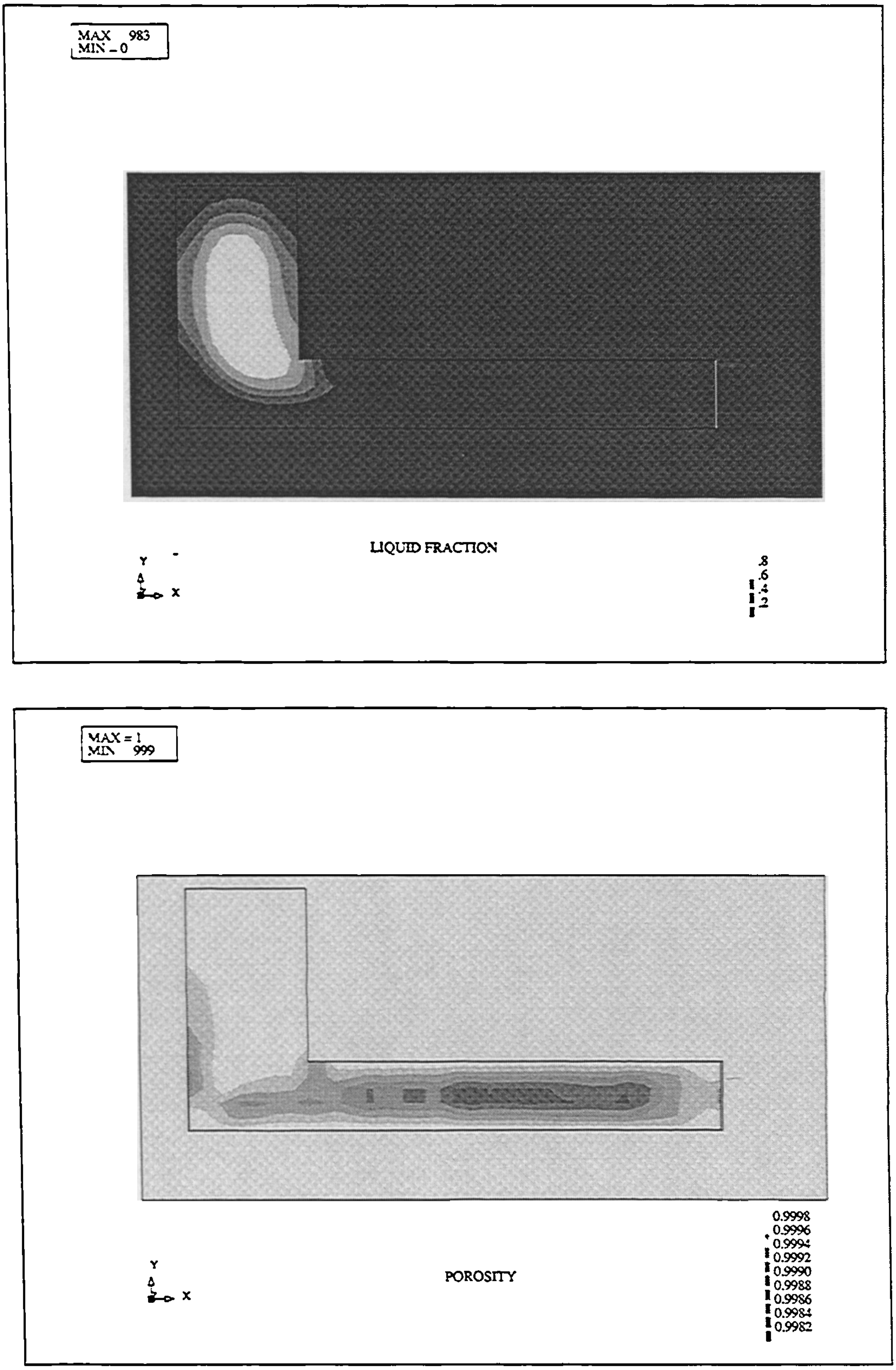

Figure 6.22: Simple Casting - Results 20 Minutes

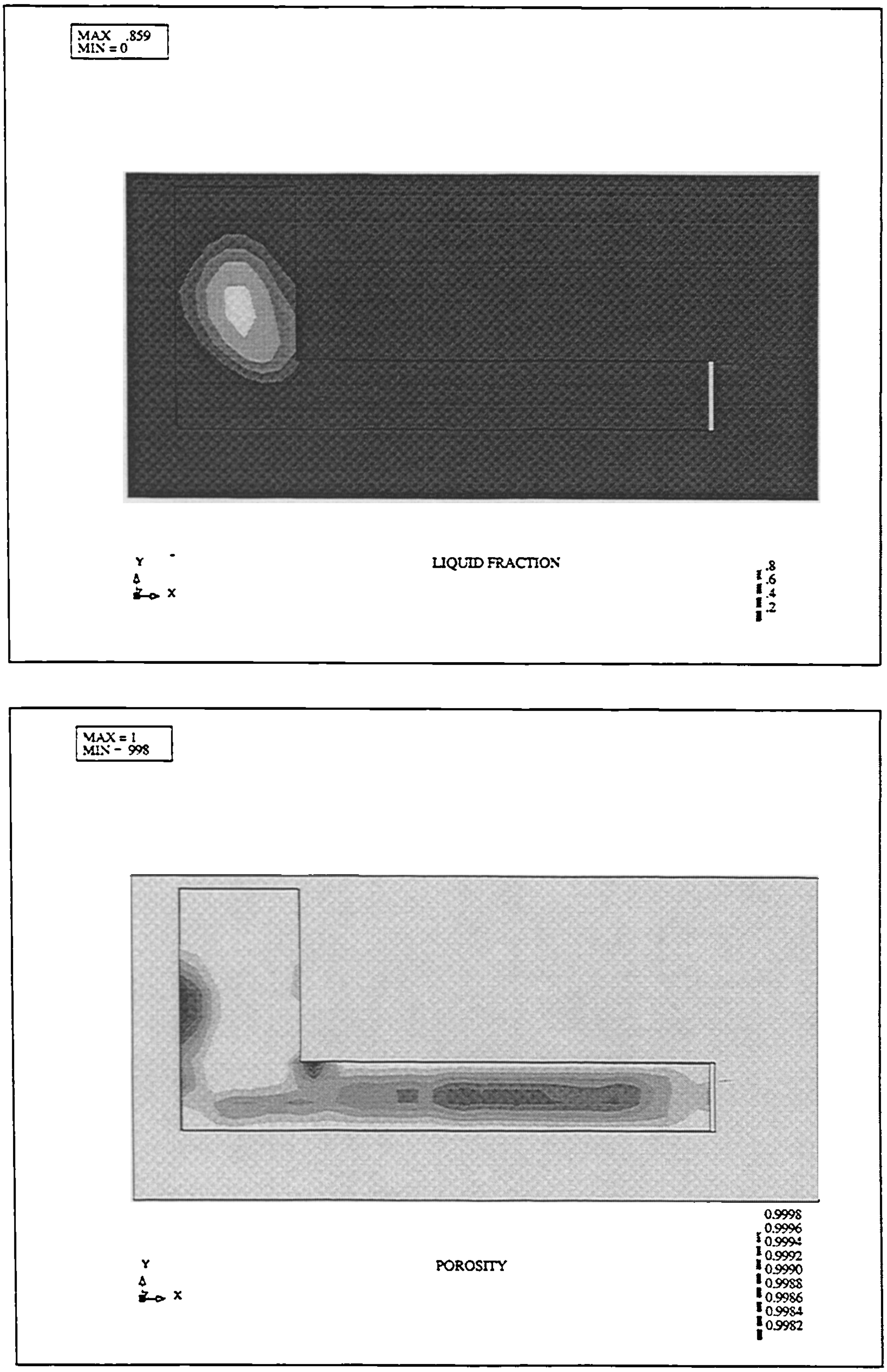

Figure 6.23: Simple Casting - Results 40 Minutes

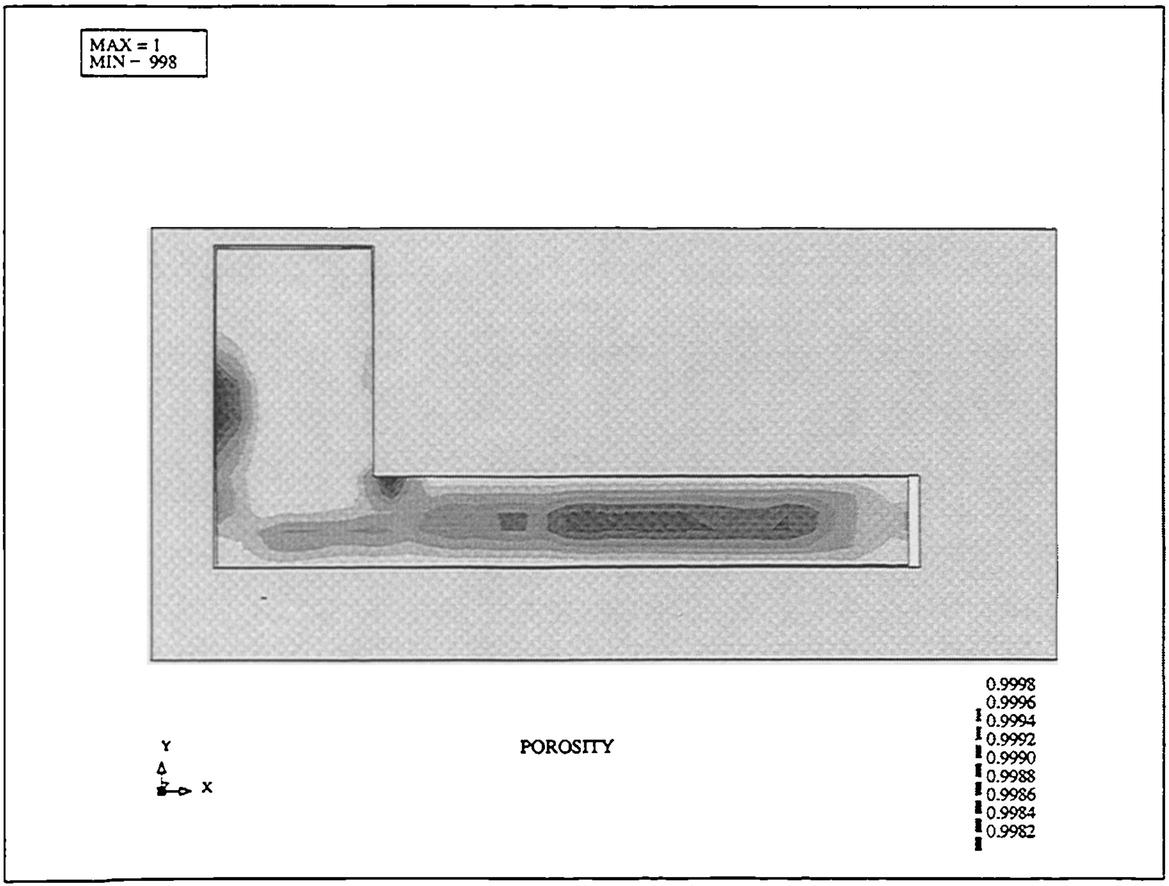

Figure 6.24: Simple Casting - Final Results

6.6.4 Comparison of Results

The control volume unstructured mesh predictions look very similar to the experimental results. The prediction of centreline shrinkage in the casting is seen to agree with the experiment and the Niyama C.A.S.T. predictions. The control volume unstructured mesh porosity results also predict sub-surface porosity where the casting meets the feeder, this agrees with the experimental observations shown in Figure 6.20, whereas the C.A.S.T. predictions are limited to predicting the centreline shrinkage in the casting and feeder.

6.7 Example 4: Stepped Casting

The test casting was obtained courtesy of Stones Foundry. The alloy used was aluminium 4.5% copper and it was cast into a resin bonded sand. The casting had been designed by Keith Preddy at Stones Foundry to follow all rules of feeding. Essentially freeing the resulting casting from macroporosity. At the time of pour into the casting the molten metal had a temperature of 720°C and was free from hydrogen so reducing the effect of gas porosity in the final casting. A thermocouple installed in the feeder head showed that the temperature of the metal after pouring was 700°C. The final casting should be free from macroporosity and have generally dispersed microporosity.

6.7.1 Problem Specification

The stepped casting comprises of four steps and on the highest a feeder is positioned. The feeder is six inches high and the biggest step two inches high. The following three steps are half the height of the preceding step, so that the final step is 1/4 inch high. The side view of the step wedge is shown in Figure 6.25, and the top view Figure 6.26.

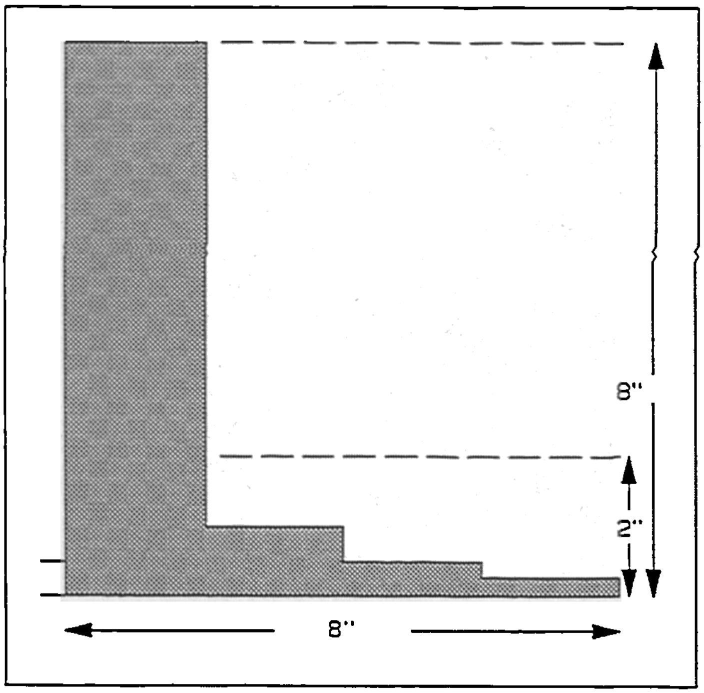

Figure 6.25: Step Wedge - Side View

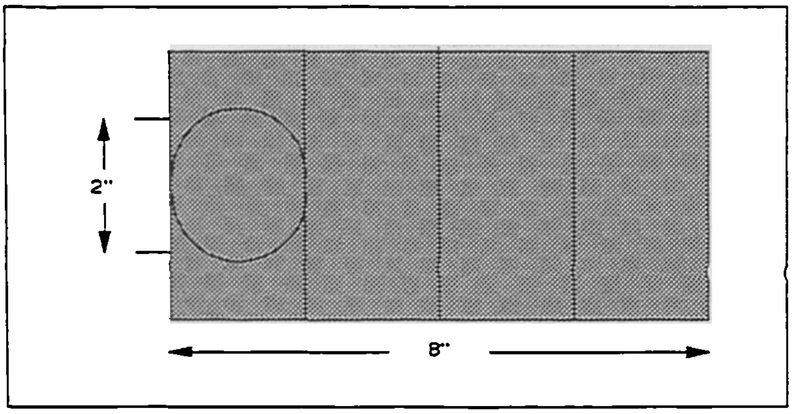

Figure 6.26: Step Wedge - Top View

The ingate is positioned at the back of the step wedge at the feeder end and is 2 inches wide and 0.5 inches high. The wedge has a width of 4 inches. A section through the centre of the step wedge is shown in Figure 6.27 along with the mould.

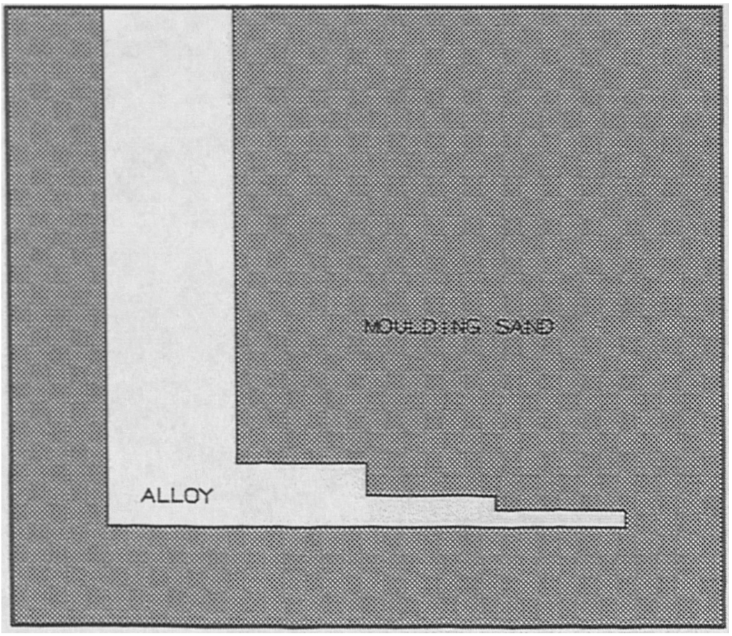

Figure 6.27: Step Wedge - 2-D Slice

The mesh used for the computer simulation is shown in Figure 6.28, it has 4352 elements of varying sizes. There are 4656 nodes including the coincident nodes used at the mould/metal interface boundary to allow the casting to deform away from the mould

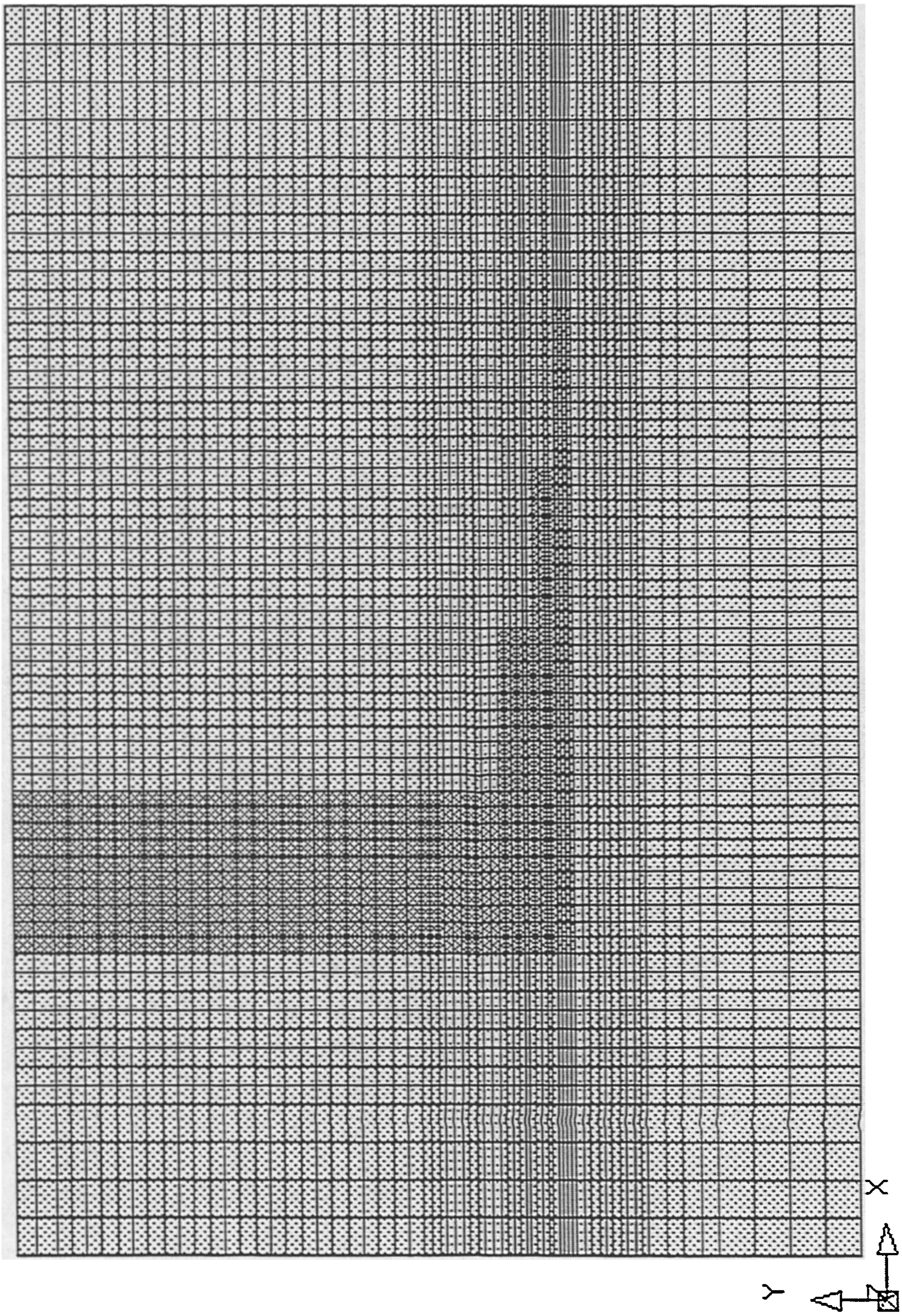

Figure 6.28: Step Wedge - Initial Mesh

during cooling. The heat transfer coefficient is altered according to the gap distance of adjoining elements on the mould/metal interface as in chapter 5.

For the material properties of the moulding sand and the alloy simplified constant values were used as shown in Table 6.2, where the thermal properties are for the premium casting alloy A357 (L169), aluminium, 7% silicon and 0.6% magnesium [Moosbrugger and Berry (1986)] and typical elastic values are used.

	Moulding Sand	Alloy
Conductivity (W/m°C)	0.84	187.0
Specific Heat Capacity (J/kg°C)	1,120.0	1,050.0
Density (kg/m^3)	1,682.0	2,670.0
Young's Modulus	$21\mathrm{x}10^{10}$	$21\mathrm{x}10^{10}$
Poisson's Ratio	0.0	0.29
Coefficient of Thermal Expansion (°C^{-1})	0.0	0.00012
Latent Heat Coefficient (J/kg)	-	432,600.0
Solidus Temperature (°C)	-	613.0
Liquidus Temperature (°C)	-	660.0
Initial Temperature (°C)	25.0	700.0

Table 6.2: Step Wedge - Thermal and Elastic Properties

6.7.2 Experimental Results

Xrays of the casting showed dispersed microporosity through each of the steps. The casting was then cut in half down the middle and polished. The polished surface revealed random surface pores that viewed through a microscope were visible as microporosity. Photographs of a section of the polished casting are shown in Figures 6.29 and 6.30. The surface pores as visible are pale dots in Figure 6.29. Though the microporosity was generally dispersed, from the general polished casting surface it was clear that a slight band of microporosity stretched from the bottom surface of the casting to the last step.

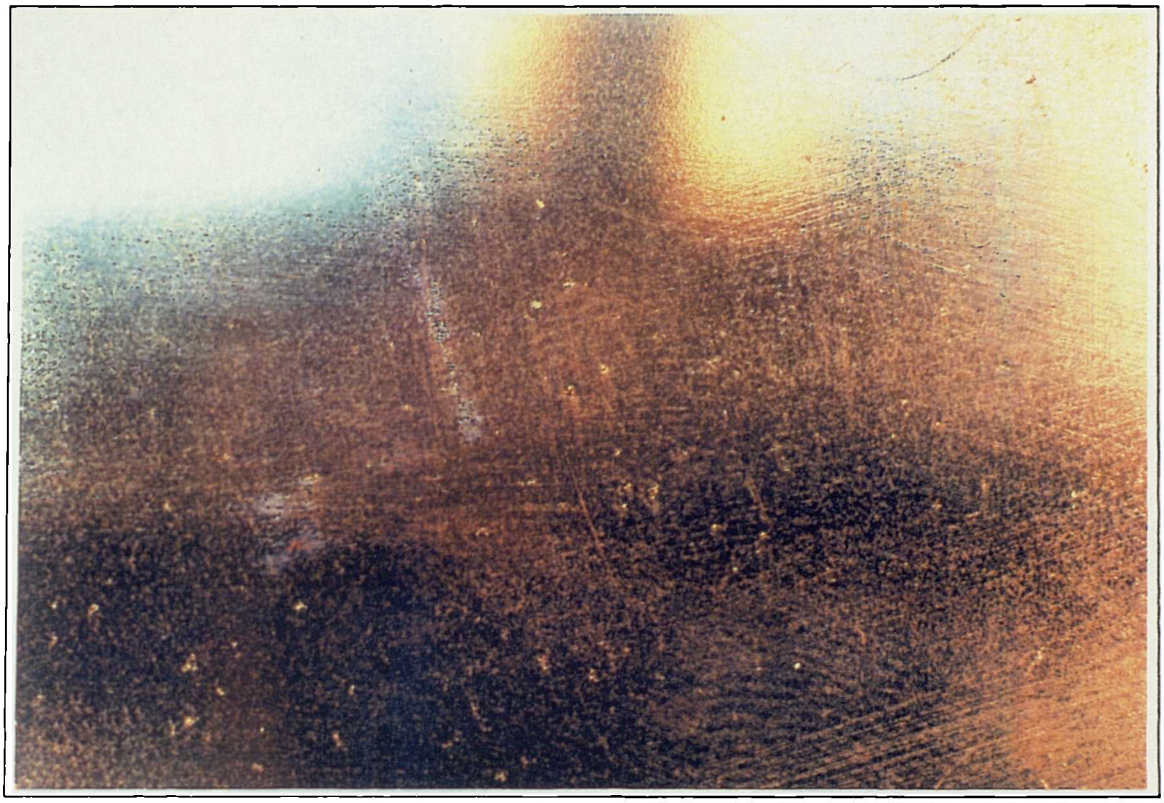

Figure 6.29: Step Polished Surface x 5

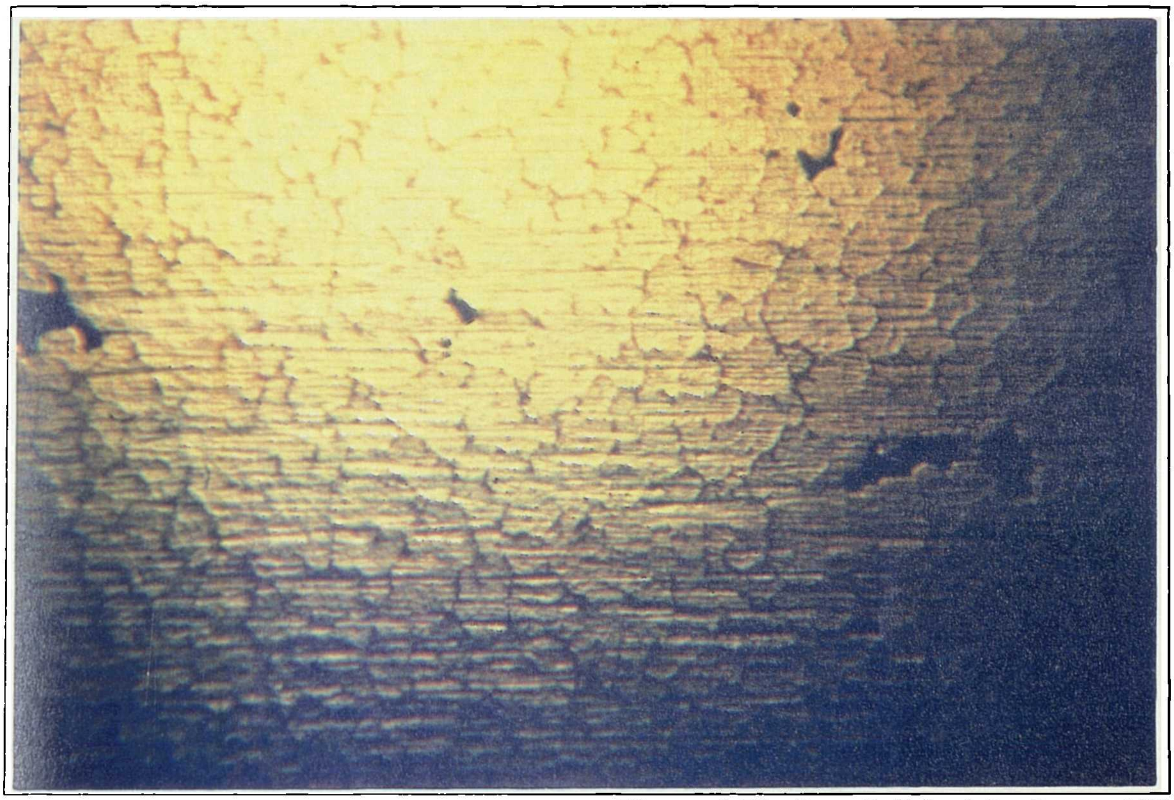

Figure 6.30: Step Polished Surface x 100

6.7.3 UIFS Results

The computer simulation of the step wedge solidification was obtained using the coupled code with the porosity algorithm. After 2 minutes solidification time the two steps furthest from the feeder had already frozen, as seen in Figure 6.31. The liquid fraction results display progressive freezing. The porosity predictions indicate a maximum porosity of 0.999, which corresponds to less than 0.1%, dispersed through the solidified steps.

Figure 6.32 shows the solidification results after 5 minutes when the slight deformation of the end step away from the mould is visible. From the liquid fraction results it is apparent that the third step is now solid as well. The remaining step and feeder are mushy as expected for a freezing alloy. The porosity has now developed further along the wedge. A slight layer appears to have formed, though this still only shows elements with a maximum porosity of 0.2%.

The final solidification of the casting at 16 minutes is shown in Figure 6.33. The maximum porosity in any element still measures no more than 0.2%, 2 in 1000, and there is a slight microporosity visible in the feeder.

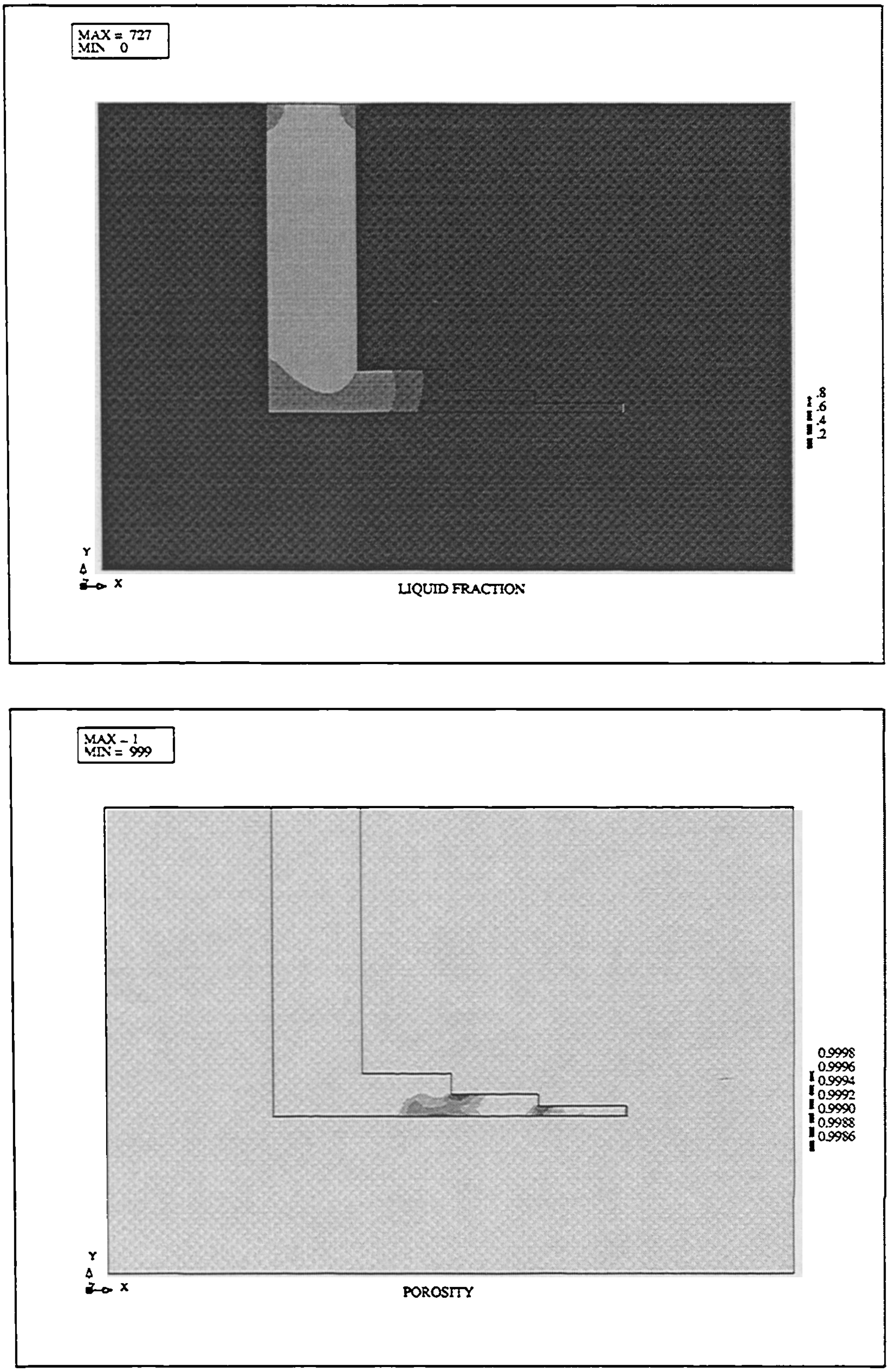

Figure 6.31: Step Wedge - Results 2 Minutes

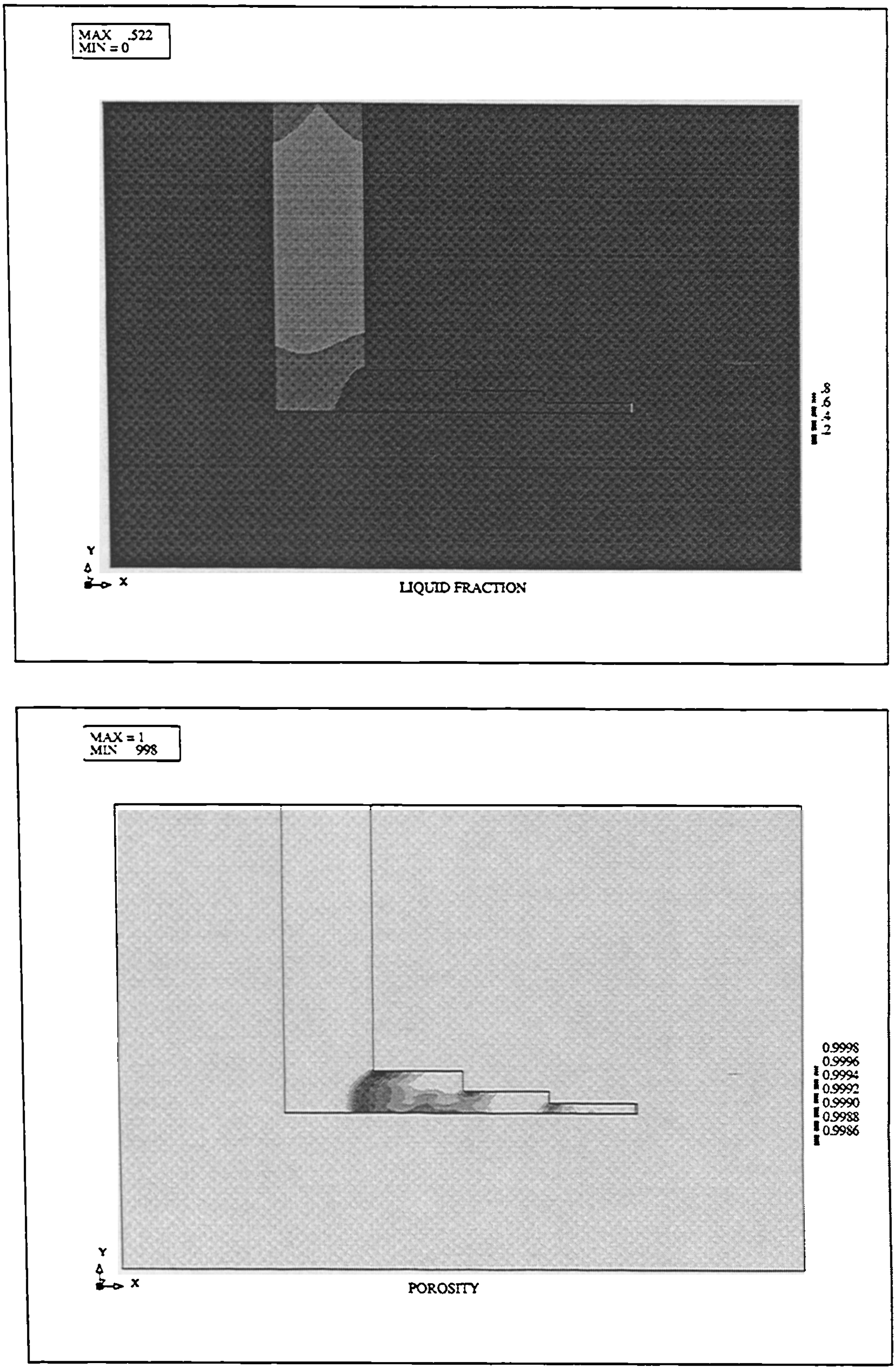

Figure 6.32: Step Wedge - Results 5 Minutes

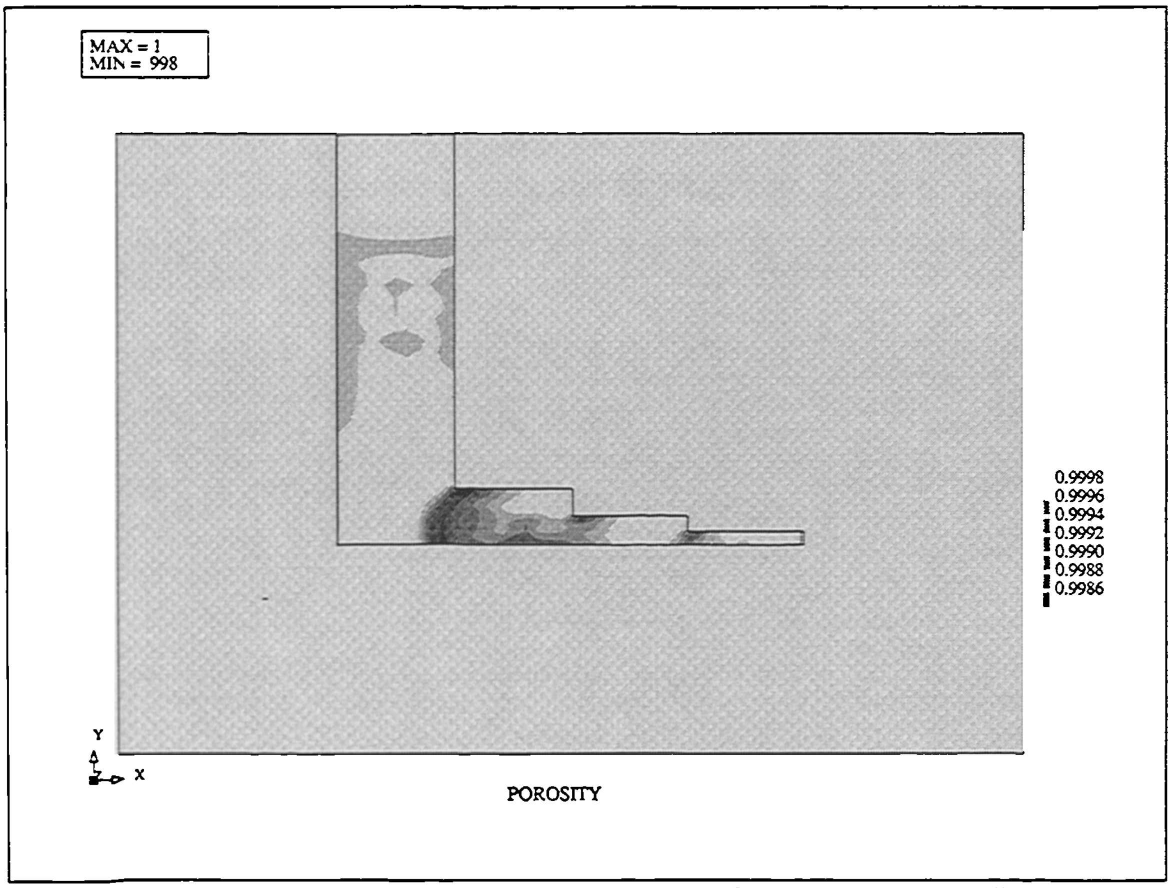

Figure 6.33: Step Wedge - Final Results

6.7.4 Comparison of Results

The porosity predictions obtained for the coupled heat transfer and deformation code do not predict any macroporosity or centreline shrinkage. This is consistent with observing only dispersed microporosity in the casting section. A slight band of microporosity was noticed in both the experimental results and the simulation results, from the bottom of the casting to the top of the casting near the third step. The predictions are very small values which also indicates microshrinkage, so comparing reasonably well to the actual casting.

6.8 Conclusions

The simple porosity model included in the fully coupled solidification and deformation code produces reasonable results. Example 3 in section 6.6 produces porosity predictions of centreline shrinkage in the casting and a small region of sub-surface porosity near the feeder. The results agree very well with the experimental results of Walther (1987) for the problem.

The step wedge casting shows general dispersed porosity which is also indicated in the porosity prediction of the coupled code. The quantity of porosity in any element of the domain is found to be extremely small. The porosity algorithm relies on information concerning the deformation of the casting, whereas most casting software uses the empirical Niyama criterion relying solely on information obtained when the casting solidifies.

The porosity is a very simple technique that can be adapted and modified to include other porosity effects such as gravity and fluid feeding. Further work may entail prediction of the shrinkage pipes formed in feeders as the casting solidifies and the molten metal is drained from the feeder to the casting. Mechanisms for pore nucleation may be looked at in more detail and added to the model.

Gas evolution as a porosity cause is not considered, but at some later stage it may be possible to consider the chemical structure and gas content of the molten metal as it solidifies and how this influences the porosity present in the final casting.

Chapter 7
Conclusion

In Chapter 1 the existing major methods for numerically solving the elastic stress-strain equations were reviewed from a historical point of view. Generally it is concluded that existing software for the deformation process was finite element oriented, with the advantage of solving irregular domains. Boundary elements and finite difference schemes also provide solutions to solid mechanics problems but are not favoured so much by the solid mechanics community for a variety of reasons. The need for a discretisation technique that could couple well with computational fluid mechanics problems lead to the analysis of the suitability of a control volume unstructured mesh approach to the solution of the elastic stress-strain equations. Similar unstructured mesh control volume techniques have successfully been applied to fluid flow and heat transfer problems in the 1980's and more recently to solidification [Chow (1993), Chow and Cross (1992)].

7.1 Control Volume-Unstructured Mesh Deformation Algorithm

The elasticity equations for force conservation, including both thermal and mechanical loading, were discretised in Chapter 2 for the special two-dimensional cases of plane stress and plane strain in cartesian coordinates and axisymmetry in cylindrical polar coordinates. The discretisation technique divides the domain into an unstructured mesh of elements, typically quadrilaterals or triangular elements or both. The control volumes were then formed around the element vertices, completely filling the domain. Shape functions were used to map global to local coordinate geometries, in typical finite element fashion, and finally a set of equations to be solved to obtain the nodal displacements were formed. On solution of the deformation equations just a simple step is then required to obtain the element stresses and strains, followed by the nodal stresses and strains if required.

A general FORTRAN program was written to enable the solution of elastic problems with thermal loads and applied forces, for the instances of plane stress, plane strain and axisymmetry. To increase the speed of the program a conjugate gradient solver with Jacobi preconditioning was used to solve the system of deformation equations. When using the program for solution of a two-dimensional elastic problem, there are options available to alter which include; global residual tolerance, relaxation parameter, maximum number of global iterations and whether the problem to be solved is one of plane stress, plane strain or axisymmetry. The other information required by the program such as nodal coordinate points, element arrangement, boundary conditions, material properties and initial conditions are read into the program from various data files.

The displacement and stress results were collected for a selection of problems in Chapter 3, for various residual tolerances, relaxation parameters values, mesh types and mesh refinements. The rectangular domain problems of the cantilever and thermal beam, as described in sections 3.1 and 3.2 are found to be more suited to quadrilateral meshes than triangular meshes. The control volume unstructured mesh problem agrees totally with the finite element results for the multi-material problem in section 3.3. The nodal stresses produced in the hole problem in section 3.4 are very close to the analytical solution with this problem being more suited to a triangular mesh. The axisymmetric problems of section 3.5 and 3.6 produce displacements that agree very closely to a standard finite element program results, the analytical solution and for section 3.6 existing boundary integral equation results.

The time taken to obtain the results was approximately twice the time taken by the finite element program, even when the most efficient relaxation parameter was used. Further work could involve inclusion of a routine for generation of the optimum relaxation parameter to use. With modifications to the two-dimensional stress-strain code, such as an improved solver and better structuring of the code it is thought the time taken to generate results could improve, but whether it could equal the time of the standard finite element code is uncertain. To decrease the computational time taken further parallel processing and vectorisation offer an inexpensive option.

The extension of the algorithm to three-dimensions can be accomplished, a necessity for objects that cannot be approximated by the two-dimensional special cases of plane stress, plane strain and axisymmetry. Work is currently under way at the University developing a three-dimensional stress-strain code based on the control volume unstructured mesh technique.

At present purely elastic objects have been considered by the two-dimensional stress-strain code, there is a need to include non-linear stress-strain relationships. Chapter 4 details the inclusion of a friction algorithm in the stress-strain code, for non-linear boundary conditions. The example problem results give reasonable answers though the convergence of the control volume unstructured mesh algorithm is not achieved. Although the solution does not converge it does not diverge either. From existing numerical methods often using the finite element method it is seen in section 4.1.3 that this is often a problem with friction routines. A method for combatting the non-convergence problem needs to be implemented. At present a simple contact condition is invoked with the friction boundary condition, future work should include a general contact algorithm that allows for extension to three-dimensions, as contact theory and friction are often synonymous. There is current work in the department for two-dimensional and three-dimensional contact algorithms that can transfer the forces between domain boundaries as necessary.

7.2 The Casting Software

In Chapter 5 the two-dimensional stress-strain deformation procedure is fully coupled with the two-dimensional heat transfer, fluid flow, solidification procedure of Chow (1993). The fully integrated code is able to model thermal convection, solidification, heat transfer, deformation and stress formation simultaneously. An example of a casting approximated to two-dimensions shows the intermediate results as the casting solidifies and deforms away from the mould. The results appear very encouraging with full transfer of information; such as temperature from the heat transfer part to the deformation part, and the updated coordinate geometry from the deformation part to the rest of the procedures. The inclusion of the deformation code allows the air gap formed as the casting solidifies between the casting and the mould to be calculated. The air gap details enable the heat transfer coefficient at the mould/metal boundary to be adjusted according to the air gap distance. The value of including the deformation code, therefore the air gap formation, is seen when the same example is simulated with and without the deformation prediction. The lack of the air gap alters the temperature of the casting and so the casting solidification time will be artificially reduced as shown in section 5.5.2. Previous examples using the control volume unstructured mesh code have shown that the cooling rate of a particular casting may be over estimated by as much as 2% [Bailey, Fryer, Cross and Chow (1993)].

The displacements produced in the two-dimensional control volume unstructured mesh casting simulation are correct, but the stresses produced by the coupled code are much larger than they should be, this is because of the linear elastic relationships used. It follows that there is a need for inclusion of visco-elastic, visco-plastic and other non-linear stress-strain relationships in the casting software so that the very high temperatures of the metals can be modelled correctly.

The stresses that form in the mould as the casting solidifies are not yet modelled in the casting software. With the implementation of more accurate contact algorithms in the casting software the transfer of stress information from casting to mould and from mould to casting is currently under research at the University.

Generally casting shapes are too complex to approximate to the special two-dimensional cases of plane stress, plane strain or axisymmetry. Current research at the University has involved the extension of the two-dimensional heat transfer and solidification code to three-dimensions. The success of this has lead to the extension of the elastic stress-strain algorithm to three-dimensions using the same control volume unstructured mesh technique, a three-dimensional casting software is then to be created.

A simulation of a casting solidifying can take over a day of continual use of a SUN workstation. If the casting software is ever going to be of practical help in the foundry, then the simulation time needs to be greatly reduced. The inclusion of faster algorithms and general neatening of code may reduce the time taken slightly, but achieving a real time simulation may be difficult at present. A sizable reduction in the computational time used can be achieved by relatively inexpensive parallel processing and vectorisation.

A simple porosity model was included in the fully coupled code in Chapter 6. The porosity model, unlike other empirical models, is based on the deformation of the casting as it solidifies. The porosity results produced in Chapter 6, sections 6.6 and 6.7, look very encouraging when compared to experimental results. Additional work on the porosity model may produce even better porosity prediction. At present fluid flow is not considered when the porosity module is used, future inclusion should produce more realistic results. No gravity effects are included but modifications to the model should take this into account as well as the fluid feeding effects. The density of liquid at present is kept artificially constant future work needs to look at ways of avoiding this without compromising other properties of the code such as mass continuity. The inclusion of the shrinkage pipe prediction in feeders is a future consideration, with work currently under way in the department to take these into account. The possible inclusion of the concept of pore nucleation at a micro level can be considered. There are many ways that the porosity model can be modified and improved. The present model shows how easily other physical effects can be included with in the context of a control volume unstructured mesh framework.

To model the complete casting process, the further integration of the coupled casting code with a filling algorithm of similar discretisation method can be considered. The inclusion of the filling routine would enable a much more complete prediction of the casting simulation, at present the mould cavity is assumed to be filled completely before the start of the casting simulation. Linking the casting software with an automatic mesh generator would save time and make the program easier to use.

Current work at the University of Greenwich is the creation of a multi-physics software environment, where standard procedures can be applied to a variety of problems. The casting software is one application of the elastic stress-strain routine but it is not the only one.

Appendix A
Standard Formulae

A.1 Stokes's Theorem

$$\oint_c F.dr = \iint curlF.dS$$

A.1.1 Plane Stress/Plane Strain

where $F = (f_1, f_2)$

$$\oint_c (f_1 dx + f_2 dy) = \iint \left(\frac{\partial f_2}{\partial x} - \frac{\partial f_1}{\partial y} \right) dxdy$$

A.1.2 Axis-symmetric

where $F = (f_r, f_z)$

$$\oint_c (f_r dr + f_z dz) = \iint \left(\frac{\partial f_r}{\partial z} - \frac{\partial f_z}{\partial r} \right) drdz$$

A.2 Cartesian Coordinates

Stress Equations of Equilibrium

$$\frac{\partial \sigma_{xx}}{\partial x} + \frac{\partial \sigma_{xy}}{\partial y} + \frac{\partial \sigma_{xz}}{\partial z} + F_x = 0$$

$$\frac{\partial \sigma_{yx}}{\partial x} + \frac{\partial \sigma_{yy}}{\partial y} + \frac{\partial \sigma_{yz}}{\partial z} + F_y = 0$$

$$\frac{\partial \sigma_{zx}}{\partial x} + \frac{\partial \sigma_{zy}}{\partial y} + \frac{\partial \sigma_{zz}}{\partial z} + F_z = 0$$

Strain-Displacement Relationships

$$e_{xx} = \frac{\partial u}{\partial x} \qquad e_{xy} = e_{yx} = \frac{\partial u}{\partial y} + \frac{\partial v}{\partial x}$$

$$e_{yy} = \frac{\partial v}{\partial y} \qquad e_{yz} = e_{zy} = \frac{\partial v}{\partial z} + \frac{\partial w}{\partial y}$$

$$e_{zz} = \frac{\partial w}{\partial z} \qquad e_{zx} = e_{xz} = \frac{\partial w}{\partial x} + \frac{\partial u}{\partial z}$$

Stress-Strain Relationships

$$\sigma_{xx} = \frac{E}{(1+\nu)(1-2\nu)}\{\,(1-\nu)e_{xx}+\nu(e_{yy}+e_{zz})-(1+\nu)\alpha T\,\}$$

$$\sigma_{yy} = \frac{E}{(1+\nu)(1-2\nu)}\{\,(1-\nu)e_{yy}+\nu(e_{xx}+e_{zz})-(1+\nu)\alpha T\,\}$$

$$\sigma_{zz} = \frac{E}{(1+\nu)(1-2\nu)}\{\,(1-\nu)e_{zz}+\nu(e_{xx}+e_{yy})-(1+\nu)\alpha T\,\}$$

$$\sigma_{xy} = \frac{E}{2(1+\nu)}e_{xy} \qquad \sigma_{xz} = \frac{E}{2(1+\nu)}e_{xz} \qquad \sigma_{zx} = \frac{E}{2(1+\nu)}e_{zx}$$

A.3 Cylindrical Polar Coordinates

Stress Equations of Equilibrium

$$\frac{\partial\sigma_{rr}}{\partial} + \frac{1}{r}\frac{\partial\sigma_{r\theta}}{\partial\theta} + \frac{\partial\sigma_{rz}}{\partial z} + \frac{\sigma_{rr}-\sigma_{\theta\theta}}{r} + F_r = 0$$

$$\frac{\partial\sigma_{r\theta}}{\partial r} + \frac{1}{r}\frac{\partial\sigma_{\theta\theta}}{\partial\theta} + \frac{\partial\sigma_{\theta z}}{\partial z} + \frac{2\sigma_{r\theta}}{r} + F_\theta = 0$$

$$\frac{\partial\sigma_{zr}}{\partial r} + \frac{1}{r}\frac{\partial\sigma_{z\theta}}{\partial\theta} + \frac{\partial\sigma_{zz}}{\partial z} + \frac{\sigma_{zr}}{r} + F_z = 0$$

Strain-Displacement Relationships

$$e_{rr} = \frac{\partial u}{\partial r} \qquad e_{r\theta} = \frac{1}{r}\frac{\partial u}{\partial\theta} + \frac{\partial v}{\partial r} - \frac{v}{r}$$

$$e_{\theta\theta} = \frac{u}{r} + \frac{1}{r}\frac{\partial v}{\partial\theta} \qquad e_{rz} = \frac{\partial u}{\partial z} + \frac{\partial w}{\partial r}$$

$$e_{zz} = \frac{\partial w}{\partial z} \qquad e_{z\theta} = \frac{\partial v}{\partial z} + \frac{1}{r}\frac{\partial w}{\partial\theta}$$

Stress-Strain Relationships

$$\sigma_{rr} = \frac{E}{(1+\nu)(1-2\nu)}\{\,(1-\nu)e_{rr}+\nu(e_{\theta\theta}+e_{zz})-(1+\nu)\alpha T\,\}$$

$$\sigma_{\theta\theta} = \frac{E}{(1+\nu)(1-2\nu)}\{\,(1-\nu)e_{\theta\theta}+\nu(e_{rr}+e_{zz})-(1+\nu)\alpha T\,\}$$

$$\sigma_{zz} = \frac{E}{(1+\nu)(1-2\nu)}\{\,(1-\nu)e_{zz}+\nu(e_{rr}+e_{\theta\theta})-(1+\nu)\alpha T\,\}$$

$$\sigma_{r\theta} = \frac{E}{2(1+\nu)}e_{r\theta} \qquad \sigma_{rz} = \frac{E}{2(1+\nu)}e_{rz} \qquad \sigma_{z\theta} = \frac{E}{2(1+\nu)}e_{z\theta}$$

A.4 Shape Functions

A.4.1 Quadrilateral Elements

$$N_1(s,t) = \frac{(1+s)(1+t)}{4} \qquad N_2(s,t) = \frac{(1-s)(1+t)}{4}$$

$$N_3(s,t) = \frac{(1-s)(1-t)}{4} \qquad N_4(s,t) = \frac{(1+s)(1-t)}{4}$$

Local derivatives

$$\frac{\partial N_1}{\partial s} = \frac{1}{4}(1+t) \qquad \frac{\partial N_1}{\partial t} = \frac{1}{4}(1+s)$$

$$\frac{\partial N_2}{\partial s} = -\frac{1}{4}(1+t) \qquad \frac{\partial N_2}{\partial t} = \frac{1}{4}(1-s)$$

$$\frac{\partial N_3}{\partial s} = -\frac{1}{4}(1-t) \qquad \frac{\partial N_3}{\partial t} = -\frac{1}{4}(1-s)$$

$$\frac{\partial N_4}{\partial s} = \frac{1}{4}(1-t) \qquad \frac{\partial N_4}{\partial t} = -\frac{1}{4}(1+s)$$

A.4.2 Triangular Elements

$$N_1(s,t) = \frac{(1+2s)}{3} \qquad N_2(s,t) = \frac{(1-s+\sqrt{3}\,.t)}{3}$$

$$N_3(s,t) = \frac{(1-s-\sqrt{3}\,.t)}{3}$$

Local derivatives

$$\frac{\partial N_1}{\partial s} = \frac{2}{3} \qquad \frac{\partial N_2}{\partial s} = -\frac{1}{3} \qquad \frac{\partial N_3}{\partial s} = -\frac{1}{3}$$

$$\frac{\partial N_1}{\partial t} = 0 \qquad \frac{\partial N_2}{\partial t} = \frac{\sqrt{3}}{3} \qquad \frac{\partial N_3}{\partial t} = -\frac{\sqrt{3}}{3}$$

Appendix B

Application to Solid Mechanics

B.1 Cantilever/Thermal Beam Meshes

B.1.1 Quadrilateral Mesh

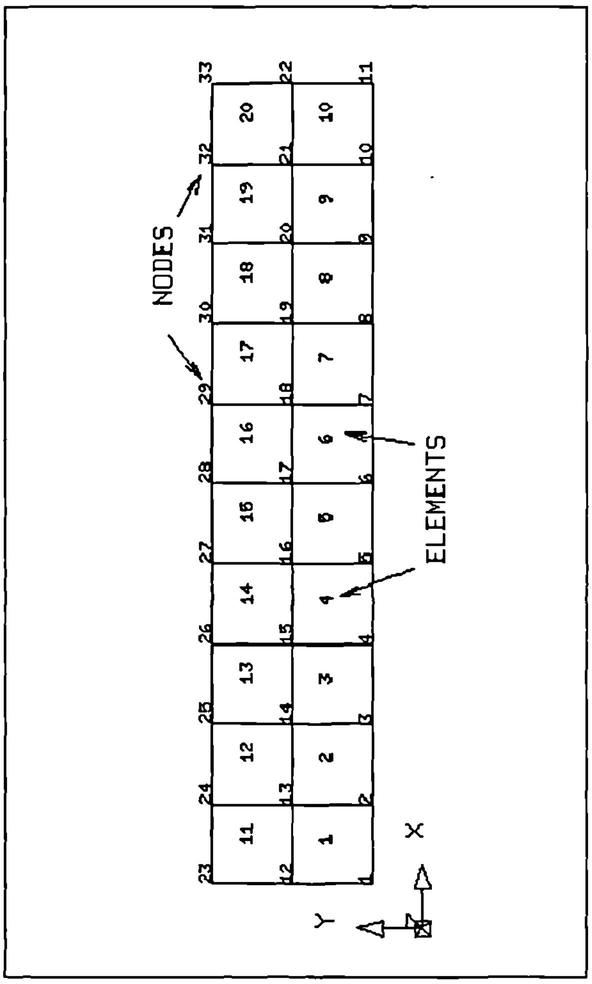

Figure B.1: 33 Node Quadrilateral Mesh for Cantilever and Thermal Beam

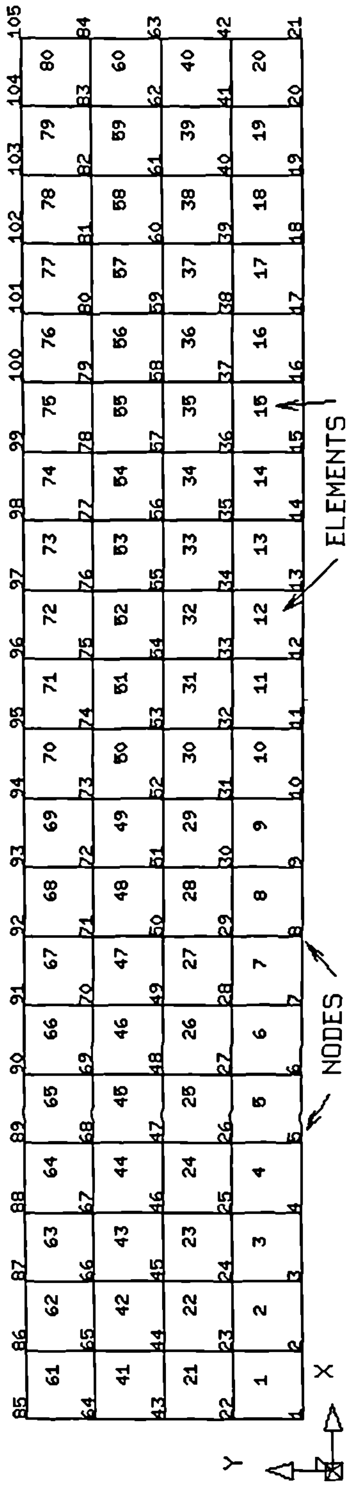

Figure B.2: 105 Node Quadrilateral Mesh for Cantilever and Thermal Beam

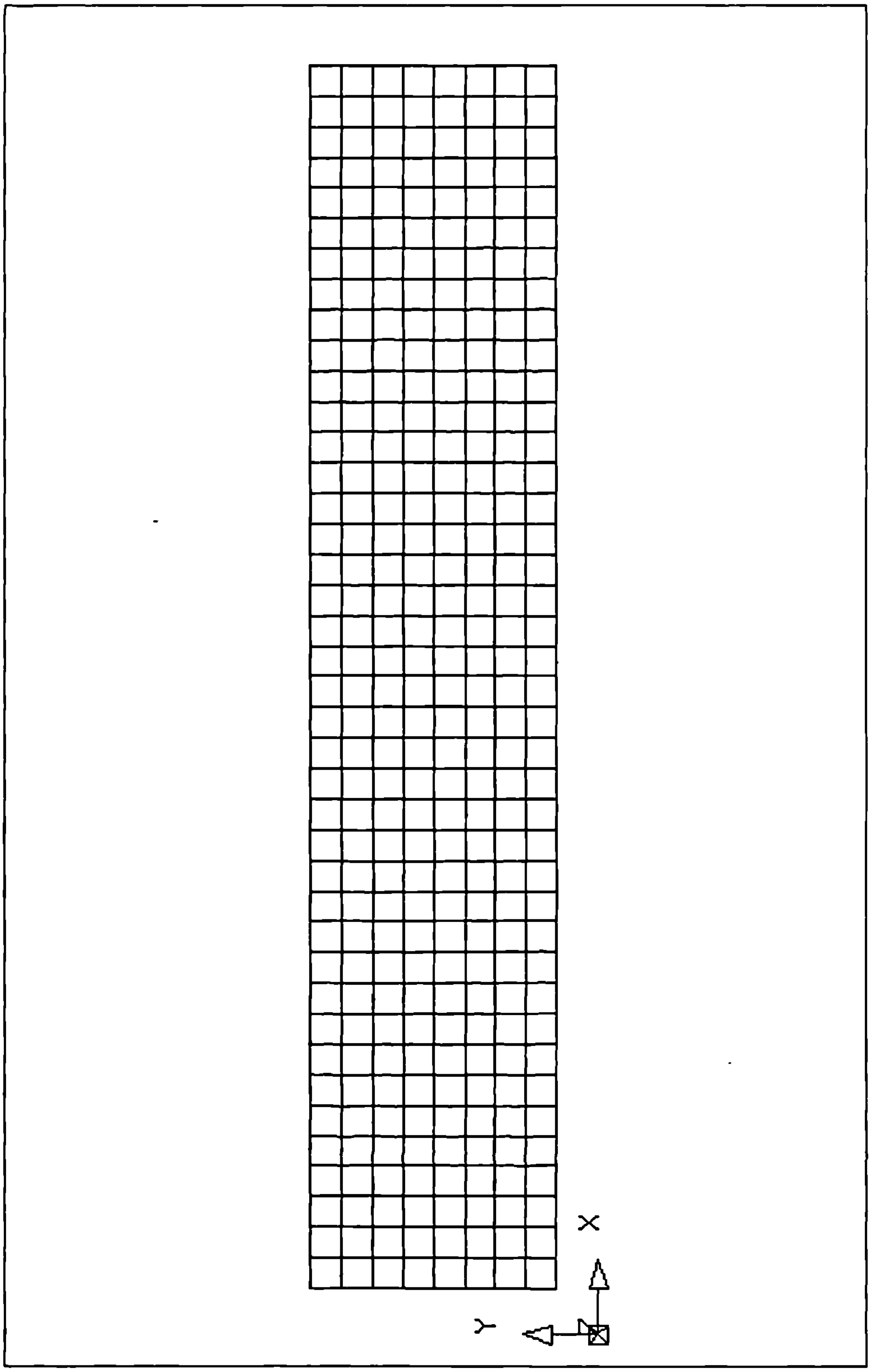

Figure B.3: 369 Node Quadrilateral Mesh for Cantilever and Thermal Beam

B.1.2 Triangular Mesh

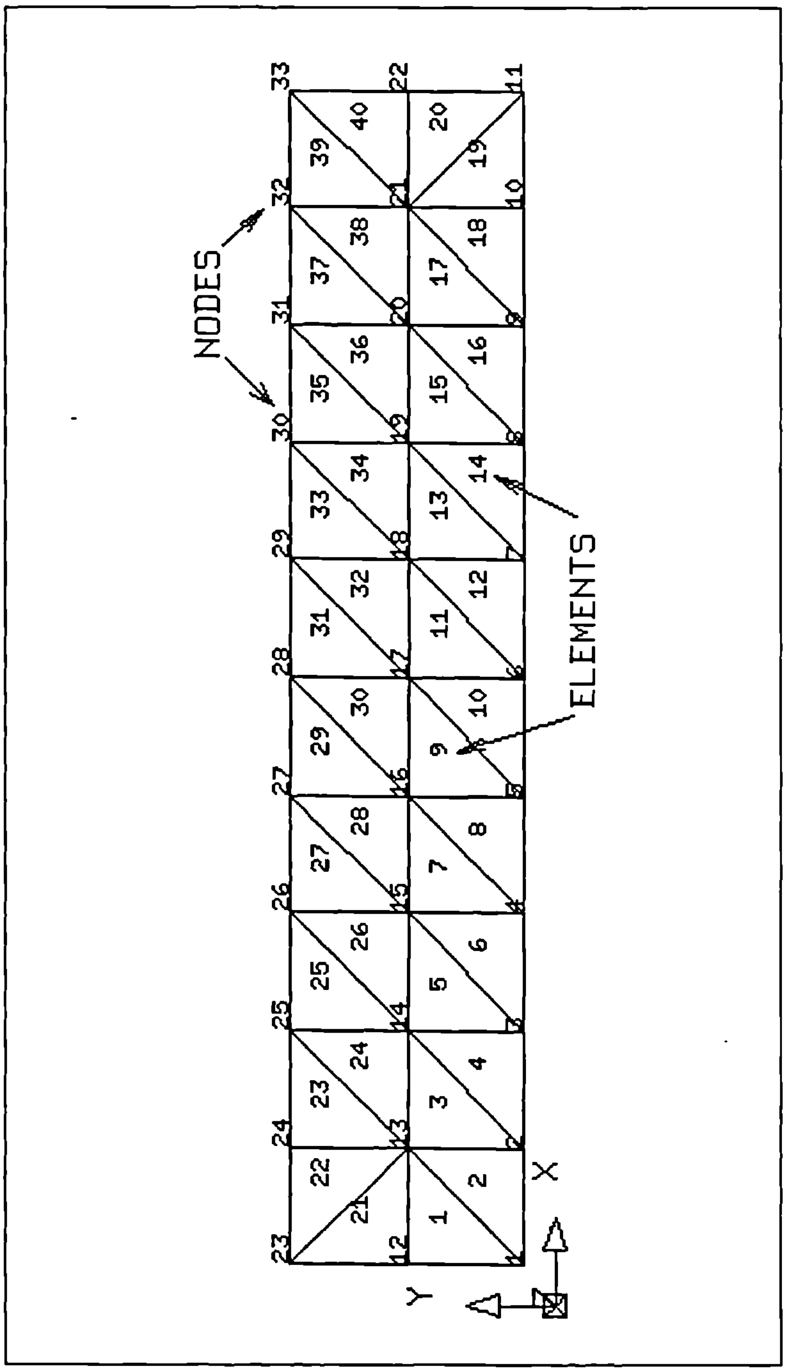

Figure B.4: 33 Node Triangular Mesh for Cantilever and Thermal Beam

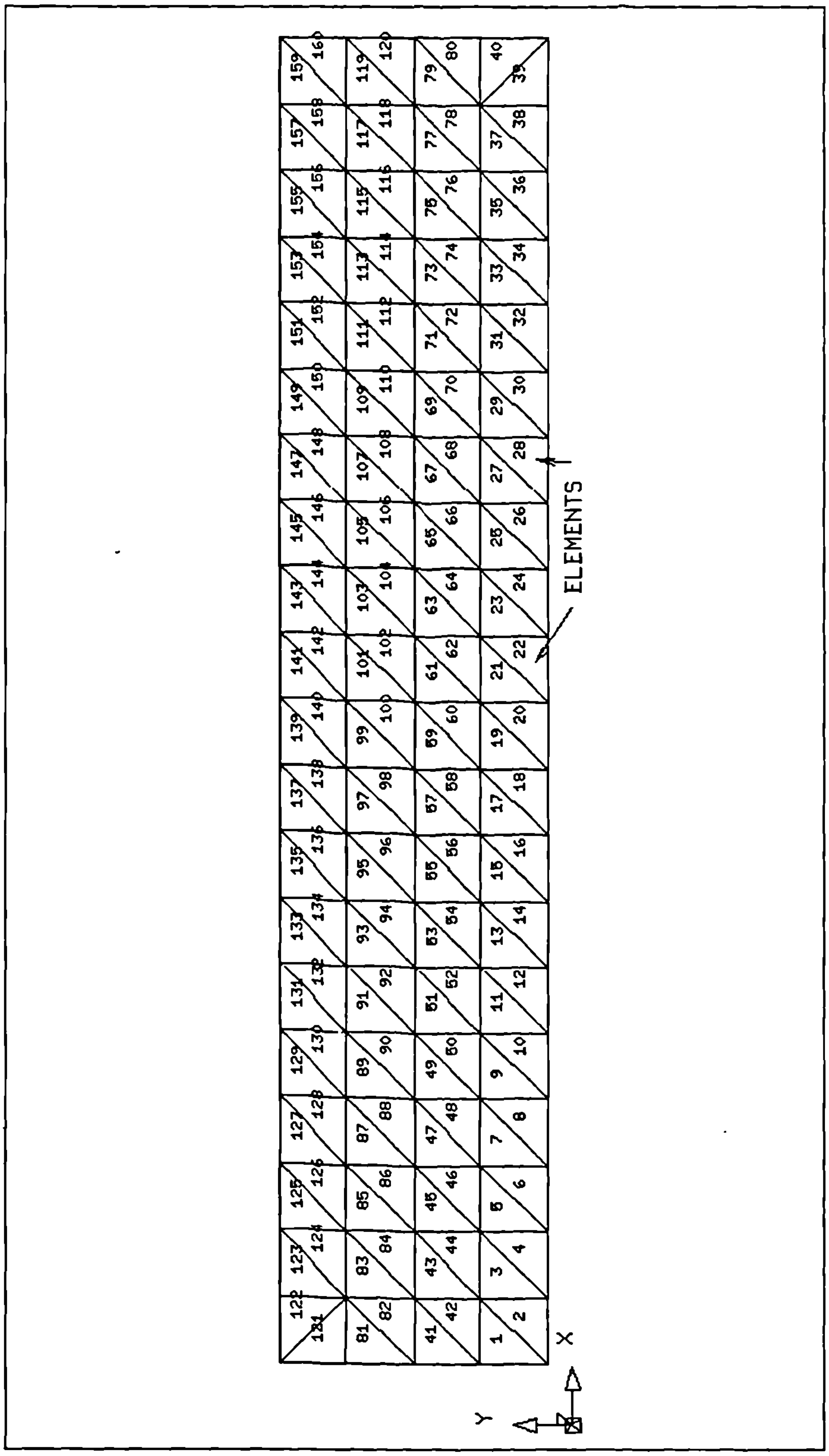

Figure B.5: 105 Node Triangular Mesh for Cantilever and Thermal Beam

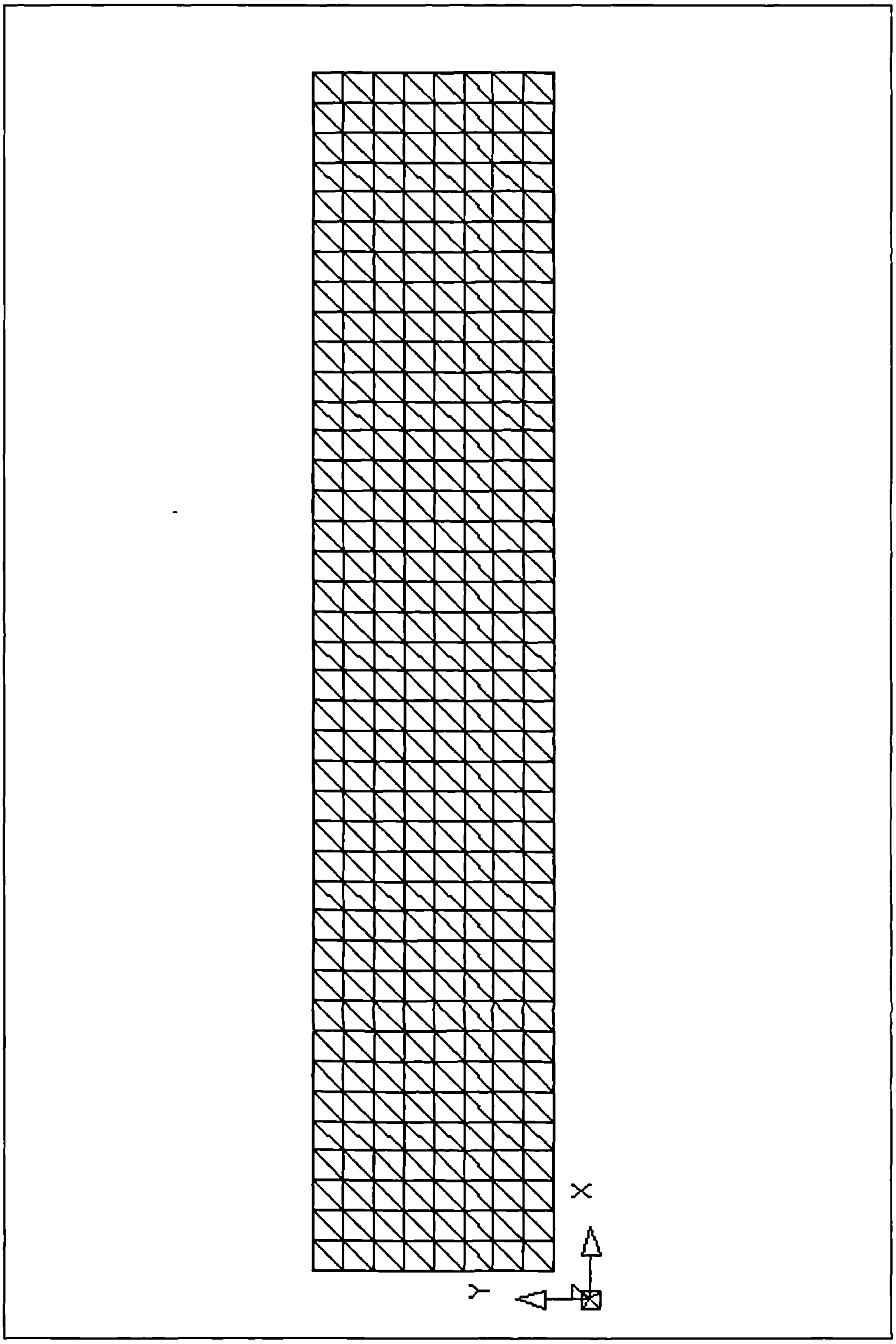

Figure B.6: 369 Node Triangular Mesh for Cantilever and Thermal Beam

B.1.3 Mixed Mesh

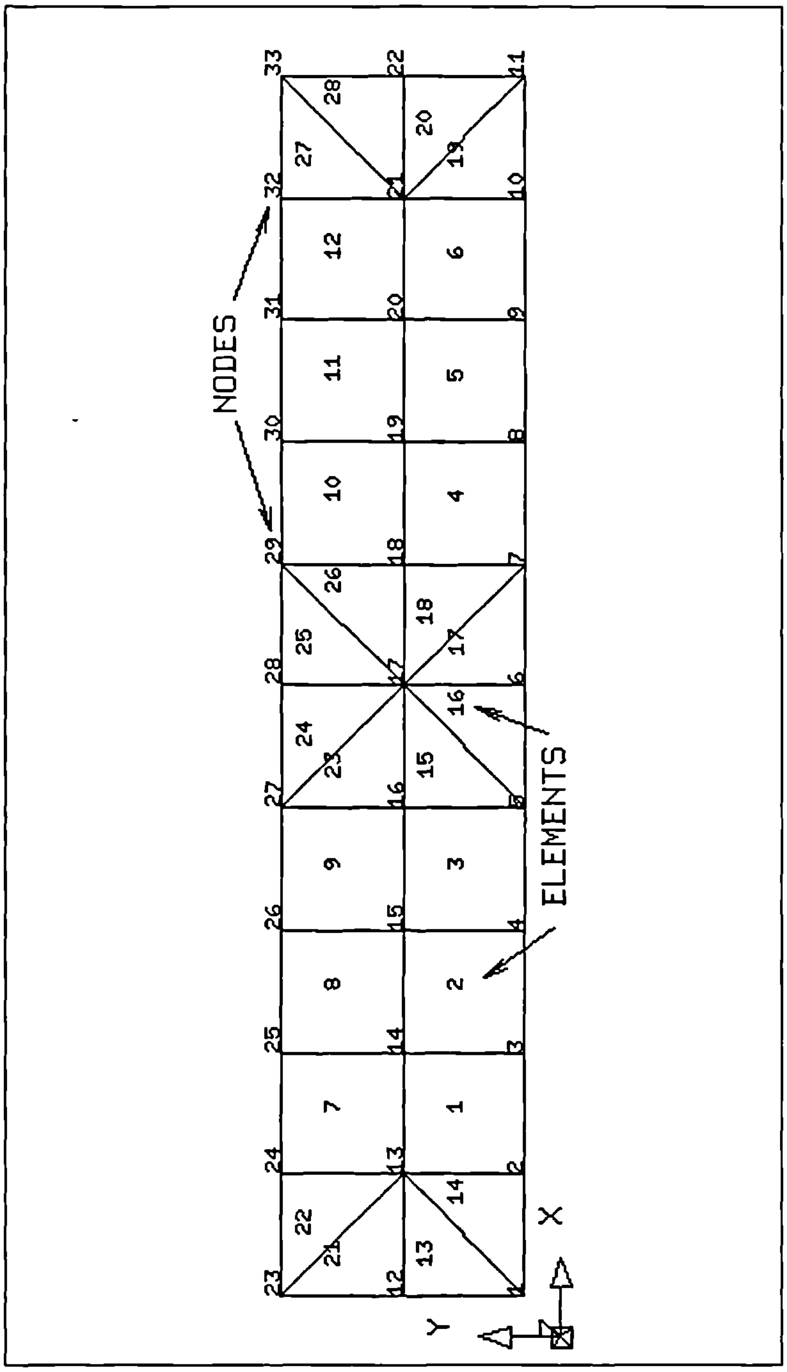

Figure B.7: 33 Node Mixed Mesh for Cantilever and Thermal Beam

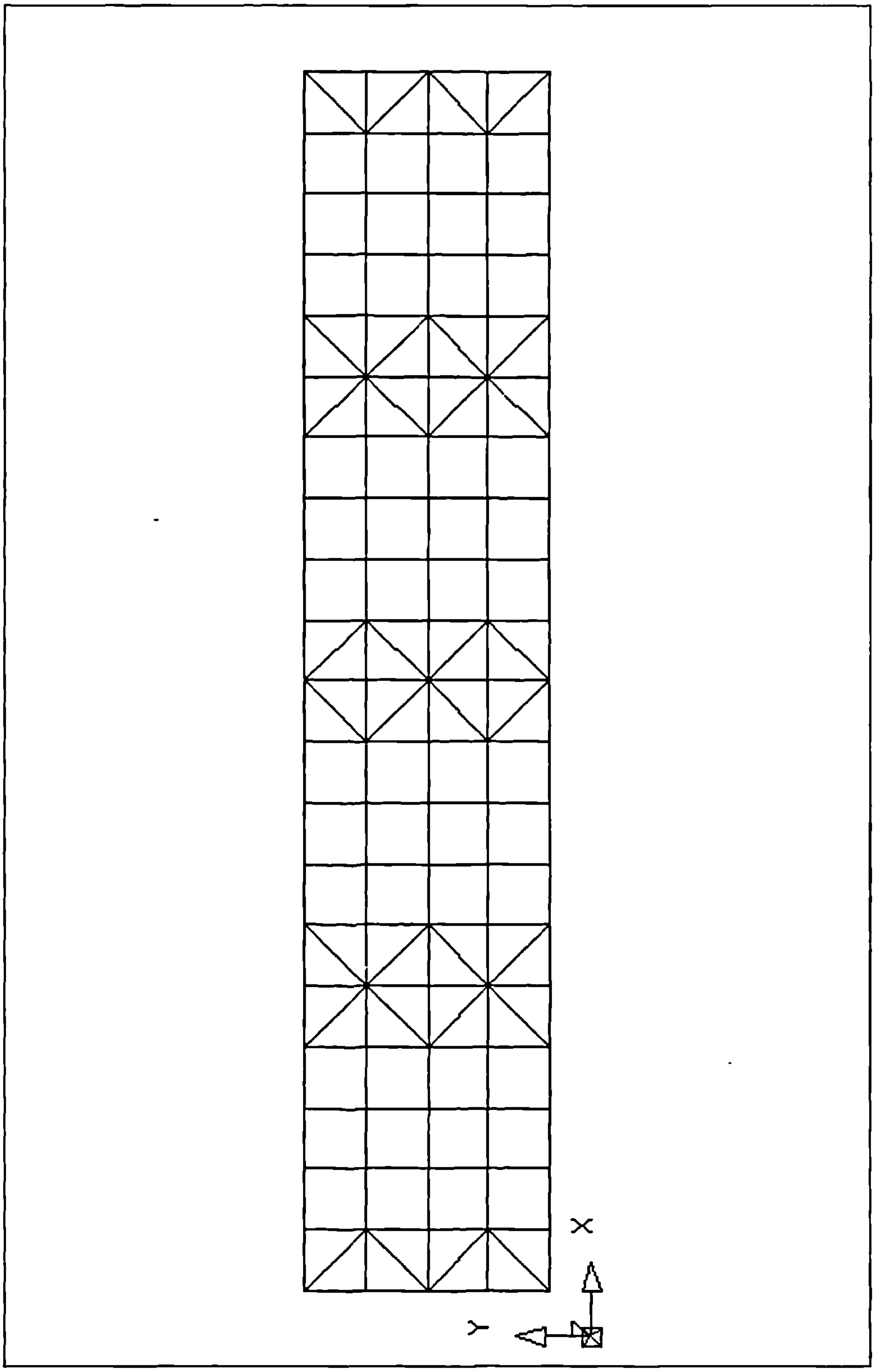

Figure B.8: 105 Node Mixed Mesh for Cantilever and Thermal Beam

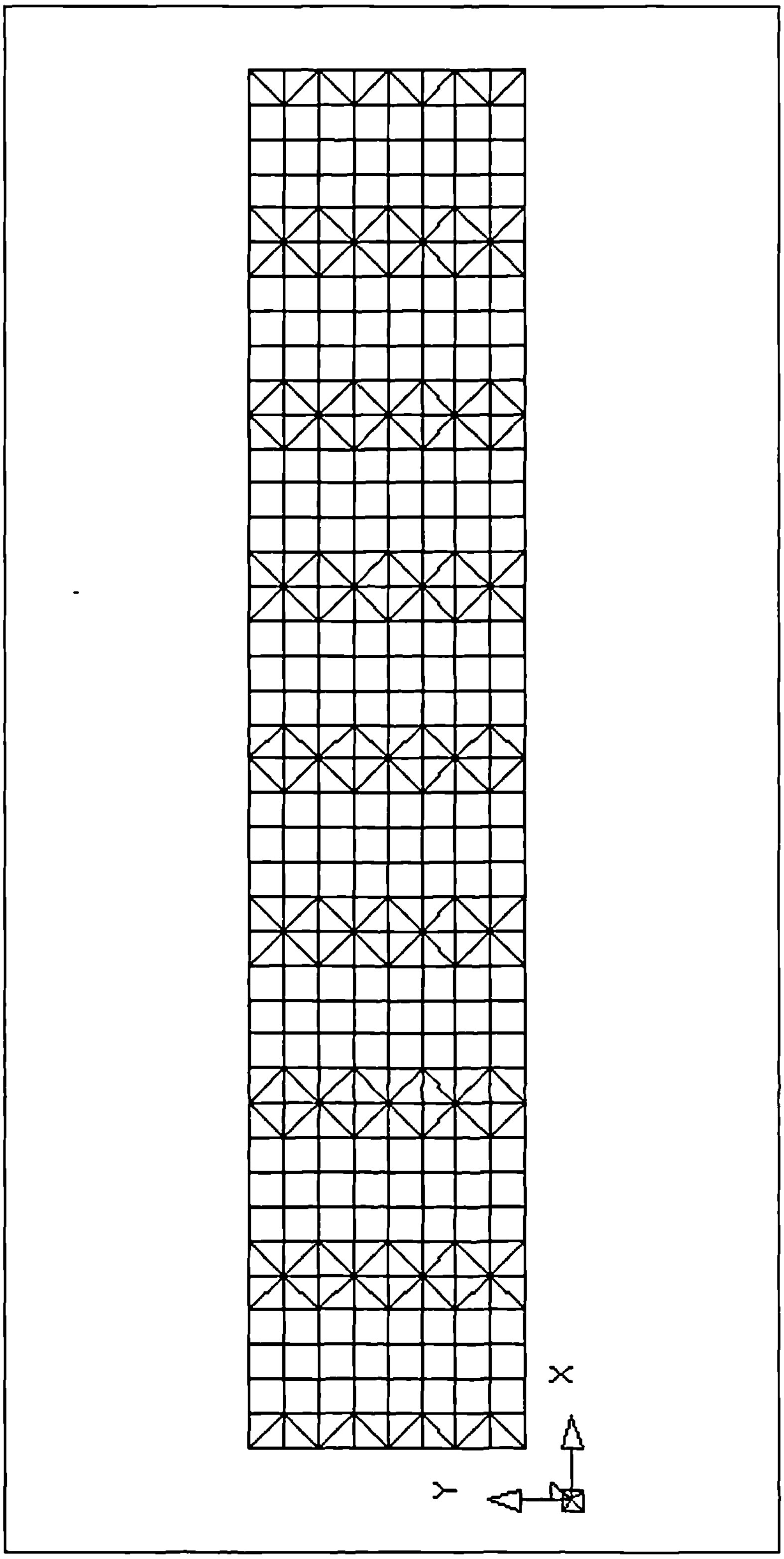

Figure B.9: 369 Node Mixed Mesh for Cantilever and Thermal Beam

B.2 Cantilever Results

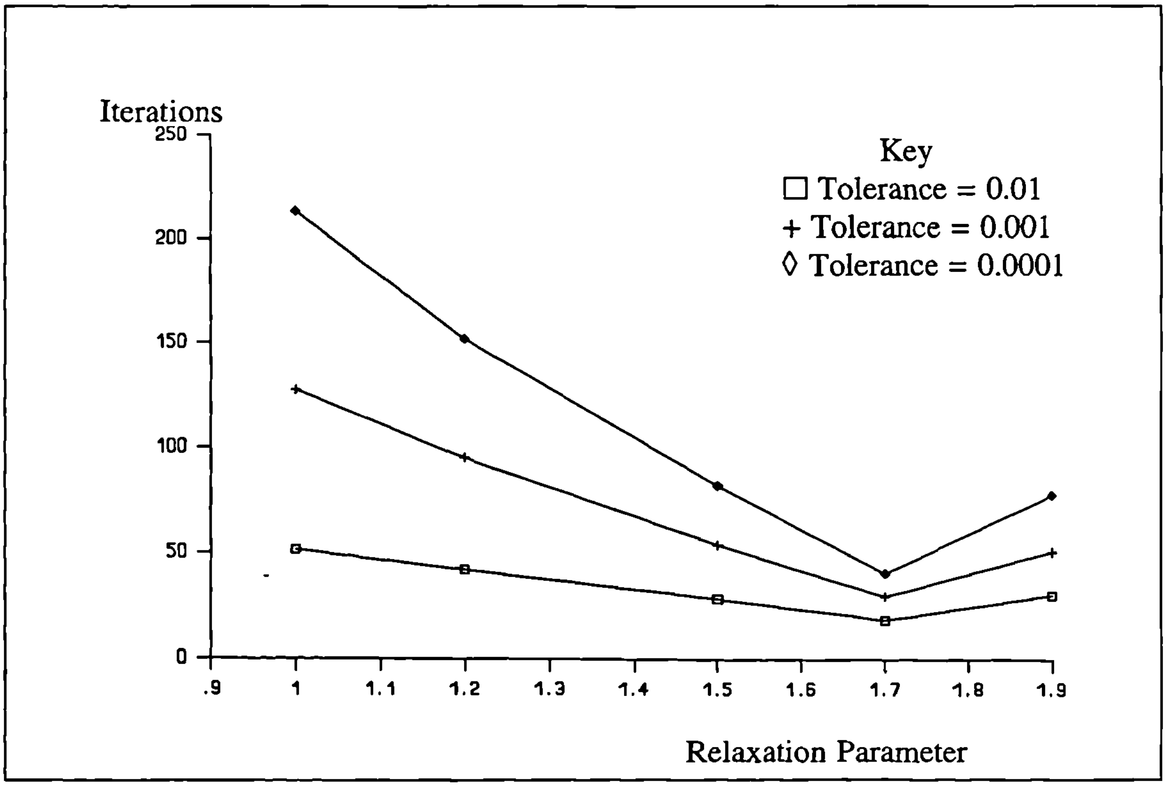

Figure B.10: Quadrilateral Cantilever Iteration Results 33 nodes

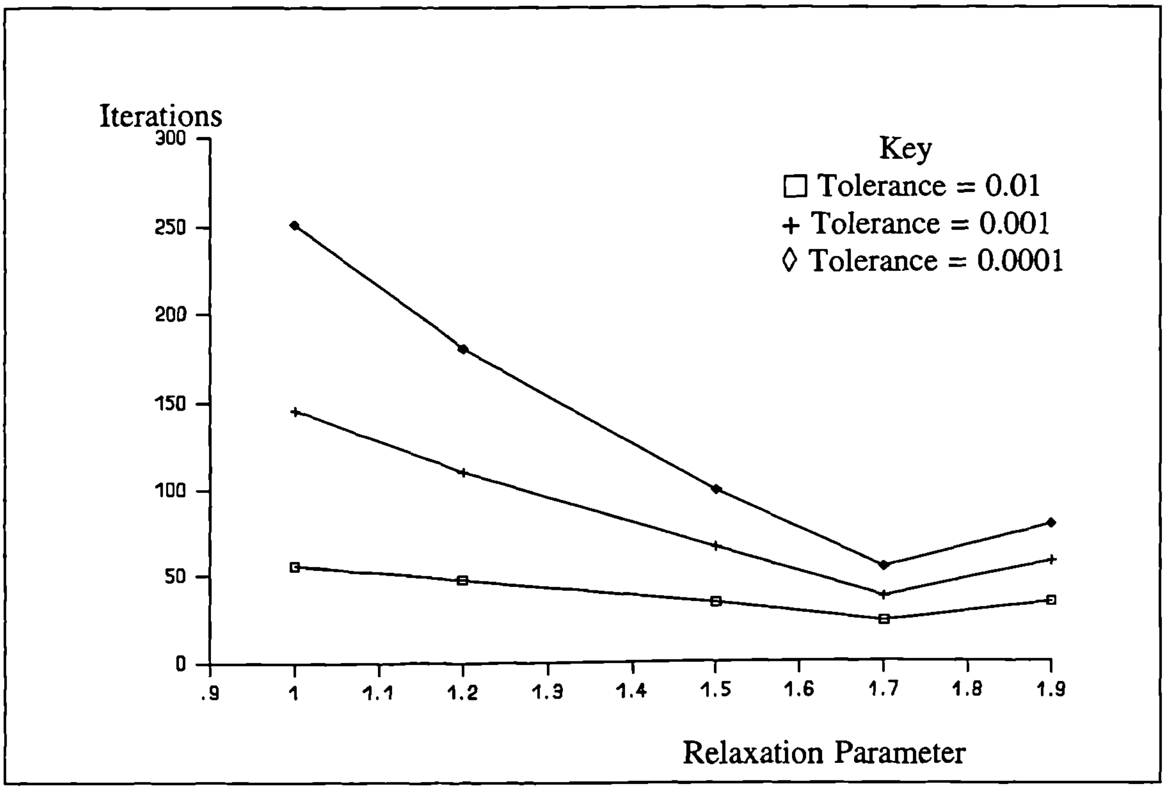

Figure B.11: Quadrilateral Cantilever Iteration Results 105 nodes

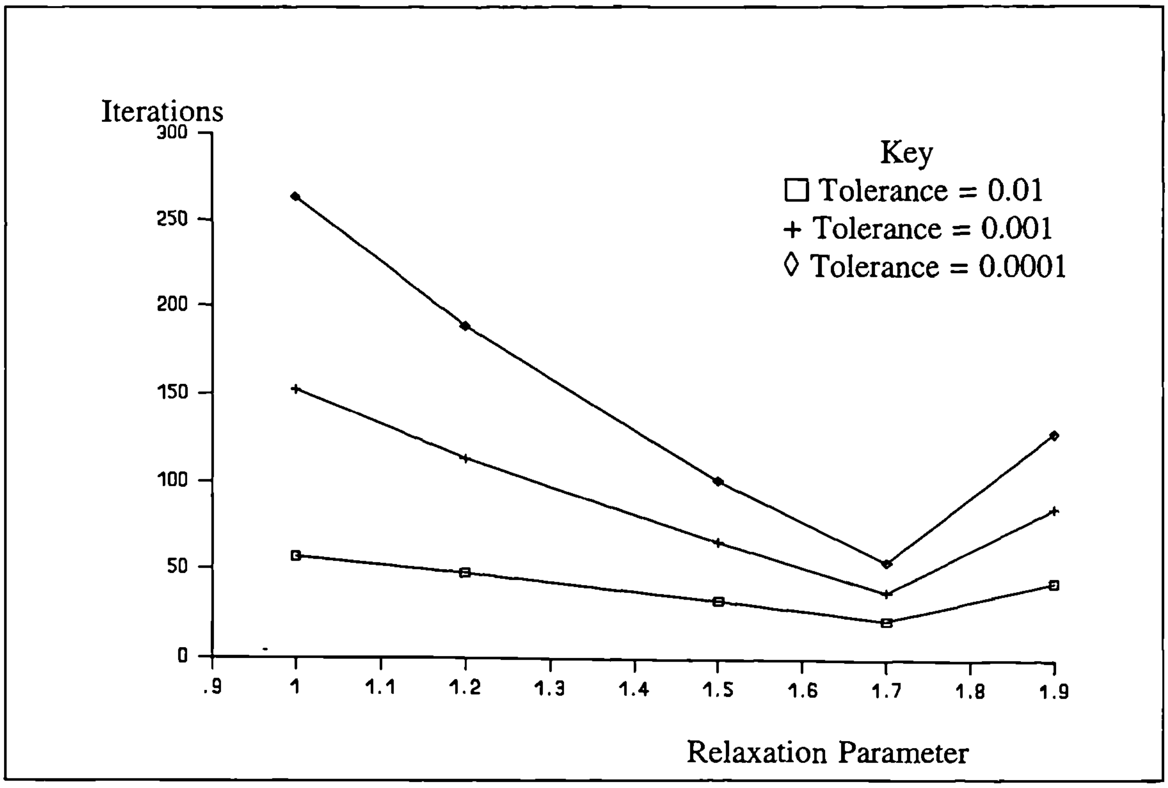

Figure B.12: Quadrilateral Cantilever Iteration Results 369 nodes

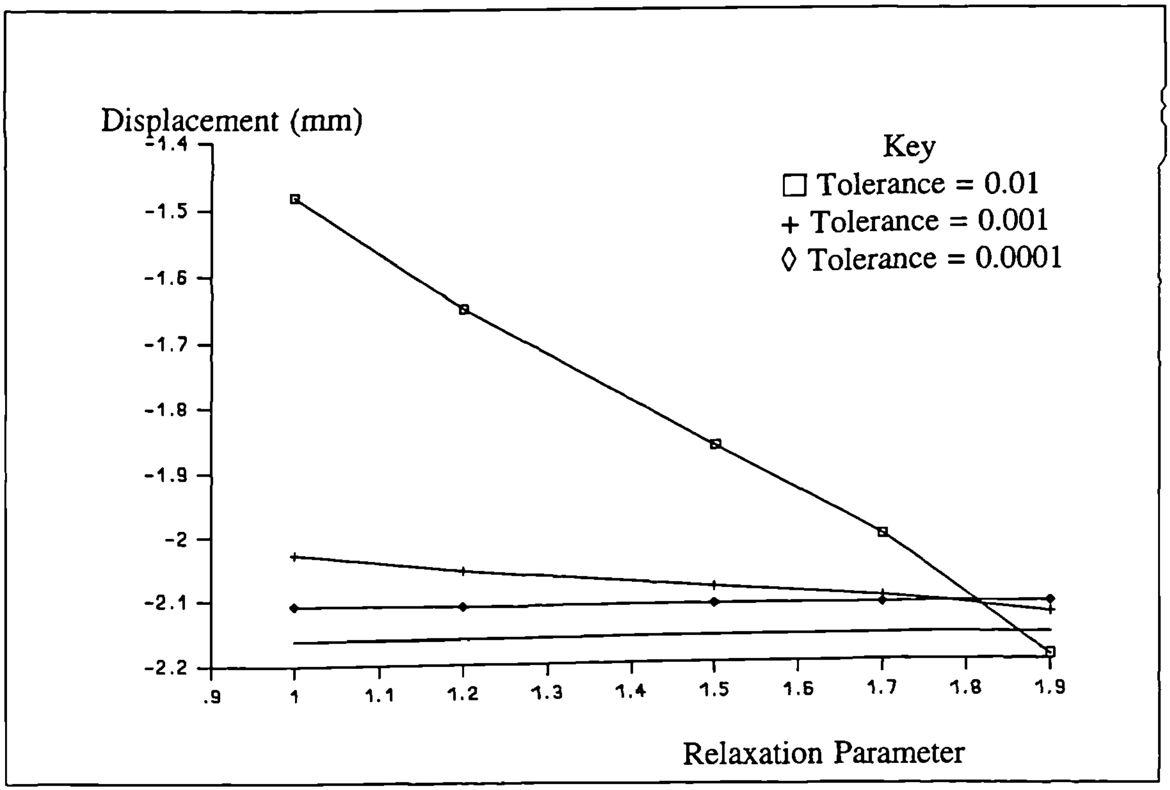

Figure B.13: Cantilever Comparison Displacement Results Quadrilateral Elements 369 Nodes

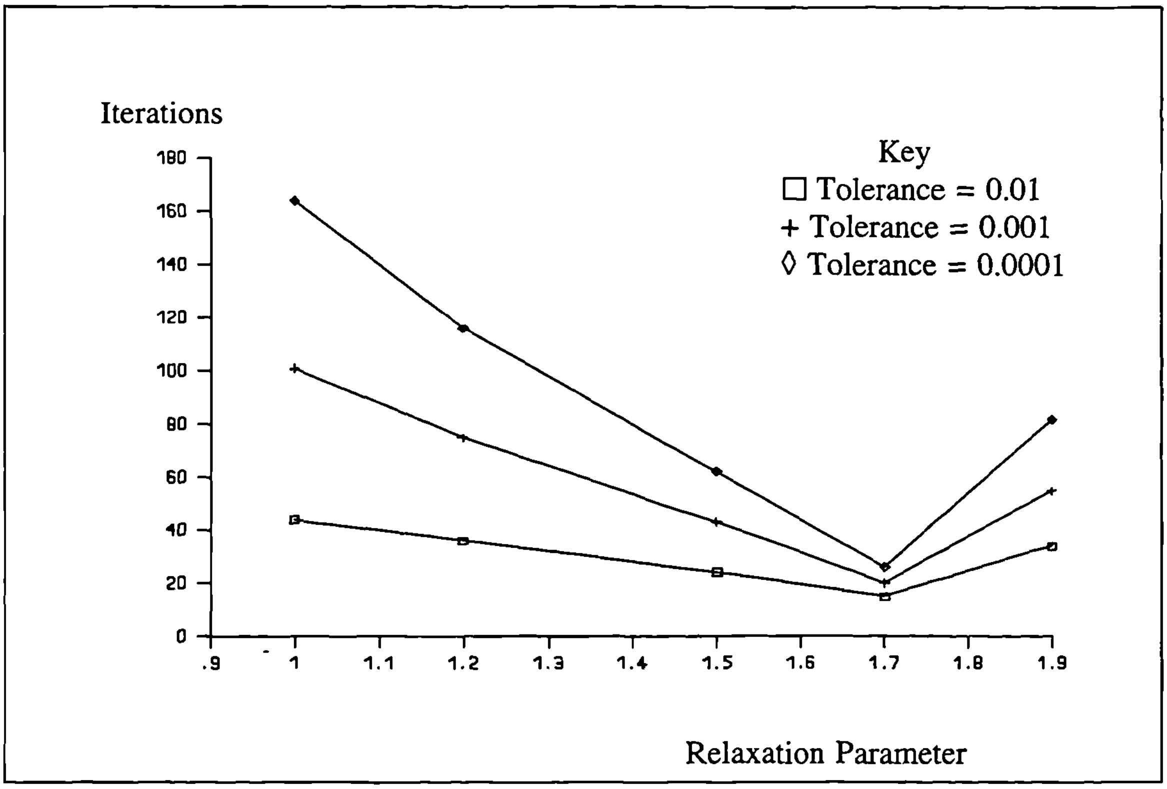

Figure B.14: Triangular Cantilever Iteration Results 33 nodes

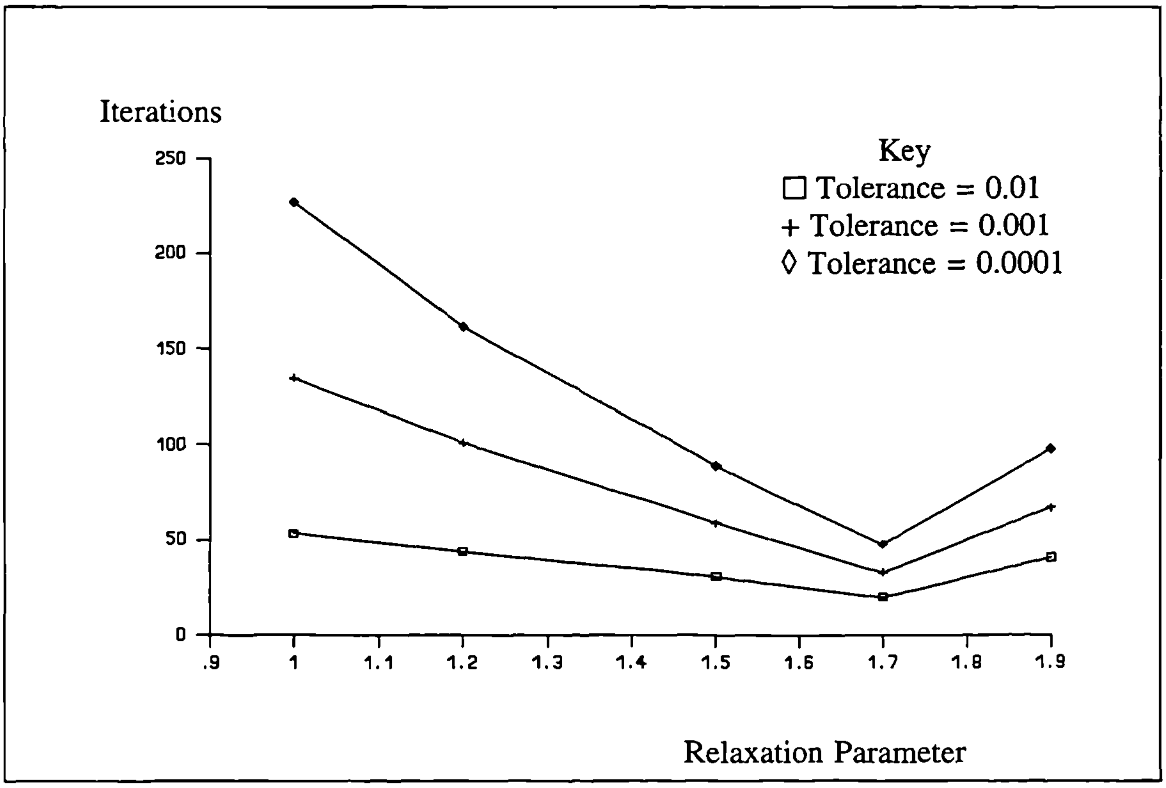

Figure B.15: Triangular Cantilever Iteration Results 105 nodes

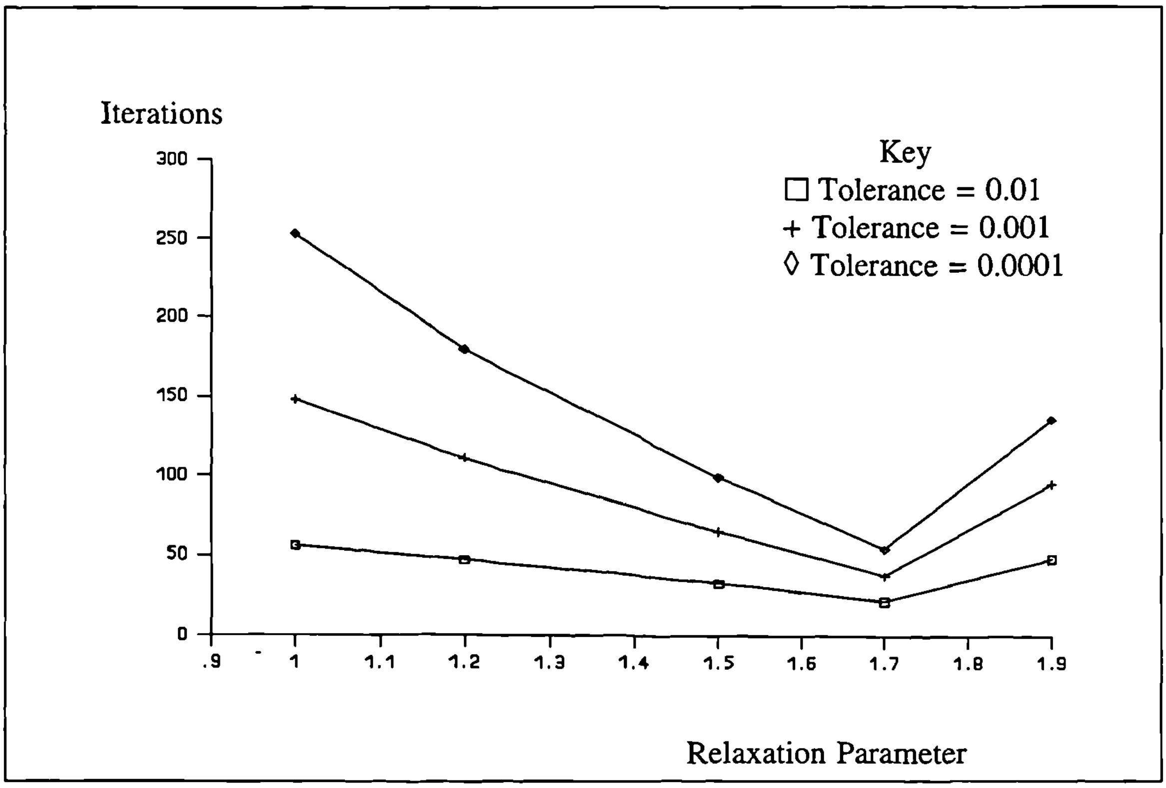

Figure B.16: Triangular Cantilever Iteration Results 369 nodes

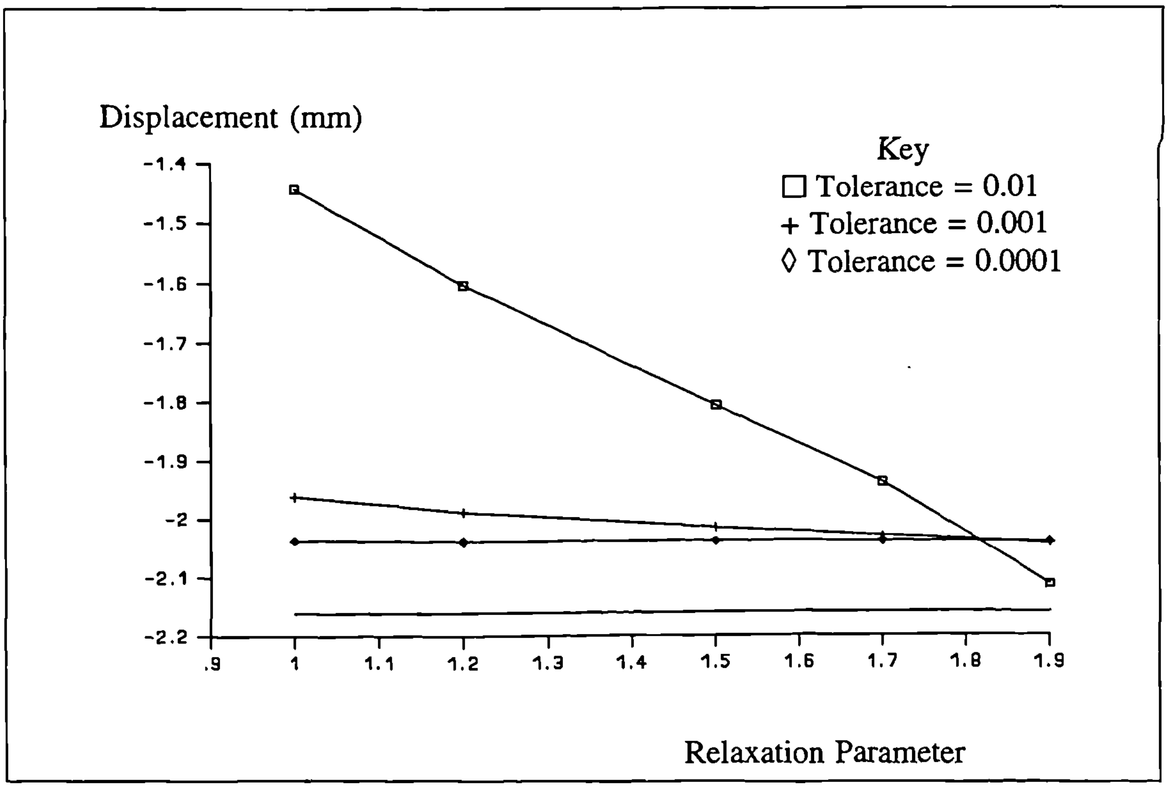

Figure B.17: Cantilever Comparison Displacement Results Triangular Elements 369 Nodes

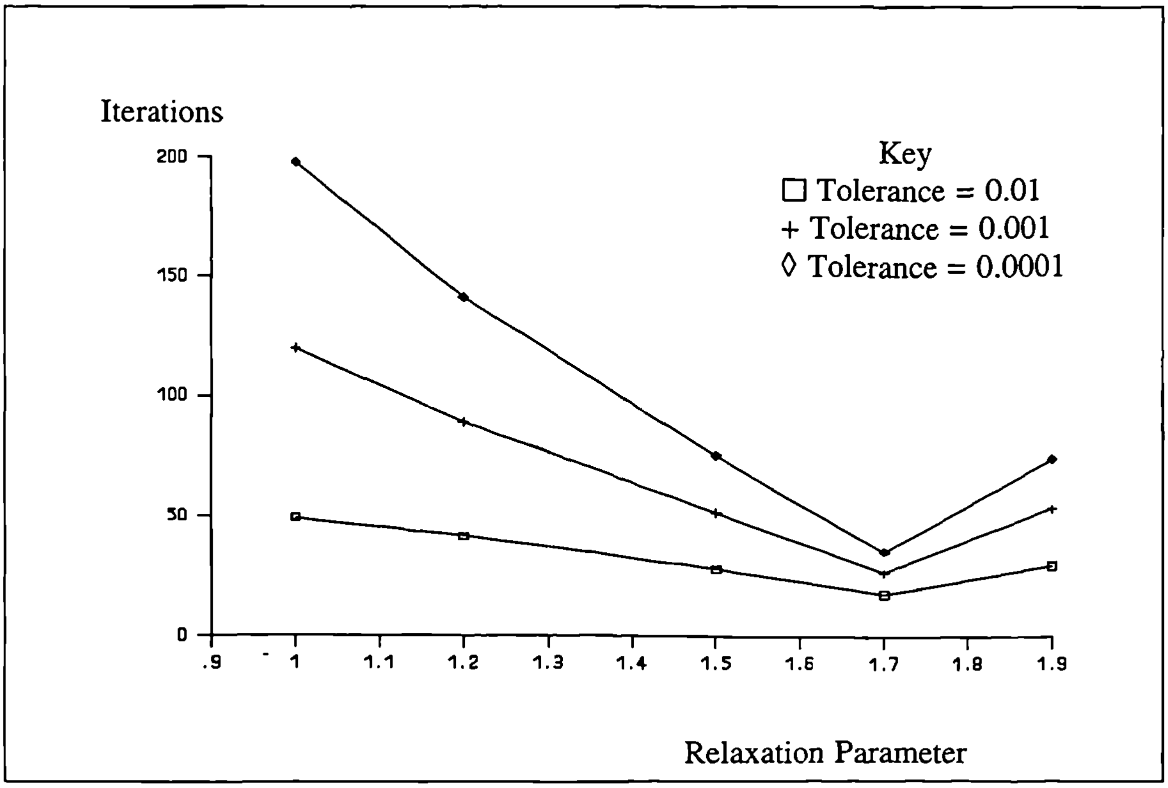

Figure B.18: Mixed Cantilever Iteration Results 33 nodes

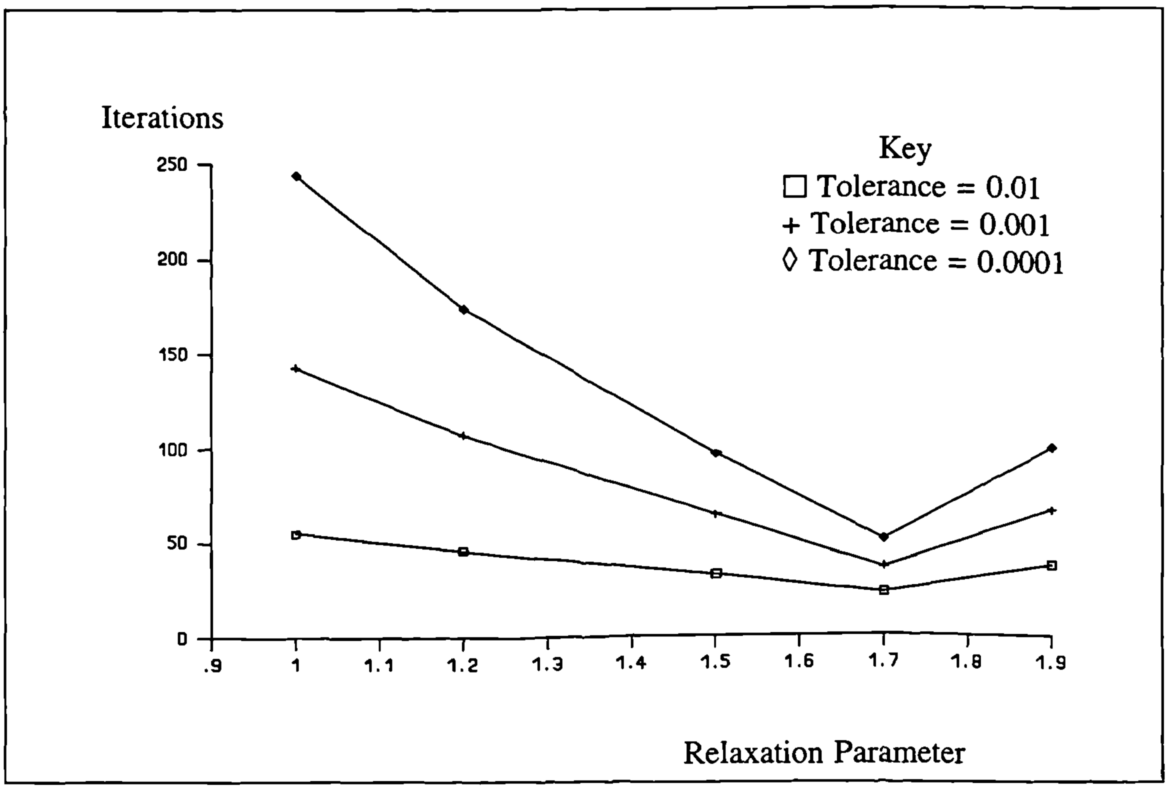

Figure B.19: Mixed Cantilever Iteration Results 105 nodes

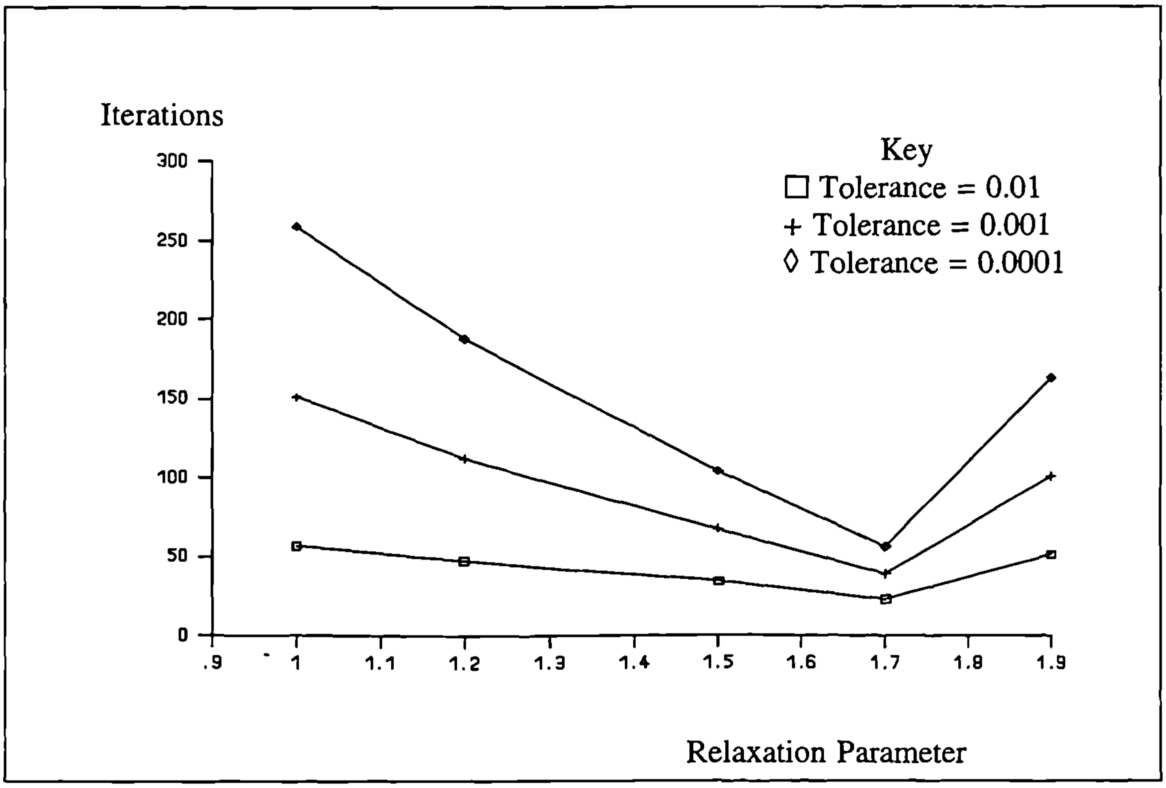

Figure B.20: Mixed Cantilever Iteration Results 369 nodes

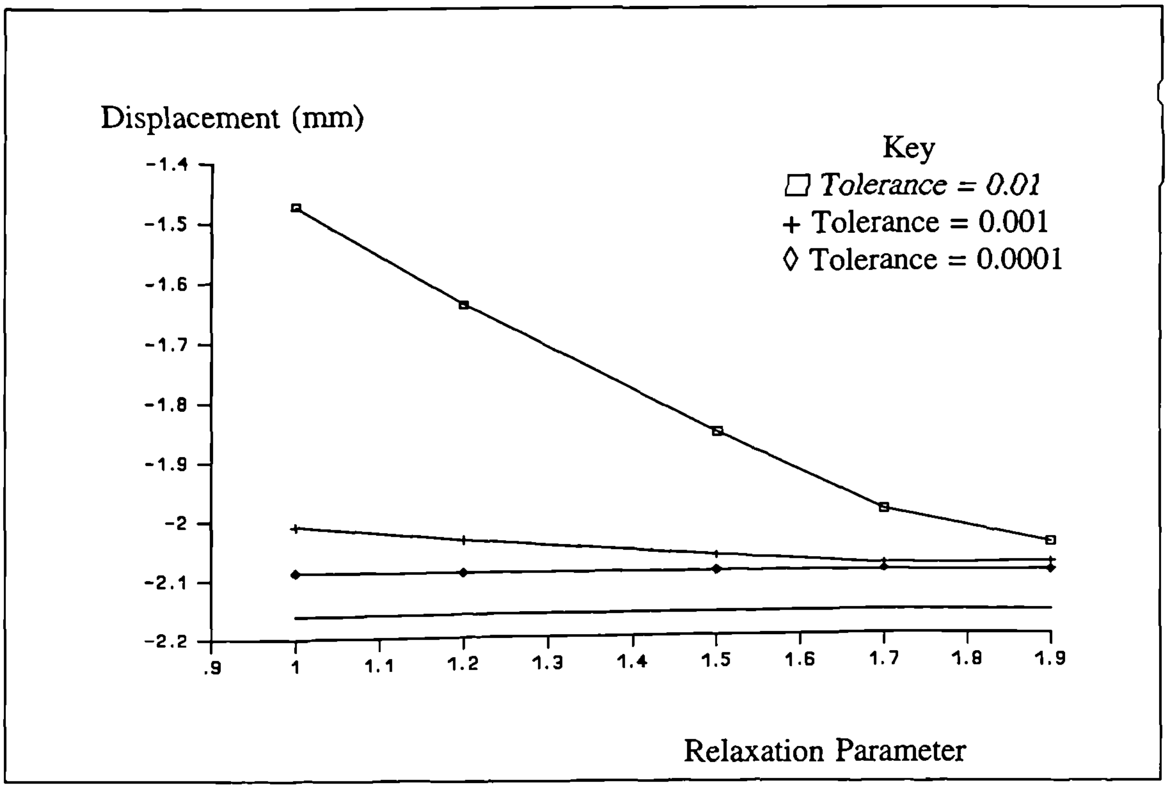

Figure B.21: Cantilever Comparison Displacement Results Mixed Elements 369 Nodes

B.3 Thermal Beam Results

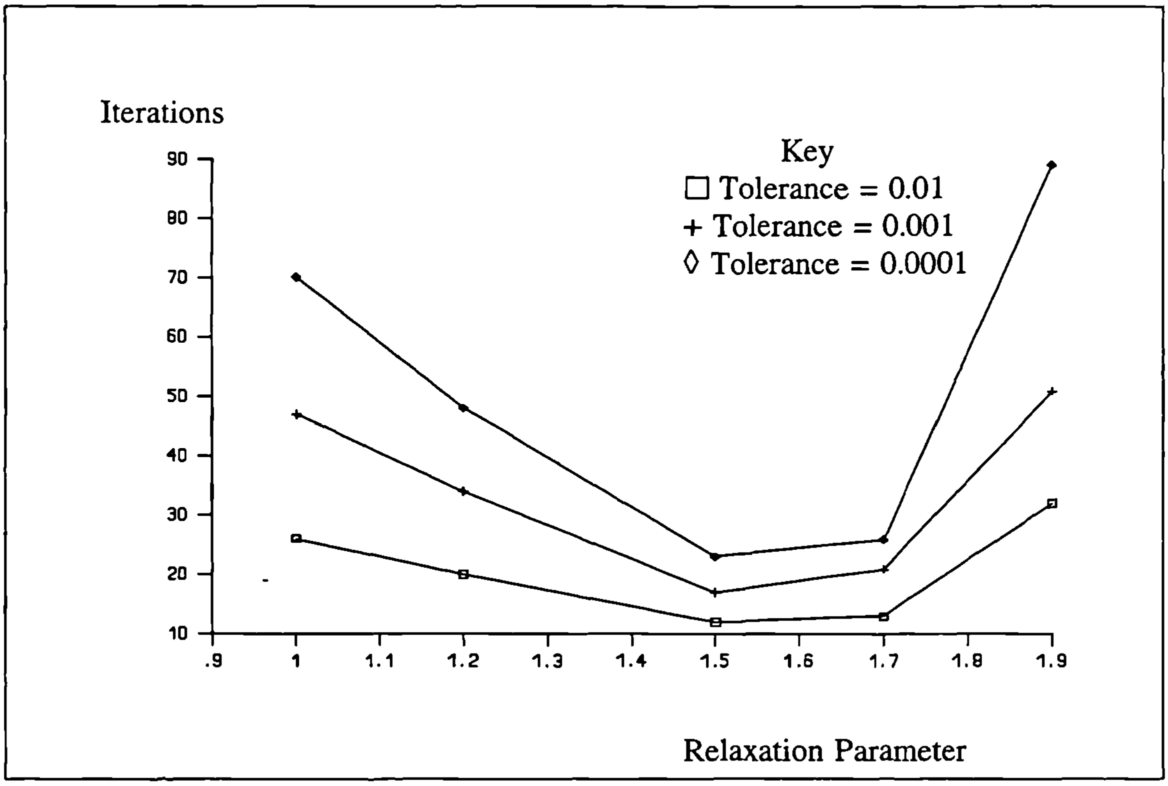

Figure B.22: Quadrilateral Thermal Beam Iteration Results 33 nodes

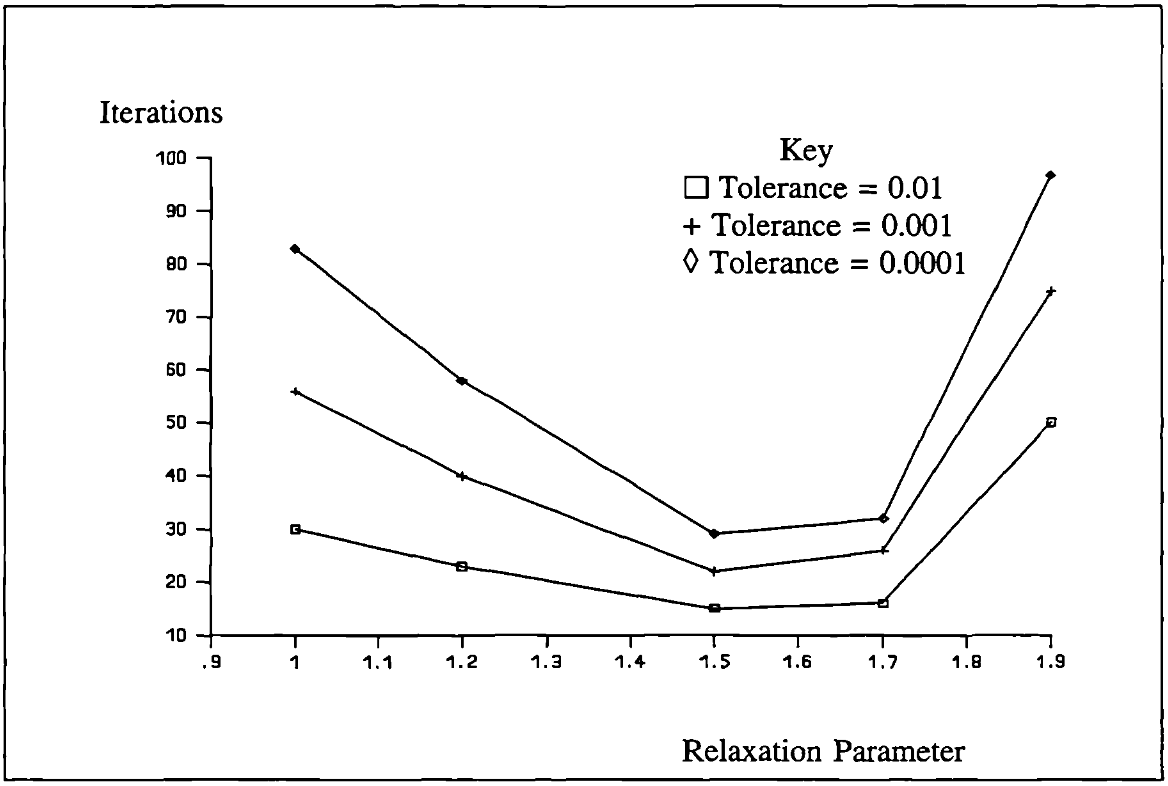

Figure B.23: Quadrilateral Thermal Beam Iteration Results 105 nodes

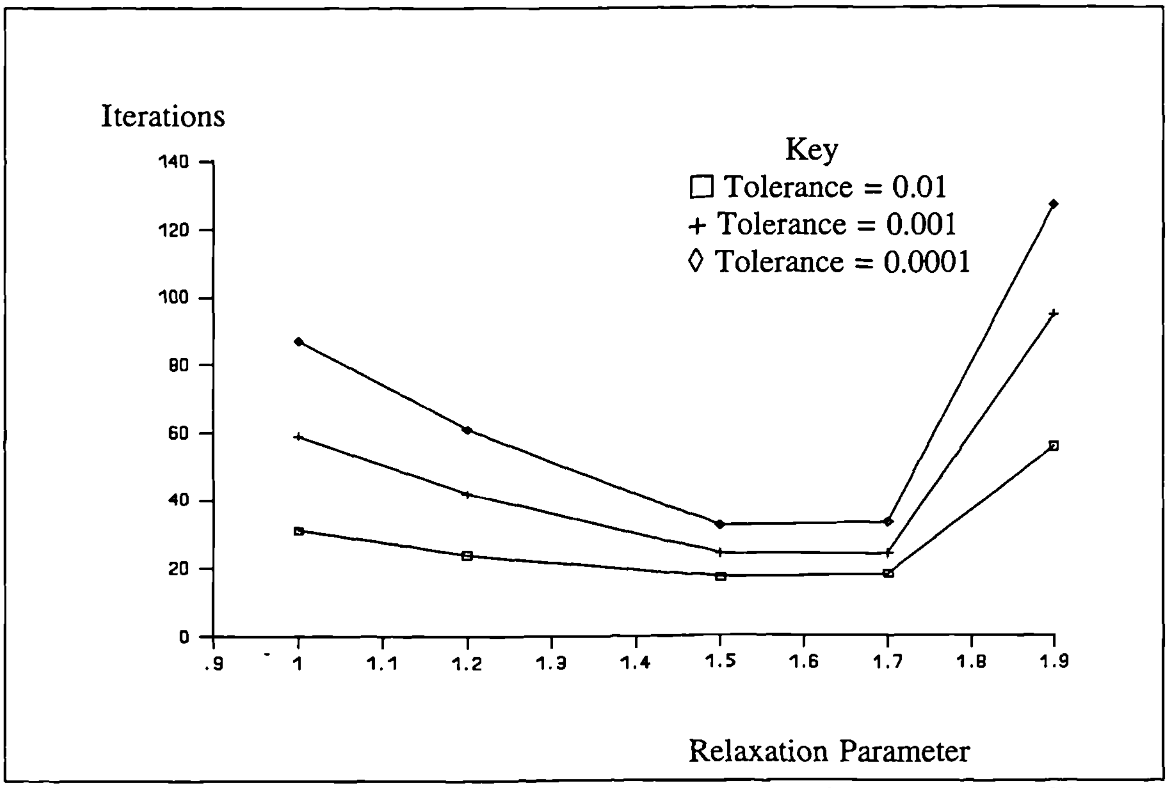

Figure B.24: Thermal Beam Comparison Displacement Results Quadrilateral Elements 369 Nodes

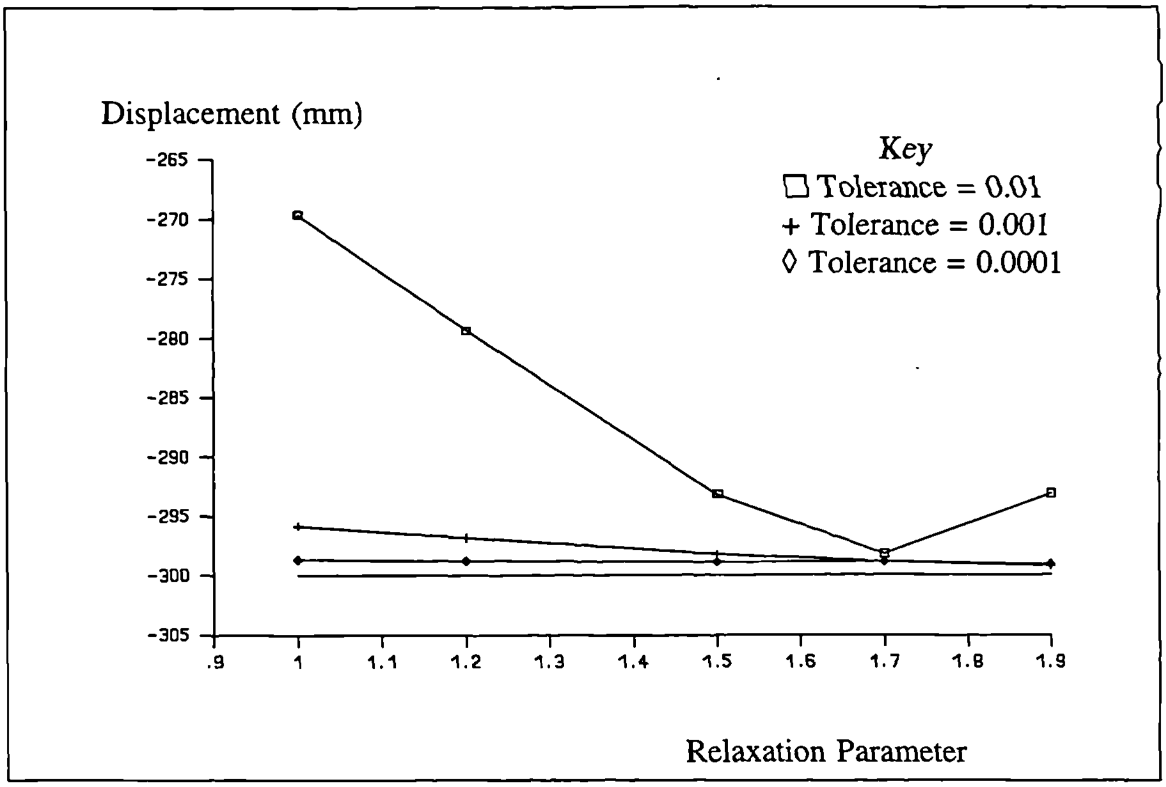

Figure B.25: Thermal Beam Comparison Displacement Results Quadrilateral Elements 369 Nodes

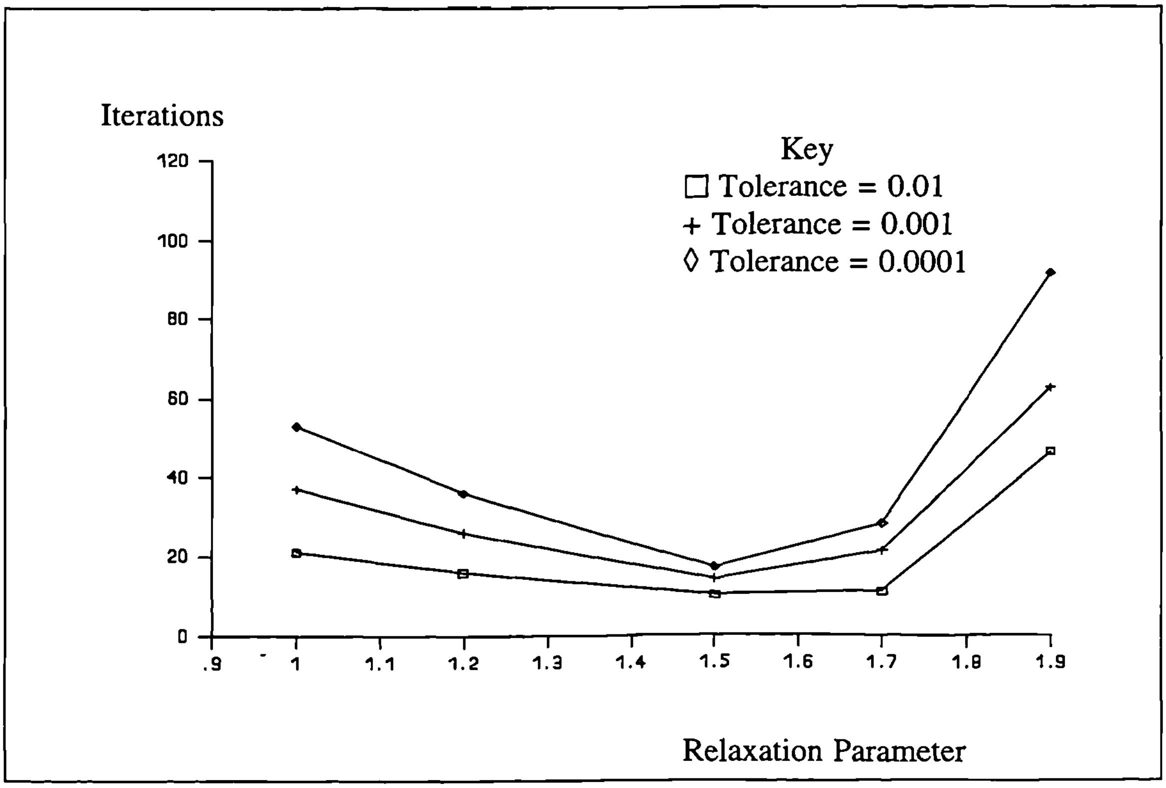

Figure B.26: Triangular Thermal Beam Iteration Results 33 nodes

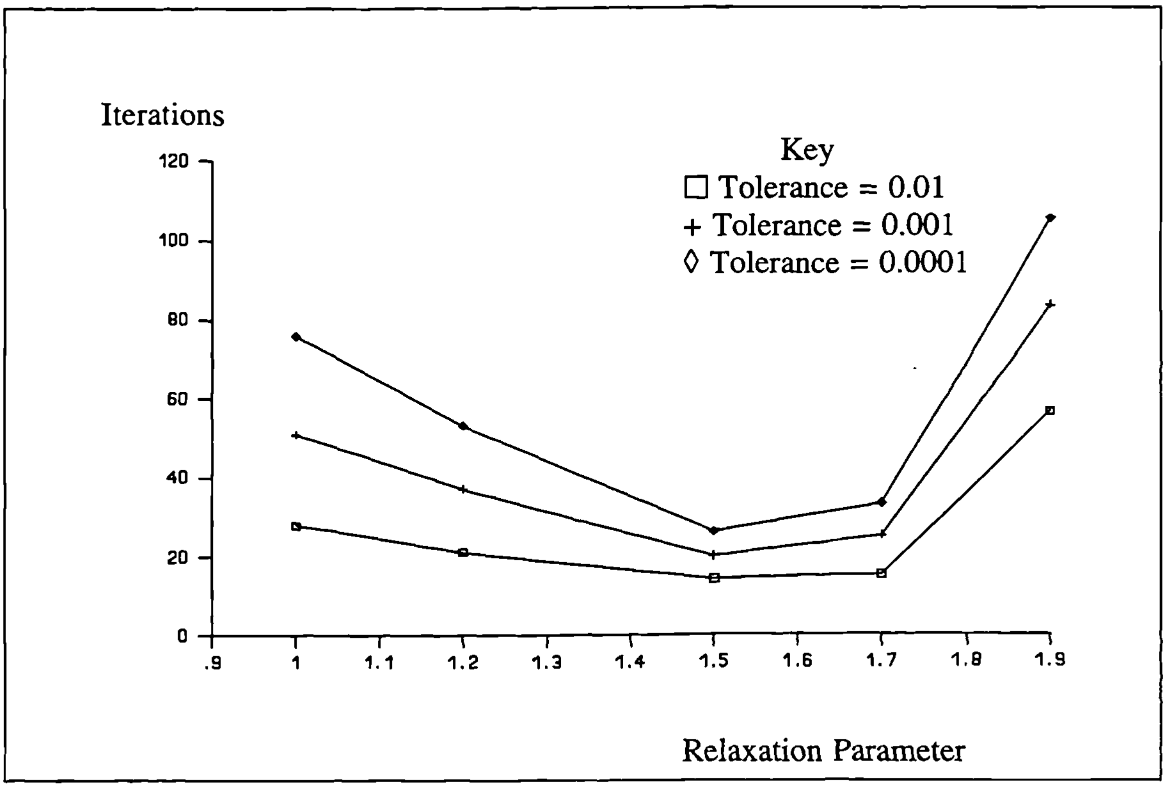

Figure B.27: Triangular Thermal Beam Iteration Results 105 nodes

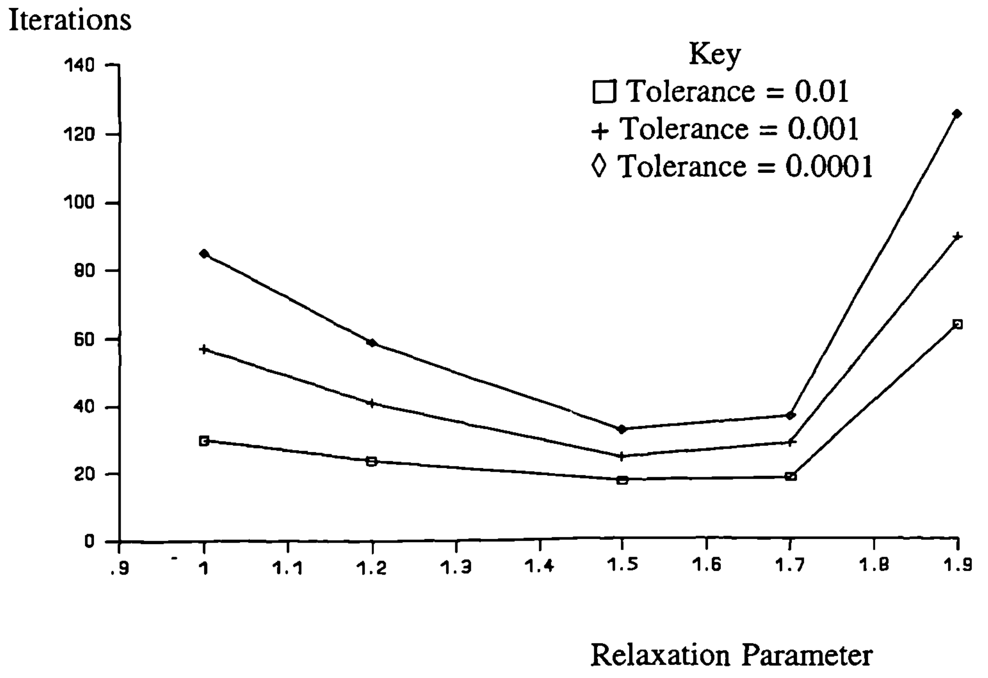

Figure B.28: Triangular Thermal Beam Iteration Results 369 nodes

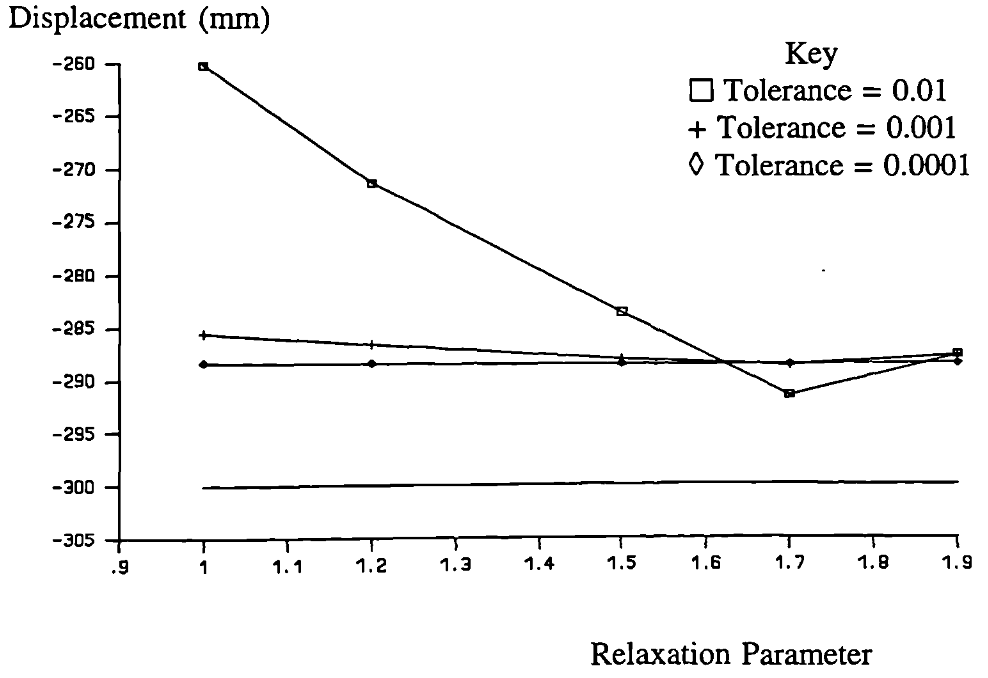

Figure B.29: Thermal Beam Comparison Displacement Results Triangular Elements 369 Nodes

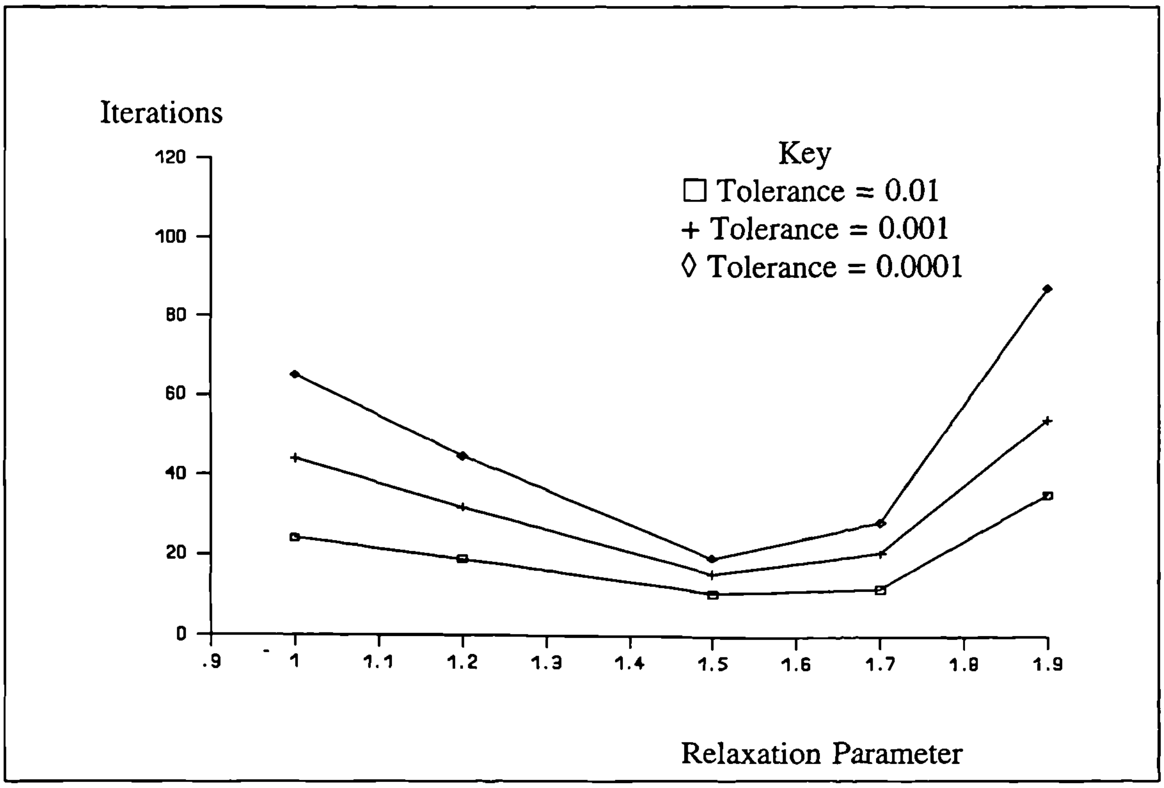

Figure B.30: Mixed Thermal Beam Iteration Results 33 nodes

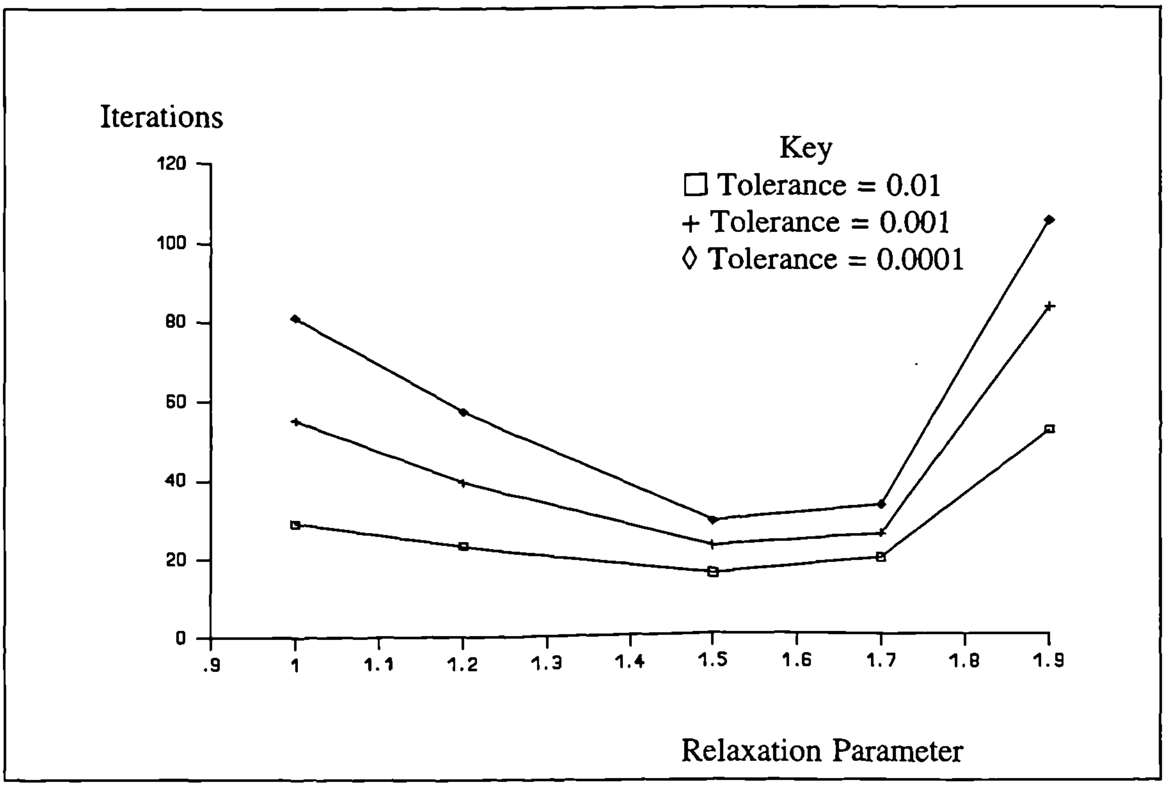

Figure B.31: Mixed Thermal Beam Iteration Results 105 nodes

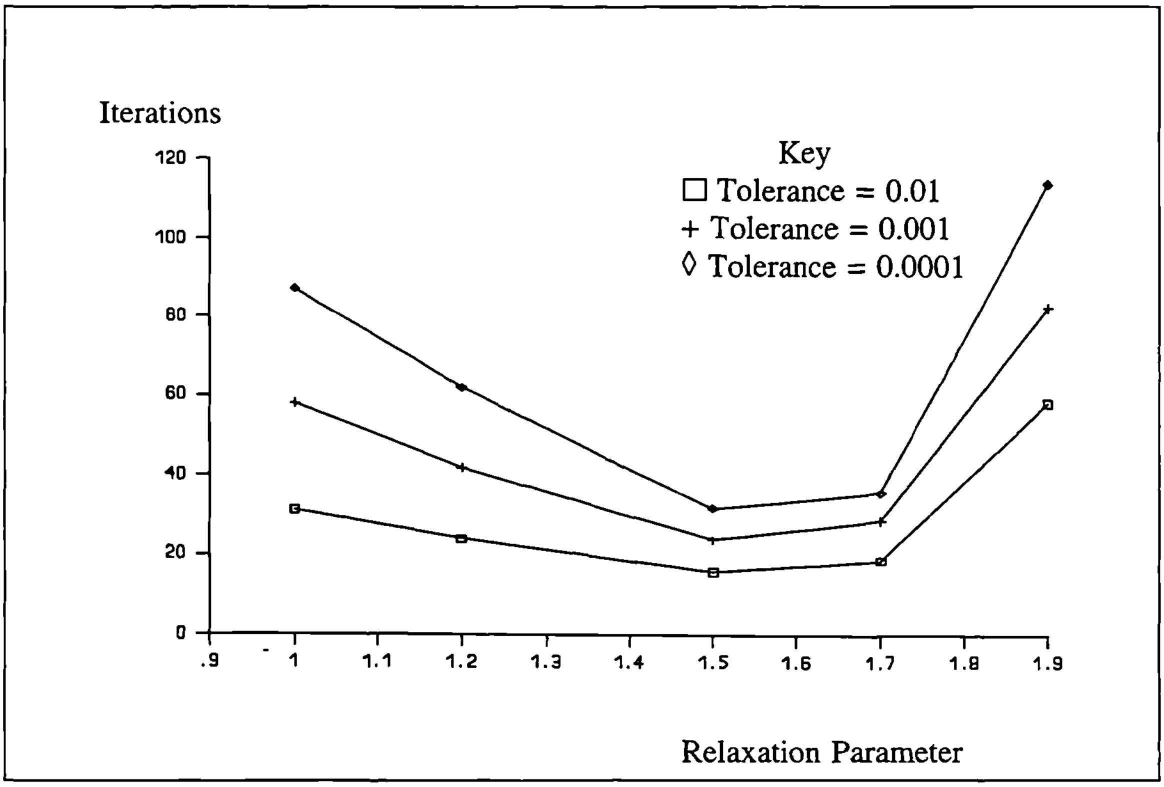

Figure B.32: Mixed Thermal Beam Iteration Results 369 nodes

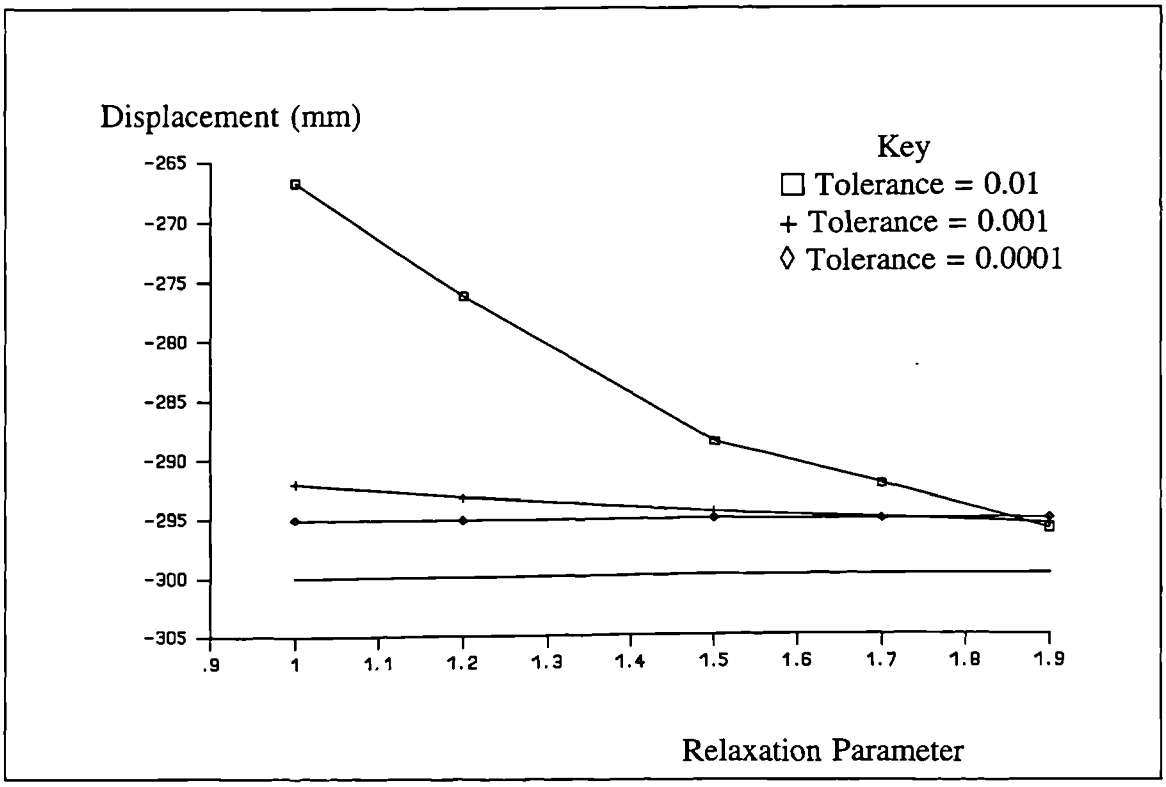

Figure B.33: Thermal Beam Comparison Displacement Results Mixed Elements 369 Nodes

Appendix C

Material Properties

C.1 1% Cr Steel

C.1.1 Conductivity

Conductivity (Btu/hr-ft-R)	Temperature Range T (R)
K = 34.10 - 0.00991 T	$T \leq 1931$
K = 8.44 + 0.00338 T	$1931 < T \leq 3140$
K = 144.65 - 0.04000 T	$3140 < T \leq 3200$
K = 16.65	$3200 < T$

Table C.1: Conductivity - Imperial

Conductivity (W/m°K)	Temperature Range T (°K)
K = 59.0183 - 0.030873 T	$T \leq 1072.778$
K = 14.6075 + 0.0105298 T	$1072.778 < T \leq 1744.444$
K = 250.352 - 0.124614 T	$1744.444 < T \leq 1777.778$
K = 28.8168	$1777.778 < T$

Table C.2: Conductivity - Metric

C.1.2 Specific Heat

Specific Heat (Btu/lb-R)	Temperature Range T (R)
Cp = 0.0924 + 0.00004094 T	$T \leq 1211$
Cp = -0.00828 + 0.0001241 T	$1211 < T \leq 1751$
Cp = -6.6322 + 0.003907 T	$1751 < T \leq 1859$
Cp = 11.6047 - 0.005903 T	$1859 < T \leq 1931$
Cp = 0.9247 - 0.0003722 T	$1931 < T \leq 2111$
Cp = 0.1038 + 0.00001667 T	$2111 < T \leq 3140$
Cp = -207.618 + 0.06617 T	$3140 < T \leq 3200$
Cp = 0.156	$3200 < T$

Table C.3: Specific Heat - Imperial

Specific Heat (J/kg°K)	Temperature Range T (°K)
Cp = 386.855 + 0.30853 T	$T \leq 672.7778$
Cp = -34.6663 + 0.935235 T	$672.7778 < T \leq 972.7778$
Cp = -27767.3 + 29.4436 T	$972.7778 < T \leq 1032.778$
Cp = 48586.1 - 44.486 T	$1032.778 < T \leq 1072.778$
Cp = 3871.49 - 2.80496 T	$1072.778 < T \leq 1172.778$
Cp = 434.584 + 0.125628 T	$1172.778 < T \leq 1744.444$
Cp = 653.132	$1744.444 < T$

Table C.4: Specific Heat - Metric

C.1.3 Density

Density (lb/cu ft)	Temperature Range T (R)
$\rho = 494 - 0.0112\ T$	$T \leq 3140$
$\rho = 1768.4 - 0.4167\ T$	$3140 < T \leq 3200$
$\rho = 581.1 - 0.04565\ T$	$3200 < T$

Table C.5: Density - Imperial

Density (kg/m^3)	Temperature Range T (°K)
$\rho = 7000$	for all T

Table C.6: Density - Metric

C.2 Moulding Sand

C.2.1 Conductivity

Conductivity (Btu/hr-ft-R)
$K = 0.44163 - 1.9380\times10^{-4}\ T + 1.385\times10^{-7}\ T^2$

Table C.7: Conductivity - Imperial

Conductivity (W/m°K)
$K = 0.76437 - 0.0006037518\ T + 0.0000007741295\ T^2$

Table C.8: Conductivity - Metric

C.2.2 Specific Heat

Specific Heat (Btu/lb-R)	Temperature Range T (R)
$Cp = 0.0987 + 0.000155\ T$	$T \leq 860$
$Cp = 0.1615 + 0.00008375\ T$	$860 < T \leq 1260$
$Cp = 0.2492 + 0.00001481\ T$	$1260 < T$

Table C.9: Specific Heat - Imperial

Specific Heat (J/kg°K)	Temperature Range T (°K)
$Cp = 413.232 + 1.1681\ T$	$T \leq 489.669$
$Cp = 676.159 + 0.631152\ T$	$489.669 < T \leq 706.739$
$Cp = 1043.34 + 0.11161\ T$	$706.739 < T$

Table C.10: Specific Heat - Metric

C.2.3 Density

Density - Imperial (lb/ft^3) : 105

Density - Metric (kg/m^3) : 1682.1

REFERENCE LIST

Adams, D.R. (ch6)
1993 Solidification Processes - Industrial Applications. Mathematical Modelling for Material Processing, Ed. M.Cross, J.F.T.Pittman, R.D.Wood, OUP, pp113-135.

Adams, D.R., Butlin, G., Higginbotham, G., Katgerman, L., Hills, A.W. and Charles, J.A.
1992 Modelling in Casting: Development in the UK. Metals and Minerals, September, pp496-500.

Akin, J. Ed. (ch1)
1986 Finite Element Analysis for Undergraduates. Academic Press, London.

Ampuero, J., Hoadley, A.F.A. and Rappaz, M. (ch7)
1991 Numerical and Experimental Study of Microporosity Evolution During the Solidification of Metallic Alloys. Modeling of Casting, Welding and Advanced Solidification Processes V, Ed. M.Rappaz, M.R.Ozgu and K.W.Mahin, The Minerals, Metals and Materials Society, pp449-454.

ASTEC CFDS. AEA Technology, Harwell, UK. (ch1)

Bailey, C., Fryer, Y.D., Cross, M. and Chow, P. (ch6)
1993 Predicting the Deformation of Castings in Moulds using a Control Volume Approach on Unstructured Meshes. Mathematical Modelling for Material Processing, Ed. M.Cross, J.F.T.Pittman, R.D.Wood, OUP, pp259-272.

Bakr, A.A. and Fenner, R.T. (ch4)
1983 Boundary Integral Equation Analysis of Axisymmetric Thermoelastic Problems. The Boundary Integral Equation Method in Stress Analysis. Mechanical Engineering Publications Ltd, London, pp37-49.

Baliga, B.R. and Patankar, S.V. (ch2)
1988 Elliptic Systems: Finite Element Method II. Handbook of Numerical Heat Transfer, ed. W.J.Minkowycz, E.M.Sparrow, G.E.Schneider, R.H.Pletcher, Chapter 11, John Wiley and Sons, pp421-461.

Baliga, B.R and Patankar, S.V. (ch1)
1983 A Control Volume Finite-Element Method for Two-Dimensional Fluid Flow and Heat Transfer. Numerical Heat Transfer, Volume 6, pp245-261.

Baliga, B.R. and Patankar, S.V. (ch1)
1980 A New Finite-Element Formulation for Convection-Diffusion Problems. Numerical Heat Transfer, Volume 3, pp393-409.

Baliga, B.R., Pham, T.T. and Patankar, S.V. (ch1)
1983 Solution of Some Two-Dimensional Incompressible Fluid Flow and Heat Transfer Problems, using a Control Volume Finite-Element Method. Numerical Heat Transfer, Volume 6, pp263-282.

Bellet, M., Bay, F., Brioist, J.J. and Chenot, J.L. (ch6)
1992 Modelling of the Thermomechanical Coupling in the Cooling Stage of the Casting Process. Numerical Methods in Industrial Forming Processes, NUMIFORM'92, Ed. J.-L.Chenot, R.D.Wood, O.C.Zienkiewicz, pp771-776.

Bercovier, M. and Rosenthal, A. (ch2)
1986 Using the Conjugate Gradient Method with Preconditioning for Solving FEM approximations of Elasticity Problems. Engineering Computations, March, Volume 3, pp77-80.

Boley, B.A. and Weiner, J.H. (ch4,ch2)
1967 Theory of Thermal Stresses. John Wiley and Sons, London.

Bourne, D.E. and Kendall, P.C. (ch2)
1992 Vector Analysis and Cartesian Tensors. Third Edition, Chapman and Hall, London.

Bowes, W.H. and Russell, L.T. (ch1)
1975 Stress Analysis by the Finite Element Method for Practising Engineers. Lexington Books, Massachusetts.

Bradley, F.J., Adams, T.M., Gadh, R. and Mirle, A.K. (ch6)
1993 On the Development of a Model-Based Knowledge System for Casting Process. Modeling of Casting, Welding and Advanced Solidification Processes VI, Ed. T.S.Piwonka, V.Voller, L.Katgerman, The Minerals, Metals and Materials Society, pp161-168.

Brebbia, C.A. (ch1)
1978 The Boundary Element Method for Engineers. Pentech Press, London.

Brody, H.D., Viswanathan, S. and Stoehr, R.A. (ch7)
1991 Predicting Shrinkage Microporosity in Aluminium Copper Alloys. Modeling of Casting, Welding and Advanced Solidification Processes V, Ed. M.Rappaz, M.R.Ozgu and K.W.Mahin, The Minerals, Metals and Materials Society, pp455-460.

Butlin, G.A. and Nutbourne, A.W. (ch6)
1993 A Strategy for Casting Modelling. Mathematical Modelling for Material Processing, Ed. M.Cross, J.F.T.Pittman, R.D.Wood, OUP, pp1-19.

Campbell, J. (ch6,ch7)
1991 Castings. Butterworth Heinemann Limited, Oxford.

Campbell, J. (ch7)
1969 On the Origin of Porosity in Long Freezing-Range Alloys. The British Foundryman, April, pp147-158.

Campbell, J. (ch7)
1968a Pore Nucleation in Solidifying Metals. The Iron and Steel Institute 110.

Campbell, J. (ch7)
1968b Hydrostatic Tension in Solidifying Metals. Transactions of the Metallurgical Society of AIME, Volume 242, February, pp262-271.

Campbell, J. (ch7)
1968c The Formation of Layer Porosity. Transactions of the Metallurgical Society of AIME, Volume 242, July, pp1464-1465.

Campbell, J. (ch7)
1967 Shrinkage Porosity in Castings (The Solidification of a Metal Sphere). Transactions of the Metallurgical Society of AIME, Volume 239, February, pp138-142.

Chen, G. and Zhou, J. (ch1)
1992 Boundary Element Methods. Academic Press, London, UK.

Chow, Peter M.-Y. (ch6)
1993 Control Volume Unstructured Mesh Procedure for Convection-Diffusion Solidification Processes. PhD Thesis, The University of Greenwich.

Chow, P. and Cross, M. (ch1)
1992 An Enthalpy Control Volume-Unstructured Mesh (CV-UM) algorithm for Solidification by Conduction Only. International Journal for Numerical Methods in Engineering, Volume 35, pp1849-1870.

Concus, Paul (ch1)
1967 Numerical Solution of the Nonlinear Magnetostatic-Field Equations in Two-Dimensions. Journal of Computational Physics, Volume 1, pp330-342.

Cowell, D.F., Knight, B. and Preddy, K. (ch6)
1993 A Design Support System for the Design of Casting Procedures. Applications of Artificial Intelligence in Engineering VIII, Volume 1: Design, Methods and Techniques, Ed. G.Rzevski, J.Pastor, R.A.Adey, Computational Mechanics Publications, London, pp151-159.

Cross, Mark (ch6)
1993 Development of Novel Computational Techniques for the Next Generation of Software Tools for Casting Simulation. Modeling of Casting, Welding and Advanced Solidification Processes VI, Ed. T.S.Piwonka, V.Voller, L.Katgerman, The Minerals, Metals and Materials Society, pp115-126.

Crouch, S.L. and Starfield A.M. (ch1)
1983 Boundary Element Methods in Solid Mechanics. George Allen and Unwin, London.

Curnier, A. (ch5)
1984 A Theory of Friction. International Journal of Solids Structures, Volume 20, No. 7, pp637-647.

Dalin, J.B., Le Guilly, J.M., Le Roy, P. and Maas, E. (ch7)
1992 Numerical Simulation Applied to the Production of Automotive Foundry Components. Numerical Methods in Industrial Forming Processes, NUMIFORM'92, Ed. J.-L.Chenot, R.D.Wood, O.C.Zienkiewicz, pp793-798.

Dantzig, J.A. (ch6)
1987 Mathematical Modeling of Solidification Processes. Interdisciplinary Issues in Materials Processing and Manufacturing. pp389-401.

Dow, J.O., Jones, M.S. and Harwood, S.A. (ch1)
1990 A New Approach to Boundary Modelling for finite Difference Applications in Solid Mechanics. International journal for Numerical methods in Engineering, Volume 30, pp90-113.

Fedelich, B., Mathiak, F.U. and Deisenroth, W. (ch6)
1992 Low Pressure Die Casting Simulation of a Wheel: Comparison with Experiments. Numerical Methods in Industrial Forming Processes, NUMIFORM'92, Ed. J.-L.Chenot, R.D.Wood, O.C.Zienkiewicz, pp799-804.

FEEDERCALC FOSECO Ltd, Tamworth. (ch6)

Fenner, R.T. (ch4,ch2)
1986 Engineering Elasticity. Ellis Horwood Limited, Chichester.

FIDAP FDI, Evanston, Ill., USA. (ch1)

FLOW3D CFDS. AEA Technology, Harwell, UK. (ch1)

FLUENT Creare.x, N.H., USA. (ch1)

Fryer, Y.D., Bailey, C., Cross, M. and Chow, P. (ch1)
1993 Predicting Macro Porosity in Shape Castings using an Integrated Control Volume Unstructured Mesh (CV-UM) Framework. Modeling of Casting, Welding and Advanced Solidification Processes VI, Ed. T.S.Piwonka, V.Voller, L.Katgerman, The Minerals, Metals and Materials Society, pp143-151.

Fryer, Y.D., Bailey, C., Cross, M. and Lai, C.-H. (ch1)
1991 A Control Volume Procedure for Solving the Elastic Stress-Strain Equations on an Unstructured mesh. Applied Mathematical Modelling, Volume 15, November/December, pp639-645.

Gao, D.M., Dhatt, G., Belanger, J. and Ben Cheikh A. (ch1)
1989 A Finite Element Simulation of Metal Flow in Moulds. Numerical Methods in Thermal Problems, Volume 6, Part 1, Ed. R.W.Lewis, K.Morgan, Pineridge Press, Swansea, pp421-430.

Griffin, D.S. and Kellogg, R.B. (ch1)
1967 A Numerical Solution for Axially Symmetrical and Plane Elasticity Problems. International Journal of Solids and Structures, Volume 3, pp781-794.

Griffin, D.S. and Varga, R.S. (ch1)
1963 Numerical Solution of Plane Elasticity Problems. SIAM J., Volume 11, Number 4, December, pp1046-1062.

Hansen, P.N. and Sahm, P.R. (ch7)
1988 How to Model and Simulate the Feeding Process in Casting to Predict Shrinkage and Porosity Formation. Modeling of Casting and Welding Processes IV, Ed. A.F.Giammi, G.J.Abbaschian, The Minerals, Metals and Materials Society, pp33-42.

Haslinger, Jaroslav (ch5)
1992 Signorini Problem with Coulomb's Law of Friction Shape Optimization in Contact Problems. International Journal for Numerical Methods in Engineering, Volume 34, pp223-231.

Hattel, J. and Hansen, P.N. (ch6)
1991 Simulating Distortion and Residual Stresses in Castings using FDM Techniques. Modeling of Casting, Welding and Advanced Solidification Processes V, Ed. M.Rappaz, M.R.Ozgu and K.W.Mahin, The Minerals, Metals and Materials Society, pp253-258.

Hattel, J. and Hansen, P.N. (ch1)
1990 FDM Solutions of the Thermoelastic Equations Using a Staggered Grid. Danish-German-Polish Workshop on Application of Computer Methods in Practice, Warsaw, Poland, October.

Hattel, J., Hansen, P.N. and Hansen, L.F. (ch6)
1993 Analysis of Thermal Induced Stresses in Die Casting using a Novel Control Volume FDM-Technique. Modeling of Casting, Welding and Advanced Solidification Processes VI, Ed. T.S.Piwonka, V.Voller, L.Katgerman, The Minerals, Metals and Materials Society, pp585-592.

Havner, K.S. and Stanton, E.L. (ch1)
1967 On Energy-Derived Difference Equations in Thermal Stress Problems. Journal of The Franklin Institute, Volume 284, Number 2, August, pp127-143.

Higgens, R.A. (ch6)
1989 Engineering Metallurgy Part 2. Metallurgical Process Technology. Edward Arnold, London.

Hogg, J.C. (ch6)
1991 Methoding and Numerical Modelling of Light Alloy Cast Components. The Foundryman, June, pp212-214.

Hookey, N.A. and Baliga, B.R. (ch1)
1988 Evaluation and Enhancements of Some Control Volume Finite-Element Methods - Part 2. Incompressible Fluid Flow Problems. Numerical Heat Transfer, Volume 14, pp273-293.

Hookey, N.A., Baliga, B.R. and Prakash, C. (ch1)
1988 Evaluation and Enhancements of Some Control Volume Finite-Element Methods - Part 1. Convection-Diffusion Problems. Numerical Heat Transfer, Volume 14, pp255-272.

Hrycaj, P., Serge, C. and Oudin, J. (ch5)
1991 Elasto-Plastic Finite Element Analysis of Unilateral Contact with Generalized Coulomb Friction. Engineering Computations, Volume 8, pp291-303.

Huang, H., Suri, V.K., El-Kaddah, N. and Berry, J.T. (ch7)
1993 The Effect of Interdendritic Feeding on Microporosity Formation. Modeling of Casting, Welding and Advanced Solidification Processes VI, Ed. T.S.Piwonka, V.Voller, L.Katgerman, The Minerals, Metals and Materials Society, pp219-226.

Ibrahimbegovic, A. and Wilson, E.L. (ch5)
1992 Unified Computational Model for Static and Dynamic Frictional Contact Analysis. International Journal for Numerical Methods in Engineering, Volume 34, pp233-247.

Jaswan, M.A. and Symm, G.T. (ch1)
1977 Integral Equation Methods in Potential Theory and Elastostatics. Academic Press, London.

Johnson, D.E. (ch1)
1970 A Difference Based Variational Method for Shells. International Journal of Solids and Structures, Volume 6, pp699-724.

Katona, Michael G. (ch5)
1983 A Simple Contact-Friction Interface Element with Applications to Buried Culverts. International Journal for Numerical and Analytical Methods in Geomechanics, Volume 7, pp371-384.

Kermandis, Theodor (ch1)
1975 A Numerical Solution for Axially Symmetrical Elasticity Problems. International Journal of Solids and Structures, Volume 11, pp493-500.

Kettleborough, C.F., Hussain, S.R. and Prakash, C. (ch1)
1989 Solution of Fluid Flow Problems with the Vorticity-Streamfunction Formulation and the Control-Volume-Based Finite-Element Method. Numerical Heat Transfer, Part B, Volume 16, pp31-58.

Klarbring, A. and Björkman, G. (ch5)
1992 Solution of Large Displacement Contact Problems with Friction using Newton's Method for Generalized Equations. International Journal for Numerical Methods in Engineering, Volume 34, pp249-269.

Konovalov, A.N. (ch1)
1964 Iterative Systems for Solving Problems in the Theory of Elasticity. U.S.S.R. Computational Mathematics and Mathematical Physics, Volume 4, pp217-222.

Kubo, K. and Pehlke, R.D. (ch7)
1985 Mathematical Modeling of Porosity Formation in Solidification. Metallurgical Transactions B, Volume 16B, June, pp359-366.

Kubo, K. and Pehlke, R.D. (ch7)
1986 Porosity Formation in Solidifying Castings. AFS Transactions, pp753-756.

Lai, C.-H., and Liddell, H.M. (ch2)
1987 Preconditioned Conjugate Gradient Methods on the DAP. The Mathematics of Finite Elements and Applications VI, MAFELAP 1987, Ed. J.R.Whiteman, Academic Press, pp45-54.

Laurent, V. and Rigaut, C. (ch7)
1992 An Experimental and Numerical Study of Criteria Functions for Predicting Microporosity in Cast Aluminium Alloys. A.F.S. Chicago

Lawrence, Peter (ch6)
1993 Private Communication.

Letniowski, F.W. and Forsyth, P.A. (ch1)
1991 A Control Volume Finite Element Method for Three-Dimensional NAPL Groundwater Contamination. International Journal for Numerical Methods in Fluids, Volume 13, pp955-970.

Lewis, B.A. and Cross, M (ch4)
1978 IFECS - an Interactive Finite Element Computing System. Applied Mathematical Modelling, Vol 2, September, pp165-176.

Lewis, R.W. and Roberts, P.M. (ch6)
1987 Finite Element Simulation of Solidification Problems. Modelling of Flow and Solidification of Metals, Ed. T.J.Smith, Martinus Nijhoff, pp61-92.

Lewis, R.W., Usamani, A.S. and Huang, H.C. (ch1)
1991 Casting Modelling by Finite Elements - Our Experience. Modeling of Casting, Welding and Advanced Solidification Processes V, Ed. M.Rappaz, M.R.Ozgu and K.W.Mahin, The Minerals, Metals and Materials Society, pp3-14.

Lipinski, D.M., Schaefer, W. and Flender, E. (ch7)
1993 Numerical Modelling of the Filling Sequence and Solidification of Castings. Modeling of Casting, Welding and Advanced Solidification Processes VI, Ed. T.S.Piwonka, V.Voller, L.Katgerman, The Minerals, Metals and Materials Society, pp389-396.

MAGMASOFT MAGMA GmbH, Aachen, Germany (ch6)

Martins, J.A.C., Oden, J.T. and Simoes, M.F. (ch5)
1990 A Study of Static and Kinetic Friction. International Journal of Engineering Science, Volume 28, No. 1, pp29-92.

Melosh, R.J. (ch1)
1963 Basis for Derivation of Matrices for the Direct Stiffness Method. Journal American Institute for Aeronautics and Astronautics, Volume 1, pp1631-1637.

Michalek, K.P., Kelly, J.E. and Dantzig, J.A. (ch6)
1986 Modeling of In-Mold Heat Transfer in Continuous Casting of Steel. Modeling and Control of Casting and Welding Processes, Ed. S.Kou, R.Mehrabian, AIME, pp497-516.

MICROFIELD Rockfield, ?? (ch4)

Minkowycz, W.J., Sparrow, E.M. and Schneider, G.E. (eds) (ch1)
1988 Handbook of Numerical Heat Transfer, John Wiley and Sons, London.

Moosbrugger, J.C. and Berry, J.T. (ch6,ch7)
1986 Calculation of Feeding Range for Hypoeutectic A-357 Alloy using FEM Solidification Model Results. AFS Transactions, pp373-380.

Moscardini, A.O. (ch4,ch5)
1985 Contributions to the Development of Finite Element Software in an Interactive Computing Environment. PhD Thesis, Sunderland Polytechnic.

Munday, A.J. and Farrar, R.A. (ch1)
1986 An Engineering Data Book, Macmillan Education Ltd, London, p37.

Natarajan, R., Chu, C.N. and Kashyap, R.L. (ch6)
1989 An Integrated Environment for Intelligent Design of Castings. Expert System Application in Materials Processing and Manufacturing, Ed. M.Y.Demeri, The Minerals, Metals and Materials Society, pp143-156.

Ng, S.F. and Bencharif, N. (ch1)
1989 A Finite Difference Computer Program for Modelling of Thick Rectangular Plates. Computers and Structures, Volume 33, Number 4, pp1011-1016.

Niyama, E., Uchida, T., Morikawa, M. and Saito, S. (ch7)
1982 A Method of Shrinkage Prediction and its Application to Steel Casting Practice. AFS Cast Metals Research Journal, September, pp52-63.

Oden, J.T. and Martins J.A.C (ch5)
1985 Models and Computational Methods for Dynamic Friction Phenomena. Computer Methods in Applied Mechanical Engineering, Volume 52, pp725-634.

Oñate, E., Cervera, M. and Zienkiewicz, O.C. (ch1)
1992 A Finite Volume Format for Structural Mechanics. International Center for Numerical Methods in Engineering, Barcelona, Spain, May.

Ottosen, N and Petersson, H. (ch1,2)
1992 Introduction to the Finite Element Method. Prentice Hall, London.

Owen, D.R.J. and Hinton, E. (ch1)
1980 A Simple Guide to Finite Elements. Pineridge Press, Swansea.

Patanker, S.V. (ch5)
1980 Numerical Heat Transfer and Fluid Flow. Hemisphere, Washington.

Pellini, William S. (ch7)
1953 Factors which Determine Riser Adequacy and Feeding Range. AFS Transactions, 61, pp61-80.

PHOENICS CHAM Ltd., London, UK.

Prakash, C. (ch1)
1987 Examination of the Upwind (Donar-cell) Formulation in Control Volume Finite-Element Methods for Fluid Flow and Heat Transfer. Numerical Heat Transfer, Volume 11, pp401-416.

Prakash, C. (ch1)
1986 An Improved Control Volume Finite-Element Method for Heat and Mass Transfer, and for Fluid Flow using Equal-Order Velocity-Pressure Interpolation. Numerical Heat Transfer, Volume 9, pp253-276.

Prakash, C. and Patankar, S.V. (ch1)
1987a A Control-Volume Finite-Element Method for Predicting Flow and Heat Transfer in Ducts of Arbitrary Cross Sections - Part I: Description of the Method. Numerical Heat Transfer, Volume 12, pp389-412.

Prakash, C. and Patankar, S.V. (ch1)
1987b A Control-Volume Finite-Element Method for Predicting Flow and Heat Transfer in Ducts of Arbitrary Cross Sections - Part II: Application to some Test Problems. Numerical Heat Transfer, Volume 12, pp413-437.

Prakash, C. and Patankar, S.V. (ch1)
1985 A Control Volume-Based Finite-Element Method for Solving the Navier-Stokes Equations using Equal-Order Velocity-Pressure Interpolation. Numerical Heat Transfer, Volume 8, pp259-280.

PREDICT SDRC, USA. (ch6)

Preddy, K.L. (ch6)
1993 Computer Aided Methods Engineering in Non Ferrous Foundries. Technical Meeting, The Kent Section of the Institute of British Foundrymen, Rochester, October.

PROCAST UES, Ohio, USA (ch6)

RAMPANT Creare.x, N.H., USA.

Rigaut, C., Laurent, V., Kreziak, G. and Laty, P. (ch7)
1993 Example of Prediction of Microporosity Formation of an A356 Cast Part With Simulor Software. Modeling of Casting, Welding and Advanced Solidification Processes VI, Ed. T.S.Piwonka, V.Voller, L.Katgerman, The Minerals, Metals and Materials Society, pp277-284.

Runesson, K., Klisinski, M. and Larsson, R. (ch5)
1993 Formulation and Implementation of Conditions for Frictional Contact. Engineering Computations, Volume 10, pp3-14.

Ryan, J.D., Tims, M.L., Shultz, D.M. and Worshum, T.J. (ch7)
1993 Solidification Simulation of a Large Steel Casting for Naval Application. Modeling of Casting, Welding and Advanced Solidification Processes VI, Ed. T.S.Piwonka, V.Voller, L.Katgerman, The Minerals, Metals and Materials Society, pp733-740.

Samarskii, A.A. (ch1)
1964 Economic Differencing Schemes for a Hyperbolic System of Equations with Compound Derivatives and their Application to Equations in the Theory of Elasticity. U.S.S.R Comput. Math. and Math. Physics, Volume 5, pp44-56.

Samonds, M., Lewis, R.W., Morgan K. and Symberlist, R. (ch6)
1985 Finite Element Modelling of the Mold-Metal Interface in Casting Simulation with Coincident Nodes or Thin Elements. Computational Techniques in Heat Transfer, Ed. R.W.Lewis, K.Morgan, J.Johnson and R.Smith, chapter 13, Pineridge Press, pp331-354.

Saran, M.J. and Wagoner, R.H. (ch5)
1991a A Consistent Implicit Formulation for Nonlinear Finite Element Modeling with Contact and Friction: Part I - Theory. Journal of Applied Mechanics, Volume 58, June, pp499-506.

Saran, M.J. and Wagoner, R.H. (ch5)
1991b A Consistent Implicit Formulation for Nonlinear Finite Element Modeling with Contact and Friction: Part II - Numerical Verification and Results. Journal of Applied Mechanics, Volume 58, June, pp507-512.

Schneider, G.E. (ch6,ch2)
1988 Elliptic Systems: Finite-Element Method I. Handbook of Numerical Heat Transfer, ed. W.J.Minkowycz, E.M.Sparrow, G.E.Scneider, R.H.Pletcher, Chapter 10, John Wiley and Sons, pp379-419.

Schneider, G.E. and Raw, M.J. (ch1)
1987a Control Volume Finite-Element Method for Heat Transfer and Fluid Flow using Collocated Variables - 1. Computational Procedure. Numerical Heat Transfer, Volume 11, pp363-390.

Schneider, G.E. and Raw, M.J. (ch1)
1987b Control Volume Finite-Element Method for Heat Transfer and Fluid Flow using Collocated Variables - 2. Application and Validation. Numerical Heat Transfer, Volume 11, pp391-400.

Schneider, G.E. and Raw, M.J. (ch1)
1986 A Skewed, Positive Influence Coefficient Upwinding Procedure for Control-Volume-Based Finite-Element Convection-Diffusion Computation. Numerical Heat Transfer, Volume 9, pp1-26.

Segerlind, L.J. (ch1)
1976 Applied Finite Element Analysis. John Wiley and Sons, London.

SIMULOR Aluminium Pechiney, France. (ch6)

Smith, G.D. (ch4)
1975 Numerical Solution of Partial Differential Equations. Compton Publishing Ltd, OUP.

SOLSTAR FOSECO Ltd, Tamworth. (ch6)

STAR-CD Computational Dynamics Ltd., London, UK. (ch1)

Stefanescu, Doru Michael (ch7)
1993 Critical Review of the Second Generation of Solidification Models for Castings: Macro Transport - Transformation Kinetic Codes. Modeling of Casting, Welding and Advanced Solidification Processes VI, Ed. *T.S.Piwonka, V.Voller, L.Katgerman, The Minerals, Metals and Materials* Society, pp3-20.

Tabor, David (ch5)
1981 Friction - The Present State in our Understanding. Transactions of the ASME, Series F - Lubrication Technology, Volume 103, April, pp169-179.

Takahashi, S. and Brebbia, C.A. (ch5)
1988 Boundary Elements X. Volume 3, pp353-379.

Thomas, B.G., Samaraseka, I.V. and Brimacombe, J.K. (ch6)
1986 Application of Mathematical Heat Flow and Stress Models of Steel Ingot Casting to Investigate Panel Crack Formation. Modeling and Control of Casting and Welding Processes, Ed. S.Kou, R.Mehrabian, AIME, pp479-495.

Timoshenko, S.R. and Goodier, J.N. (ch4,ch2)
1970 Theory of Elasticity. 3ed., Singapore: McGraw-Hill.

Turner, M.J., Clough, R.W., Martin, H.C. and Topp, L.J. (ch1)
1956 Stiffness and Deflection Analysis of Complex Structures. Journal of the Aeronautical Sciences, Volume 23, Number 9, pp805-823.

Upadhya, G., Paul, A.J. and Hill, J.L. (ch6)
1993 Optimal Design of Gating and Risering for Castings: An Integrated Approach using Empirical Heuristics and Geometric Analysis. Modeling of Casting, Welding and Advanced Solidification Processes VI, Ed. T.S.Piwonka, V.Voller, L.Katgerman, The Minerals, Metals and Materials Society, pp135-142.

Vick, B., Furey, M.J. and Foo, S.J. (ch5)
1991 Boundary Element Thermal Analysis of Sliding Contact. Numerical Heat Transfer, Part A, Volume 20, pp19-40.

Viswanathan, Srinath (ch7)
1990 The Relation of Solidification Parameters to Microporosity in Al-4.5% Cu Alloy Castings. PhD Thesis, University of Pittsburgh.

Viswanathan, S., Sikka, V.K. and Brody, H.D. (ch7)
1993 The Application of Quality Criteria for the Prediction of Porosity in the Design of Casting Processes. Modeling of Casting, Welding and Advanced Solidification Processes VI, Ed. T.S.Piwonka, V.Voller, L.Katgerman, The Minerals, Metals and Materials Society, pp285-292.

Viswanathan, S., Sikka, V.K. and Brody, H.D. (ch7)
1992 Using Solidification Parameters to Predict Porosity Distributions in alloy Castings. The Journal of The Minerals, Metals and Materials Society, September, pp37-40.

Walther, M.K. (ch7)
1987 Experimental Verification of C.A.S.T.. AFS Transactions, pp15-24.

Webster, C.A.G and Weller, M. (ch6)
1993 Alexsys - An Expert System for the Aluminium Pressure Die Casting Industry. Applications of Artificial Intelligence in Engineering VIII, Volume 2: Applications and Techniques, Ed. G.Rzevski, J.Pastor, R.A.Adey, Computational Mechanics Publications, London, pp205-217.

Winslow, A.M. (ch1)
1966 Numerical Solution of the Quasilinear Poisson Equation in a Nonuniform Triangle Mesh. Journal of Computational Physics, Volume 1, Number 2, November, pp149-172.

Zienkiewicz. O.C. (ch1)
1970 The Finite Element Method: From Intuition to Generality. Applied Mechanics Reviews, Volume 23, pp249-256.

Zienkiewicz, O.C. (ch1)
1977 The Finite Element Method, Third edition, McGraw-Hill, London.

Zienkiewicz, O.C. (ch1)
1983 The Generalised Finite Element Method - State of the Art and Future Directions. Transactions of the ASME Journal of Applied Mechanics, Volume 50, pp1210-1217.

Zienkiewicz, O.C. and Cheung, Y.K. (ch1)
1965 Finite Elements in the Solution of Field Problems. The Engineer, pp507-510.

Zienkiewicz, O.C. and Oñate, E. (ch1)
1990 Finite Volumes vs Finite Elements. Is There Really a Choice? International Center for Numerical Methods in Engineering, Barcelona, Spain, November.

Zienkiewicz, O.C. and Taylor, R.L. (ch1)
1989 The Finite Element Method, Volume 1. Basic Formulation and Linear Problems. Fourth Edition, McGraw-Hill, London